

論文 / 著書情報
Article / Book Information

題目(和文)	電子ビーム励起推積法の開発及びメソスコピックデバイスへの応用に関する研究
Title(English)	Study of electron-beam-induced reaction process and its applications to mesoscopic devices
著者(和文)	三浦成久
Author(English)	Naruhisa Miura
出典(和文)	学位:博士(工学), 学位授与機関:東京工業大学, 報告番号:甲第3721号, 授与年月日:1998年3月26日, 学位の種別:課程博士, 審査員:
Citation(English)	Degree:Doctor (Engineering), Conferring organization: Tokyo Institute of Technology, Report number:甲第3721号, Conferred date:1998/3/26, Degree Type:Course doctor, Examiner:
学位種別(和文)	博士論文
Type(English)	Doctoral Thesis

DOCTORAL DISSERTATION

**Study of Electron-Beam-Induced Reaction Process
and Its Applications to Mesoscopic Devices**

A DISSERTATION SUBMITTED IN PARTIAL FULFILLMENT
OF THE REQUIREMENTS FOR THE DEGREE OF
DOCTOR OF ENGINEERING

December, 1997

Presented by Naruhisa MIURA

Directed by
Associate Professor Akira YAMADA
Professor Makoto KONAGAI

*Department of Electrical and Electronic Engineering
Graduate School of Science and Engineering
Tokyo Institute of Technology*

Table of Contents

Chapter 1	Overview and Objectives of This Research	1
Chapter 2	Fundamental Aspects of Nanostructure Fabrication and Mesoscopic Devices	6
2.1	Introduction	6
2.2	Nanostructure fabrication technology	7
2.3	Superconducting weak link devices	9
2.4	Single-electron transistors	13
2.5	Summary	16
	References	17
Chapter 3	Modification of Carbon Nanostructures by Electron-Beam-Induced Deposition Technique	22
3.1	Introduction	22
3.2	Overview of this technique	23
3.3	Fabrication of carbonaceous wire	26
3.4	Application to etching mask for fabricating nanowires	35
3.5	Summary	40
	References	41
Chapter 4	Characterization of Heavily-Doped Semiconductors and Its Applications to Superconducting Devices	43
4.1	Introduction	43
4.2	Electrical properties of heavily-doped semiconductors	44
4.3	Anomalous electrical properties in n^{++} -InN	55
4.4	Theoretical consideration of weak link device for employing heavily-doped semiconductors	68
4.5	Investigation of three-terminal weak link devices	74
4.6	Summary	80
	References	81

Chapter 5	Fabrication of Superconducting Weak Link Devices Using Heavily-Doped Semiconductors	83
5.1	Introduction	83
5.2	Deposition of superconducting Nb and NbN thin films	85
5.3	Weak link device of NbN / ZnO / NbN stacked structure	103
5.4	Weak link device of Nb / n ⁺⁺ -Si / Nb coplanar structure	114
5.5	Summary	122
	References	123
Chapter 6	Evaluation of Carbonaceous Material for Microscopic Devices	125
6.1	Introduction	125
6.2	Characterization of carbon microfilm	127
6.3	Metal / insulator / metal diode of Au / a-C system	133
6.4	MIM diode of WC _x / a-C system	140
6.5	Summary	148
	References	149
Chapter 7	Single-Electron Transistors with Amorphous Carbon Nanostructures	151
7.1	Introduction	151
7.2	One-dimensional a-carbon dot arrays	153
7.3	Double junction with side-gated structure	163
7.4	Summary	175
	References	176
Chapter 8	General Conclusions	177
	Acknowledgments	181
	List of Publications	183

Chapter 1

Overview and Objectives of This Research

Recent highly-developed information-oriented society is no wonder based on the progress in semiconductor technology and semiconductor products which deals with huge quantity of information in a very few seconds being transmitted through the intelligence network. Especially the transaction speed is the key issue for the development, together with the huge data storage. For the further improvement in commercial products much more for upgrading human living activities in the society, semiconductor devices have owed and must continue to owe the significant roles for the future. Therefore, continual demands of high performance in large scale integration (LSI) devices have become severe year by year or day by day with a progress in microfabrication technology. However, the actual circumstance on the Si related technologies have come to be matured and we are about to reach the stage that drastic improvement in device performance could no longer be expected on them. Therefore, the technological breakthrough is indeed necessary, that is, a development of a new device based on new fundamentals.

One of the promising directions for the future micro-electronics lays on the single-electron technology. Single-electron transistors (SETs) are prominent in power dissipation problems as each electron is controlled one by one. They are now attracting much attentions and energetically studied from many points of view. The use of Coulomb blockade effect enables to establish a thoroughly brand-new architecture for the design of the logic circuits. But in essence, development in realizing discrete SETs is the most significant feature.

Another direction could be considered to lay on the superconducting devices. Although the operating temperature of them must be about liquid helium or liquid nitrogen temperature, their potential of overwhelming the conventional Si devices have been attracted significant attention with a progress in high T_c (superconducting transition temperature) material science. By using superconducting effect, high speed and low power dissipation devices have been realized as well as its application to the wire in the LSI circuit or to the

power devices. Especially the Josephson effect or the Josephson junction first opened practical studies for the cryoelectronic devices.

Considering from the production aspects, establishment of an easy microfabrication technique is inevitable in order to realize those devices besides the conventional electron-beam lithography. This study took notice on a beam-induced reaction process, which is one of the easy techniques for the microfabrication. It features direct processing such as direct deposition or etching in the order of a few nanometer in minimum scale which can be taken place only at the spot where the electron- or ion-beam is irradiated. Moreover, the complicated lithography using photoresist is not required and a new device fabrication process could be developed combining the conventional processes although it has problems in though put when concerns the LSI applications or in processing onto the insulating material.

Therefore, the establishment of microfabrication technique based on this beam-induced-deposition method and its applications to fabricate mesoscopic or microscopic devices are the main purposes of this study. To achieve these targets, several experimental studies were extensively supplemented such as a characterization of heavily-doped semiconductors. For the processing tool, scanning electron microscopy was mainly utilized since it enables not only to monitor the minute structures but the beam-induced deposition process without any its modification in particular just by using residual hydrocarbon molecules as depositing precursor.

This doctoral dissertation consists of eight chapters. Overview of this dissertation is summarized in Fig. 1.1. This study is to establish the microstructure fabrication technique by the electron-beam-induced process and its active and passive applications for the device fabrication; single-electron transistors using directly-deposited carbon microstructures and superconducting weak link devices using a heavily-doped semiconductor whose structure was fabricated with a carbonaceous wire as a process mask. General overview and objectives of this research were described in this chapter. In the following chapter, fundamental aspects of the nanostructure fabrication techniques and mesoscopic devices are introduced. Some of the nanoscale processing technologies are overviewed and mesoscopic or microscopic

devices such as superconducting weak link devices and single-electron transistors are concentrated for the target devices in this study. Their device operation mechanisms are briefly discussed.

Since the base technology of this research is the electron-beam-induced deposition, which is a skillful and an easy technique for microfabrication, its fundamental deposition procedure is established in Chapter 3. In this section, a minute carbonaceous wire is first deposited from the residual hydrocarbon molecules adsorbed on a substrate surface using scanning electron microscopy. After the optimization for obtaining the narrow wire, its applicability to an etching mask is verified. Skillful application of a carbon conic structure to the cantilever of the atomic force microscope (AFM) is also demonstrated to obtain a high resolution AFM image.

For realizing a superconducting weak link device using heavily-doped semiconductors, which is one of the targeted devices in this study, characterization of the various degenerated semiconductors is performed in the early part of Chapter 4. Through the characterization, epitaxial InN thin films grown on sapphire substrate were found to exhibit anomalous electrical properties at very low temperature for the first time. Origins of this superconductor-like characteristics are also evaluated. The late part of the chapter, theoretical consideration of the weak link devices using the degenerated semiconductors are carried out.

In chapter 5, fabrication of the superconducting weak link devices and its electrical characterization are performed. By using polycrystalline n^+ -ZnO and epitaxial n^{++} -Si films as normal layers, stacked and coplanar type Josephson weak link junctions are fabricated, respectively, and superconducting characteristics were observed at both devices. Especially in order to realize a sub-micron gap structure for the Nb/ n^{++} -Si/Nb coplanar junction, new fabrication process using a carbonaceous wire to define the gap length is also proposed. Deposition of superconducting Nb and NbN thin films by DC magnetron sputtering method is also carried out in advance and its conditions are optimized in the early part of this chapter.

The weak link devices are realized using the carbonaceous microstructures for the

process tool, however, its direct application to the device consisting material is an attractive approach for the simple fabrication of microscopic devices. Based on this consideration, evaluation of the carbonaceous material grown by this technique using SEM is performed in Chapter 6. Following to the Raman spectroscopy, metal/insulator/metal diodes using Au and WC_x as metal electrodes are fabricated for the electrical characterization of the carbonaceous material. From this chapter, focused ion beam system is employed to deposit metallic wires for the fine metal electrodes and for the purpose of fabricating microscopic devices.

In Chapter 7, single-electron transistors using these amorphous carbon in a dot shape are fabricated. Single-electron charging effects are observed in one-dimensional dot arrays at low temperature, and moreover, the Coulomb blockade oscillation is successfully recorded from a device of double junction with a side gate even at a room temperature for the first time.

The concluding remarks of this dissertation are stated at the final chapter, Chapter 8.

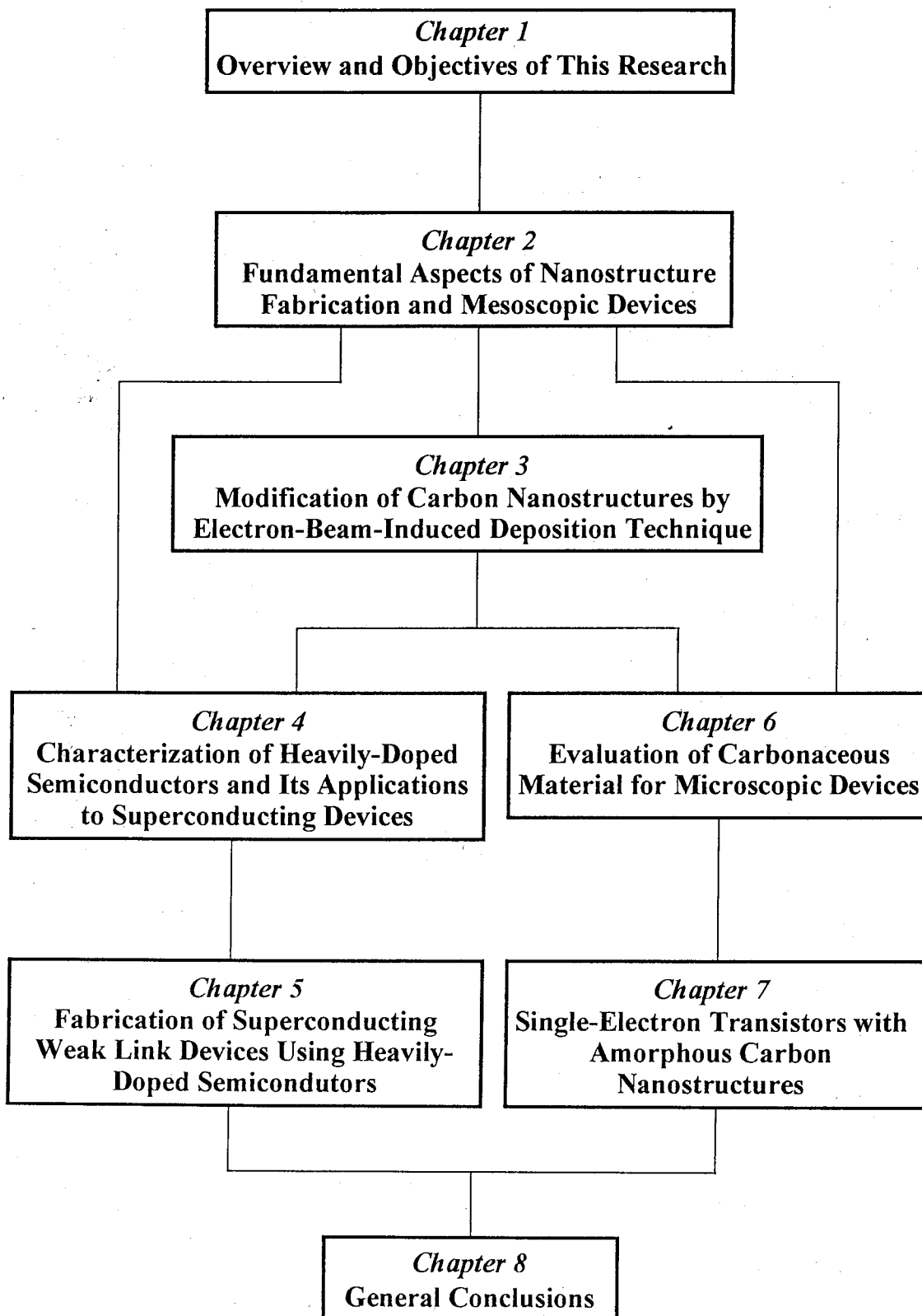


Fig. 1.1 Overview of this dissertation.

Chapter 2

Fundamental Aspects of Nanostructure Fabrication and Mesoscopic Devices

2.1 Introduction

In this chapter, the technological and historical background of the mesoscopic and microscopic devices, especially the superconducting weak link devices and the single-electron transistors are reviewed in addition to the nanostructure fabrication techniques. The operation mechanism of those devices are based on the superconducting proximity effect and the single-electron charging effect, respectively, which might not be familiar but are one of the promising fundamentals to be applied to the discrete devices in the future electronic integrated circuit. Since their successful device operation critically depends on their nature of minuteness in the device size, development in nanoscale processing technology is indispensable. Although the conventional and widely-used electron-beam (EB) lithography is the key method, other approaches should be developed for seeking better controllability or for realizing minute structures whose scale is not attainable by the EB lithography. In particular, scanning probe microscope (SPM) processing and beam-induced reaction processes are presented in the next section since these techniques are attracting significant attention in terms of nanostructure fabrication. Therefore in this section, those backgrounds are briefly introduced before describing the experimental results of this study.

2.2 Nanostructure Fabrication Technology

For producing microscopic structures and devices, development in nanostructure fabrication technology is indispensable. In place of the electron-beam lithography, various methods are studied everywhere. Scanning probe microscope (SPM) processing have attracted much attention recently. Except for its intrinsic usage to monitor the substrate surface structure in a resolution of atomic level, following versatility are reported; manipulating each atom individually [1-3], anodization of the substrate surface with negatively voltage-biased cantilever (SPM nano-oxidation process) [4-8], exposing organic resist layers (STM/AFM lithography) [9, 10], monitoring single-electron charging effect through the air barrier [11], selective STM-induced chemical vapor deposition in which a metalorganic gas is decomposed between the STM tip and the substrate [12, 13], atom transfer due to field evaporation from STM tips or AFM cantilevers [14-17] and so forth. Although they are attracting significant attention in the atomic scale or nanoscale processing mentioned above, these SPM related techniques are relatively time consuming and so they might not be suitable for the mass production.

As the other candidates, beam-induced reaction process could be listed. This is different from the EB lithography because it is not lithographic procedure but direct deposition or etching process. By employing some precursor molecules into the beam chamber, they are irradiated to decompose and form a deposit only at the beam scanned area. This is the deposition outline. In the case of etching, direct etching by the beam (normally the ion-beam) or the gas-assisted etching both occur also at the place where the beam was scanned. Since the beam diameter is of the order of a few nanometer, minimum size of that order could be processed. Although the electron or ion dose per length is generally larger than the conventional EB lithography which partly governs the throughput, total device fabrication time could be reduced since each device is to be directly fabricated by this simple process. The first experiments were carried out in 1956 to measure astigmatism in a probe forming system [18] and in 1969 to determine the highest possible information density obtainable by lithographic methods [19, 20]. Since then, wide variety of applications have been investigated including the first application to the etching masks for ion milling [21] and

the first directly-fabricated metal nanostructures [22]. The process was employed in a shadow projector to deposit materials from various precursors [23]. Some of the ever reported applications and precursors are presented in the following chapter. Due to the capability to control the beam position and dwell time per pixel (or beam dose), three-dimensional deposits are constructed with nanometer precision under computer control [24]. Particular and unique applications are the fabrication of corpuscular field emission sources with integrated extractor optics [25], sources for pixels in flat panel displays [26], three-dimensional wire structures to the nano-loops and the flux sensors close to the surface [27].

2.3 Superconducting Weak Link Devices

Recent development in superconducting electronic devices owes to the theoretical prediction of superconducting tunneling phenomena by B. D. Josephson in 1962 [28]. He theoretically manifested the Cooper pair tunneling through the ultra-thin insulator which was sandwiched by superconductors based on the BCS theory developed by J. Bardeen, L. N. Cooper and J. R. Schrieffer in 1957 [29]. It newly revealed that the superconductivity has a wave function which can directly appear in a macroscopic scale and the superconductor is applicable to the electronic devices. This tunneling effect was later experimentally supported by P. W. Anderson and J. M. Rowell [30]. Since then, superconducting digital circuits have been studied actively to realize a high switching speed and low power dissipation computing system based on the Josephson effect. Especially the IBM project in the United States was the pioneering work in this field [31].

Characteristic electrical properties of the Josephson junction is that its I - V curve shows hysteresis with the following features; non-resistive superconducting current flow, minute leakage current due to quasi-particles in the sub-gap region and voltage jump from zero to superconducting energy gap ($2\Delta \sim$ meV). The intrinsic switching speed of a Josephson junction has been shown to be $h/4\pi\Delta$, where h is the Planck's constant and Δ is the superconducting energy gap. The calculated value is 0.2 ps for Nb/AlO_x/Nb trilayer junction which is the most successful and reliable material system to date, while the record speed is about one order of magnitude greater than the intrinsic limit [32]. Also, the power dissipation is of the order of 10 μ W for a typical latching gate [33]. At that time, its superiority to the semiconductor devices was obvious, however, recent drastic growth in semiconductor technology intimidates its superiority and the superconducting digital electronics has been likely to be driven to the stage to be reconsidered its significance and the direction of its development.

For pursuing higher operation speed in Nb-based trilayer tunnel junctions, overdamped Josephson junction, which does not show hysteresis, is recently considered effective from the point of avoiding the punchthrough effect caused by the AC-biasing. Usually, the shunting resistors are externally added to obtain overdamped junctions. The

integration will be advanced if intrinsically overdamped Josephson junctions with high controllability are developed, because the externally shunting resistors cover large area in a cell. The junctions consisting of Nb/AlO_x/Al/AlO_x/Nb double barrier structure was recently developed and it showed non-hysteresis characteristics [34].

Although the fabrication of Nb/AlO_x-based superconducting tunnel junctions have been the most extensively developed in the superconducting device field, utilization of semiconductors in the superconducting device is another choice. One of them is superconducting weak link device whose device operation is based on the superconducting proximity effect. When a superconductor cleanly contacts with normal metal, the cooper pair penetrates into the normal region with damping exponentially, and superconductivity is brought about in the penetrated region which usually ranges from a few nanometer to a few hundreds of nanometer from the SN (superconductor-normal metal) boundary. This effect was theoretically studied by De Gennes [35] and experimentally supported by Werthamer [36]. Clarke showed superconducting current flow through the SNS trilayer structure using Pb/Cu system [37]. Operation mechanism in this weak link device is similar to the Josephson junction; superconducting or Josephson current flows between the superconductors through the insulator or normal metal in a sine curve relation of phase difference between the superconducting wave functions of the two electrodes.

This effect can be expanded to the usage of semiconductor instead of normal metal. Seto and Van Duzer studied this system in detail [38, 39]. They introduced the characteristic length, that is coherence length (ξ_{Se}), in case of the semiconductors as following equation;

$$\xi_{Se} = \left(\frac{\hbar^3 \mu}{6\pi k_B T m_{Se}^*} \right)^{\frac{1}{2}} (3\pi^2 n)^{\frac{1}{3}}, \quad (2-1)$$

where μ , m_{Se}^* and n represent mobility, effective mass of the carrier and carrier concentration of the semiconductor, respectively, and the T and k_B represent temperature and Boltzman constant, respectively. In the case of high electron mobility system or two-dimensional electron gas system, the ξ_{Se} can be replaced as follows [40];

$$\xi_{Se} = \left(\frac{\hbar \mu N_s}{2k_B T m_{se}^*} \right)^{\frac{1}{2}}, \quad (2-2)$$

where N_s represents the sheet carrier concentration. It is the most important that the coherence length is long because it directly reflects the maximum superconducting current in the junction and a margin for the fabrication. The maximum superconducting current (J_s) in the weak link device is roughly estimated as following relation;

$$J_s \propto \frac{T^2}{\xi_{Se}} \sin \Phi \exp\left(-\frac{L}{\xi_{Se}}\right) \approx \frac{1}{\xi_{Se}} \exp\left(-\frac{L}{\xi_{Se}}\right), \quad (2-3)$$

where T is the tunneling probability at the Schottky barrier, Φ is the phase difference and L is the channel length or length of semiconductor region.

To obtain long coherent length, utilization of a material of higher carrier concentration or higher carrier (usually electron) mobility are the direction to be targeted. In the case of degenerated system or so-called dirty limit ($l < \xi_{Se}$, where the term l indicates the mean free path) in which the transport of the cooper pair phase in the semiconductor region is diffusive, silicon (p-Si [41-43], n-Si [44, 45]) is the main semiconductor ever reported since it does not have high carrier mobility but the impurity can be doped as much as 10^{20} cm^{-3} . In this system, Schottky barrier in the superconductor-semiconductor boundary can be lowered, which is one of the significant features to obtain higher superconducting current since the cooper pair penetration occurs first through the Schottky barrier tunneling in the SSm (superconductor-semiconductor) boundary [38, 39]. In the high electron mobility system, III-V compound semiconductors are energetically studied such as InGaAs [46] or InAs [47, 48], and in the case of clean limit ($l > \xi_{Se}$), InAs/AlSb [49], InAs-inserted-channel InAlAs/InGaAs [50, 51], or AlGaAs/GaAs [52-54] were proposed in which the transport of the cooper pair phase in the semiconductor region is ballistic together with an enhanced Andreev reflection at the SSm interface [55].

One of the objectives to employ these semiconductors to the normal layer of the weak link device is to realize a superconducting three terminal transistor or Josephson field effect transistor (JOFET) which was first proposed by T. D. Clark et al. [56] since the carrier concentration can be controlled by the gate voltage which changes the Josephson coupling. Its switching speed is thought to be equal to or faster than the conventional bipolar transistor, and the power consumption is as low as that of Josephson (SIS junction) devices. Some of the discrete devices have been fabricated in both the dirty and clean limit systems and successful three-terminal operation, which is the modulation of superconducting current by the gate voltage, was demonstrated although the gate bias was relatively large compared to the $I_c R_n$ (I_c : superconducting current, R_n : normal resistance) product of the device.

2.4 Single-Electron Transistors

Technological progress in recent semiconductor nanofabrication is remarkable and structuring of the order of nanometer has become possible artificially or through self-organization. This situation motivated both the observation of single-electron charging effect which is observable only from the minute structures and the application to the electronic devices. Especially the single-electron transistor (SET) has been taken noticed theoretically and experimentally whose operation mechanism is based on a Coulomb blockade effect, which is a notable charging effect in a minute tunnel junction. This is a phenomenon of suppression of the electron tunneling in the minute capacitor when one electron tunneling have caused increase of the potential energy of the system.

During an electron tunneling event in the minute capacitor, the accumulated charge Q must discontinuously jump by the elementary charge e . The resulting change in electrostatic energy of the capacitive junction (ΔE) is described as

$$\Delta E = \frac{Q^2}{2C} - \frac{(Q-e)^2}{2C} = \frac{e\left(Q - \frac{e}{2}\right)}{C}, \quad (2-4)$$

where C is the capacitance of the junction. At zero temperature, tunneling can only occur if ΔE is positive. Therefore, the I - V curve of the junction should have an $I = 0$ region,

$$-\frac{e}{2C} < V < \frac{e}{2C} \quad \text{for } I = 0, \quad (2-5)$$

and this is the Coulomb blockade for single junctions.

The key to the development of the SET devices is the ability to fabricate very small tunnel junctions in between an island and the leads separated by tunnel barrier, which makes capacitive double junctions. Several conditions are inevitably required such as a low junction capacitance in order that the charging energy ($E_c = e^2/2C$) be much larger than the thermal energy ($k_B T$). This is due to the fact that the charging energy which is required to add a

charge to an island far exceeds the available energy of thermal fluctuations. Moreover, a tunneling resistance (R_T) should be much larger than the resistance quantum ($R_K = h/e^2 \sim 25.8$ k Ω), and this condition ensures that the wave function of an excess electron on the island is localized there, which leads the single-electron charging effect to be monitored.

Several new effects due to the quantization of charge were predicted to arise in an ultra small tunnel junction, both in the superconducting and the normal state. Likharev et al. first gave a major thrust to this new area of low temperature physics by making detailed predictions of Coulomb blockade phenomena in a single junction and by proposing various applications of the new effects [57-60]. Due to the estimation by Likharev, relation between the smallest tunnel junction size and the temperature in which the Coulomb blockade effect can be observable was predicted to be the junction size of 30 nm versus 30 K or 3 nm size versus 100 K. Therefore, the single-electron device features strong connection between the nanoscopic fabrication and the device operation temperature. In other words, without development in miniaturization of the tunnel junction, SET operation at 77 K or at room temperature can not be achieved. From this essential point of view, various nanofabrication technology have been newly established concerning the fabrication of SETs. Most commonly utilized technique is the conventional electron-beam lithography. The split-gated AlGaAs/GaAs heterostructure with extremely high electron mobility two-dimensional electron gases [61-64] or side-gated point-contact structures in delta-doped GaAs [65] using depletion layer as a potential barrier (tunneling region) are the reports using III-V materials. In the case of Si based SETs, many reports have surely been made [66-69]. By modifying EB lithography, the multiple-angle aluminum evaporation and oxidation through suspended mask fabricated by multiple resist layer system is another common and easy technique ever reported [70-73]. Recent successfully developed method is the SPM nano-oxidation process applied to the Ti [74] and Nb [75] thin films. Due to its feasibility of nano-scale processing, room temperature SET operation have been reported. Other approach is the utilization of self-organized or artificially fabricated dot structure for obtaining minute island electrode. Usage of metal nanoparticles (aluminum or indium droplet [11, 76], gold dot with granular structure [77] or gold clusters [78]), polycrystalline or nanocrystalline Si dot array [79-81],

dithiol-linked gold colloidal particles [82] or beam-induced deposition of metal carbide dot [83] are the particular cases.

2.5 Summary

In this chapter, superconducting devices and single-electron technology were historically and theoretically overviewed together with the nanofabrication processing technology. Construction of minute structures and microscopic devices are now practicable and realized by not only the conventional electron-beam lithography but also the scanning probe microscope processes or the beam-induced reaction processes which in each has original features in the fabrication and has wide variety of ways to be used that contribute to diversify the device to be realized. Since their feature size is of the order of nanometer, they would be applicable to the complementary techniques with the EB lithography for defining discrete structures.

In the superconducting device fields, Nb/AIO_x Josephson junction is the most successful devices to be applied to the superconducting LSIs. Recent researches revealed the needs for the overdamped junction for the higher operation speed, and not only Nb/AIO_x system but also superconducting weak link devices have taken noticed as well as for the application to the Josephson field effect transistors. However, surrounding environment has become severe with the drastic progress in Si devices. Although the Josephson devices are thought to be superior in switching speed and power consumption problems, necessity to be operated at down to 77 K or 10 to 4.2 K is the eternal bottleneck for their commercial and future application unless room temperature superconductor should be developed. However, further development in compact cooling system and continual research for the LSI application would generate demands for its high speed operation.

Single-electron transistors are one of the ultimate future electron devices which can control electron one by one based on the Coulomb blockade effect. Extremely low power dissipation is the particular feature and research of single-electron charging effect would be the ultimate as for the Si LSIs. However, its road to the application to the practical or consumer products could be considered optimistic now judging from the uniformity of each device operation in the integrated SETs or the stable operation at room temperature. Similar to the superconducting devices, co-existing or complementary device in the Si LSI would be the potential application for the future integrated circuit.

References

- [1] D. M. Eiger and E. K. Schweizer: *Nature* **344** (1990) 524.
- [2] M. F. Crommie, C. P. Lutz and D. M. Eiger: *Science* **262** (1993) 218.
- [3] J. W. Lyding, T. C. Shen, J. S. Hubacek, J. R. Tucker and G. C. Abeln: *Appl. Phys. Lett.* **64** (1994) 2010.
- [4] A. Dagata, J. Seneir, H. H. Harary, C. J. Evans, M. T. Postek and J. Bennett: *Appl. Phys. Lett.* **56** (1990) 2001.
- [5] H. Sugimura, T. Uchida, N. Kitamura and H. Masuhara: *Jpn. J. Appl. Phys.* **32** (1993) L553.
- [6] D. Wang, L. Tsau, K. L. Wang and P. Chow: *Appl. Phys. Lett.* **67** (1995) 1295.
- [7] N. Kramer, H. Birk, J. Jorritsma and C. Schonenberger: *Appl. Phys. Lett.* **66** (1995) 1325.
- [8] J. Shirakashi, M. Ishii, K. Matsumoto, N. Miura and M. Konagai: *Jpn. J. Appl. Phys.* **35** (1996) L1524.
- [9] E. A. Dobisz and C. K. Marrian: *Appl. Phys. Lett.* **58** (1991) 2526.
- [10] L. Stockman, G. Nuttiens, C. van Haesendonck and Y. Bruynserade: *Appl. Phys. Lett.* **62** (1993) 2935.
- [11] R. Wilkins, E. Ben-Jacob and R. C. Jaklevic: *Phys. Rev. Lett.* **63** (1989) 801.
- [12] M. A. McCord and R. F. P. Pease: *J. Vac. Sci. Technol. B* **4** (1986) 86.
- [13] E. E. Ehrichs, R. M. Silver and A. L. de Lozanne: *J. Vac. Sci. Technol. A* **6** (1988) 540.
- [14] H. J. Mamin, P. H. Guethner and D. Ruger: *Phys. Rev. Lett.* **65** (1990) 2418.
- [15] G. S. Hsiao, R. M. Penner and J. Kingsley: *Appl. Phys. Lett.* **64** (1994) 1350.
- [16] C. S. Chang, W. B. Su and T. T. Tsong: *Phys. Rev. Lett.* **72** (1994) 574.
- [17] D. Fujita, Q. D. Jiang and H. Nejhoh: *J. Vac. Sci. Technol. B* **14** (1996) 3413.
- [18] W. Scheffels: *Proc. Stockholm Conf. Electron Microscopy*, eds. F. S. Sjostrand and J. Rhodin (Almquist & Wishell, Stockholm, 1958)-pp. 77.
- [19] R. Schief: *Optik* **29** (1969) 416.

- [20] K. H. Muller: *Optik* **33** (1971) 296.
- [21] A. N. Broers, W. W. Molzen, J. J. Cuomo and N. D. Wittels: *Appl. Phys. Lett.* **29** (1976) 596.
- [22] S. Matsui and K. Mori: *J. Vac. Sci. Technol. B* **4** (1986) 299.
- [23] V. Scheuer, H. W. P. Koops and T. Tschudi: *Microelectron. Eng.* **5** (1986) 423.
- [24] H. W. P. Koops, J. Kretz, M. Rudolph and M. Weber: *J. Vac. Sci. Technol. B* **11** (1993) 2386.
- [25] H. W. P. Koops and M. Weber: *Proc. IVMC (1994)* pp.422.
- [26] H. W. P. Koops: German Patent No. p. 44350433.0.
- [27] K. L. Lee: US Patent No. 5171992.
- [28] B. D. Josephson: *Phys. Lett.* **1** (1962) 251.
- [29] J. Bardeen, L. N. Cooper and J. R. Schrieffer: *Phys. Rev.* **108** (1957) 1175.
- [30] P. W. Anderson and J. M. Rowell: *Phys. Rev. Lett.* **10** (1963) 230.
- [31] W. Anacker: *IEEE Trans. Magn.* **MAG-5** (1969) 968.
- [32] S. Kotani, T. Imamura and S. Hasuo: *Tech. Digest Int. Electron Devices Meeting (1988)* pp. 884.
- [33] S. Hasuo: “*Ultrafast Josephson Devices*” ed. H. Hayakawa (Baifukan, Tokyo, 1986) Chap. 4.
- [34] M. Maezawa and A. Shoji: *Appl. Phys. Lett.* **70** (1997) 3603.
- [35] P. G. De Gennes: *Phys. Lett.* **3** (1963) 168.
- [36] N. R. Werthamer: *Phys. Rev.* **132** (1963) 2440.
- [37] J. Clarke : *Proc. R. Soc. London A* **308** (1969) 447.
- [38] J. Seto and T. V. Duzer: *Appl. Phys. Lett.* **19** (1971) 488.
- [39] J. Seto and T. V. Duzer: *Low Temp. Phys.* **LT-13** (Plenum Press, New York, 1974) pp 328.
- [40] T. Kawakami and H. Takayanagi: *Jpn. J. Appl. Phys.* **26** (1987) 2059.
- [41] M. Shyfter, J. Maah-sango, N. Raley, R. Ruby, B. T. Ulrich and T. V. Duzer: *IEEE Trans. Magn.* **MAG-13** (1977) 862.
- [42] T. Nishino, M. Miyake, Y. Harada and U. Kawabe: *IEEE Electron Devices Lett.* **EDL**

6 (1985) 297.

- [43] M. Hatano, F. Murai, T. Nishino, H. Hasegawa, T. Kure and U. Kawabe: *IEEE Electron Devices Lett.* **EDL-10** (1989) 61.
- [44] A. Serfaty, J. Aponte and M. Octavio: *J. Low Temp. Phys.* **63** (1986) 23.
- [45] D. R. Heslinga, W. M. V. Huffelen, T. M. Klapwijk, S. J. M. Bakker and E. W. J. M. Drift: *Cryogenics* **30** (1990) 1009.
- [46] A. W. Kleinsasser, T. N. Jackson, D. McInturff, F. Rammo, G. D. Pettit and J. M. Woodall: *Appl. Phys. Lett.* **55** (1989) 1909.
- [47] K. Inoue and T. Kawakami: *J. Appl. Phys.* **65** (1989) 1631.
- [48] H. Takayanagi and T. Kawakami: *Phys. Rev. Lett.* **54** (1985) 2449.
- [49] C. Nguyen, J. Werking, H. Kroemer and E. L. Hu: *Appl. Phys. Lett.* **57** (1990) 87.
- [50] J. Nitta, T. Akazaki, H. Takayanagi and K. Arai: *Phys. Rev. B* **46** (1992) 14286.
- [51] J. Nitta, T. Akazaki and H. Takayanagi: *Phys. Rev. B* **49** (1994) 3659.
- [52] K. M. Lenssen, M. Matters, C. J. P. M. Harmans, J. E. Mooji, M. R. Leys, W. van der Vleuten and J. H. Wolter: *Appl. Phys. Lett.* **63** (1993) 2079.
- [53] J. R. Gao, J. P. Heida, B. J. van Wees, T. M. Klapwijk, G. Borghs and C. T. Foxon: *Surf. Sci.* **305** (1994) 470.
- [54] A. M. Marsh, D. A. Williams and H. Ahmed: *Phys. Rev. B* **50** (1994) 8118.
- [55] A. F. Andreev: *Sov. Phys. JETP* **19** (1964) 1228.
- [56] T. D. Clark, R. J. Prance and A. D. C. Grassie: *J. Appl. Phys.* **51** (1980) 2736.
- [57] A. Widom, G. Megaloudis, T. D. Clark, H. Prance and R. J. Prance: *J. Phys. A* **15** (1982) 3877.
- [58] K. K. Likharev and A. B. Zorin: *J. Low Temp. Phys.* **59** (1985) 347.
- [59] E. Ben-Jacob and Y. Gefen: *Phys. Lett. A* **108** (1985) 289.
- [60] D. V. Averin and K. K. Likharev: *J. Low Temp. Phys.* **62** (1986) 345.
- [61] U. Meirev, M. A. Kastner and S. J. Wind: *Phys. Rev. Lett.* **65** (1990) 771.
- [62] L. P. Kouwenhoven, A. T. Johnson, N. C. van der Vaart, C. J. P. M. Harmans and C. T. Foxon: *Phys. Rev. Lett.* **67** (1991) 1626.
- [63] J. Weis, R. J. Haug, K. V. Klitzing and K. Ploog: *Phys. Rev. Lett.* **71** (1993) 4019.

- [64] K. Jinushi, H. Okada, T. Hashizume and H. Hasegawa: *Jpn. J. Appl. Phys.* **35** (1996) 1132.
- [65] K. Nakazato, R. J. Blaikie, J. R. A. Cleaver and H. Ahmed: *Electron. Lett.* **26** (1993) 384.
- [66] A. Toriumi, J. Koga, K. Uchida and A. Ohata: *Ext. Abstr. 3rd Int. Workshop on Quantum Functional Devices (1997)* pp. 23.
- [67] T. Sakamoto, H. Kawaura and T. Baba: *Ext. Abstr. 3rd Int. Workshop on Quantum Functional Devices (1997)* pp. 69.
- [68] H. Ishikuro and T. Hiramoto: *Appl. Phys. Lett.* **71** (1997) 3691.
- [69] A. Fujiwara, Y. Takahashi, H. Namatsu, K. Kurihara and K. Murase: *Ext. Abstr. Int. Conf. Solid State Devices and Materials (1997)* pp. 482.
- [70] G. J. Dolan: *Appl. Phys. Lett.* **31** (1977) 337.
- [71] L. S. Kuzmin, P. Delsing, T. Claeson and K. K. Likharev: *Phys. Rev. Lett.* **62** (1989) 2539.
- [72] L. Ji, P. D. Dresselhaus, S. Han, K. Lin, W. Zheng and J. E. Lukens: *J. Vac. Sci. Technol. B* **12** (1994) 3619.
- [73] Y. Nakamura, C. D. Chen and J. S. Tsai: *Jpn. J. Appl. Phys.* **35** (1996) L1465.
- [74] K. Matsumoto, M. Ishii, K. Segawa, Y. Oka, B. J. Vartanian and J. S. Harris: *Appl. Phys. Lett.* **68** (1996) 34.
- [75] J. Shirakashi, K. Matsumoto, N. Miura and M. Konagai: *Tech. Digest Int. Electron Devices Meeting (1997)* pp. 175.
- [76] P. J. M. van Bentum, R. T. M. Smokers and H. van Kempen: *Phys. Rev. Lett.* **60** (1988) 2543.
- [77] R. G. Woodham and H. Ahmed: *Ext. Abstr. 3rd Int. Workshop on Quantum Functional Devices (1997)* pp. 73.
- [78] H. Launois, C. Lebreton, M. Mejias, A. Pepin, C. Vieu, F. Carcenac, Y. Jin and J. Gierak: *Ext. Abstr. 3rd Int. Workshop on Quantum Functional Devices (1997)* pp. 145.
- [79] K. Yano, T. Ishii, T. Sano, T. Mine, F. Murai and K. Seki: *Ext. Abstr. IEEE Int. Solid-State Circuits Conf. (1996)* pp. 266.

- [80] S. Oda, M. Kimura and M. Otobe: *IEEE Silicon Nanoelectronics Workshop (1996)*.
- [81] S. Tiwari, F. Rana, H. Hanafi, A. Hartstein, E. F. Crabbe and K. Chan: *Appl. Phys. Lett.* **68** (1996) 1377.
- [82] T. Sato, H. Ahmed, D. Brown and B. F. G. Johnson: *Ext. Abstr. Int. Conf. Solid State Devices and Materials (1997)* pp. 498.
- [83] M. Komuro and H. Hiroshima: *Microelectron. Eng.* **35** (1997) 273.

Chapter 3

Modification of Carbon Nanostructures by Electron-Beam-Induced Deposition Technique

3.1 Introduction

When scanning electron microscope (SEM) is used to monitor microscopic structures, the surface being observed is inevitably contaminated. This is due to the fact that residual hydrocarbon molecules remain in the SEM chamber even at a low base pressure ($\sim 10^{-6}$ Pa) and are decomposed by irradiation due to the electron-beam. This results in the deposition of the carbonaceous material on the area that is exposed. This phenomena is now widely recognized by those engaging on the SEM, and this mechanism is called electron-beam-induced deposition (EBID). First successful report on the application of this technique for the fabrication of microscopic structures was done by Broer et al. [1, 2] and since then its simplicity for fabricating microscopic structures has been attracted much attention. Its progress in fabrication of nanostructures is widely spread to the etching mask for milling [2-4], repair of metal masks [5-7] or tip for scanning probe microscope [8-12] just because of the easy direct fine patterning and that it is resistless process.

For the start of the microprocessing to realize minute quantum effect devices, fabrication of minute carbonaceous material was first performed. In particular, the EBID was studied using conventional SEM without introducing any gases in order to establish the simplest processing. This standpoint is the basic concept of this study, and aims to draw a new functionality from the conventional technology.

3.2 Overview of This Technique

Electron-beam-induced deposition is one of the direct writing techniques which enables to deposit carbonaceous material at only electron-beam scanning area. Mechanism of the deposition is considered as a result of the interaction of the electron-beam with reactant gases adsorbed on a substrate surface. These precursor molecules are decomposed locally by the electron-beam irradiation and a sort of polymerization occurs. Since each electron is scattered inside the growing material, the growth occurs toward not only the vertical direction but lateral as well. Moreover, some of the electrons are forced backscattering events causing its growth around the beam-irradiated spot. Therefore, if the electron-beam is focused in a spot, the shape of the deposited material exhibits like a conical or Gaussian round structure with having a considerable length of tail.

One of the characteristics of this EBID is that it is not precursor selective. When a metal-carbonyl [6, 7, 13-16] or a metal-acetylacetonate [6, 16-19] is employed as a precursor, a metal carbide is deposited, together with a carbon or a diamond-like carbon (DLC) from styrene [3]; isopropyl alcohol (IPA) [20] or CH_4 [21]. Typical examples are summarized in Table 3.2.1. One of the notable precursors is the pump oil [1, 2]. This means that carbonaceous material grows without introducing any gases into the chamber and also it grows under a high vacuum pressure although the deposition rate becomes low compared to the case of introducing gases. Through the effect of this carbon contamination, the deposited material contains considerable amount of carbon even if any carbon-less precursor was employed. However, by optimizing the deposition conditions and choosing suitable precursors, this technique enables to make wide variety of conducting or semi-insulating materials.

Another feature of this technique is that we can deposit carbonaceous material on a conducting substrate in arbitrary three-dimensional structures only by changing the scanning patterns of the electron-beam. Some of the examples are shown in Fig. 3.2.1. They were grown on a Si substrate from the residual hydrocarbon molecules in a SEM chamber. Focusing the electron-beam makes a conical structure (a), one-dimensional scan makes a wire (b) and two-dimensional scan does a microfilm (c). As the radius of the electron-beam

is about a few nanometer, size of the deposited structures is very small (of the order of a few tens of nanometer). Therefore, an application of this technique for fabricating microstructures and microdevices is considered effective.

Table 3.2.1 Typical precursors for EBID.

Precursor		Deposit	Reference
Metal Carbonyl	W(CO) ₆	WC _x	6, 7
	Mo(CO) ₆	MoC _x	13, 16
	Fe(CO) ₅	FeC _x	14
	Ni(CO) ₆	NiC _x	15
Metal Acetylacetonate	(CH ₃) ₂ Au(tfac) ₂	AuC _x O _y	16-19
	(CH ₃) ₂ Au(acac) ₂	AuC _x O _y	6, 17-19
Hydrocarbon	CH ₄	Carbon	21
	Styrene	Carbon	3
	MIBK	Carbon	20
	IPA	Carbon	20
	pump oil	Carbon	1, 2, 5, 8, 21

- tfac : trifluoro-acetylacetonate
- acac : acetylacetonate
- Styrene : C₆H₅CH=CH₂
- MIBK : methyl isobutyl ketone
- IPA : isopropyl alcohol

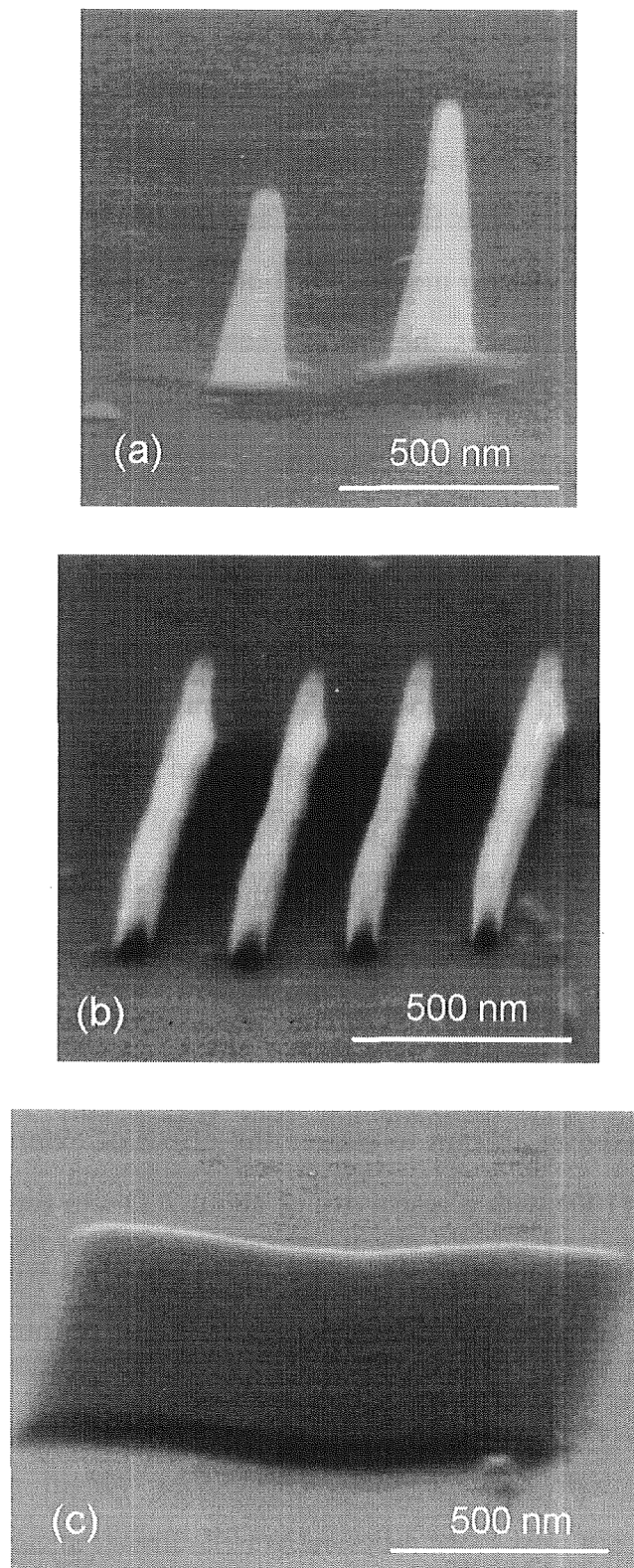


Fig. 3.2.1 SEM images of the various carbonaceous microstructures deposited by SEM from residual hydrocarbon molecules. Conic (a), wire (b) and square (c) shapes can be obtained by changing scanning patterns of the electron-beam.

3.3 Fabrication of Carbonaceous Wire

3.3.1 Experimental procedure

This study basically concentrated on the usage of the residual gases in the chamber as precursors for the microstructure fabrication, and SEM was utilized for the deposition system. This concept means that no modification of SEM is required for introducing some metal organic gases, and this makes the process easier for ultrafine patterning. Moreover, utilizing the SEM system enables the EBID process while monitoring the substrate surface and aligning electron-beam to the device position.

The experiments were carried out in an SEM (Hitachi Co., Ltd. S-800) system without introducing any precursor gases, such as metal carbonyls or metal acetylacetonates. The residual gases, mainly consisting of hydrocarbon molecules which originate from vacuum pump oil, were used to deposit carbonaceous material. No modifications were carried out on the SEM and it was operated in a standard manner. Detail process conditions are summarized in Table 3.3.1. The base pressure near the sample was $1\sim 5 \times 10^{-6}$ Pa during evacuation by the diffusion pump. The shapes of the deposited carbonaceous material were changed by selection of a particular SEM scanning mode equipped for the use of energy dispersive X-ray spectroscopy (EDX) measurements. They were conic with spot analysis mode, line-shaped with line mode, and square-shaped with surface analysis mode. The working distance was fixed at 10 mm to reduce the effect of external magnetic field. The substrate was n-type Si (100) with a resistivity of about $2 \Omega \cdot \text{cm}$ for the optimization of the deposition conditions of carbonaceous materials. It was cleaned with organic solvents and the native oxide on the substrate was etched with 5 % HF before being loaded into the chamber.

Table 3.3.1 Deposition condition of carbonaceous wire.

Process Chamber	Scanning Electron Microscope (Hitachi S-800)
Precursor	pump oil
Pressure	$1\sim 5 \times 10^{-6}$ Pa
Acceleration Voltage	10~30 kV
Electron-Beam Current	15~95 pA
Magnification during Writing	20,000~100,000
Electron-Beam Dose	2.8~14 $\mu\text{C}/\text{cm}$
Working Distance	10 mm

3.3.2 Optimization for obtaining narrow carbonaceous wire

For the first step of establishing microfabrication technique, deposition of carbonaceous wire was performed. This process was carried out by selecting the line analysis mode of SEM, and the electron-beam conditions were optimized for obtaining narrow carbon nanowires. Especially, the dependence of carbon wire height and width on the acceleration voltage, the electron-beam current and the magnification during the writing were investigated.

Figure 3.3.1 shows the dependence of the carbon wire height and width on the acceleration voltage. The magnification during the writing was 50000. The electron-beam was scanned once in each experiment with line-analysis mode. The height of the carbon wire increases with increasing the voltage while the width decreases. Since the electron-beam becomes sharper with higher acceleration voltage, it is thought that the growth of carbonaceous material occurs vertically not laterally. Moreover, the amount of the secondary electrons which are scattered in the substrate and emit back to the vacuum from the substrate decreases with increasing the acceleration voltage as the electron goes deeper into the substrate. This effect also results in less unintentional carbon growth around the electron-

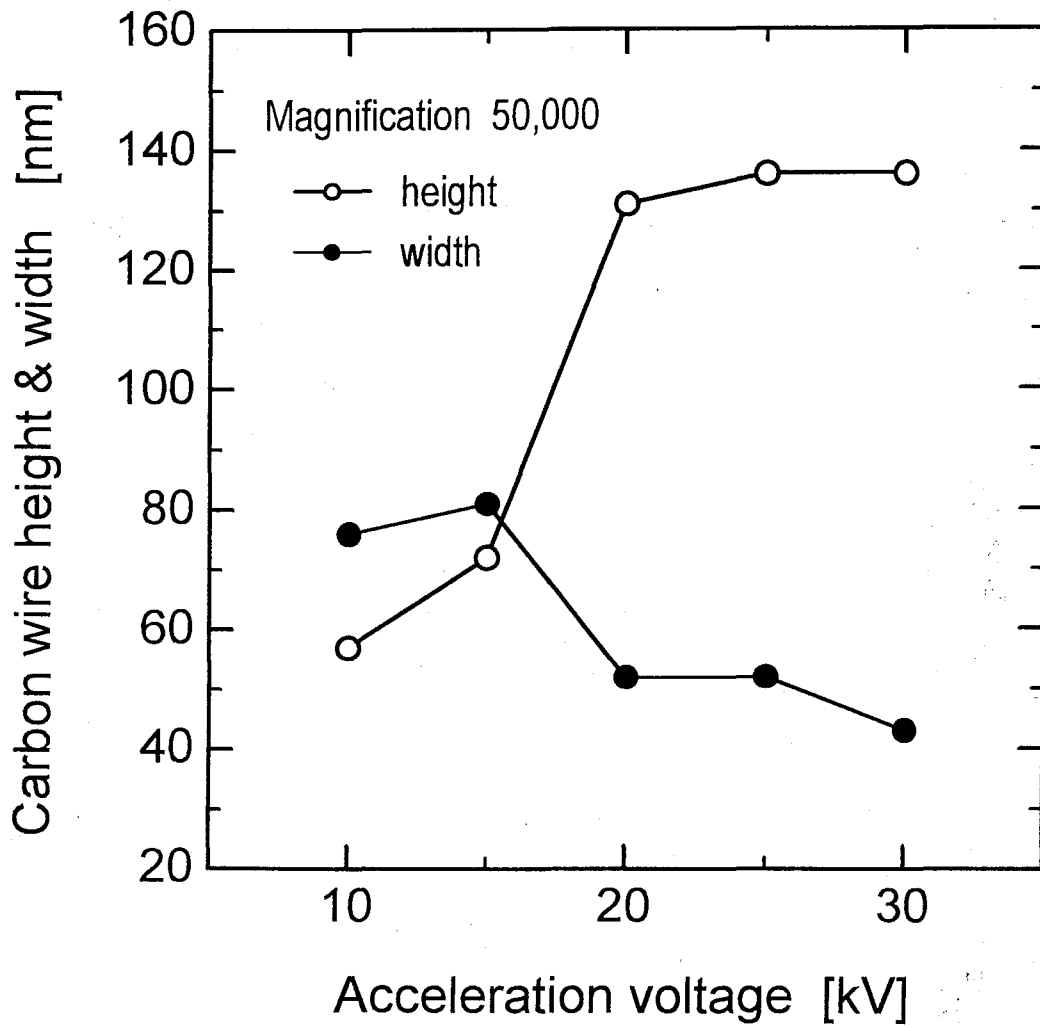


Fig. 3.3.1 Dependence of the shape of the carbon wire on acceleration voltage written at magnification of 50,000.

beam irradiated area, and causes the wires finer with higher voltage. The vertical growth saturates in the voltage range of over 20 kV and this is attributed to the local heating effect resulting in the re-evaporation of the deposited material. The cross section of the lines was also observed and its shape was found to be almost cylindrical. From this result, volume of each carbon wire was calculated and it was found that the volume increased with increasing acceleration voltage, indicating an increase of growth rate. This enhancement of growth rate is considered to be due to the increase of the decomposition rate of the molecules adsorbed on the substrate as a result of the production of high-energy electrons by the high acceleration voltage.

The dependence of the wire shape on the electron-beam current is shown in Fig. 3.3.2. The acceleration voltage was set at 30 kV and a wire of about 2 μm long was characterized. Carbonaceous wires with a width of 30 nm were obtained at a low beam current of 15 pA. The height of the carbon wire decreased with increasing beam current, whereas the width increased, which suggests that a high aspect ratio and narrow wire can be obtained by using a low beam current. The increase of the beam current causes both local heating and re-evaporation of the carbon, and consequently the vertical growth is suppressed. Furthermore, the increase of the beam current also causes electron scattering at the surface of the growing carbon, resulting in its lateral growth. Therefore, we obtained a narrower wire with a high aspect ratio for a low beam current.

The dependence of the carbon wire shape on the magnification is shown in Fig. 3.3.3(a). The acceleration voltage was 30 kV. This experimental result corresponds to its dependence on the writing velocity or electron-beam dose per length. Typical SEM image of the wires written at various magnification is supplemented in Fig. 3.3.3(b). From right to left, the wire was written at higher magnification. We can see from the Fig. 3.3.3(a) that the width of the wire was not significantly affected by the magnification and a value of about 30 nm was maintained, whereas the height was almost linearly proportional to the magnification. The increase of the volume per second showed an almost constant value of $4 \times 10^{-17} \text{ cm}^3/\text{s}$ at any magnification. The independence of the growth rate can be considered that the growth of the carbonaceous material occurs due to the interaction between electrons and hydrocarbon

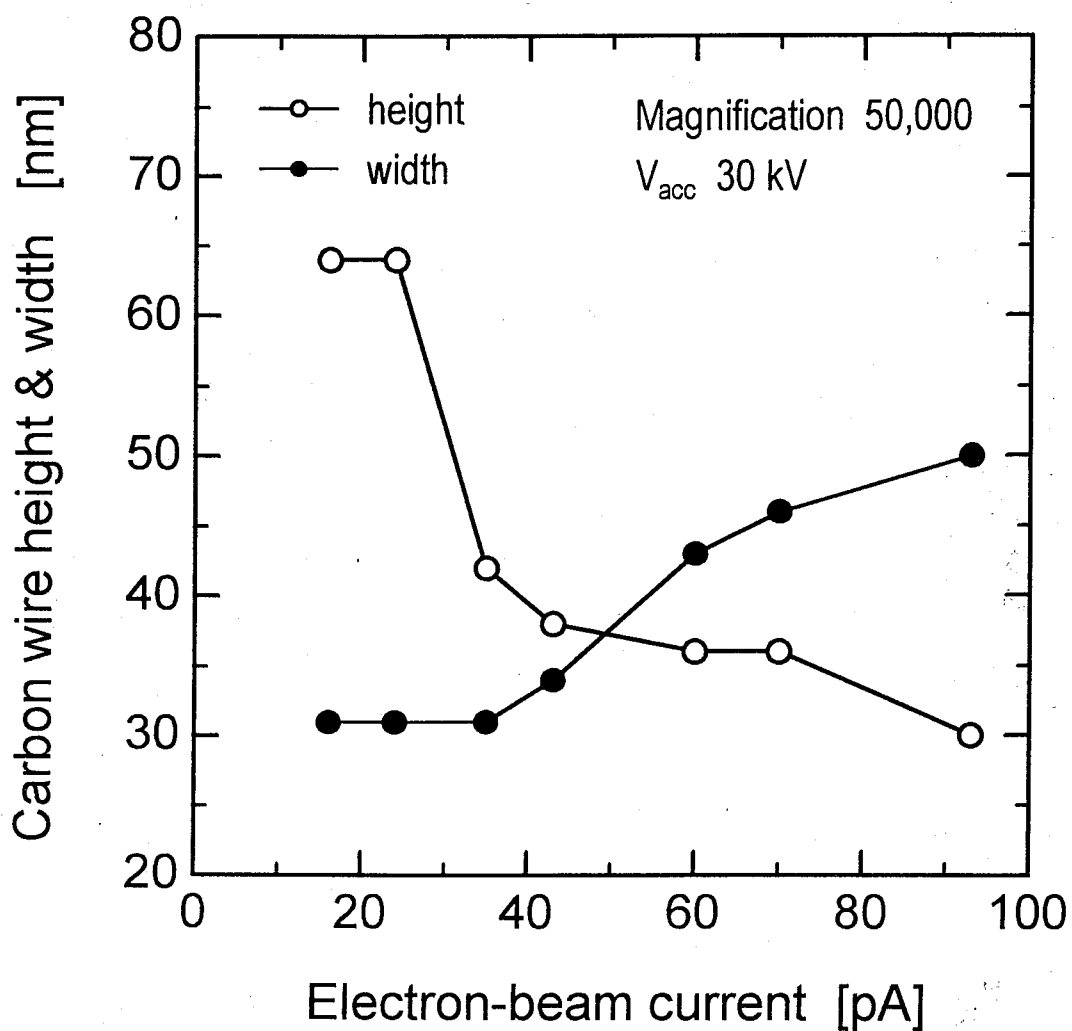


Fig. 3.3.2 Dependence of the shape of the carbon wire on electron-beam current written at magnification of 50,000 and acceleration voltage of 30 kV.

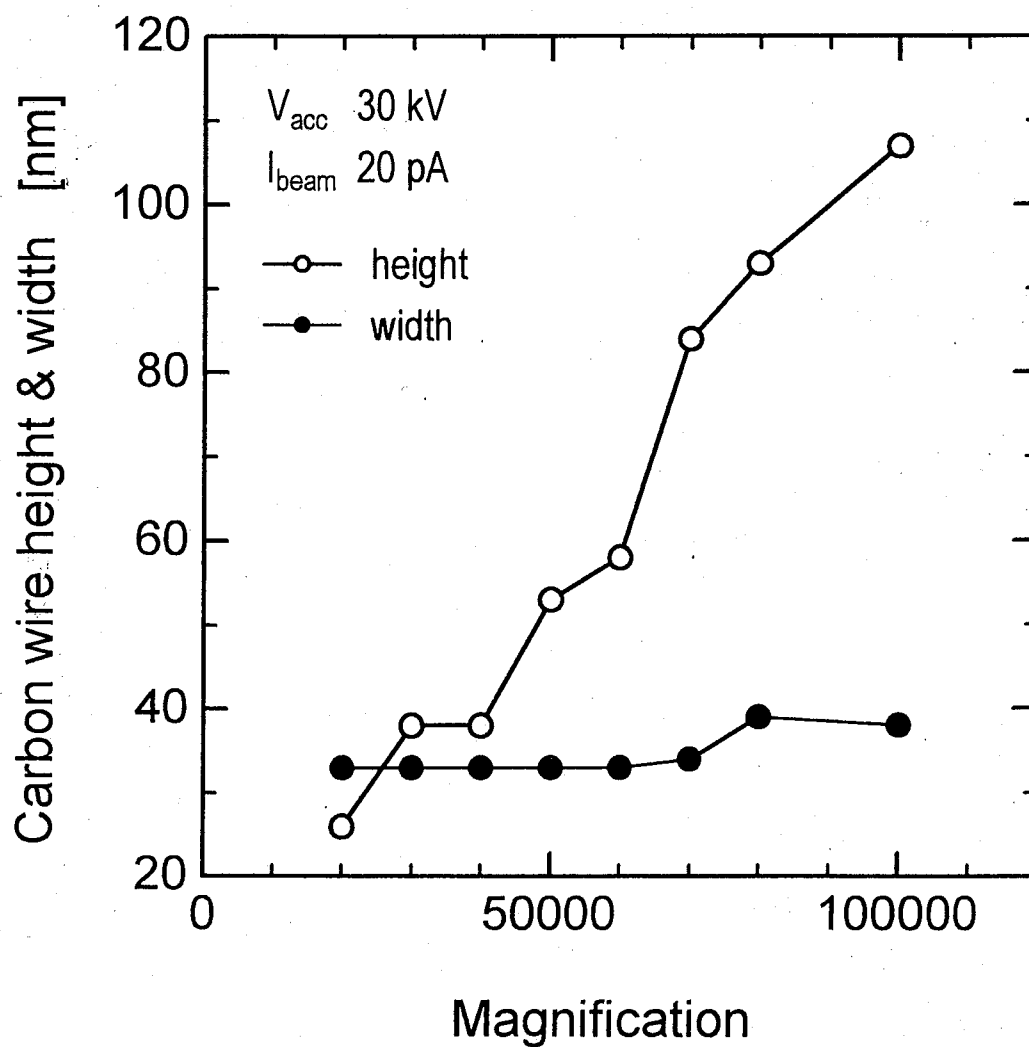


Fig. 3.3.3 (a) Dependence of the shape of the carbon wire on magnification written at acceleration voltage of 30 kV and electron-beam current of 20 pA.

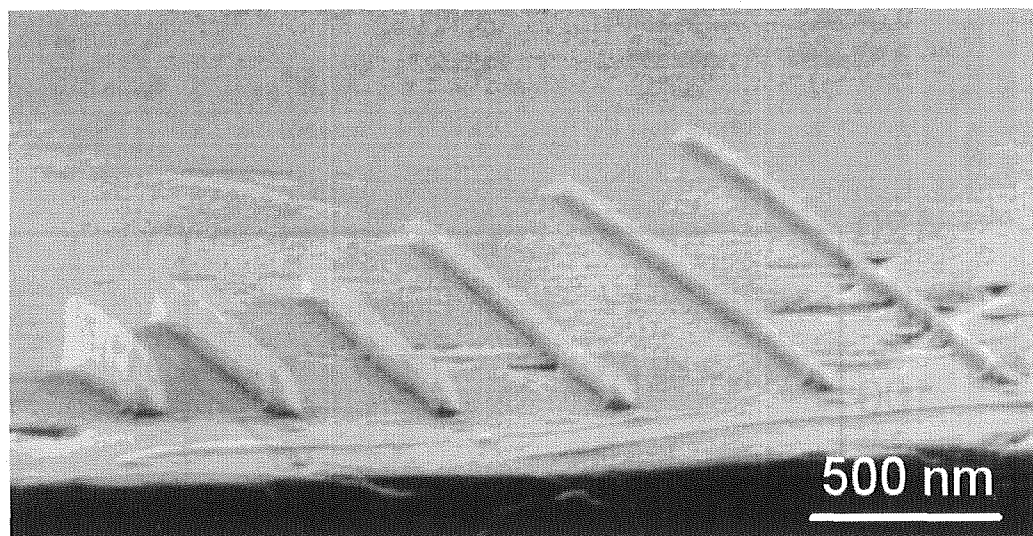


Fig. 3.3.3 (b) SEM image of the carbonaceous wires deposited in various magnification conditions. Wires were deposited in higher magnification at left.

molecules, so that the electron energy and the number of electrons determine the growth rate. Therefore, the growth rate was invariant with the magnification because both the acceleration voltage and the current density were kept constant in this experiment. However, if the magnification is increased, the electron dose per unit length increases from $2.8 \mu\text{C}/\text{cm}$ at a magnification of 20,000 to $14 \mu\text{C}/\text{cm}$ at that of 100,000. This results in the enhancement of the decomposition of adsorbed molecules per unit length, and the wire with a high aspect ratio was achieved with a high magnification whereas its growth rate had almost constant value.

3.3.3 *AFM observation of carbonaceous wire with carbon needle cantilever*

In order to demonstrate the EBID process, a conic-shaped carbonaceous structure was fabricated on top of the tip of an atomic force microscope (AFM) cantilever. Generally,

the resolution of the AFM is significantly dependent on the probe structure, especially the radius of curvature of the tip. Although the conventional tip has a regular pyramid structure with 90 degrees at the top and a radius of curvature of 50 nm, usage of a finer tip or a tip of high aspect ratio is inevitable so as to monitor very rugged surface or minute structures. For obtaining a sharper AFM tip, application of ZnO whisker [22], modification using focused ion beam etching system [23, 24], or utilization of EBID process [8-12] are particular reported cases. In the latter case, they have studied this technique to observe trench structures, but in this study, the deposited carbonaceous wire structures with a small line width and spacing were tried to resolve by the EBID tip. A sample for the AFM observation consisted of four carbonaceous wires with a width of 50 nm and spacing of 200 nm. We could not obtain a clear AFM image with a normal cantilever shown in Fig. 3.3.4(a) because the line width and spacing of the wires was less than the resolution. Namely, the top of the tip could not sense the atomic force because of the physical disturbance of the side wall of consisting cantilever against the wire of high aspect ratio. Therefore, conic carbonaceous needle was used for the new AFM cantilever in order to obtain its image in high resolution.

An AFM image of the wires taken by a conic-shaped carbon needle is shown in Fig. 3.3.4(b). The SEM image of the new cantilever is also shown in Fig. 3.3.4(c). The base cantilever consisted of insulating Si_3N_4 . Therefore, before the growth of the carbon needle, a small amount of Pt-Pd alloy was deposited on it by RF sputtering to make the surface electrically conducting for the EBID process. The carbon growth was performed by just focusing the electron-beam onto a spot for 15 minutes. The carbon needle had a height of 1 μm and a diameter of 60 nm, and the radius of curvature at the top of the tip is about 20 nm. The needle was also coated with Pt-Pd alloy to strengthen its adhesion to the base cantilever. By using this cantilever, clear picture of the carbonaceous wires was obtained as shown in Fig. 3.3.4(b). The left wall of the wires is seen to be blurred, while the right is sharp. This is attributed to the slight curvature of the needle as shown in Fig. 3.3.4(c). Through this experiment, it was demonstrated that this carbonaceous needle is very effective especially for the observation of nanoscaled structures of high aspect ratios.

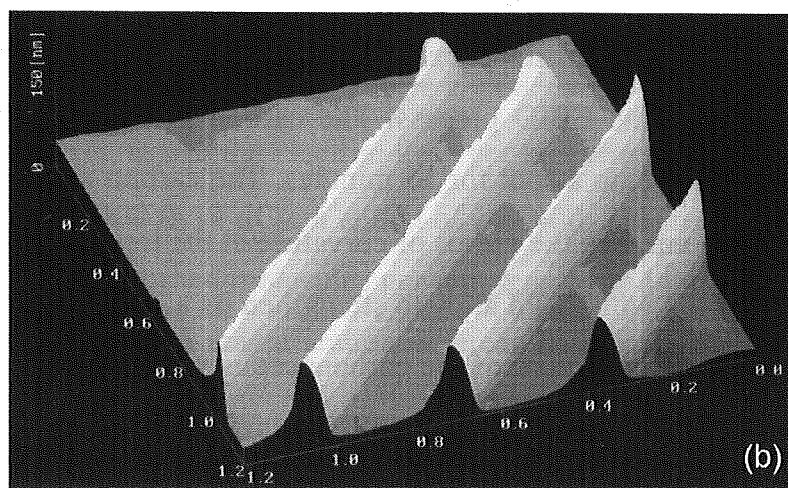
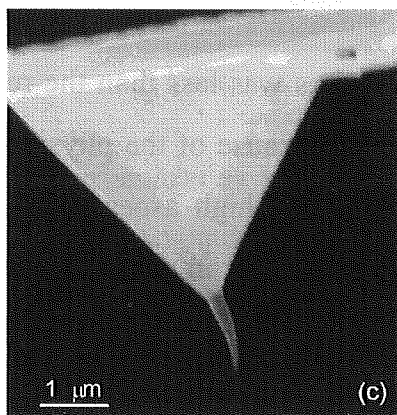
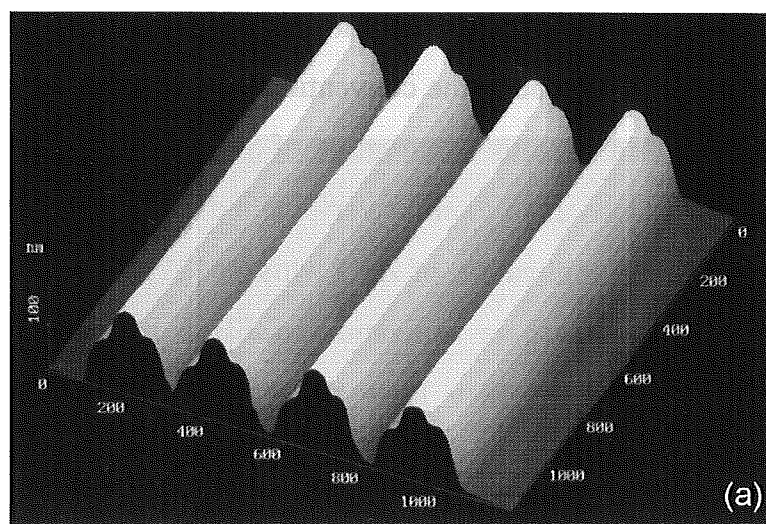


Fig. 3.3.4 AFM images of the carbonaceous wires monitored by (a) normal cantilever and (b) cantilever with carbonaceous needle on top of the tip whose SEM image is shown in (c).

3.4 Application to Etching Mask for Fabricating Nanowires

3.4.1 Fabrication process and result

As an application of the carbon wire for device fabrication processes, its use for an etching mask to obtain a Si nanowire was investigated. Although the wires or masks can be deposited in very fine structures, its removal after the etching or patterning is one of the key issues. At first, the carbon wires were subjected to HCl, HNO₃, HF or H₂SO₄ acids for long time, however, they were unaffected by the reagents. This indicates that the carbonaceous wires are more resistant to chemical etching, and their potential use as chemical barriers for microelectronic applications would be regarded as another point of view. Namely, the carbon itself is very stable against acids or organic solvents. An oxygen (O₂) plasma ashing is a typical method in dry process [3, 25-27], however, plasma damage and/or oxidation of the wire surface should be avoided considering its application to electronic devices. Therefore, a lift-off technique which is one of the typical wet processes was employed using SiO₂ to remove the carbon masks in this study. As the selective ratio of wet etching is nearly infinity in the Si/SiO₂ system, we can easily remove the carbon mask. Through this wet process, no etching damage on the surface of the wire occurs.

The procedure is illustrated in Fig. 3.4.1. First, a SiO₂ layer was deposited on a Si substrate by spin-coating and followed by a bake at 180 °C for 30 min. As a coating solution, OCD type-2 (Tokyo Ohka Kogyo Co., Ltd.) was used, which is composed of a glass-forming agent and an organic binder dissolved in organic solvents. The thickness of this spin-on glass (SOG) layer was about 30 nm. Then the electron-beam-induced deposition of carbon wires was carried out. Even though SiO₂ is an insulator, it was thin enough for the electron-beam current to tunnel through the layer, therefore, carbon wires can be deposited on it as well as on silicon. Using these carbon wires as the mask, both SiO₂ and Si were etched by means of reactive ion etching (RIE) in which the RF power and CF₄ pressure were 50 W and 40 mTorr, respectively. Finally, the SiO₂ layer under the carbon wires was etched away using diluted HF together with the removal of the carbon mask. The Si nanowires whose width was equivalent to the carbon wire were thus fabricated.

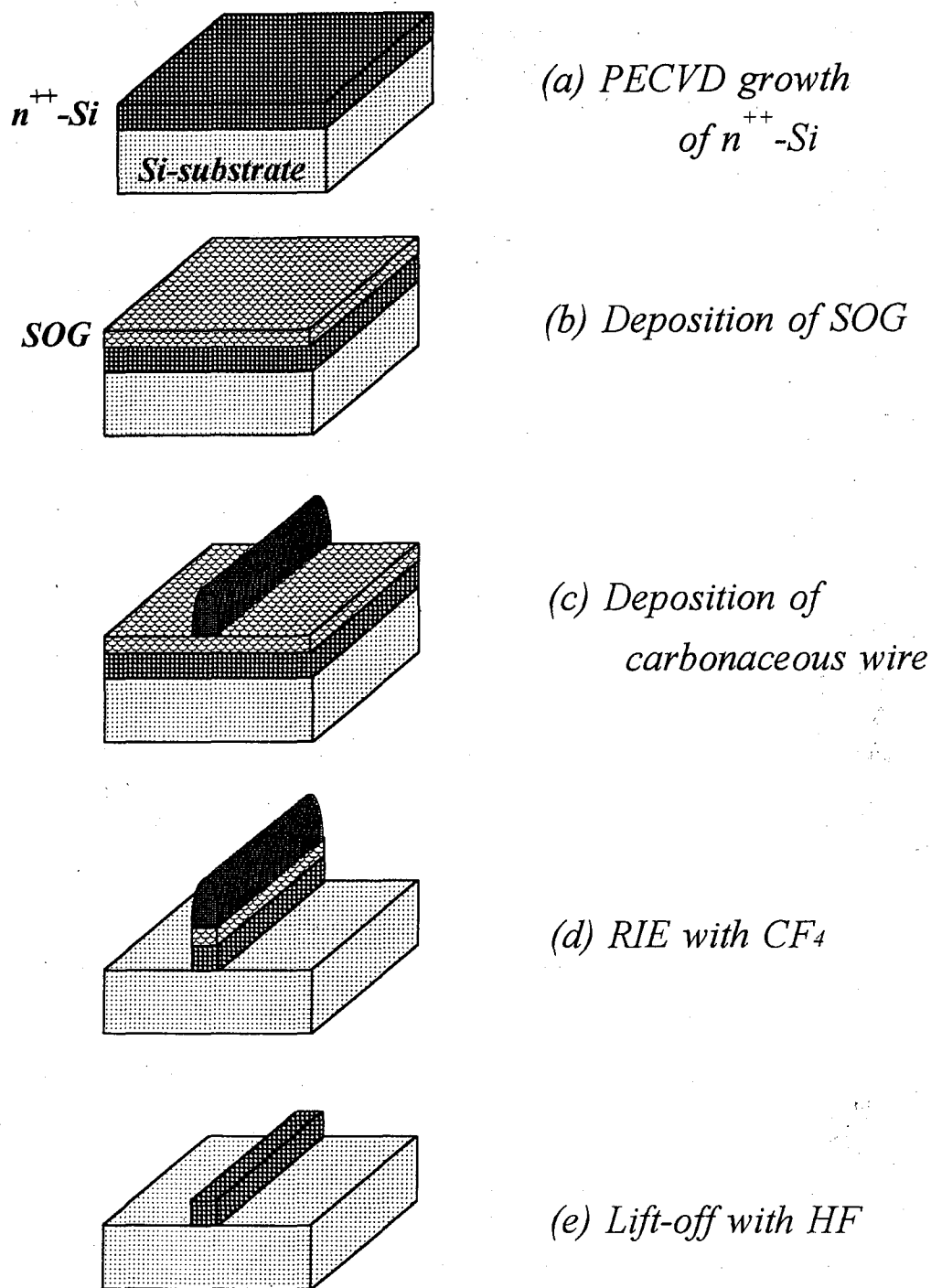


Fig. 3.4.1 Fabrication process for n^{++} -Si wire.

The SEM image of the Si wires is shown in Fig. 3.4.2. The width is 60 nm and the length is 1 μm , 1.5 μm and 2 μm , which are equal to the width and length of the carbon masks. As each carbon wire mask was written in different electron dose per length (about 25, 15, 40, 55 $\mu\text{C}/\text{cm}$ from left to right in Fig. 3.4.2), the mask height was different in each. The Si wires whose carbon masks were written in higher electron dose have smooth surfaces indicating the complete and clear removal of carbon masks. However, a Si-wire in the center of the Fig. 3.4.2 has a rough surface. In this wire, the height of the carbon mask was small, and the Si was resulted to be etched during the RIE following the carbon mask and the SiO_2 layer. Therefore the height of the carbon mask was found to be very important, since it was also subjected to be physically etched during the RIE.

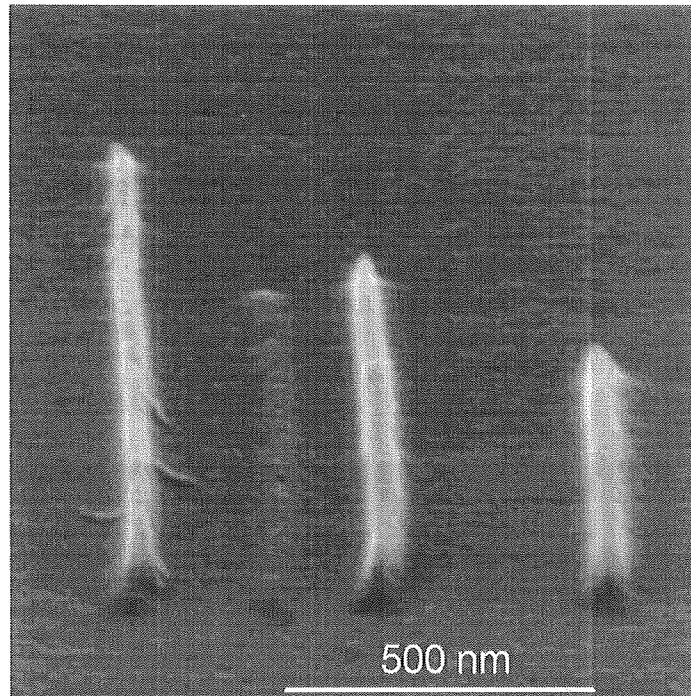


Fig. 3.4.2 SEM image of the Si wires of 60 nm width.

3.4.2 *Electrical property of n^{++} -Si nanowire*

For measuring the electrical properties of Si nanowires, heavily phosphorous-doped Si thin film was employed as a wire material. The epitaxial n^{++} -Si was grown by means of plasma-enhanced chemical vapor deposition (PECVD) at a temperature of as low as 250 °C [28]. The resistivity and the electron concentration of the film were measured by Van der Pauw method and they were $3 \times 10^{-4} \Omega \cdot \text{cm}$ and $1 \times 10^{21} \text{ cm}^{-3}$, respectively. The thickness of the film was 50 nm. The n^{++} -Si nanowire was fabricated through the above process after the conventional photolithography for patterning the contact and lead line regions. Figure 3.4.3 shows the SEM image of the resist patterns for contact pads and bridged carbon wire on the SOG/ n^{++} -Si/Si substrate before the RIE procedure. We can see that the carbon wire was clearly written on the insulating resists. In order to prepare a carbon mask with a high aspect ratio, the electron-beam was scanned three times. Therefore, a little fat wire whose width was about 60 nm was obtained.

The electrical characteristics was measured at 77 K and shown in Fig.3.4.4. The current-voltage curve shows linear property and the resistance of the wire was estimated to be 3.2 k Ω at 77 K, which was almost comparable to the calculated resistance of 4.1 k Ω . This discrepancy would be attributed to the parallel electrical path through Si substrate. From these results, it could be concluded that the carbon wires fabricated by the EBID method could be employed as a dry etching mask and that this process with Si/SiO₂ system was effective for nanostructure fabrication.

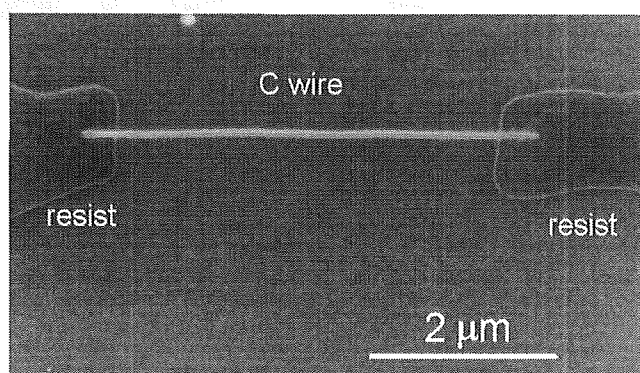


Fig. 3.4.3 SEM image of the bridged carbon mask.

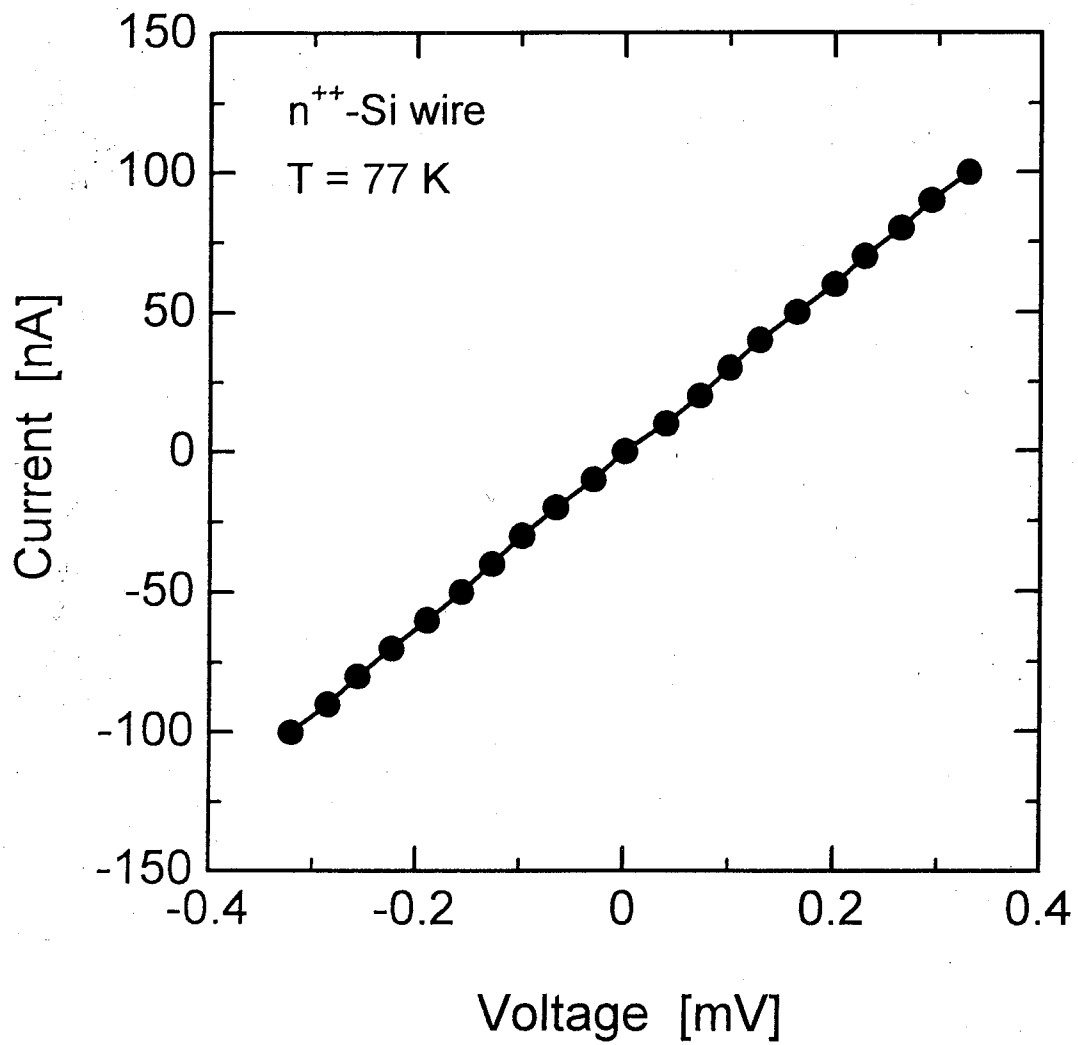


Fig. 3.4.4 Electrical characteristic of n^{++} -Si nanowire measured at 77 K whose width was about 60 nm.

3.5 Summary

In this chapter, modification of carbonaceous microstructures was extensively investigated. Especially, the EBID technique was concentrated for fabrication of nanowires. The residual gases in the chamber were taken as precursors, and the deposition of the carbonaceous material on any conducting substrate was achieved by no modification of the SEM. Optimization of the writing conditions was performed so as to create narrower carbon wires. A high acceleration voltage, low electron-beam current and high magnification were found to be optimum for making carbonaceous wires of high aspect ratio. A carbon wire with a minimum width of 30 nm was obtained. They were observed by AFM with its cantilever modified with a deposition of conic-shaped carbon needle, and a drastic improvement of the planar resolution was demonstrated by using this cantilever. For application of the wire to nanostructure fabrication, spin-coated SiO₂ was employed to remove the carbon mask through the lift-off process. As a demonstration of the Si nanowire fabrication, the heavily phosphorous-doped Si epitaxial film was used as a wire material, and the conducting n⁺⁺-Si wires with a 60 nm width were successfully fabricated with this novel technique.

Reference

- [1] A. N. Broers, W. W. Molzen, J. J. Cuomo and N. D. Wittels: *Appl. Phys. Lett.* **29** (1976) 596.
- [2] W. W. Molzen, A. N. Broers, J. J. Cuomo, J. M. E. Harper and R. B. Laibowitz: *J. Vac. Sci. Technol.* **16** (1979) 269.
- [3] Y. Ochiai, H. Watanabe, J. Fujita, M. Baba, S. Manako and S. Matsui: *Jpn. J. Appl. Phys.* **32** (1993) 6147.
- [4] K. Y. Hur, T. P. McKenna and T. E. Kazior: *J. Vac. Sci. Technol. B* **12** (1994) 3046.
- [5] S. Matsui and K. Mori: *J. Vac. Sci. Technol. B* **4** (1986) 299.
- [6] H. W. P. Koops, R. Weiel, D. P. Kern and T. H. Baum: *J. Vac. Sci. Technol. B* **6** (1988) 477.
- [7] K. T. K. Platen, L. -M. Buchmann, H. -C. Petzold and W. H. Brunger: *J. Vac. Sci. Technol. B* **10** (1992) 2690.
- [8] Y. Akama, E. Nishimura, A. Sakai and H. Murakami: *J. Vac. Sci. Technol. A* **8** (1990) 429.
- [9] K. L. Lee, D. W. Abraham, F. Secord and L. Landstein: *J. Vac. Sci. Technol. B* **9** (1991) 3562.
- [10] T. Fujii, M. Suzuki, M. Miyashita, M. Yamaguchi, T. Onuki, H. Nakamura, H. Yamada and K. Nakayama: *J. Vac. Sci. Technol. B* **9** (1991) 666.
- [11] U. A. Griesinger, C. Kaden, N. Lichtenstein, J. Hommel, G. Lehr, A. Menschig, H. Schweitzer, H. Hillmer, H. W. P. Koops, J. Kretz and M. Rudolph: *J. Vac. Sci. Technol. B* **11** (1993) 2441.
- [12] K. I. Schiffmann: *Nanotechnology* **4** (1993) 163.
- [13] C. C. Cho, F. L. Bernasek: *J. Appl. Phys.* **65** (1989) 3035.
- [14] R. R. Kunz and T. M. Mayer: *J. Vac. Sci. Technol. B* **6** (1989) 1557.
- [15] E. E. Ehrichs, W. F. Smith and A. L. Delozamme: *Ultramicroscopy* **42** (1992) 1438.
- [16] H. W. P. Koops, J. Kretz, M. Rudolph and M. Weber: *J. Vac. Sci. Technol. B* **11** (1993) 2386.

- [17] H. W. P. Koops, J. Kretz, M. Rudolph, M. Weber, G. Dahm and K. L. Lee: *Jpn. J. Appl. Phys.* **33** (1994) 7099.
- [18] J. Kretz, M. Rudolph, M. Weber and H. W. P. Koops: *Microcircuit Eng.* **23** (1994) 477.
- [19] M. Weber, M. Rudolph and J. Kretz: *J. Vac. Sci. Technol. B* **13** (1995) 461.
- [20] H. W. P. Koops: German Patent No. p. 4418930.3.
- [21] A. Abe, H. Adachi and H. Nakane: *Diamond and Related Mater.* **1** (1992) 267.
- [22] H. Kado, K. Yokoyama and T. Tohda: *Rev. Sci. Instrum.* **63** (1992) 3330.
- [23] H. Ximen and P. Russel: *Ultramicroscopy* **42** (1992) 1526.
- [24] T. R. Albrecht, S. Akamine, T. E. Carver and C. F. Quate: *J. Vac. Sci. Technol. A* **8** (1990) 3386.
- [25] H. Hiroshima and T. Komuro: *Jpn. J. Appl. Phys.* **32** (1993) 6153.
- [26] Y. Yamazaki, K. Ohotoshi, I. Sakai, K. Sugihara and M. Miyoshi: *Optik* **97** (1994) 67.
- [27] J. S. Park and W. I. Milne: *Jpn. J. Appl. Phys.* **35** (1996) L1550.
- [28] Y. Jia, T. Oshima, A. Yamada, M. Konagai, K. Takahashi, S. Tanigawa and L. Wei: *Jpn. J. Appl. Phys.* **32** (1993) 262.

Chapter 4

Characterization of Heavily-Doped Semiconductors and Its Applications to Superconducting Devices

4.1 Introduction

One of the key features in the semiconductor is that its electrical characteristics can be changed drastically by controlling the amount of doped impurities which generate carriers in the solid films. If the impurities were doped to as much as the solid solubility, this heavily-doped semiconductor is known to exhibit metallic conducting properties, such as the carriers do not freeze out but maintain low resistivity at low temperature. This metallic semiconductor is now attracting significant attention for the applications to the non-alloy ohmic contact layer with metal electrodes, the base layer of the heterojunction bipolar transistors or the cryoelectronic devices combining a superconducting material. In particular, this study took notice on the latter devices which are known as Josephson devices and are one of the promising candidates for future integrated circuit components.

In this chapter, several degenerated semiconductors are introduced and the dependence of their electrical properties on temperature is extensively studied together with the theoretical fittings in order to concern the above applications. Surprisingly, one of them showed superconductor-like properties below 4.2 K, and characterization of the film quality was also supplemented. For the device applications, Josephson weak link device was targeted using the heavily-doped semiconductors which function as a normal layer. And preliminary calculation is carried out on them from the point of the superconducting coherence length. The three-terminal device based on the proximity effect is also proposed.

4.2 Electrical Properties of Heavily-Doped Semiconductors

4.2.1 Heavily impurity-doped Si and GaAs epitaxial films

In our previous works, an extremely high impurity doping to Si and GaAs epitaxial films were achieved which were grown by plasma enhanced chemical vapor deposition (PECVD) or mercury sensitized photo CVD and metalorganic molecular beam epitaxy (MOMBE) methods with a carrier concentration of $3.2 \times 10^{21} \text{ cm}^{-3}$ and $1.5 \times 10^{21} \text{ cm}^{-3}$, respectively [1, 2]. The latter was successfully employed to the base layer of heterojunction bipolar transistors (HBTs) of InGaP/GaAs system [3, 4]. In this study, their application to the cryoelectronic devices is considered so that its electrical investigation at low temperature is inevitable.

Figure 4.2.1(a) shows the temperature dependence of the resistivity of the epitaxial n^{++} -Si thin film grown by PECVD with a thickness of about 100 nm. Since the growth proceeded under the non-thermal equilibrium conditions, phosphorous can be doped over the solid solubility and the film has an electron concentration of $3.2 \times 10^{21} \text{ cm}^{-3}$ with the phosphorous atoms activated almost 100 %. In Fig. 4.2.1(b), similar result from the C-doped GaAs was referred and replotted for the comparison [2]. The resistivity in both samples gradually decreases with decreasing temperature and exhibited constant value under about 50 K which is a residual resistivity.

Generally, the carriers in a degenerated semiconductor do not freeze out at low temperature and it is called the Mott transition [5]. Since the temperature dependence showed metallic conductance, theoretical consideration was carried out using equations developed at the metal system.

Temperature dependence of the resistivity ($\rho(T)$) is expressed by Matthiessen's rule as follows;

$$\rho(T) = \rho_r + \rho_i(T) \quad (4-1)$$

where ρ_r represents the residual resistivity which is independent on the temperature but

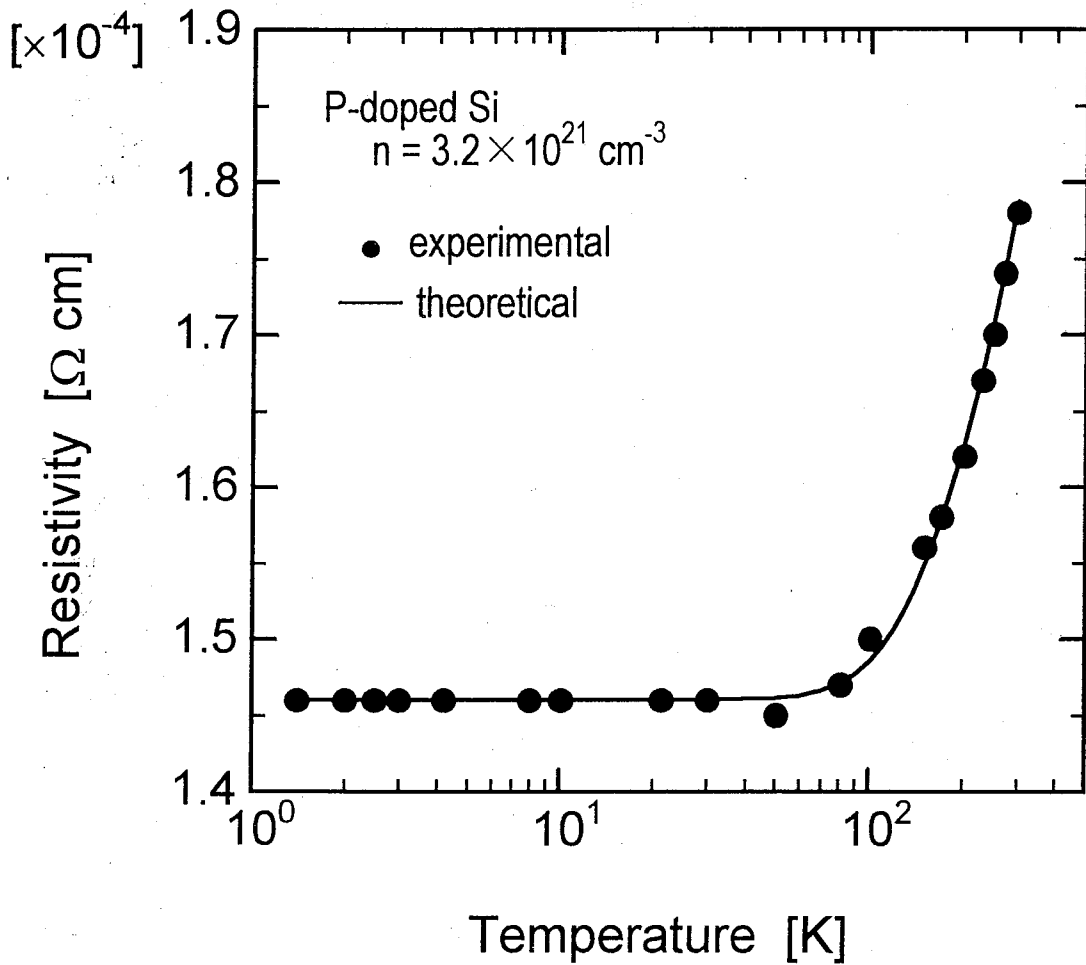


Fig. 4.2.1 (a) Temperature dependence of the resistivity of heavily P-doped Si.

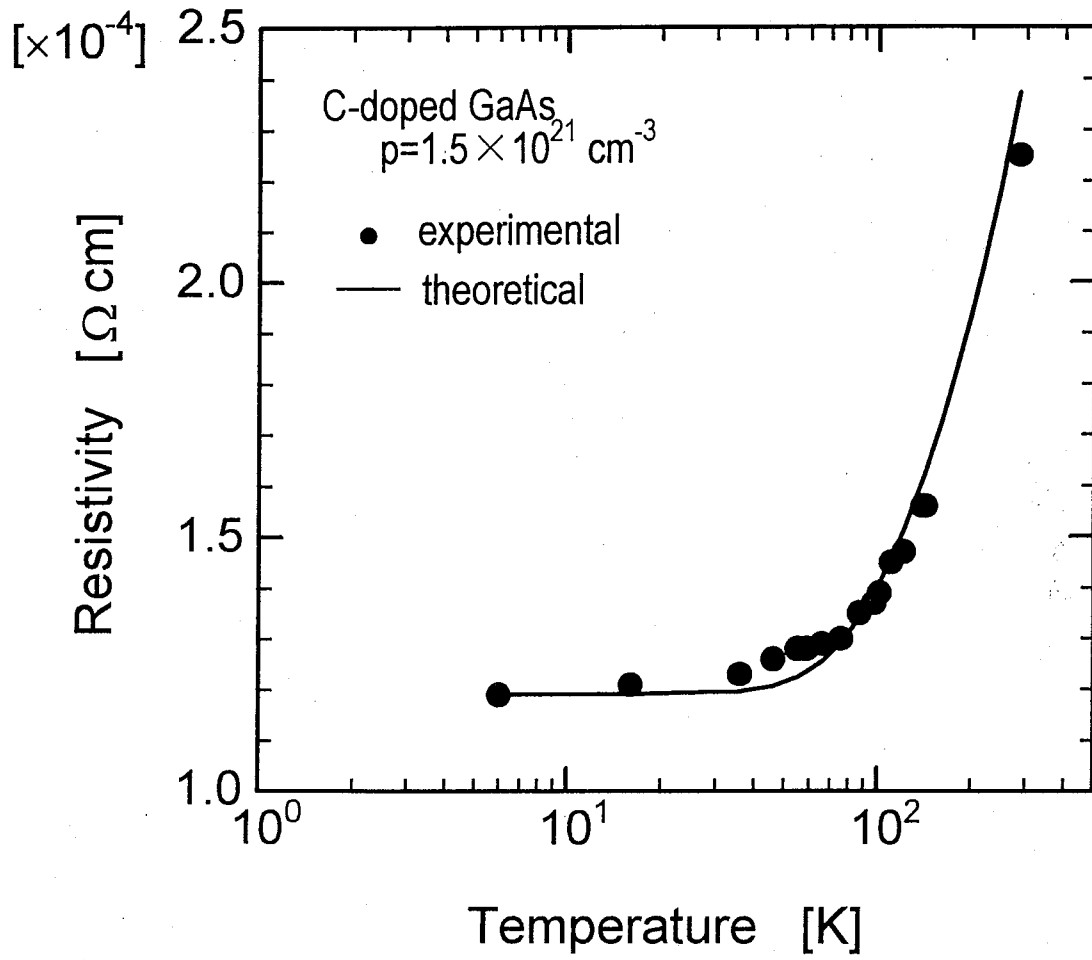


Fig. 4.2.1 (b) Temperature dependence of the resistivity of heavily C-doped GaAs. Experimental data were replotted from Ref. 2.

depends on the concentration of impurities or defects in the film. The $\rho_i(T)$ is the intrinsic resistivity originated from the phonon scattering process in the solid and expressed in the following equation using Bloch-Gruneisen's formula;

$$\rho_i(T) = \frac{4\rho_{High}T^5}{\theta_D^4} \int_0^{\frac{\theta_D}{T}} X^3 \left\{ \frac{X}{2 \sinh\left(\frac{X}{2}\right)} \right\}^2 dX \quad , \quad (4-2)$$

where θ_D represents the Debye temperature and ρ_{High} represents the $d\rho/dT$ at high temperature. Parameters for the calculation are ρ_r , ρ_{High} and θ_D , however, the former two of them could be deduced from the experimental data. For example, ρ_r is $1.46 \times 10^{-4} \Omega \cdot \text{cm}$ and ρ_{High} is $0.14 \times 10^{-6} \Omega \cdot \text{cm/K}$ in the n^{++} -Si case. As for the θ_D , the value from a bulk material is known. But there might exist considerable differences in between the bulk value and that from the heavily impurity-doped thin film. Therefore, the Debye temperature was taken valuable and chosen to best fit the experimental data. From the numerical integration and theoretical fittings shown in Fig. 4.2.1(a), the experimental data were clearly explained by the theory based on the metallic behavior, and the Debye temperature was 650 K from the calculation which is found to be close to the value of 658 K of bulk silicon [5]. In the case of C-doped GaAs, its dependence was also explained by the equations shown in Fig. 4.2.1(b) and the θ_D from the fitting was 400 K compared to the bulk value of 345 K.

Further investigation of the dependence of the resistivity on temperature was performed on the heavily P-doped Si thin film. At this measurement, the ρ - T curve was recorded in detail and the sample was cooled down to the order of 0.01 K. Typical characteristic is shown in Fig. 4.2.2. Below 0.1 K region, any change of the resistivity was not observed just exhibiting a residual resistivity down to 80 mK. However, there clearly appeared minimum resistivity or supercooling-like characteristics at around 50 K. In fact, this characteristic could be observed from Fig. 4.2.1(a). The origin of this phenomena could be thought to be related to the excess incorporation of phosphorous atoms in the silicon

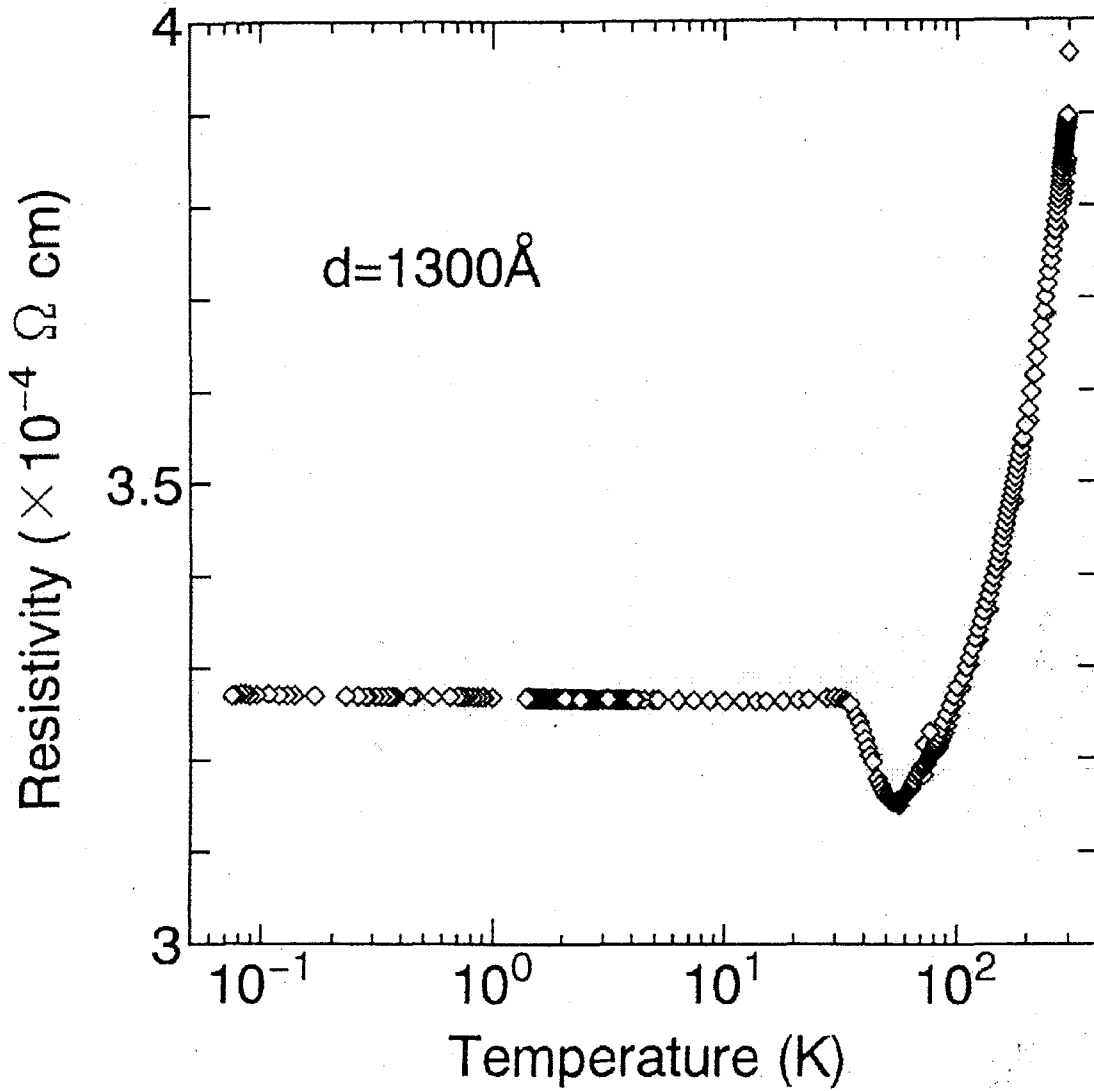


Fig. 4.2.2 Temperature dependence of the resistivity of heavily P-doped Si epitaxial film whose electron concentration is $1 \times 10^{21} \text{ cm}^{-3}$.

network, but it has not yet been clarified.

4.2.2 Heavily B-doped ZnO polycrystalline films

For use in the transparent conducting material in the solar cell applications, zinc oxide (ZnO) was taken noticed by one of our groups [6, 7]. By doping boron into the ZnO, n-type polycrystalline thin film can be deposited on glass or semiconductor substrate by metalorganic chemical vapor deposition (MOCVD) method. The resistivity of the film can be controlled by the doping level of boron and the film having the electron concentration of the order of $1 \times 10^{20} \text{ cm}^{-3}$ has been achieved. Detail deposition conditions are summarized in Chapter 5. Since this ZnO film has a polycrystalline structure, it could be applicable to the stacked junction with flexible structures.

The ρ - T curves of the ZnO thin films with various thicknesses were recorded in each and shown in Fig. 4.2.3. They were deposited on Si substrate in same condition but different in deposition time to control each thickness. Since the grain size becomes larger with increasing the film thickness, the film quality improves by thickening the film resulting to exhibit lower resistivity and higher electron concentration at room temperature. Moreover, its temperature dependence was found to be more metallic in thicker ZnO film but almost constant throughout this temperature range. The resistivity of ZnO film of 55 nm thick showed gradual increase with decreasing temperature but maintained low resistivity. This thin film will be employed to the cryoelectronic device in a stacked structure, which will be described afterward.

4.2.3 Nitride semiconductors having high electron concentration

In the previous sections, heavily impurity-doped semiconductor thin films were investigated. In the case of nitride semiconductors, native defects in the film are thought to generate carriers. This situation means that a film of poor crystallinity exhibits low resistivity although any impurities were not doped. In particular, the nitride semiconductors

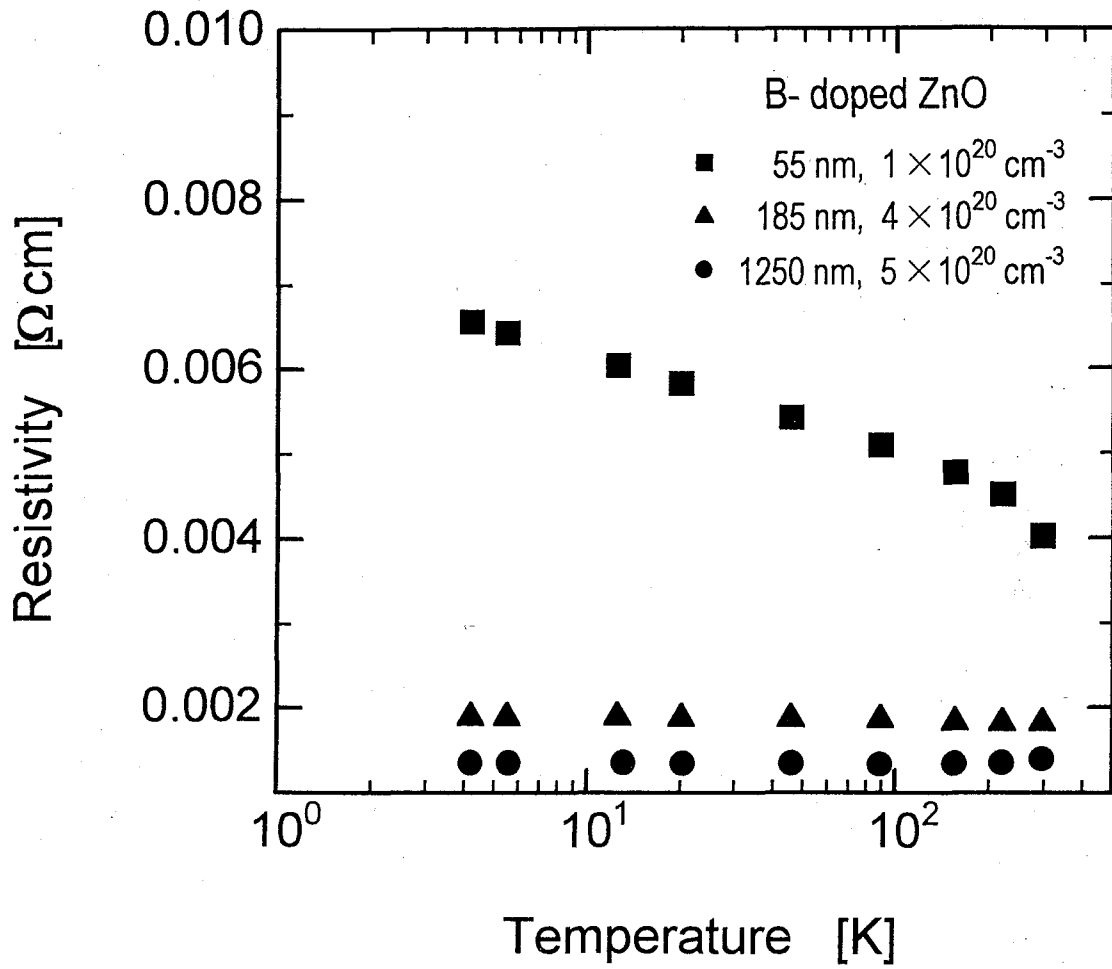


Fig. 4.2.3 Temperature dependence of the resistivity of B-doped ZnO with various thicknesses.

such as GaN or InN epitaxial films have the electron concentration of the order of 10^{20} cm^{-3} in the as-grown state providing that any special treatments were not employed. Since this study concentrates on the electrical properties of the heavily-doped semiconductors or the semiconductors having high carrier concentration, these nitrides were next investigated. Surprisingly, an InN thin film grown on a sapphire substrate showed peculiar electrical characteristics so that the results related to this film were discussed in detail in the next section. Here, experimental results from an InN epitaxial thin film grown on a GaAs substrate were stated.

Figure 4.2.4 shows a X-ray diffraction profile from the InN film grown on a GaAs(111)B substrate. It was grown by MOCVD method and growth conditions are almost the same as that grown on a sapphire substrate which is described in the following section. Clear InN(0002) and (0004) peaks were observed indicating its heteroepitaxial growth on the substrate. In the figure, small peak of GaN(0002) was also observed. For the epitaxial growth of InN on the GaAs, nitridation of the substrate surface before the InN growth is indispensable, which relaxes the lattice mismatch between these materials by forming GaN buffer layer. Surface of the InN film was monitored by atomic force microscopy and its image was shown in Fig. 4.2.5. We can see that the surface is not so smooth with a roughness of about 30 nm, however, the reflection high-energy electron diffraction (RHEED) pattern showed spotty pattern supporting the film as being epitaxial.

Temperature dependence of the resistance of the n^{++} -InN thin film is shown in Fig. 4.2.6. Since the electron concentration of the sample was estimated to be about $1 \times 10^{21} \text{ cm}^{-3}$, the film was degenerated and the ρ - T curve showed the same tendency with the n^{++} -Si or p^{++} -GaAs as discussed previously. Theoretical fitting using eqs.4-1 and 4-2 was also performed and the characteristic was almost reproduced with the Debye temperature of 640 K. These theoretical consideration are summarized in Table 4.2.1. The estimated Debye temperatures in each materials are consistent with their bulk values. A little difference between the calculated and bulk temperatures would be due to the large number of impurity concentration incorporated in the crystal network or the existence of the native defects.

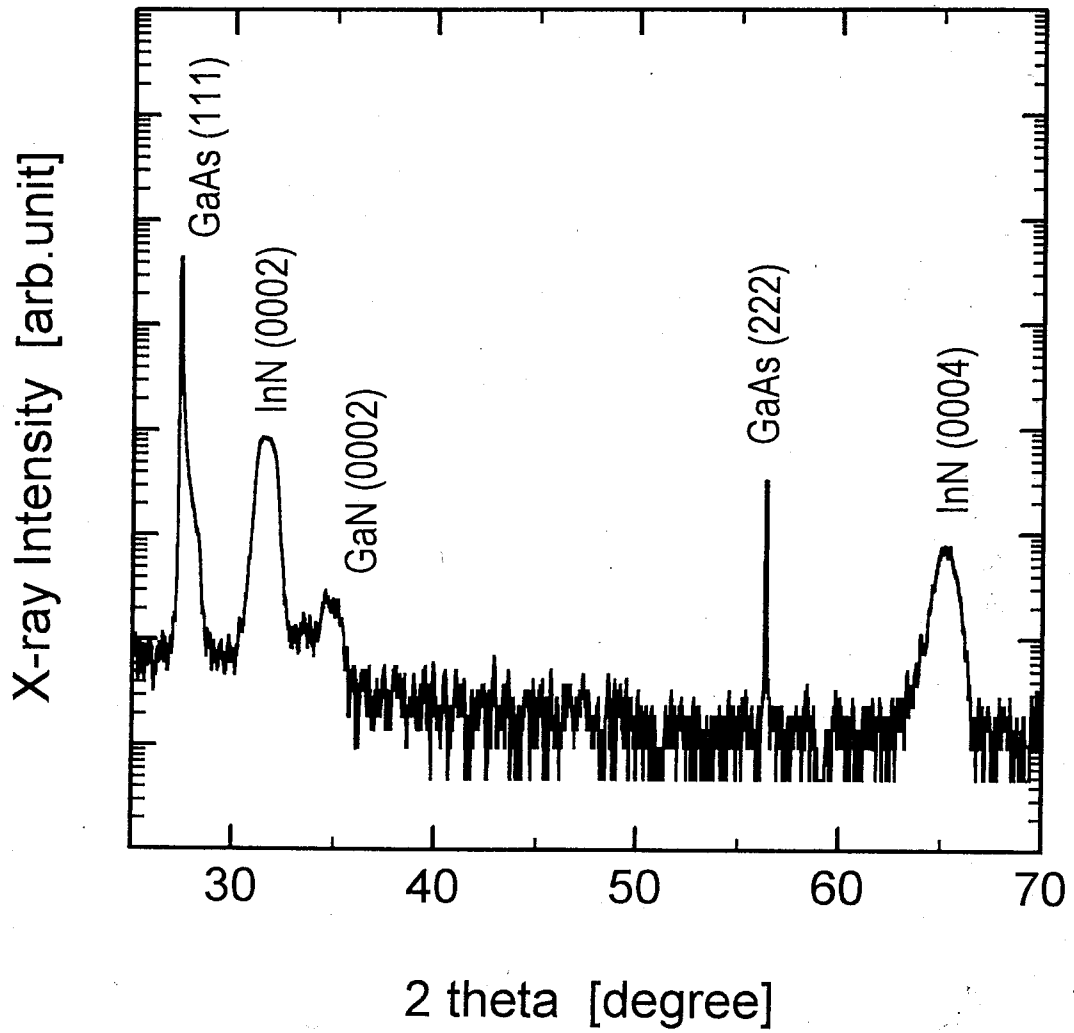


Fig. 4.2.4 X-ray rocking curve of the InN film grown on GaAs(111)B.

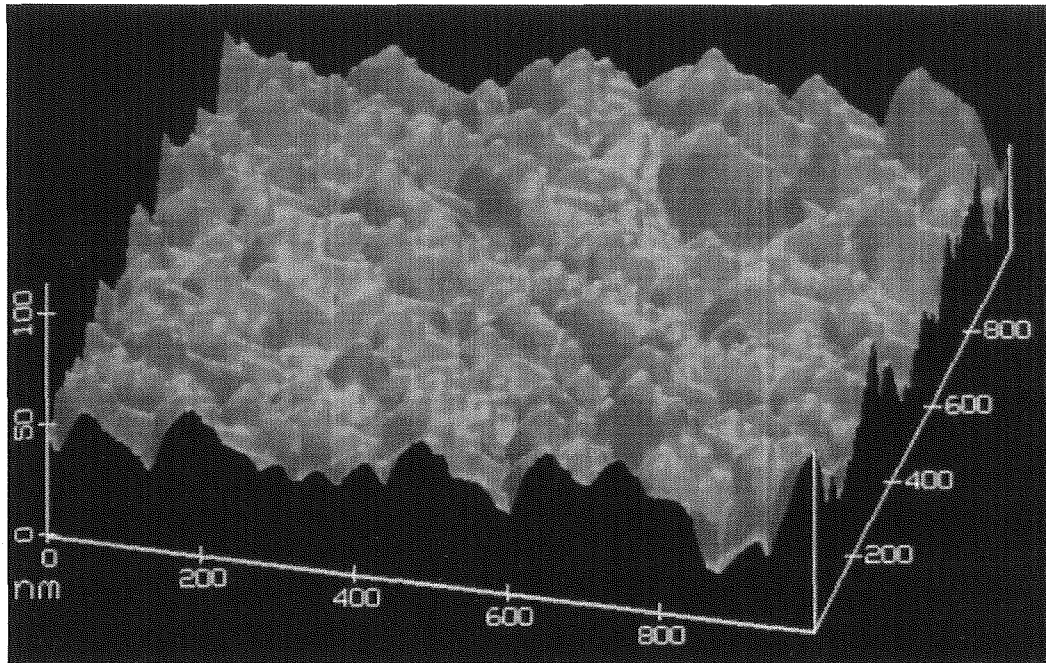


Fig. 4.2.5 AFM image of InN epitaxial thin film grown on GaAs(111)B substrate whose electron concentration is $1 \times 10^{21} \text{ cm}^{-3}$.

Table 4.2.1 Theoretical fittings on the temperature dependence of resistivity.

Material	Carrier Concentration [cm^{-3}]	Residual Resistivity ρ_r [$\Omega \cdot \text{cm}$]	θ_D [K] (calculation)	θ_D [K] (Reference)
n^{++} -Si	3.2×10^{21}	1.46×10^{-4}	650	658
p^{++} -GaAs	1.5×10^{21}	1.19×10^{-4}	400	345
n^{++} -InN	1×10^{21}	3.41 [Ω]	640	—
n^+ -ZnO	5×10^{20}	1.36×10^{-3}	—	415

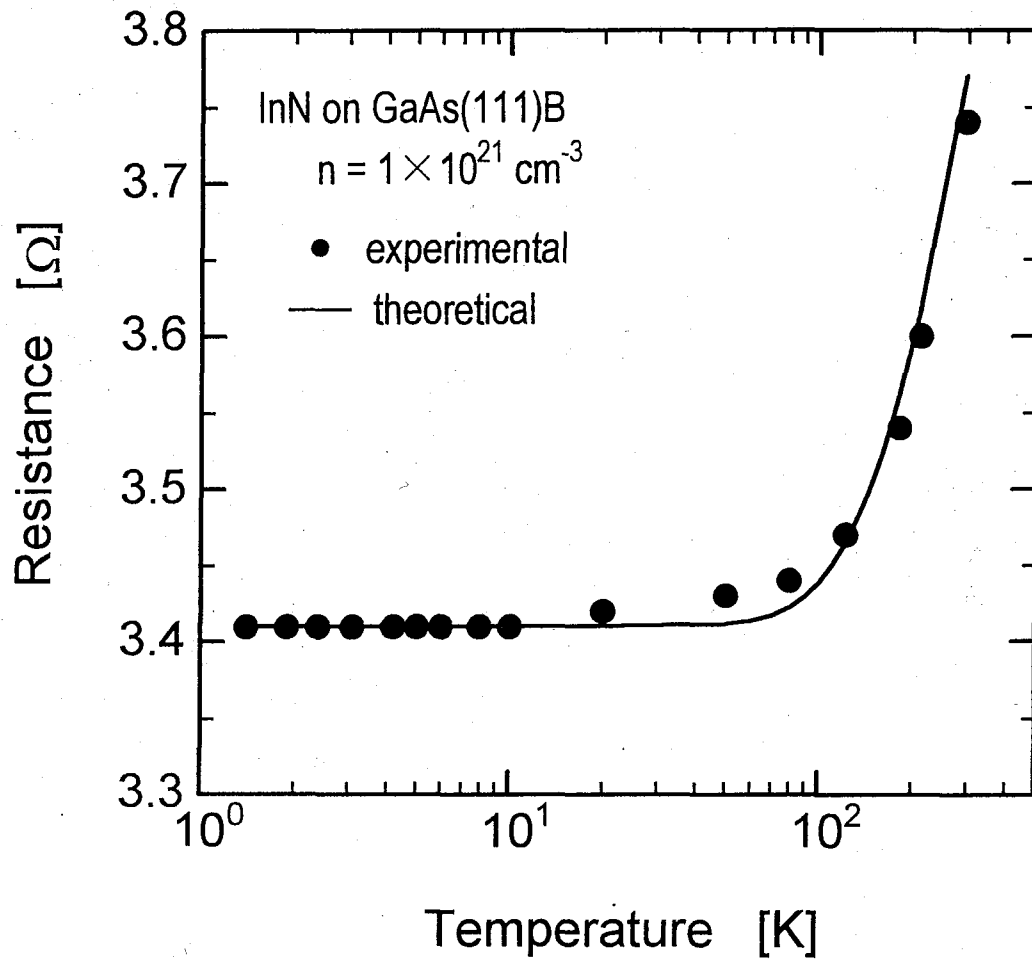


Fig. 4.2.6 Temperature dependence of the resistivity of InN grown on GaAs(111)B.

4.3 Anomalous Electrical Properties in n^{++} -InN

4.3.1 Background and properties of InN

In this section, the investigation of degenerated semiconductors continues further. Particularly, an epitaxial indium nitride (InN) thin film grown on a sapphire (α -Al₂O₃) substrate is taken into consideration because the anomalous electrical and magnetic characteristics were recorded at very low temperature for the first time and its properties resembled with that of superconductor. Therefore, the extensive characterization as well as the electrical measurement are performed in order to investigate the origin of this anomaly.

The InN belongs to the III-V nitride semiconductors which are now promising materials for blue light emitting devices, and a lot of experimental efforts have been made on the epitaxial growth and control of carrier concentration [8-10]. Among the nitrides, only a few papers have dealt with the growth of InN. Consequently, the practical application of InN has been restricted to its alloys such as GaN or AlN. From the standpoint of growth, epitaxial InN has less nitrogen similar to the other nitride semiconductors. Its vacancy is thought to generate carriers and the undoped epitaxial film has the electron concentration of over $1 \times 10^{20} \text{ cm}^{-3}$. Therefore, InN is one of the degenerated semiconductors, though its electrical properties at the low temperature are not well understood. In order to clarify its applicability to the cryoelectronic devices, the epitaxial growth of n^{++} -InN and the measurement of the temperature dependence of its electrical properties are performed and in particular, their dependence on the magnetic field. The investigation of the properties of these epilayers are supplemented by AFM and SEM observations and X-ray spectroscopy.

4.3.2 Electrical properties of InN films

The n^{++} -InN was epitaxially grown on a sapphire (0001) substrate (α -Al₂O₃) by MOCVD method using trimethylindium (TMI) and ammonia (NH₃) as the sources for indium and nitrogen, respectively. The details of the growth conditions have been described elsewhere [11]. The thickness of the films were about 150 to 300 nm. The temperature dependence of the electrical properties of the InN film with an electron concentration of 1.3

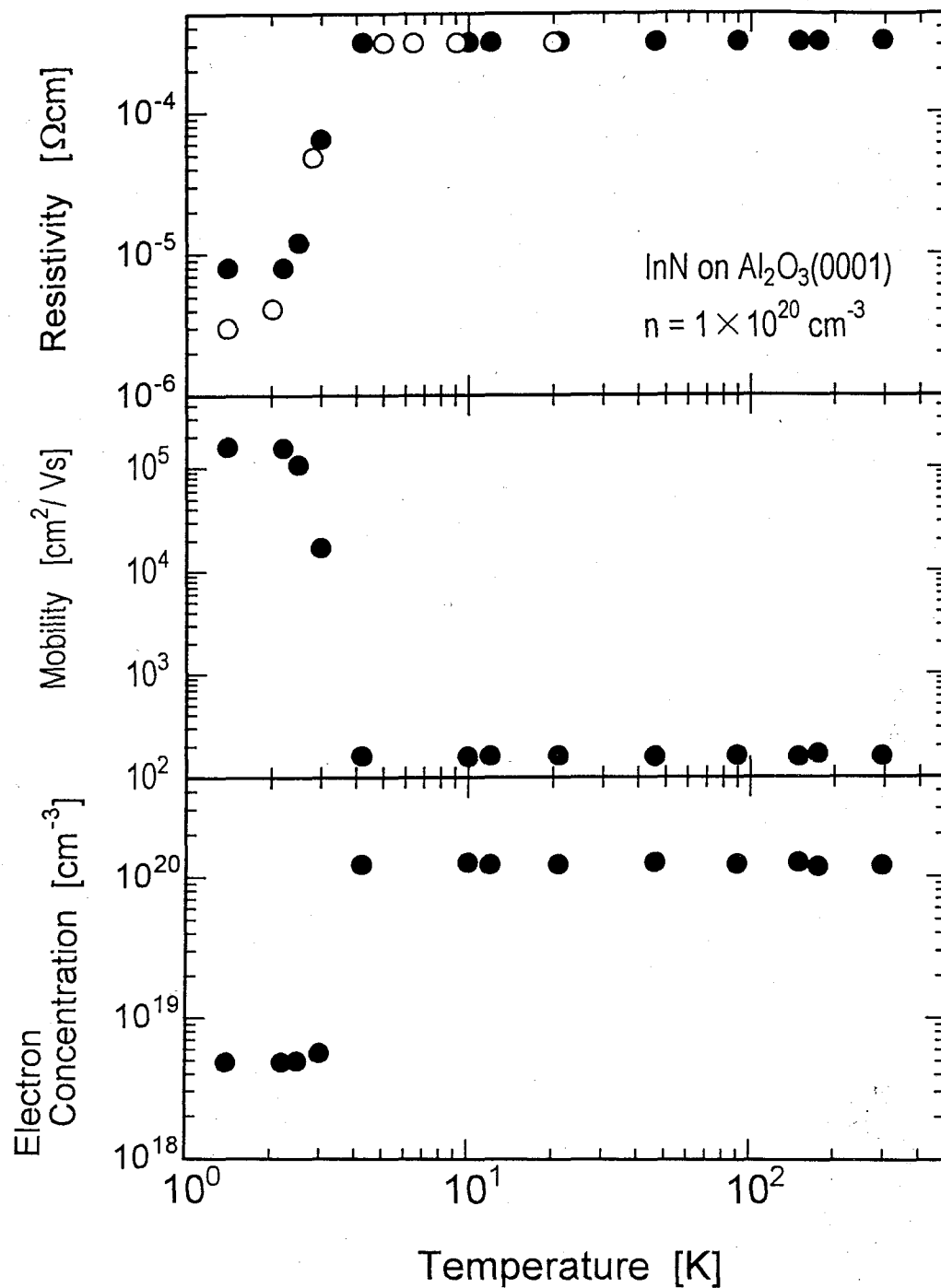


Fig. 4.3.1 Temperature dependence of the electrical properties of the InN film with an electron concentration of $1 \times 10^{20} \text{ cm}^{-3}$ measured by means of van der Pauw (●) and the four-point probe method (○).

$\times 10^{20} \text{ cm}^{-3}$ was at first investigated. The resistivity, mobility and electron concentration were measured by the van der Pauw method in the range from room temperature (R.T.) to as low as 1.4 K. The results are summarized in Fig. 4.3.1. The dependence of these parameters on temperatures from R.T. to 4.2 K showed the common tendencies of a degenerated semiconductor. However, unlike the InN epitaxial film grown on a GaAs(111)B substrate, both the resistivity and the electron concentration showed sudden decrease below about 3 K, and the mobility increased to as much as $1 \times 10^5 \text{ cm}^2/(\text{V}\cdot\text{s})$ at 1.4 K. The results from the four-point-probe method are also shown in the figure, and a similar dependence of resistivity on the temperature were obtained. This anomaly in the mobility and the electron concentration is attributed to the sharp decrease of resistivity as will be discussed later.

Further electrical characterization was carried out on the sample. Current-voltage curve measured at 1.4 K and 4.2 K are shown in Fig. 4.3.2. Between room temperature and 4.2 K, the film exhibits ohmic behavior. However, below 3 K, a non-linear characteristic begins to appear. The differential resistance (dV/dI) becomes quite small (about 8 m Ω) particularly in the low current bias region. Furthermore, this non-linearity can be removed by adding a magnetic field perpendicular to the film. In Fig. 4.3.3, it is shown that the non-linearity of the I - V curve becomes weaker with increasing magnetic field. At 650 mT, a linear I - V characteristic is again observed. Another magnetic characteristics was considered from the point of the Hall effect. Since the film is degenerated and it has an electron concentration of $1.3 \times 10^{20} \text{ cm}^{-3}$, the Hall effect was relatively small and its modulation was only 6 % in resistance at 4.2 K or at room temperature by applying a 0.7 T magnetic field. However, the film exhibited a low resistance state at 1.4 K and the Hall effect became extremely large compared to the normal state at 4.2 K. The amplitude of modulation is of the order of 100 at 1.4 K by same magnetic field. Furthermore, the dV/dI at 1.4 K almost coincided with the resistance at 4.2 K both under a magnetic field of 650 mT, which can be understood that the I - V curve in the Fig. 4.3.3 under 650 mT coincided with the normal ohmic curve at 4.2 K or at room temperature. Considering the magnetic field dependence of the I - V curve, it could be said that such a large modulation is due to the occurrence of some low resistance state rather than due to the Hall effect and that the state can be easily broken

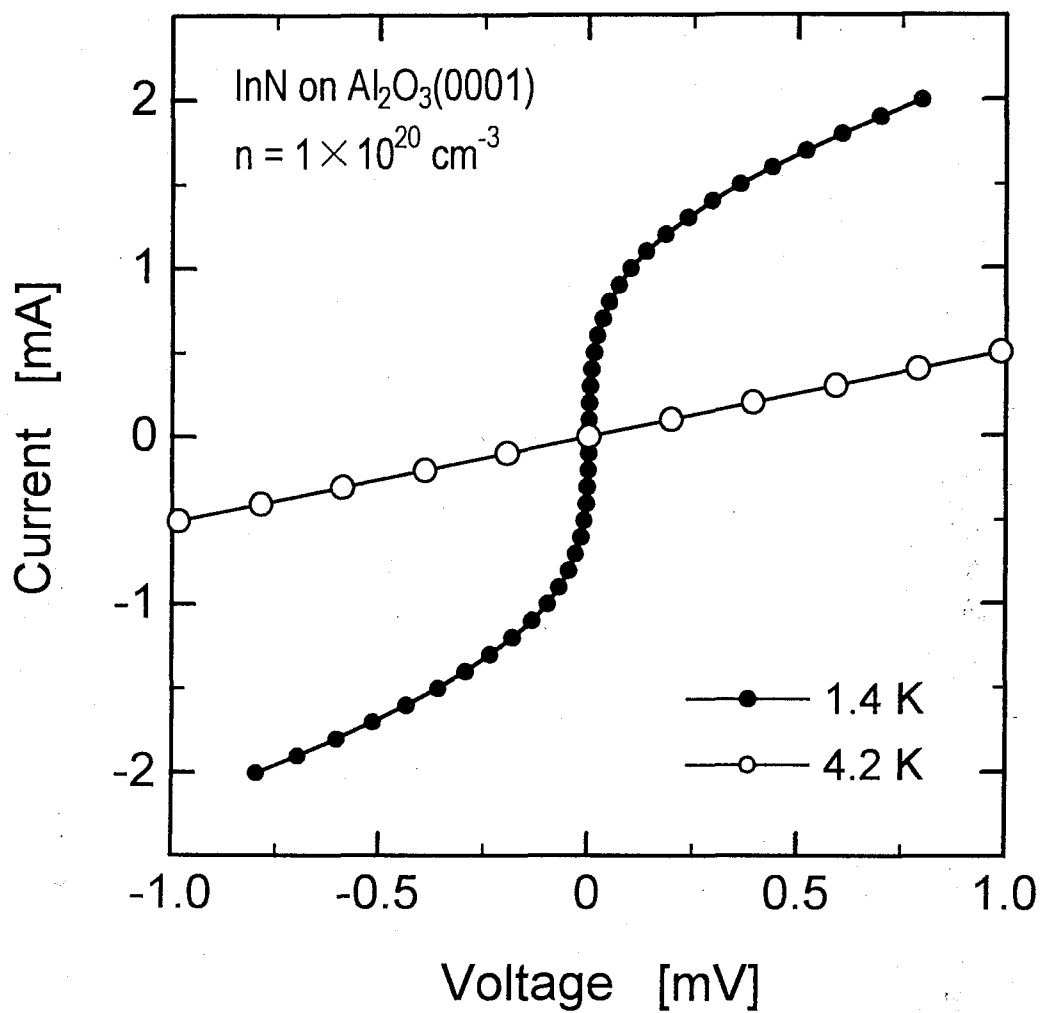


Fig. 4.3.2 Temperature dependence of I - V characteristics of the InN thin film whose electron concentration is $1 \times 10^{20} \text{ cm}^{-3}$.

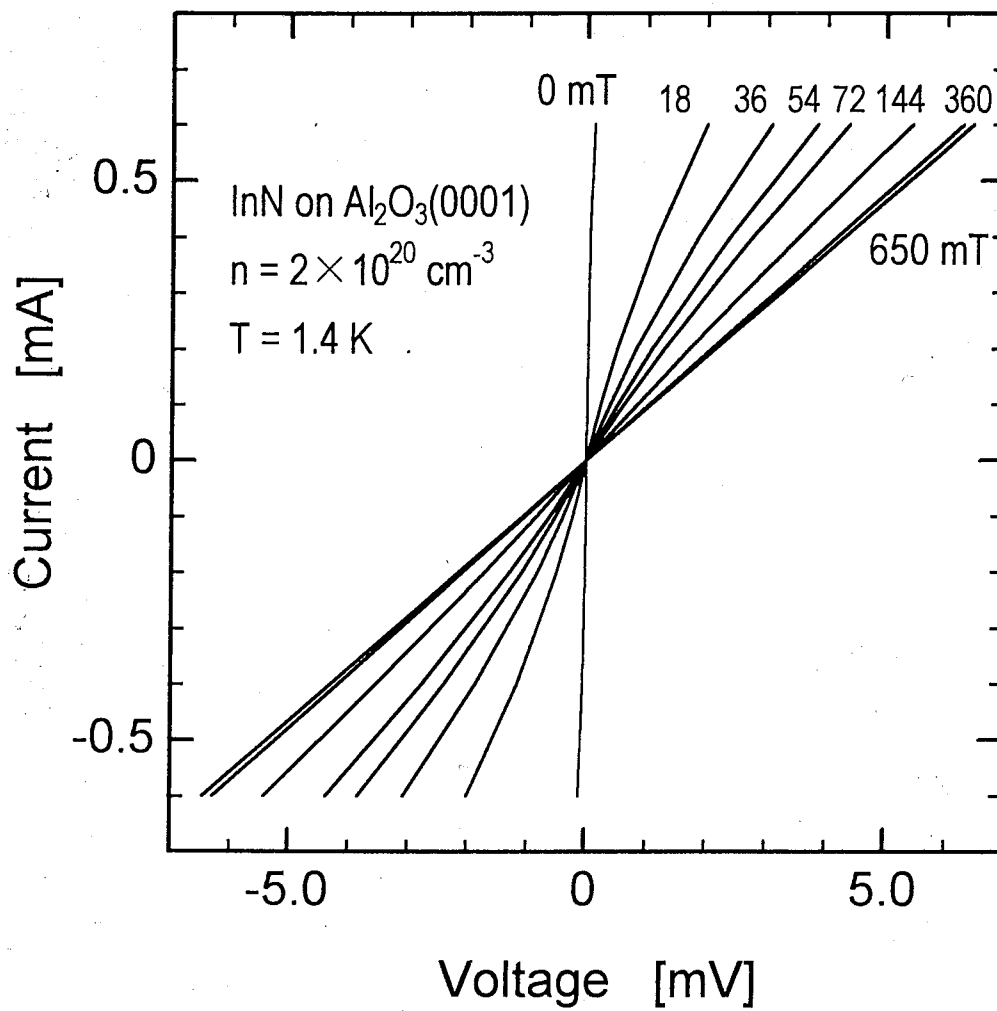


Fig. 4.3.3 Magnetic field dependence of I - V characteristics of InN thin film at 1.4 K whose electron concentration is $2 \times 10^{20} \text{ cm}^{-3}$.

by the magnetic field. These electrical and magnetic properties might indicate the possibility of the occurrence of a phase transition in InN films such as the transition from metallic to superconductors.

From the BCS theory, it is essential for the low carrier density materials that the material should have as many carriers as possible in order to exhibit superconductivity [17]. Therefore, the InN film with a much higher electron concentration could be expected to show much lower resistivity at 1.4 K than previously studied film. However, the anomaly of the film was found to gradually disappear at higher electron concentrations. The temperature dependence of the resistivity of the films having different electron concentrations is summarized in Fig. 4.3.4. The temperature range is varied from 1.4 K to 4.2 K. Each resistivity is normalized by that at 4.2 K. The thermal slope of the resistivity as a function of the electron concentration is less sharp at higher electron concentrations. The "normal" characteristic was observed for the film with an electron concentration of $2 \times 10^{21} \text{ cm}^{-3}$.

Though the InN films did not show a perfect zero resistance state, the following comments could be made concerning the superconductivity. Comparing this InN with the other superconducting semiconductors such as GeTe [13] and SnTe [14], the superconducting transition temperature (T_c) in the InN was one order of magnitude higher than these telluride superconducting semiconductors, and the critical temperature does not depend on the electron concentration. A possible candidate for this transition is the existence of superconducting elemental indium in the film whose T_c is 3.4 K, and this temperature is quite close to the temperature range of the InN films. Since the InN is considered to have many electrons supplied from nitrogen vacancies, it is possible that the In-rich film led to the indium precipitation inside the film, and it caused such characteristics. Furthermore, the condition of the surface should be noted. InN is said to be easily oxidized and make In-N-O complexes when exposed to the ambient [15]. Therefore in the next section, the surface and the film quality were carefully investigated in order to clarify the situation.

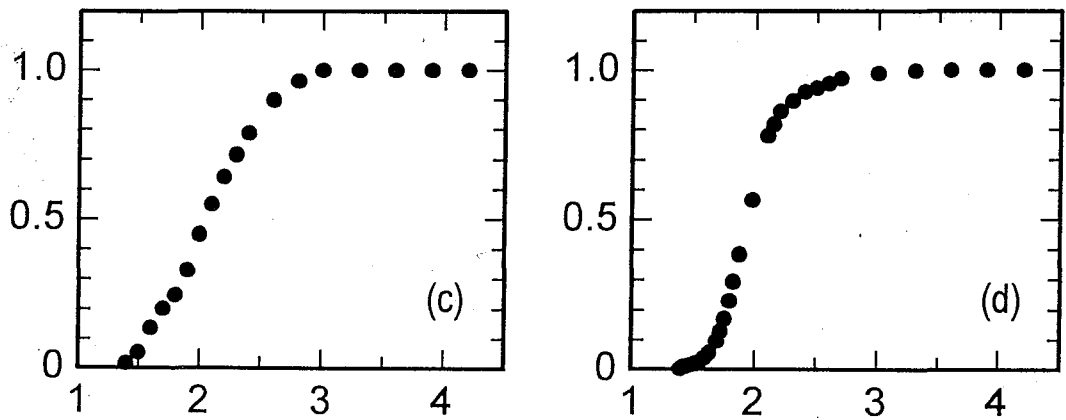
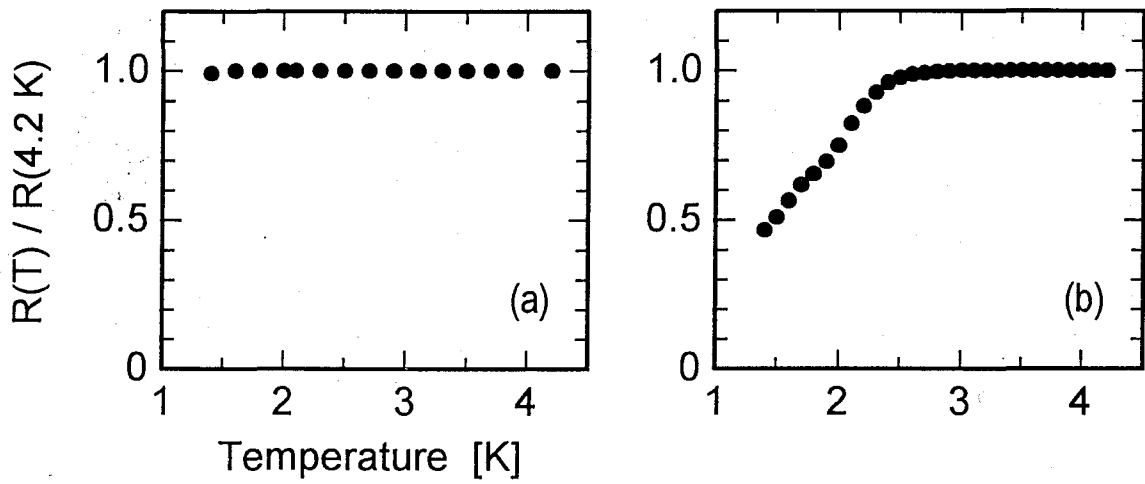


Fig. 4.3.4 Temperature dependence of the resistivity of InN films with an electron concentration of (a) $2 \times 10^{21}\text{ cm}^{-3}$, (b) $7 \times 10^{20}\text{ cm}^{-3}$, (c) $2 \times 10^{20}\text{ cm}^{-3}$ and (d) $1 \times 10^{20}\text{ cm}^{-3}$.

4.3.3 Characterization of InN films

For the characterization of the film quality, X-ray rocking curves of InN films with electron concentrations of $1 \times 10^{20} \text{ cm}^{-3}$, $2 \times 10^{20} \text{ cm}^{-3}$, $7 \times 10^{20} \text{ cm}^{-3}$ and $2 \times 10^{21} \text{ cm}^{-3}$ are shown in Fig. 4.3.5. These spectra were measured by the X-ray rocking curves with copper target ($\lambda_{\text{CuK}\alpha 1} = 0.1540562 \text{ nm}$) radiation from a high-power X-ray generator (40 kV, 55 mA) using a high-resolution computer-controlled PHILIPS X' Pert four-crystal material research diffractometer (MRD) system. The clear peaks of InN (0002) and (0004) are observed indicating epitaxial growth on the $\alpha\text{-Al}_2\text{O}_3$ substrate with the wurtzite structure. Any other small peaks originating from the other phase of InN or the elemental indium were not observed. The reflection high-energy electron diffraction (RHEED) pattern from these films were also recorded, and their epitaxial growth were verified as they showed spotty patterns.

Next, atomic force microscopy (AFM) images were taken to obtain information about the InN surface. Figures 4.3.6(a) and 4.3.7(a) show the surface morphology of the samples with an electron concentration of $1 \times 10^{20} \text{ cm}^{-3}$ and $2 \times 10^{21} \text{ cm}^{-3}$, respectively. Corresponding SEM images were also displayed in Figs. 4.3.6(b) and 4.3.7(b). The sample with the electron concentration of $1 \times 10^{20} \text{ cm}^{-3}$ exhibits the anomaly in the electrical property. The surface of both samples is not so smooth with a surface roughness of 50 nm. Furthermore, samples show columnar fibrous structures with a diameter of each column of about 100 nm. This columnar fibrous growth was also observed by SEM images. However, no significant differences were found in the surface morphology of these two films. Furthermore, indium droplets did not exist on the surface.

Figures 4.3.8(a) and (b) show the results from the reciprocal space mapping of the films with an electron concentration of $1 \times 10^{20} \text{ cm}^{-3}$ and $2 \times 10^{21} \text{ cm}^{-3}$, respectively. The InN (0002) peak was monitored in comparison with the substrate peak of $\alpha\text{-Al}_2\text{O}_3(0006)$. Vertical axis in those figures is the inclined angle (ω direction) of the samples and horizontal is the diffraction angle. Since the InN films were heteroepitaxially grown on the sapphire substrate, each X-ray diffraction angles are not close compared to the mosaicity of each film. Therefore the mosaicity of the each peak was shown individually in inset of the figures. We

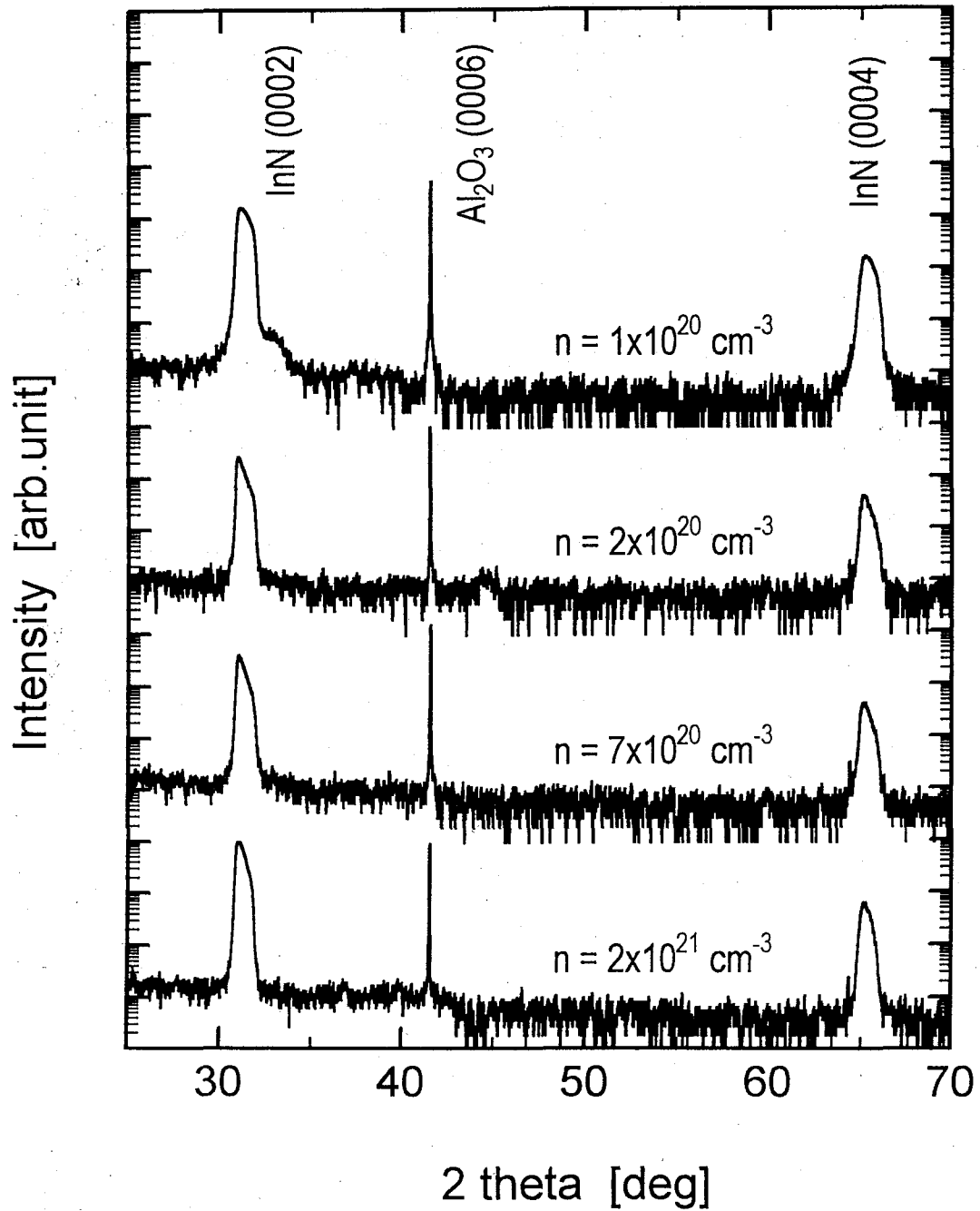


Fig. 4.3.5 X-ray rocking curves of InN films with various electron concentrations grown on the sapphire (0001) substrate.

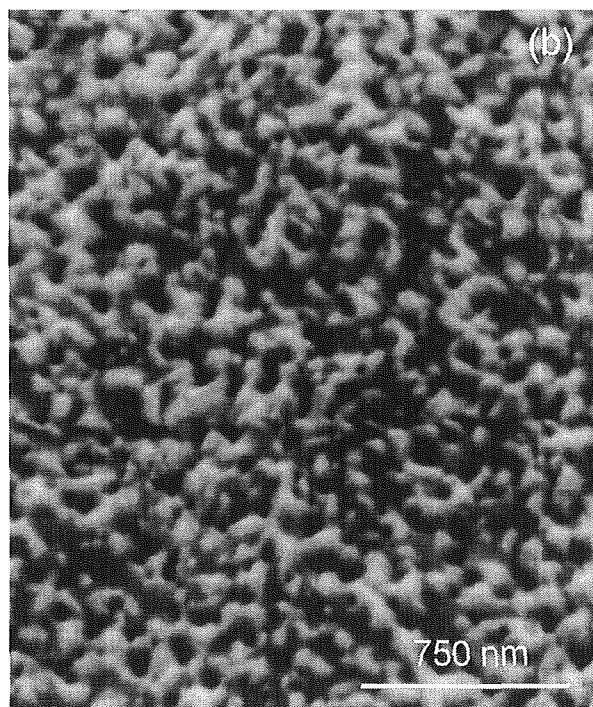
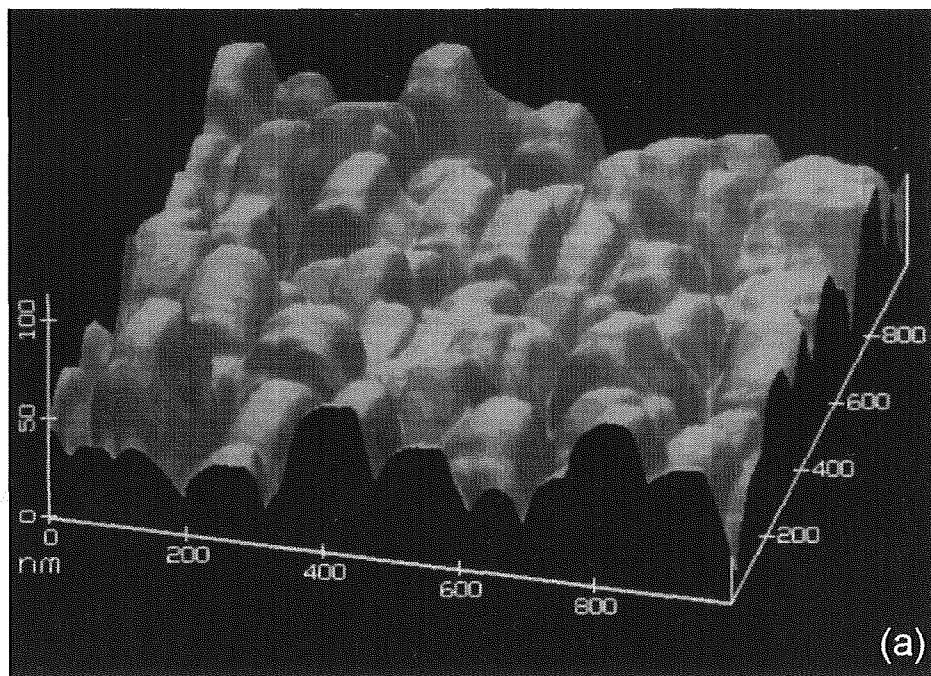


Fig. 4.3.6 AFM (a) and SEM (b) images of the InN epitaxial thin film grown on α Al_2O_3 substrate whose electron concentration is $1 \times 10^{20} \text{ cm}^{-3}$.

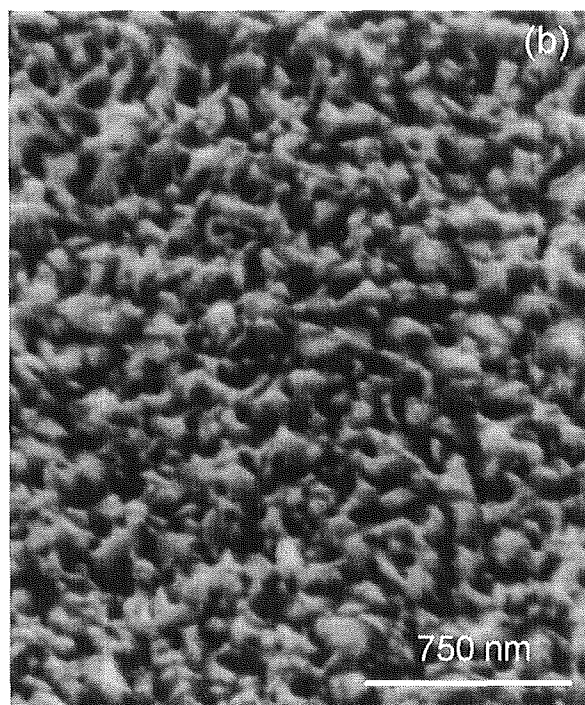
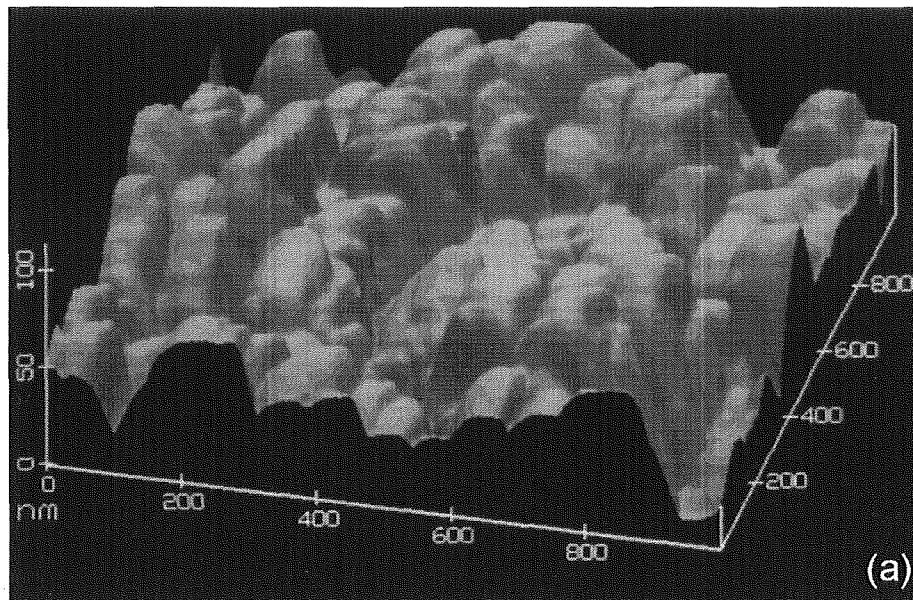


Fig. 4.3.7 AFM (a) and SEM (b) images of the InN epitaxial thin film grown on α - Al_2O_3 substrate whose electron concentration is $2 \times 10^{21} \text{ cm}^{-3}$.

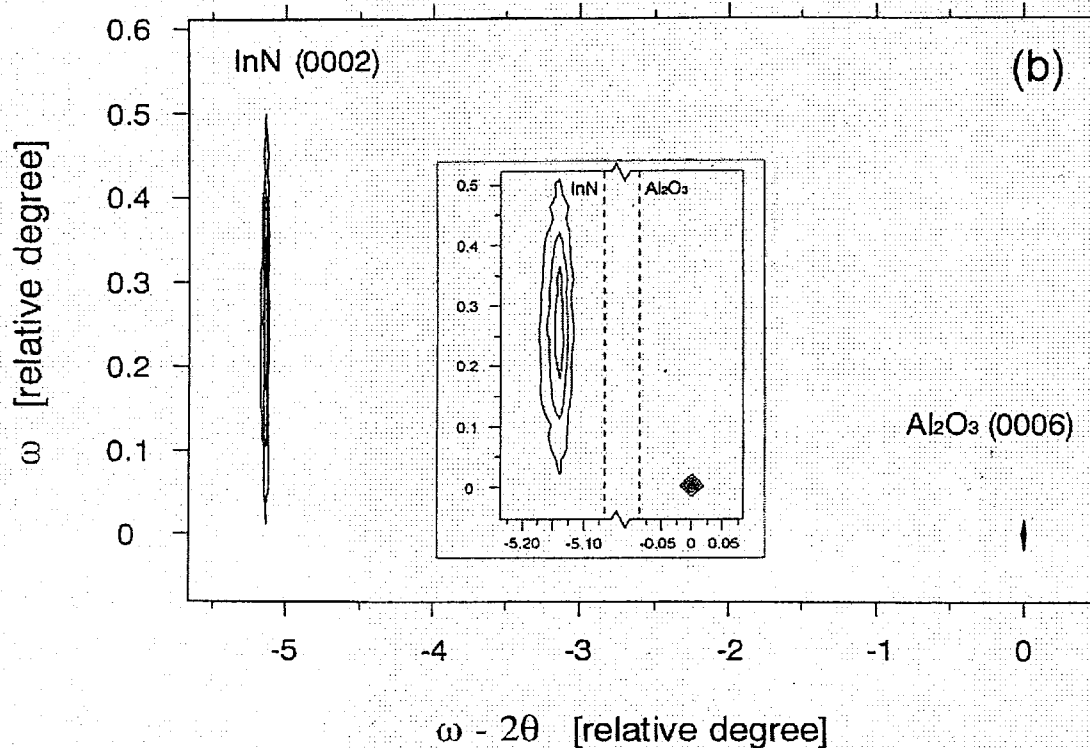
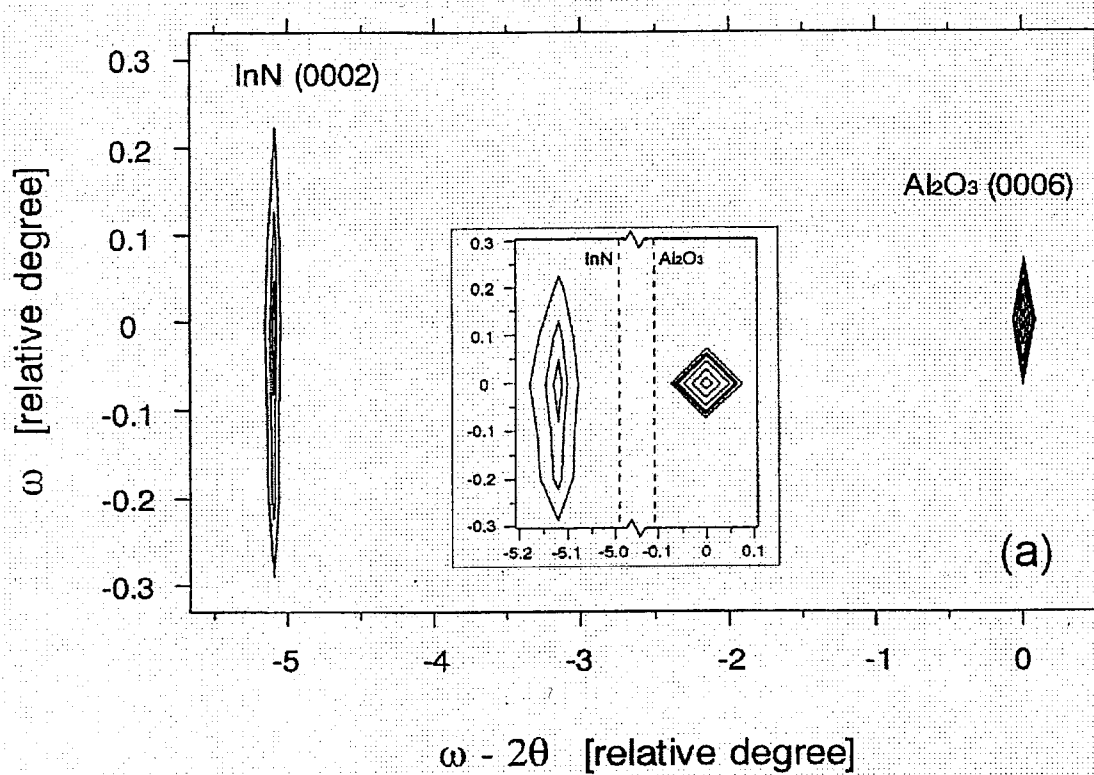


Fig. 4.3.8 Reciprocal space mappings of InN epitaxial films whose electron concentration are (a) $1 \times 10^{20} \text{ cm}^{-3}$ and (b) $2 \times 10^{21} \text{ cm}^{-3}$.

can see from the figures that the center of the peak of InN(0002) shifted to the ω direction in the film of higher electron concentration which did not show anomaly at low temperature, but the peak did not shift in the film of $1 \times 10^{20} \text{ cm}^{-3}$ electron concentration. This result means that the InN film of $2 \times 10^{21} \text{ cm}^{-3}$ electron concentration was epitaxially grown on the substrate with being inclined to the c-axis in a certain degree, which corresponds to the fact from the electrical properties that the less nitrogen are incorporated in the film having higher electron concentration and the film quality is worse. This consideration might indicate that the film of better quality exhibit more drastic electrical anomaly at low temperature.

As discussed before, in order to show the unusual electrical characteristics due to the elemental superconducting indium, the InN films should contain a significant amount of elemental indium. However, neither indium droplets nor its precipitation were observed by the AFM images and also by the X-ray rocking curves. From these studies, the sharp decrease in resistivity of the InN films and its dependence on the electron concentration can not be attributed to be due to the elemental indium. A transmission electron microscopy (TEM) observation might reveal this point clearly. The fact that the film with a lower electron concentration showed the superconductor-like characteristics might indicate that the epitaxial InN would appear to be a superconducting semiconductor when its film quality is much improved, which means that the InN must be epitaxially grown to have lower nitrogen vacancies.

4.4 Theoretical Consideration of Weak Link Device for Employing Heavily-Doped Semiconductors

4.4.1 Proximity effect

As was discussed extensively, the heavily-doped semiconductors show low resistivity at low temperature whose characteristics are very different from that of lightly-doped one. For the device application of this film, superconducting weak link device operated at liquid helium or just above temperature is noticed and its applicability is examined in this section. This weak link device belongs to the so-called Josephson devices which features utilization and control of superconducting current, which was discussed in detail at Chapter 2. One of the significant parameters is the coherence length (or decay length) in the normal region (in this case, it corresponds to the heavily-doped semiconductor thin film). When the normal metal contacts with superconductor, cooper pairs in the superconductor tunnels through the barrier (or Schottky barrier) and penetrates to the normal region to some distance where the superconductivity is induced in the normal metal near the boundary. Therefore, by sandwiching the normal metal by superconductors, cooper pairs can travel from one superconducting electrode to another through the non-superconducting material. This effect is called proximity effect and the influential length was again described as follows;

$$\xi_{Se} = \left(\frac{\hbar^3 \mu}{6\pi k_B T m_{Se}^*} \right)^{\frac{1}{2}} (3\pi^2 n)^{\frac{1}{3}} \left(1 + \frac{2}{\ln \frac{T}{T_{cSe}}} \right)^{\frac{1}{2}}, \quad (4-3)$$

where k_B , m^* , μ , n , and T_{cSe} represent Boltzman constant, effective mass of the carrier, mobility, carrier concentration and superconducting transition temperature of semiconductor (usually equals to zero). Rough estimation was performed in several semiconductors, and calculated coherence length is summarized in Table 4.4.1. The referred values are from the single crystalline films characterized at room temperature except for n-InN. In the calculation, the values of mobility and carrier concentration were from the room temperature

measurement and estimated coherence length was the one at 4.2 K. Therefore, they are not exact values since the electrical properties of each semiconductors at 4.2 K are not well known. In general, we can see from the table that this coherence length in degenerated semiconductor ranges from a few 10 nm to 100 nm. Therefore, microfabrication technology is required to achieve this range of processing and to realize a superconducting weak link devices.

Table 4.4.1 Coherence length in various semiconductors.

Semiconductor	Carrier Concentration [cm^{-3}]	Mobility [cm^2/Vs]	ξ (4.2 K) [nm]	Reference
p-Si	1×10^{20}	48	12	[16]
	5×10^{20}	50	20	
	1×10^{21}	42	23	
n-Si	1×10^{20}	84	22	
	5×10^{20}	57	31	
	1×10^{21}	37	32	
p-GaAs	1×10^{20}	39	11	[16]
	5×10^{20}	25	15	
	1×10^{21}	16	15	
n-GaAs	1×10^{19}	1645	91	
	5×10^{19}	893	115	
	1×10^{20}	625	121	
n-InAs	2.0×10^{18}	1×10^4	200	[22]
p-InGaAs	1.3×10^{18}	76	4	[20]
	7.0×10^{18}	47	5	
n-InGaAs	1.0×10^{15}	1×10^4	13	[19]
p-GaP	2.0×10^{18}	65	3	[18]
	n-GaP	1.2×10^{19}	50	
n-InP	1.0×10^{17}	1500	17	[21]
	1.0×10^{18}	1000	30	
	5.0×10^{18}	600	40	
	1.5×10^{19}	60	18	
n-InGaP	1.5×10^{17}	700	9	[24]
	1.0×10^{18}	450	14	
	3.2×10^{18}	350	18	
n-InN	1.3×10^{20}	18	17	[23]
n-GaN	1.0×10^{17}	440	6	[17]

4.4.2 *Coherence length in heavily-doped semiconductors*

In Fig. 4.4.1, the coherence length of n^{++} -Si and p^{++} -GaAs as a function of carrier concentration is shown. The curves were calculated using eq. 4-3, and the mobility and the carrier concentration were assumed constant throughout the entire temperature range (from room temperature to 4.2 K) since the film is supposed to be degenerated in the calculated range. Relation between the carrier concentration and resistivity was deduced from the ref. [16]. We can see from the figure that the coherence length becomes large with increasing the carrier concentration, which indicates that the heavily-doped n-type Si and p-type GaAs are advantageous from a point of the application to the normal layer of the superconducting weak link device. Since we have achieved heavy impurity doping of the order of 10^{21} cm^{-3} in both systems, larger superconducting critical current and fabrication margin are expected.

Furthermore, Figure 4.4.2 shows the dependence of the coherence length of InN on temperature. As was discussed in this chapter, one of the InN thin films grown on the sapphire substrate showed electrical anomaly at very low temperature. Therefore, the curve was plotted using experimental data not from theoretical values. Since it showed superconductor-like electrical transition, the coherence length was in addition plotted assuming the superconducting transition temperature (T_c) of 0.1 K. Without anomaly, the coherence length is not so much different from the n^{++} -Si or p^{++} -GaAs at 4.2 K, however, it was surprisingly estimated to reach almost 1 μm at 1.4 K in a sample with the electrical anomaly. This result indicates that the InN with electrical anomaly was considered quite effective for the weak link application if the device was supposed to function at such a low temperature.

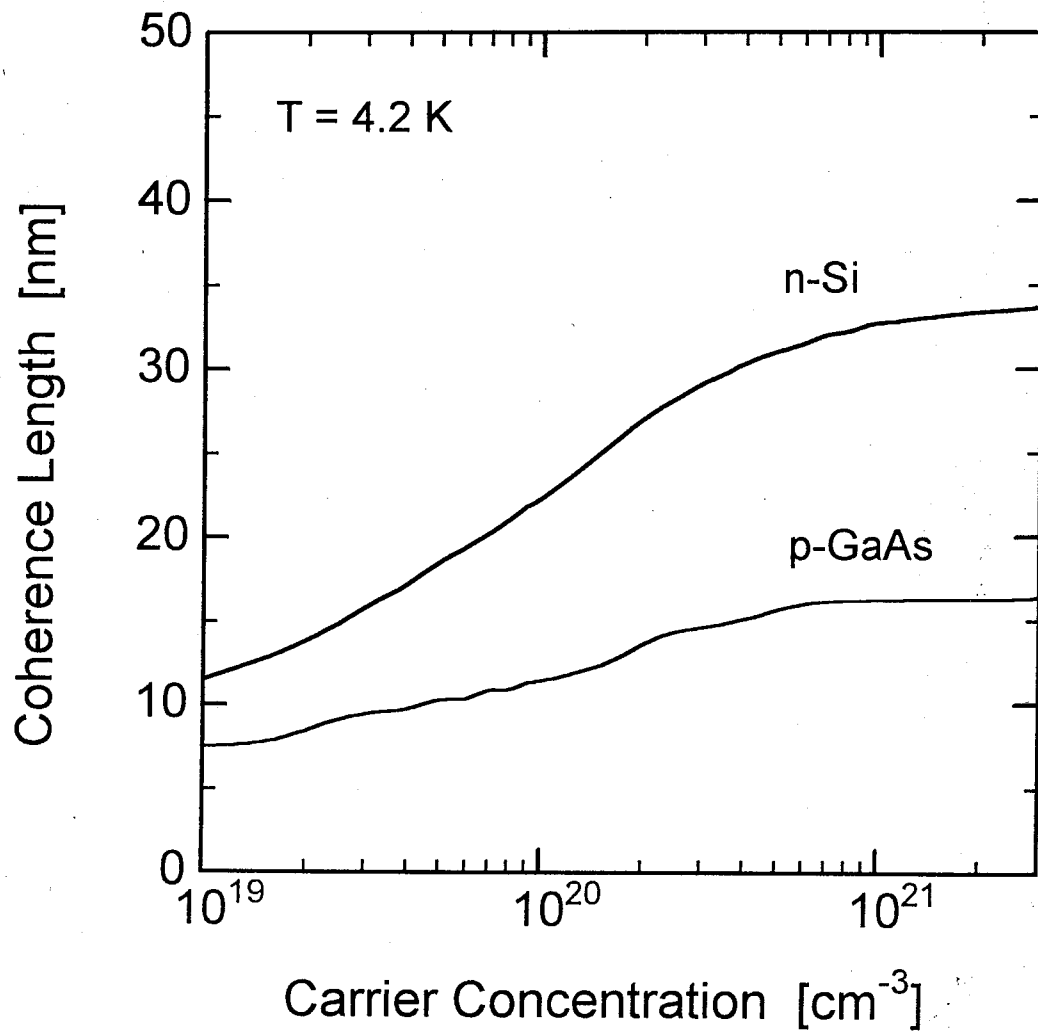


Fig. 4.4.1 Calculated coherence length in n-Si and p-GaAs.

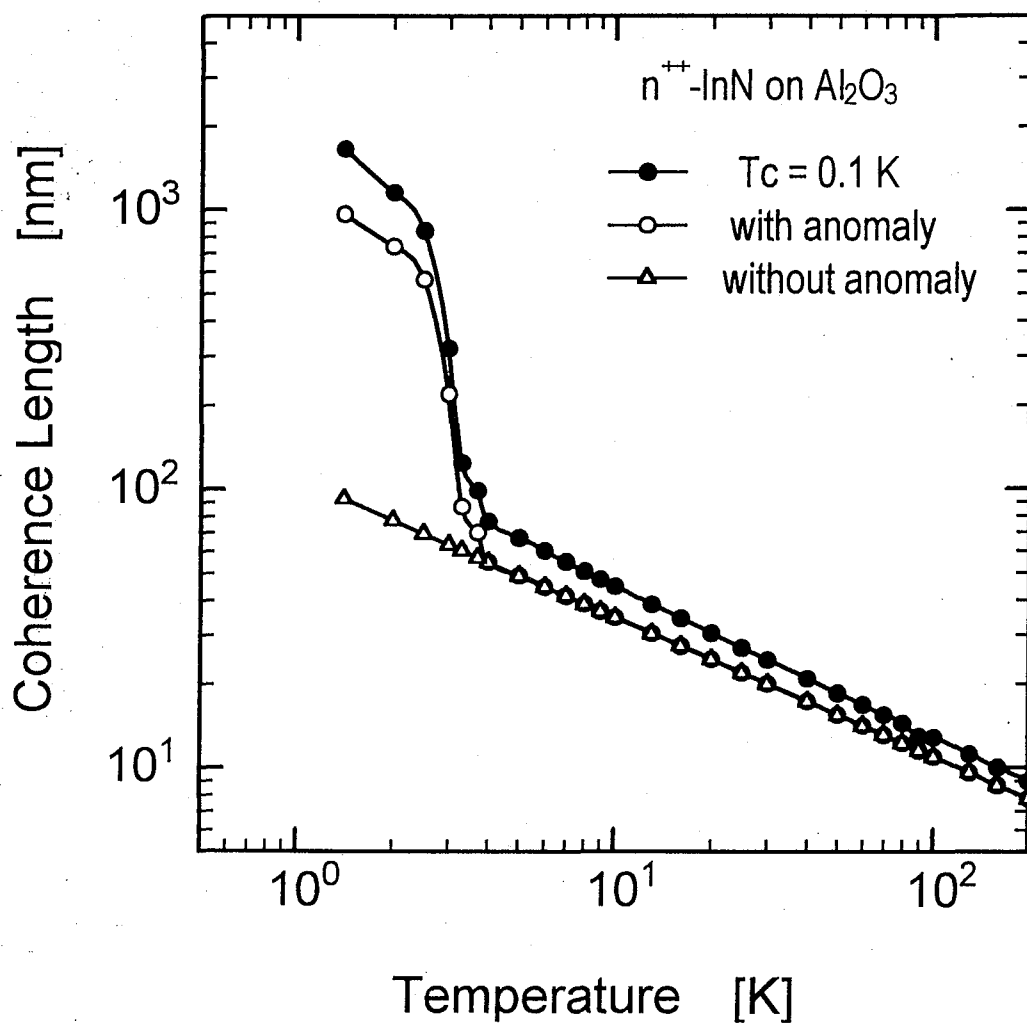


Fig. 4.4.2 Calculated coherence length in n-InN grown on α -Al₂O₃ whose carrier concentration is $1 \times 10^{20} \text{ cm}^{-3}$.

4.5 Investigation of Three-Terminal Weak Link Devices

4.5.1 Background of three-terminal weak link devices

For three-terminal device operation, controlling the superconducting current by gate electrode is the basic concept in the weak link device. In other words, it is expected to function as a switching device with low power dissipation since the finite voltage does not rise during the superconducting current flow. By lowering the critical superconducting current (I_c) of the device in some way, biased point shifts to the finite voltage region which operates as an “on” stage. One of the typical ways to control the critical current is to employ a FET type structure with coplanar or back gate electrodes. By applying gate voltage to the normal layer, carriers can be controlled from accumulated to depleted stages resulting to control the coherence length in the channel or to control the Josephson coupling between the superconducting electrodes. This type of device operation is widely studied using various degenerated semiconductors [25-28] or high electron mobility system using III - V compounds [27-31]. As for the degenerated system, the doping level was controlled to be about $5 \times 10^{18} \sim 1 \times 10^{20} \text{ cm}^{-3}$ because of the effective carrier modulation. However in our case, the carrier concentration reaches as much as $1 \times 10^{21} \text{ cm}^{-3}$ in n^{++} -Si or p^{++} -GaAs epitaxial thin films, the electric field was found not to be able to collect so much carriers, which was revealed from the following calculations although it is more effective to obtain higher critical superconducting current by employing higher carrier concentration as discussed in the previous section.

Figure 4.5.1 shows the calculated result from the dependence of the electron concentration accumulated in Si/SiO₂ boundary by applying gate voltage in a stacked metal/oxide/semiconductor (MOS) structure. When the MOS junction is positively biased, the electrons are accumulated near the Si/SiO₂ boundary. Generally, the electrons are considered to be accumulated in a range of Debye length (λ_D) from the boundary [32]. However, it should be replaced with the Thomas Fermi screening length (λ_{TF}) when dealing with the higher carrier concentration. The length is described as,

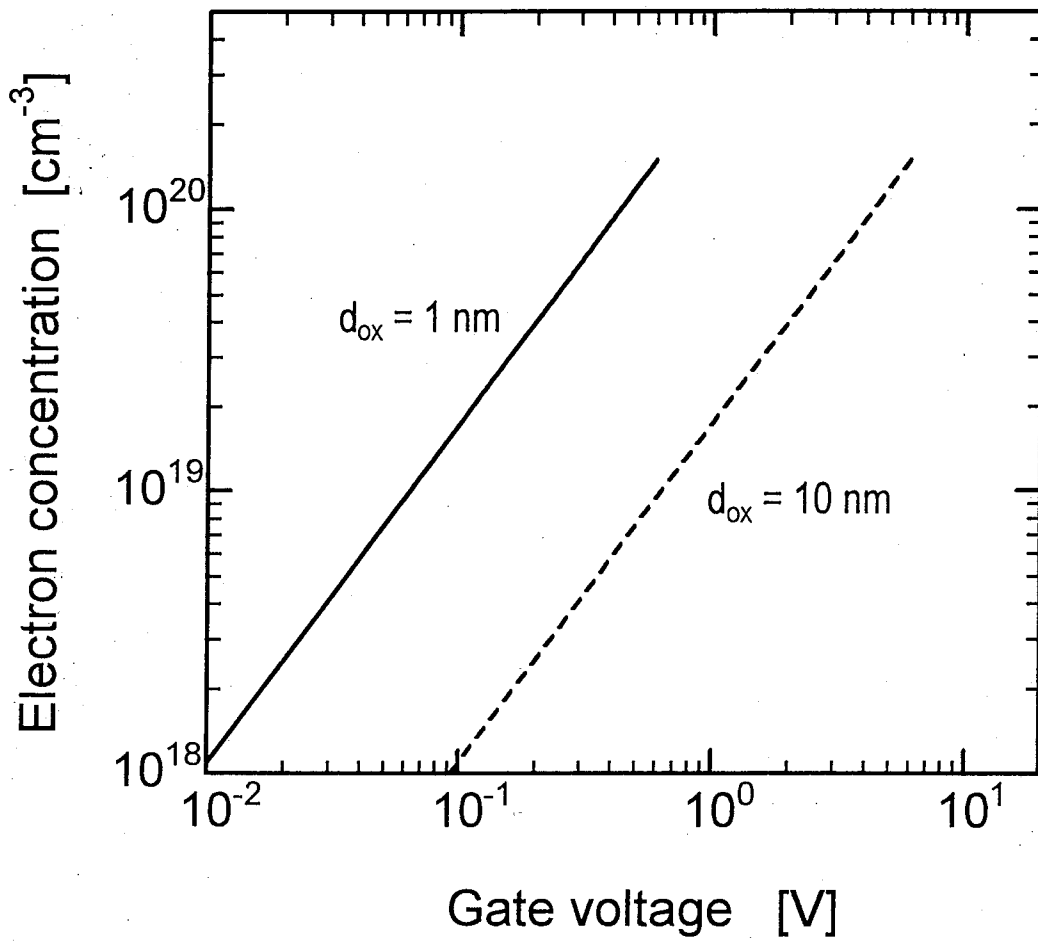


Fig. 4.5.1 Relation of accumulated electron concentration versus applied gate voltage in MOS structure. The d_{ox} represents thickness of the oxide layer.

$$\lambda_{TF} = \pi^{\frac{2}{3}} \frac{\hbar}{e} \sqrt{\frac{\epsilon_{Se} \epsilon_0}{m^* (3n)^{\frac{1}{3}}}}, \quad (4-4)$$

where the ϵ_{Se} and n represent the dielectric constant of the semiconductor and carrier concentration, respectively. Since the net charge is proportional to the applied voltage and capacitance ($Q = CV$), we obtain following relation,

$$n = \frac{\epsilon_{ox} \epsilon_0}{e d_{ox} \lambda_{TF}} V, \quad (4-5)$$

where the ϵ_{ox} and d_{ox} mean the dielectric constant and thickness of the oxide layer, respectively. Therefore, we can theoretically predict the relation between the carrier concentration and applied voltage by using these two equations (eqs. 4-4 and 4-5) and are deduced as

$$n^{\frac{5}{6}} = \frac{\epsilon_{ox}}{\hbar d_{ox}} \sqrt{\frac{\epsilon_0 m^*}{\epsilon_{Se}}} \sqrt{\frac{3}{\pi^4}} V \quad (4-6)$$

As was expected, the electron concentration increases with increasing applied voltage. However, there exists a limit of the breakdown voltage in the insulator. If the conventional silicon dioxide was assumed, its maximum sustainable electric field is about 6×10^8 V/m. These investigation was plotted in Fig. 4.5.1. We can see that the carriers could not be controlled by the gate bias even if the thickness of the SiO_2 was changed on condition that the semiconductor has more than $1 \times 10^{21} \text{ cm}^{-3}$ electron concentration. In other words, such a degenerated semiconductor is favorable to the weak link device but control of the carrier modulation or that of superconducting current can not be achievable by applying gate voltage.

4.5.2 Superconducting current modulation by gate current

As described previously, FET-type three-terminal weak link device was not thought to function when employing a degenerated semiconductor whose carrier concentration is of the order of 10^{21} cm^{-3} . Therefore, this study took notice on the magnetic field dependence of the superconducting current in the Josephson devices. Josephson current is known to be able to be modulated by the external magnetic field and critical current of the junction shows Fraunhofer diffraction pattern against the magnetic field as described in the following equation,

$$I_{max} = I_0 \left| \frac{\sin \frac{\pi \Phi}{\Phi_0}}{\frac{\pi \Phi}{\Phi_0}} \right| \quad (4-7)$$

where the I_{max} and I_0 represent maximum Josephson current and that at 0 T, respectively. The Φ and Φ_0 represent the applied magnetic flux and flux quantum ($\Phi_0 = h/2e$), respectively. Therefore, the Josephson current in our device could be controlled by the magnetic field which is generated by the current flowing through the gate line situated over the channel as schematically shown in Fig. 4.5.2. In this device, output signal is perfectly separated from the input, and also it features considerable number of fanouts by employing a series junction.

Preliminary estimation was carried out next. Relation between control gate current (I_{cont}) and magnetic flux is deduced as following equation,

$$I_{cont} = \frac{2\pi\Phi}{\mu_{ox} x \ln(1 + \frac{r_0}{r})} \quad (4-8)$$

where r and r_0 represent thickness of insulator and channel, respectively, and x is the effective junction length, μ_{ox} is the magnetic permeability of gate oxide. On condition that $r_0/r=100$, $x=0.2 \mu\text{m}$, and $\Phi=\Phi_0$, I_{cont} was calculated to be about 5 mA. This current would

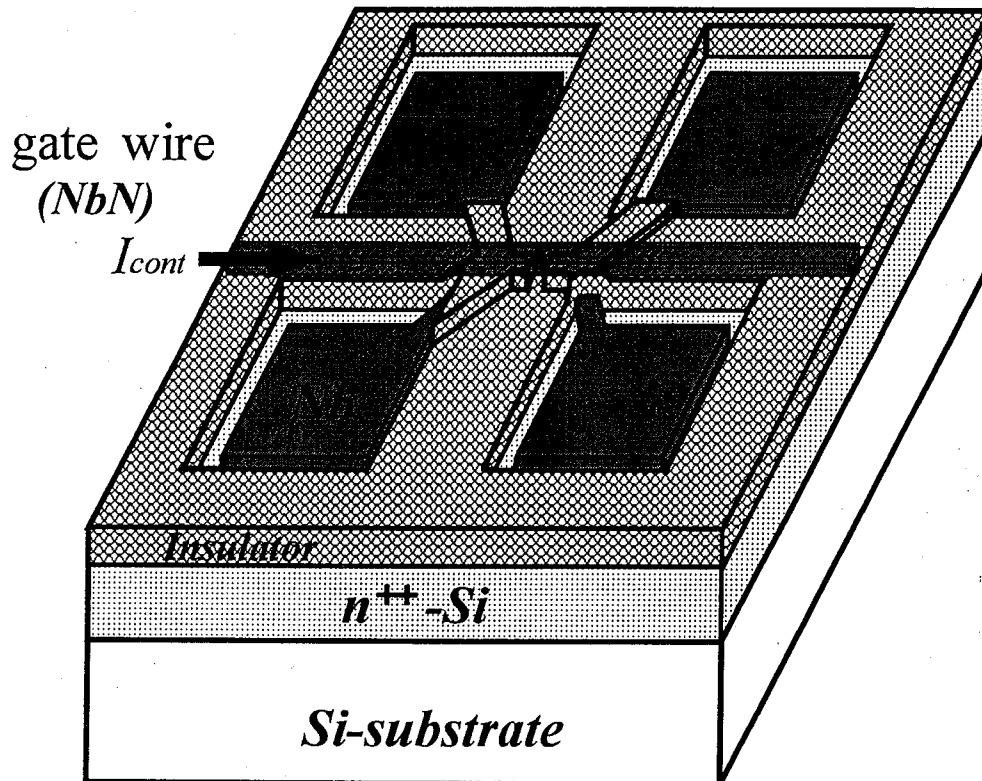


Fig. 4.5.2 Schematic of the three-terminal superconducting weak link device. Gate current flowing through the gate line controls superconducting channel current.

work to completely suppress the superconducting current flowing through the semiconductor region. However, it is not always necessary to completely suppress the I_c , which means that the gate current of about a few milli ampere would be enough for the device operation which depends on a bias current of the logic circuit. This value would be practicable since the high superconducting current is expected owing to the usage of heavily-doped semiconductor.

4.6 Summary

In order to investigate the applicability of heavily-doped semiconductors not only to the conventional p-n junction devices but to the cryoelectronic devices, temperature dependence of their electrical properties were extensively studied in this chapter. Heavily impurity doped semiconductors such as P-doped Si, B-doped ZnO, C-doped GaAs and also n^+ -InN grown on GaAs showed metallic characteristics on temperature and they were theoretically studied. Furthermore, in the case of n^+ -InN epitaxial film grown on a sapphire substrate, peculiar electrical characteristics were observed below 4.2 K such as the sharp decrease of the resistivity, the increase of the mobility, extremely large magnetic field dependence of the differential resistance, and their dependence on the electron concentration. To clarify the origin of these superconductor-like characteristics, a number of experimental evaluations on the InN films were performed, however, it is still under investigation.

These degenerated semiconductors were considered to be employed to the channel (or normal) material in superconducting weak link device and fundamental calculation was carried out in terms of the coherence length in the semiconductor region. In the case of n^{++} -Si and p^{++} -GaAs, films having higher carrier concentration were found to be preferable for the device, and the InN with anomalous property was also a good candidate.

Three terminal weak link device using heavily-doped semiconductor channel was considered and control of the superconducting channel current by the gate current which rises magnetic field was proposed since the conventional control by the gate voltage was not practicable because of the extremely high carrier concentration in the channel region.

Reference

- 1] A. Yamada, Y. Jia, M. Konagai and K. Takahashi: Jpn. J. Appl. Phys. **28** (1989) L2284.
- 2] M. Konagai, T. Yamada, T. Akatsuka, K. Saito, E. Tokumitsu and K. Takahashi: J. Cryst. Growth **98** (1989) 167.
- 3] J. Shirakashi, T. Azuma, F. Fukuchi, M. Konagai and K. Takahashi: J. Cryst. Growth **150** (1995) 585.
- 4] J. Shirakashi and M. Konagai: Solid-State Electron. **38** (1995) 1675.
- 5] K. W. Boer: "Survey of Semiconductor Physics" (Van Nostrand Reinhold, New York, 1990).
- 5] W. W. Wenas, A. Yamada, M. Konagai and K. Takahashi: Jpn. J. Appl. Phys. **30** (1991) L441.
- 7] M. Yoshino, W. W. Wenas, A. Yamada, M. Konagai and K. Takahashi: Jpn. J. Appl. Phys. **32** (1993) 726.
- 3] A. Wakahara, T. Tsuchiya and A. Yoshida: J. Cryst. Growth **99** (1990) 385.
- 9] T. J. Kistenmacher, S. A. Ecelberger and W. A. Bryden: J. Appl. Phys. **74** (1993) 1684.
- 10] A. Yamamoto, M. Tsujino, M. Ohkubo and A. Hashimoto: Sol. Energy Mater. Sol. Cells **35** (1994) 53.
- 11] A. Yamamoto, M. Tsujino, M. Ohkubo and A. Hashimoto: J. Cryst. Growth **137** (1994) 415.
- 12] J. Bardeen, L. N. Cooper and J. R. Schrieffer: Phys. Rev. **108** (1957) 1175.
- 3] R. A. Hein, J. W. Gibson, R. Mazelsky, R. C. Miller and J. K. Hulm: Phys. Rev. Lett. **12** (1964) 320.
- 4] R. A. Hein, J. W. Gibson, R. S. Allegaier, B. B. Houston, Jr., R. Mazelsky and R. C. Miller : "Low Temperature Physics" LT-9 ed. J. G. Daunt, D. O. Edwards, F. J. Milford and M. Yaquab (Plenum Press, New York, 1965) pp. 604.
- 5] C. P. Foley and J. Lyngdal: J. Vac. Sci. Technol. **A5** (1987) 1708.
- 6] S. M. Sze: "SEMICONDUCTOR DEVICES Physics and Technology" (John Wiley & Sons, New York, 1985).

- [17] M. Ilegems: *J. Cryst. Growth* **13/14** (1972) 360.
- [18] Y. C. Kao and O. Eknayan: *J. Appl. Phys.* **54** (1983) 2468.
- [19] K. T. Chan, L. D. Zhu and J. M. Ballantyne: *Appl. Phys. Lett.* **47** (1985) 44.
- [20] J. Shirakashi: Dr. Thesis, Faculty of Engineering, Tokyo Institute of Technology, Tokyo (1994) pp. 116.
- [21] J. Shirakashi: Dr. Thesis, Faculty of Engineering, Tokyo Institute of Technology, Tokyo (1994) pp. 153.
- [22] D. L. Rode: “*Semiconductors and Semimetals*” **10**, eds. R. K. Willardson and A. C. Beer, (Academic Press, New York, 1975).
- [23] N. Miura, H. Ishii, A. Yamada, M. Konagai, Y. Yamauchi and A. Yamamoto: *Jpn. J. Appl. Phys.* **36** (1997) L256.
- [24] N. Nihanda: private communication.
- [25] T. Nishino, M. Miyake, Y. Harada and U. Kawabe: *IEEE Trans. Device Lett.* **EDL-6** (1985) 297.
- [26] T. Nishino, M. Hatano, H. Hasegawa, F. Murai, T. Kure, A. Hiraiwa, K. Yagi and U. Kawabe: *IEEE Trans. Device Lett.* **10** (1989) 61.
- [27] T. D. Clark, R. J. Prance and A. D. C. Grassie: *J. Appl. Phys.* **51** (1980) 2736.
- [28] A. W. Kleinsasser and T. N. Jackson: *IEEE Trans. Magn.* **25** (1989) 1274.
- [29] H. Takayanagi and T. Kawakami: *Phys. Rev. Lett.* **54** (1985) 2449.
- [30] A. W. Kleinsasser, T. N. Jackson, D. McInturff, F. Rammo, G. D. Pettit and J. M. Woodall: *Appl. Phys. Lett.* **55** (1989) 1909.
- [31] H. Takayanagi, T. Akazaki, J. Nitta and T. Enoki: *Ext. Abstr. Int. Conf. Solid State Devices and Materials* (1994) pp. 580.
- [32] K. W. Boer: “*Survey of Semiconductor Physics*” (Van Nostrand Reinhold, New York, 1990) pp.363.

Chapter 5

Fabrication of Superconducting Weak Link Devices Using Heavily-Doped Semiconductors

5.1 Introduction

One of the possible applications of the heavily-doped semiconductor thin films to the electronic devices is the Josephson weak link junction. By changing the doping level of the semiconductor layer, new functionality could be expected which is not obtainable in the superconductor/normal metal system. Furthermore, recent Si related large scale integration technology could be easily transferred to its fabrication.

As the applicability of degenerated semiconductors to the cryoelectronic devices was theoretically confirmed in the previous chapter, experimental procedure follows in this chapter. As for the superconducting material, niobium (Nb) and its nitride (NbN) were selected. The Nb not only has the highest critical or superconducting transition temperature of the elementary superconductors but possesses characteristics of high physical hardness and high durability against thermal cycling from liquid helium temperature to room temperature. Moreover, it can be easily deposited using sputtering technique and we can obtain a fairly good film quality even if it was deposited at room temperature. It is thus favored for superconducting applications such as the Josephson junctions of Nb/AlO_x system [1-8] or the superconducting weak link devices [9-15]. In this chapter, deposition of Nb and NbN is first described, and it is employed to the superconducting electrodes of the weak link devices using a heavily impurity-doped semiconductor as a normal layer. Especially polycrystalline boron-doped zinc oxide (B-doped ZnO) and epitaxial phosphorous-doped silicon (P-doped Si) thin films are employed there whose electron concentrations were about $1.5 \times 10^{20} \text{ cm}^{-3}$ and $1 \times 10^{21} \text{ cm}^{-3}$, respectively. Together with considering their properties, the device structure is in each modified and new process for fabricating sub-micron gap structure is also proposed through the realization of coplanar-

type metal electrodes. Successful fabrication of single-electron transistors by AFM nano-oxidation process using the extremely thin Nb film is also presented for reference.

5.2 Deposition of Superconducting Nb and NbN Thin Films

5.2.1 Deposition condition

Deposition of niobium (Nb) and niobium nitride (NbN) was carried out for concerning its application to the superconducting electrodes of weak link devices. Figure 5.2.1 shows a schematic deposition chamber and its picture used in this study. It is a DC magnetron sputtering system with a niobium target placed opposite to the substrate. The chamber has two gas inlets and sputtering is performed using argon (Ar) gas for Nb deposition and a little amount of nitrogen (N₂) added to Ar for NbN deposition. Purity of the gases and the target are 99.9999 % and 99.95 %, respectively. The substrate can be negatively biased for the bias-sputtering which is one of the effective ways that contributes to purify the depositing film. Deposition conditions are summarized in Table 5.2.1. Sputtering was performed at relatively low gas pressure (of the order of 1×10^{-3} Torr) so that the chamber was evacuated by turbo molecular pump during the deposition. Prior to the film deposition, pre-sputtering was performed for about 3 to 10 minutes to remove any contaminated layer on the Nb target and to stabilize the DC plasma. The substrate temperature was not controlled and the sputtering was performed at room temperature. Due to the self-heating effect in the plasma process, the substrate temperature goes up to around 140 °C after 10 minutes deposition. For obtaining Nb and NbN thin films in better quality, sputtering conditions and the partial pressure of N₂ were optimized.

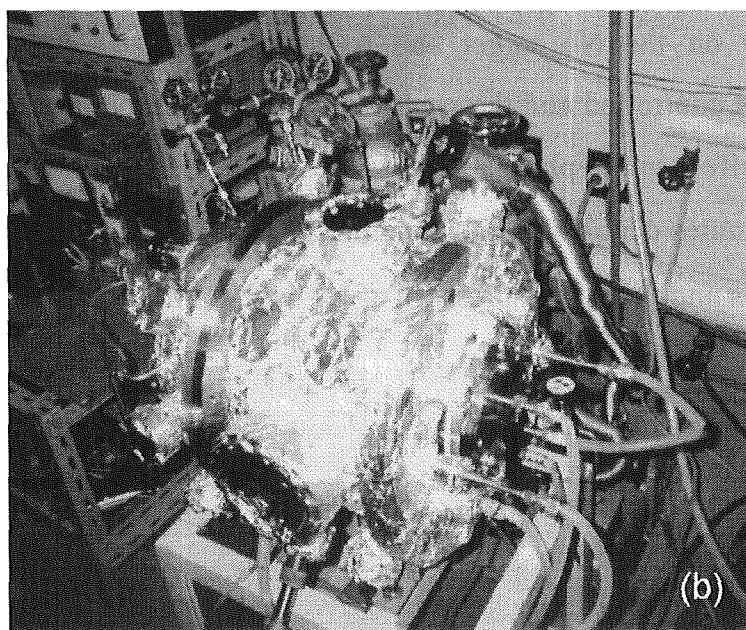
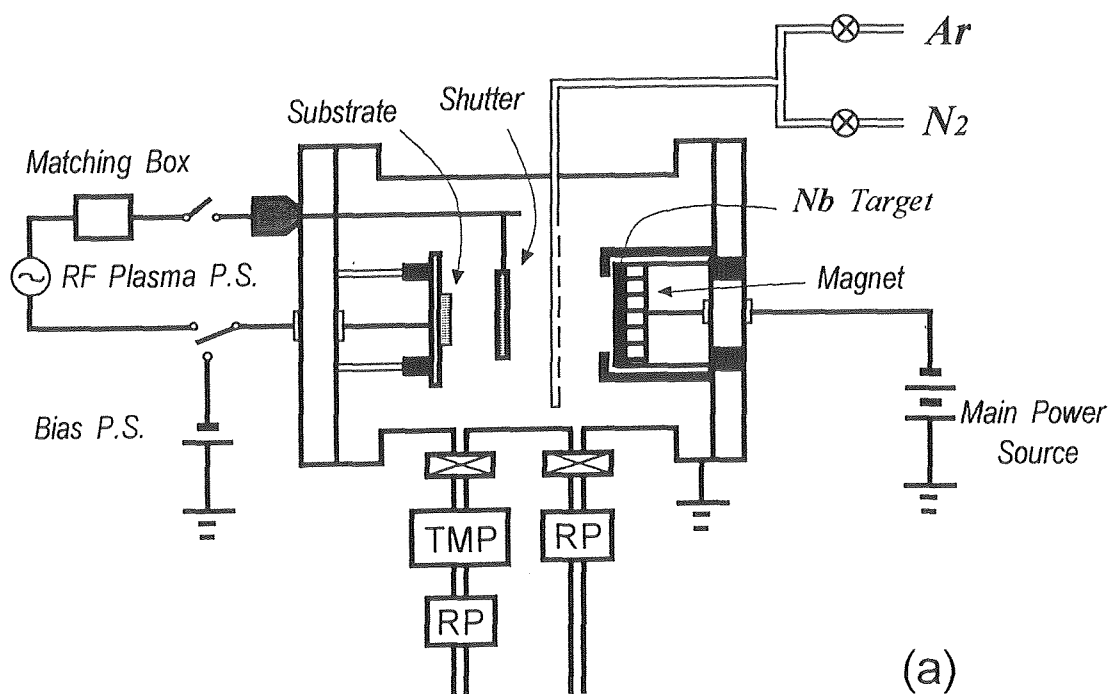


Fig. 5.2.1 Schematic (a) and picture (b) of DC magnetron sputtering system used this study for obtaining Nb and NbN superconducting thin film.

Table 5.2.1 Conditions for depositing Nb and NbN thin films by DC magnetron sputtering.

Back Pressure	1×10^{-5} Torr
Total Gas Pressure	2.0×10^{-3} Torr
N ₂ Partial Pressure (for NbN)	$0.2 \sim 1.0 \times 10^{-3}$ Torr
Substrate Temperature	R. T.
DC Voltage	-250 ~ -300 V
DC Current	0.3 ~ 0.7 A
Substrate Bias Voltage (for NbN)	0 ~ -60 V
Pre-Sputtering	3 ~ 10 min.

5.2.2 Characterization of Nb thin film

Deposition of Nb was at first carried out on a n-Si substrate of high resistivity ($\sim 1 \text{ k}\Omega \cdot \text{cm}$). Figure 5.2.2 shows the dependence of the electrical properties and the deposition rate on DC plasma current. The Ar gas pressure was fixed at 2.0 mTorr as the low pressure was found to be effective to obtain a Nb film in better quality from the previous experiment. The Nb films were deposited in about 100 nm thick. We can see from the figure that the high DC current is optimum for better quality. This is because the increase of the deposition rate more prevents from the incorporation of impurities in the depositing films, such as an oxygen. Moreover, that makes the resistivity of the film at room temperature decrease and the residual resistance ratio (RRR) as well as the superconducting transition temperature (T_c) increase. Although our equipment could no longer increase the DC current, Nb thin film with T_c of 8.1 K was ever achieved. For further improvement in the film quality, bias sputtering is one of the additive technique, however, drastic improvement was not observed in the case of Nb but in the NbN, which will be discussed later. One point should be noted here that the

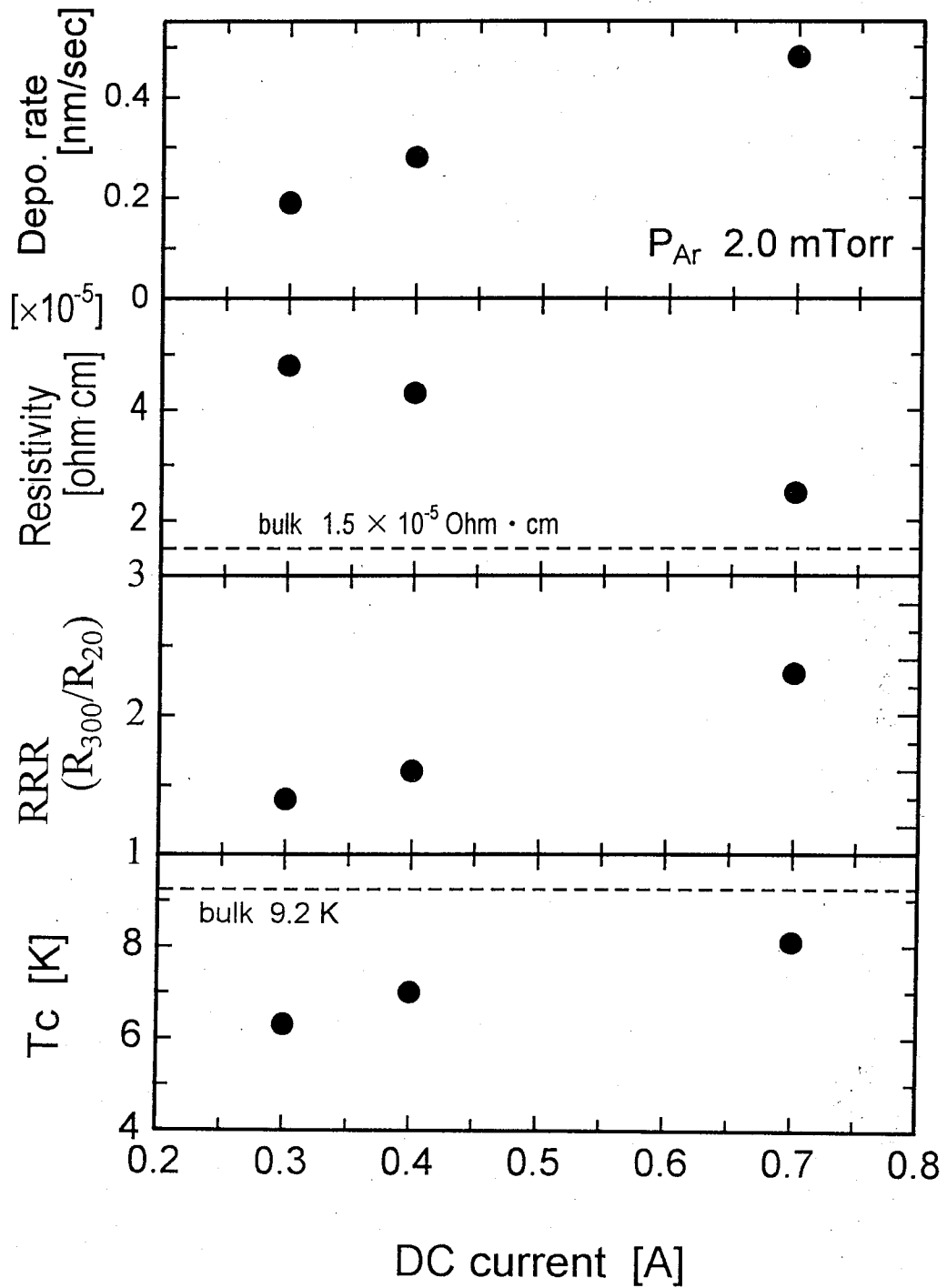


Fig. 5.2.2 Dependence of the electrical properties of Nb thin film on DC plasma current.

deposition was performed with the substrate neither externally biased nor electrically grounded, which means that the self-bias was unintentionally applied to the substrate (about -10 V) due to the Ar^+ bombardment. This effect should have prevented from the disastrous bombardment from secondary electrons in a certain degree. Figure 5.2.3 shows an X-ray diffraction profile of the Nb thin film with a thickness of about 500 nm. Peak of Nb (110) was clearly observed and no other phase was detected. The Nb film is polycrystalline and has a strong preference for the (110) lattice plane to be parallel to the substrate. In Fig. 5.2.4, dependence of the resistivity at room temperature on Nb thickness is shown. They were deposited in optimized conditions on a SiO_2/Si substrate. It is well known that the resistivity reflects the electrical properties at low temperature, especially the superconducting properties. Films having larger than about 40 nm thickness showed both lowest resistivity obtainable from this experiment and T_c was about 8 K. However, the resistivity increases with the film becomes thinner and also the superconducting transition width (ΔT_c) becomes larger. The T_c was measured to be about 2.3 K and below 1.4 K for the films of 6.5 nm and 3 nm, respectively. As the Nb is easily oxidized in the ambient atmosphere and forms a stable niobium oxide layer in about a few nanometer [16-18], this oxidation effect causes film degradation and especially it was influential in extremely thin films.

Although the electrical properties of Nb film degrade with decreasing the film thickness, the surface of the film was found to be quite smooth with a roughness of 0.5~1.0 nm from the AFM observation shown in Figs. 5.2.5(a) and (b) [19]. The Nb film was deposited in about 3 nm thickness on a thermally oxidized silicon substrate. In the AFM image of Fig. 5.2.5(b), Nb oxides wires were modified by AFM nano-oxidation process. This technique is considered to be the anodization process [20-23]. By applying negative bias to the conducting cantilever of AFM, anodization reaction occurs between the metal or semiconductor thin film and oxygen containing species absorbed on the film surface. Besides, by scanning the cantilever at constant speed while applying negative bias voltage, we can obtain an oxidized wire whose width can be ranged from 20 to 50 nm by adjusting the applied bias voltage or the scanning speed, which is shown in Fig. 5.2.5(b). For proceeding this process, it is fairly known that the surface should be smooth enough to modify a fine

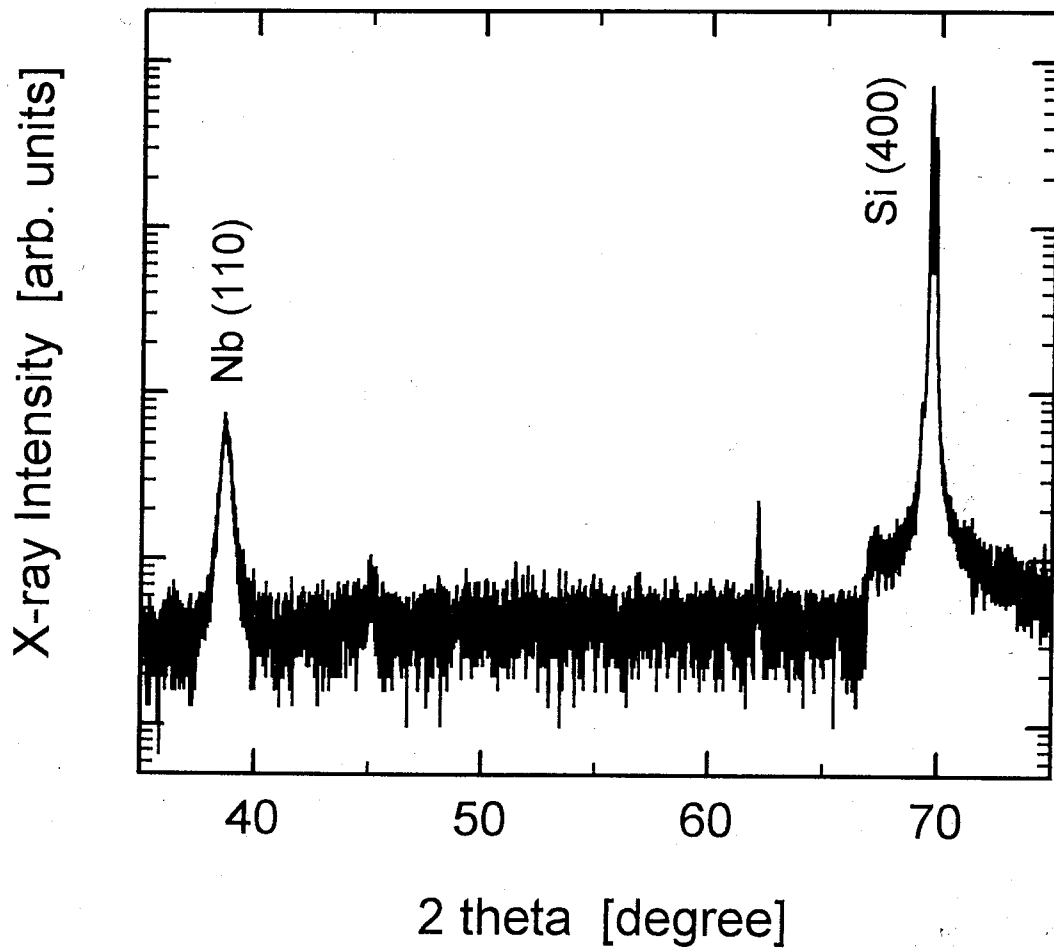


Fig. 5.2.3 X-ray diffraction profile from Nb thin film.

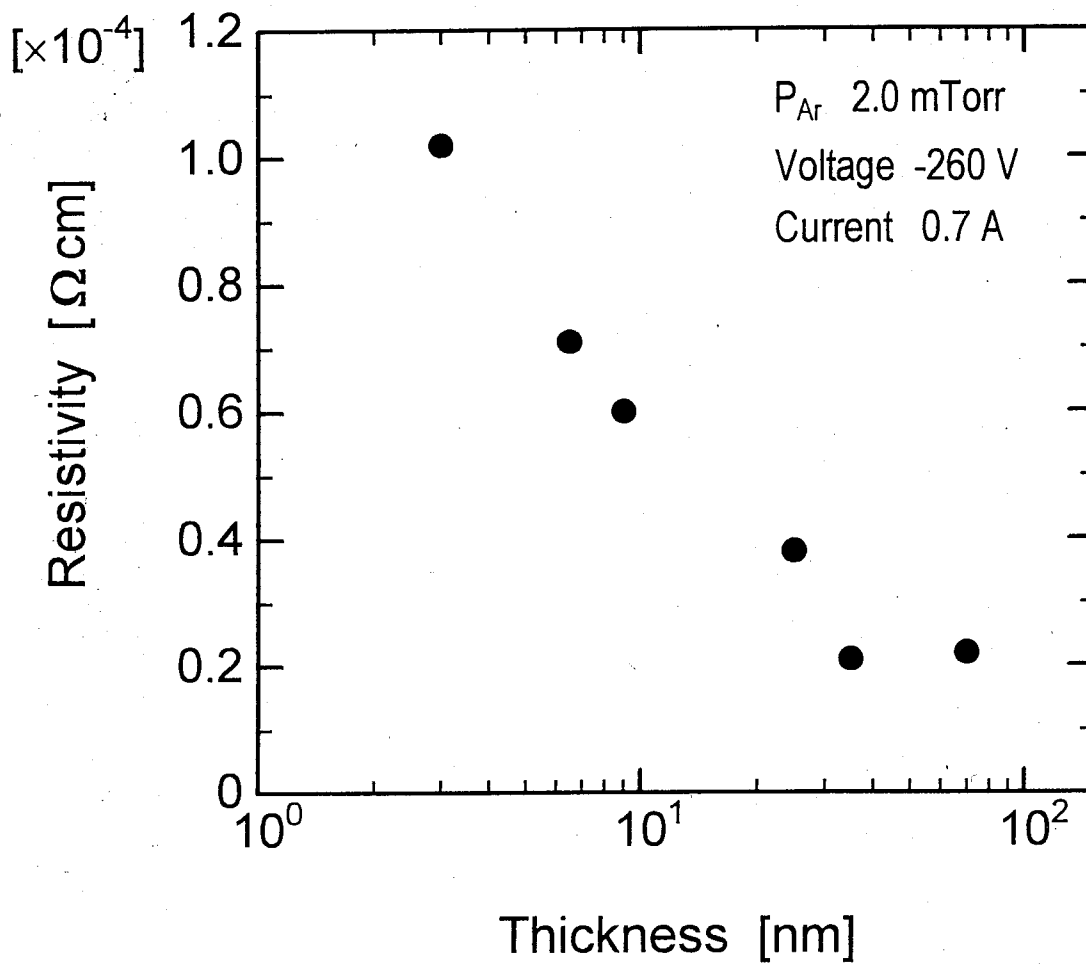


Fig. 5.2.4 Dependence of the resistivity of Nb thin film on thickness.

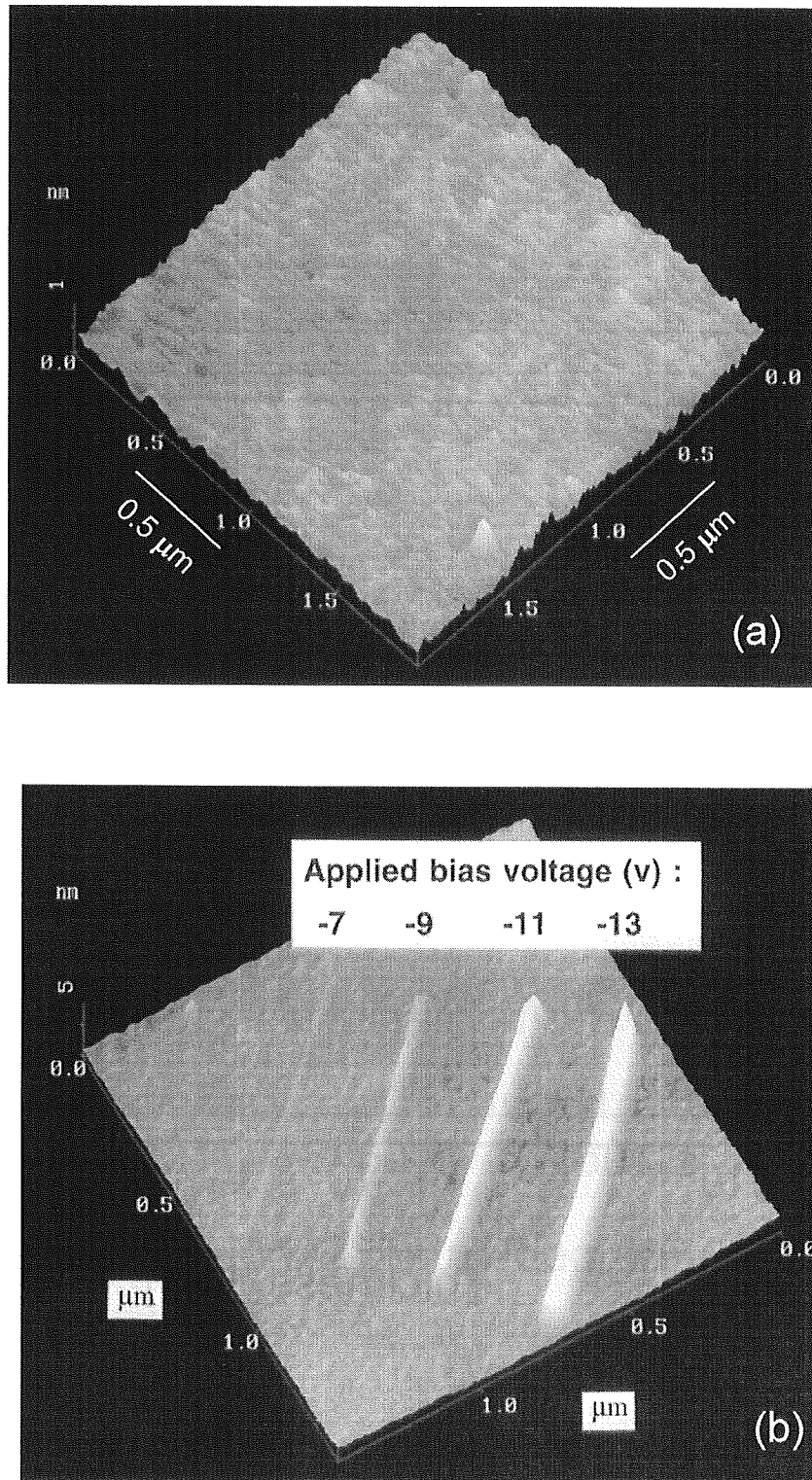


Fig. 5.2.5 AFM images of the Nb surface with a thickness of about 3 nm. In (b) AFM nano-oxidation process was performed to modify Nb oxide wire (cited from Ref. 19).

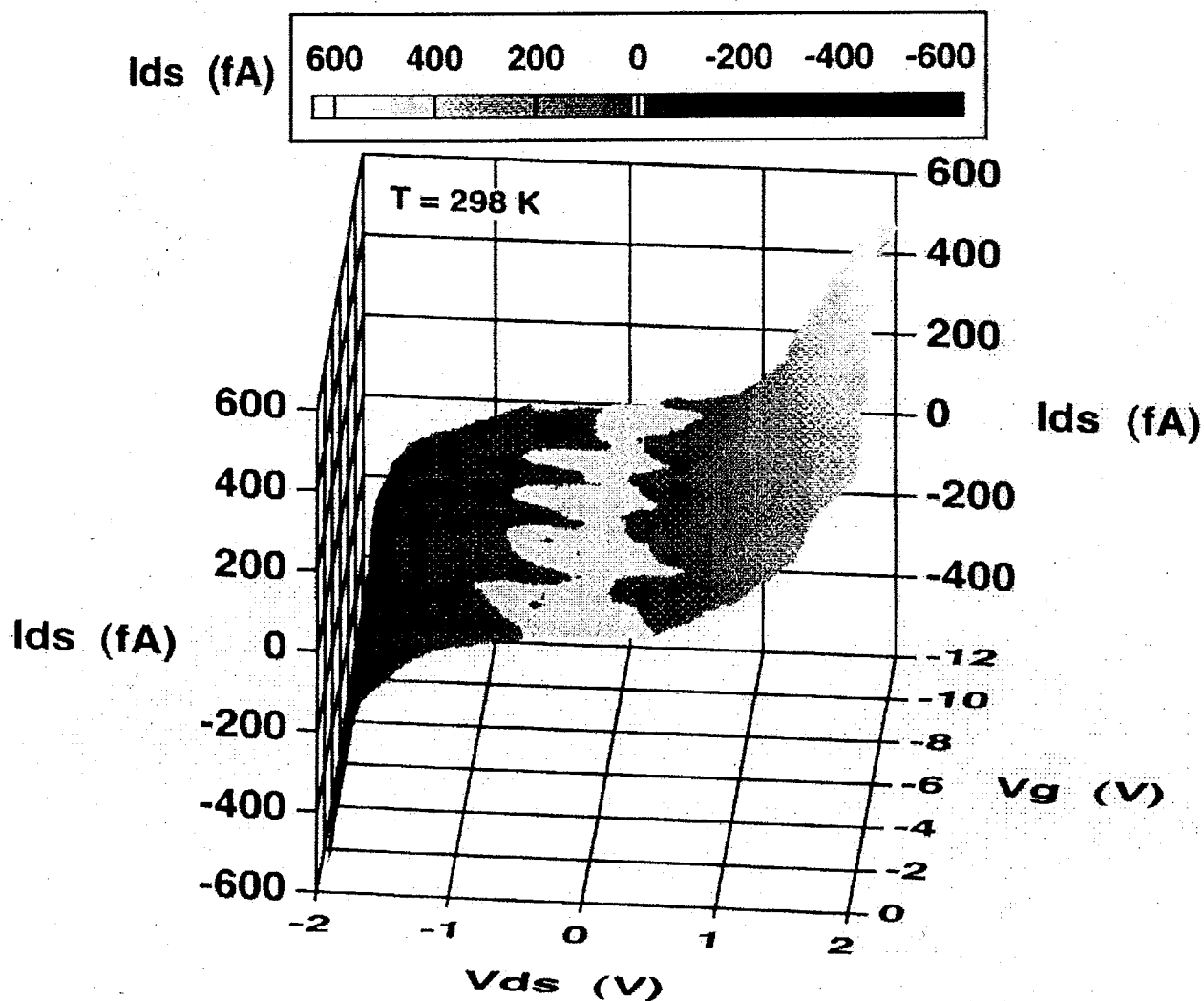


Fig. 5.2.6 Drain current-drain voltage characteristics with various side-gate voltages in a single-electron transistor of Nb/Nb oxide system fabricated by AFM nano-oxidation process. The characteristics were measured at room temperature ($T = 298$ K). Drain current with ± 2 fA is colored white (cited from Ref. 24).

structure. By using the extremely thin Nb film deposited in above optimized condition, the technique was successfully applied to fabricate a single-electron transistors (SETs) by our group, and especially its perfect operation at room temperature was first reported as referred in Fig. 5.2.6 [24]. One of the key features of this successful demonstration lays on a flatness of the Nb thin film and it may be due to the slight bias sputtering which caused surface flattening during the deposition.

5.2.3 *Characterization of NbN thin film*

Problems on the metal of Nb are that it is not so much stable against thermal process over room temperature and is easily affected by oxygen diffusion forming a niobium oxide (NbO_x) at the surface, which degrades the superconducting properties. Therefore, it is not always suitable for its application to the superconducting devices which consist of any oxide material or to the case that requires thermal process after the Nb deposition although it has the highest transition temperature ($T_c = 9.4$ K) among the entire elements. As this study considers utilization of polycrystalline ZnO grown by thermal metalorganic chemical vapor deposition (MOCVD) for the normal layer of superconducting weak link device in a stacked structure, other material which is stable against thermal process should be employed. Therefore, NbN thin film was taken noticed. Since this NbN can be easily deposited by a small amount of N₂ addition during the Nb sputtering and it features thermal stability, physical hardness, superior in heat cycle and relatively high T_c (the highest of the binary compound semiconductors with a NaCl-type structure and a value of 17.3 K has ever been reported [25]), its deposition is next considered. Niobium nitride has a lot of crystal structures depending on a concentration of nitrogen in the film which is shown in Table 5.2. and superconducting properties are strongly affected by deviation from stoichiometric composition [25-28]. The aim of this study is to obtain a film of high T_c and it corresponds to the δ -phase NbN.

Table 5.2.2 Structural properties of NbN_x system.

Phase	Structure	Compositional Ratio (NbN _x)	Lattice Constant [nm]	Notes
β-Nb ₂ N	hexagonal	0.40 ~ 0.50	a=0.305, c=0.459 a=0.305, c=0.499	N poor N rich
γ-Nb ₄ N ₃	tetragonal irregular-B1	0.75 ~ 0.80	a=0.438, c=0.431 a=0.439, c=0.433	N poor N rich
δ-NbN	B1 (cubic)	0.88 ~ 0.98 1.10 ~ 1.06	0.438 ~ 0.440	T _c =15 ~ 17.3 K
δ'-NbN	reverse NiAs (hexagonal)		a=0.297, c=0.553	
ε-NbN	hexagonal	0.92 ~ 1.00	a=0.296, c=1.127	T _c <1.77 K
Nb ₅ N ₆	hexagonal			T _c <1.77 K
Nb ₄ N ₅	tetragonal		a=0.687, c=0.430	T _c =8.0 ~ 8.5 K

Deposition of NbN film was performed on an i-Si substrate and its thickness was controlled to be about 100 nm. Figure 5.2.7 shows the dependence of the electrical properties of NbN thin films on partial pressure of N₂ during the sputtering. Total gas pressure and DC power were controlled at 2.0 mTorr and 2.2 mW/cm², respectively. Parameters of the electrical estimation are resistivity at room temperature, residual resistance ratio (*RRR*, corresponds to the R_{300K}/R_{20K}) and measured superconducting transition temperature (T_{c0}). The figure also shows the electrical dependence of films on negative voltage bias applied to the substrate. We can see that large bias made the film low resistivity and high T_c . This is attributed to the fact that Ar⁺ reaches not only to the Nb target but also to the substrate by applying negative voltage to the substrate, which causes sputtering of the weakly-bonded impurities, such as an oxygen, in the depositing film, resulting to make a film in better quality. The fact that the substrate was also sputtered during the NbN deposition is

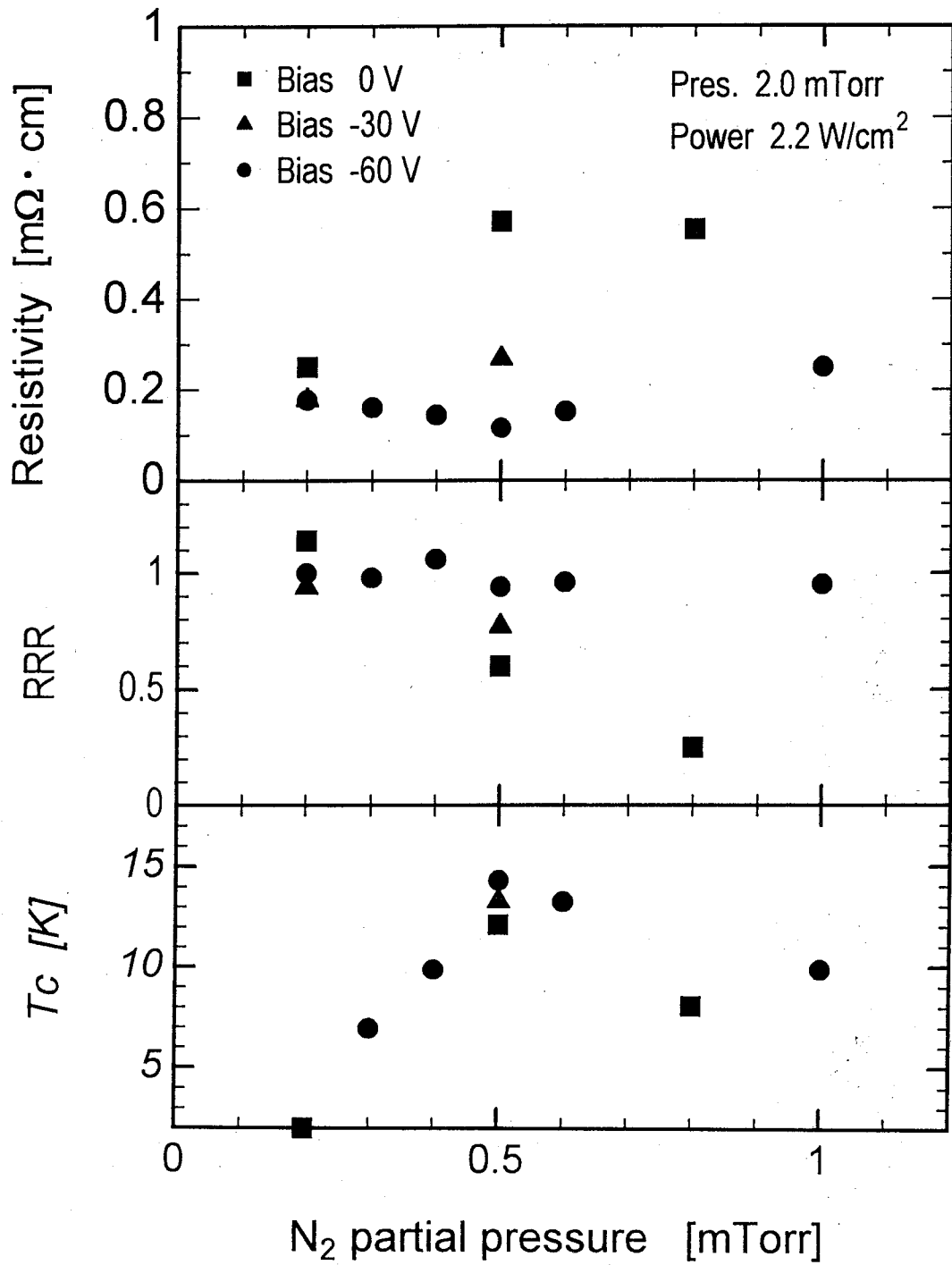


Fig. 5.2.7 Dependence of the electrical properties of NbN thin films on N₂ partial pressure.

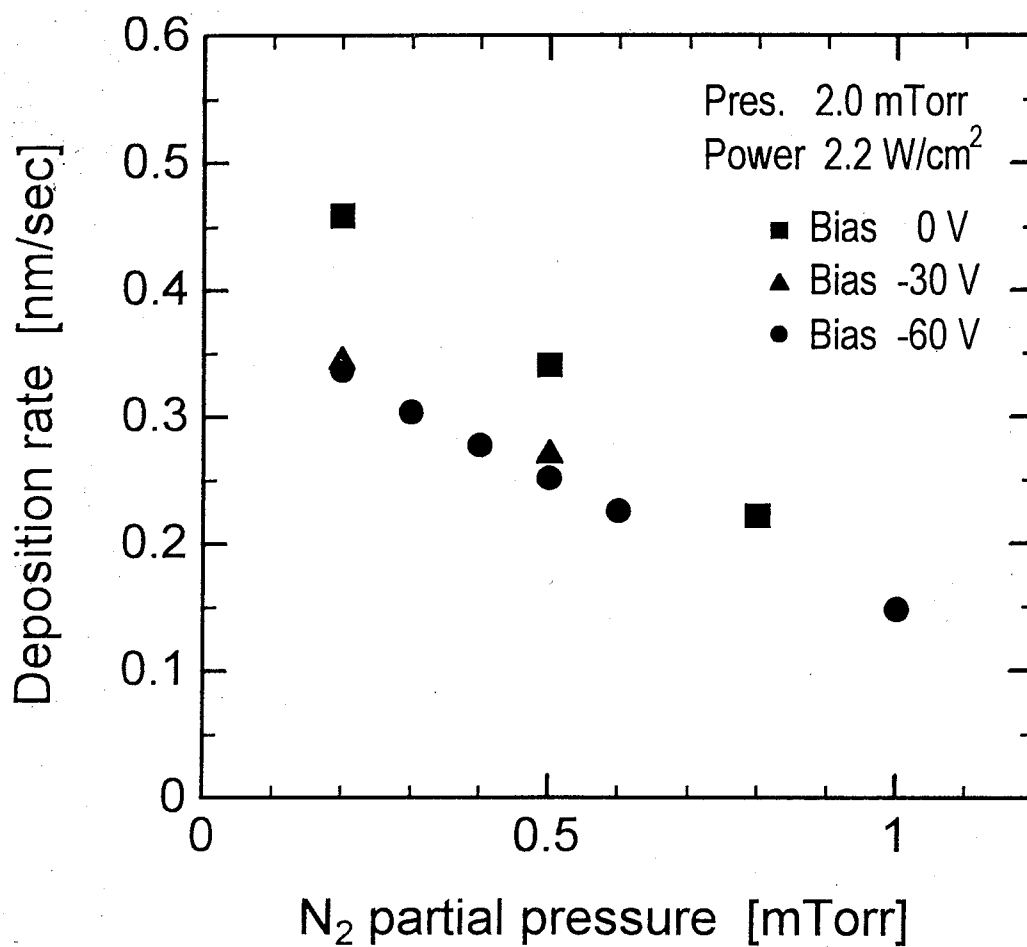


Fig. 5.2.8 Dependence of the NbN deposition rate on the N₂ partial pressure.

confirmed from the Fig. 5.2.8. This figure shows the dependence of deposition rate on the partial pressure of N_2 and bias voltage, which reveals that the rate is low at higher bias voltage. In general, this bias sputtering is known to be one of the effective techniques to obtain a film of better quality [29], and this result is consistent with the fact. From Fig. 5.2.9, the dependence of the electrical properties on the partial pressure of N_2 reveals that the 0.5 mTorr is the optimized condition and T_c of 14.2 K was achieved. Although the resistivity of the film deposited at the bias of -60 V is not so much affected by the N_2 , influence on T_c is drastic. This would be due to the existence of multiple phases in NbN and especially the difference in superconducting properties among them. The deposition rate monotonously decreases with increasing partial pressure of N_2 , and this would be due to the difference in sputtering yield of Nb between Ar and N_2 .

Figures 5.2.9(a) and (b) show the results from the X-ray diffraction spectroscopy measurements performed on the NbN films. The former shows the dependence of lattice constant of NbN on the bias voltage and the latter does that of lattice constant on partial pressure of N_2 , which are estimated from the X-ray diffraction peak position of δ -NbN (111) since it has a preference for that lattice plane to be parallel to the substrate. These figures also support the result from the electrical properties that the film deposited in optimized condition ($V_{\text{bias}} = -60$ V and $P_{N_2} = 0.5 \times 10^{-3}$ Torr) is close to the value of stoichiometric bulk NbN.

Figure 5.2.10 shows the temperature dependence of the critical current density. In this experiment, the NbN was patterned to the stripe line by lift-off technique whose width and length were 20 μm and 2 mm, respectively. The film deposited in higher negative DC bias shows higher T_c and higher critical current density (J_c). The superconducting current flowed as much as 3×10^6 A/cm² at 4.2 K in the film deposited in -60 V bias and it is about two orders of magnitude larger than the film deposited without applying bias. Here again we can confirm the effectiveness of bias sputtering.

Finally, the dependence of the superconducting transition temperature of NbN films on thickness was investigated and the result is shown in Fig. 5.2.11. The superconducting properties degrade with decreasing the film thickness. This is due to the existence of critical

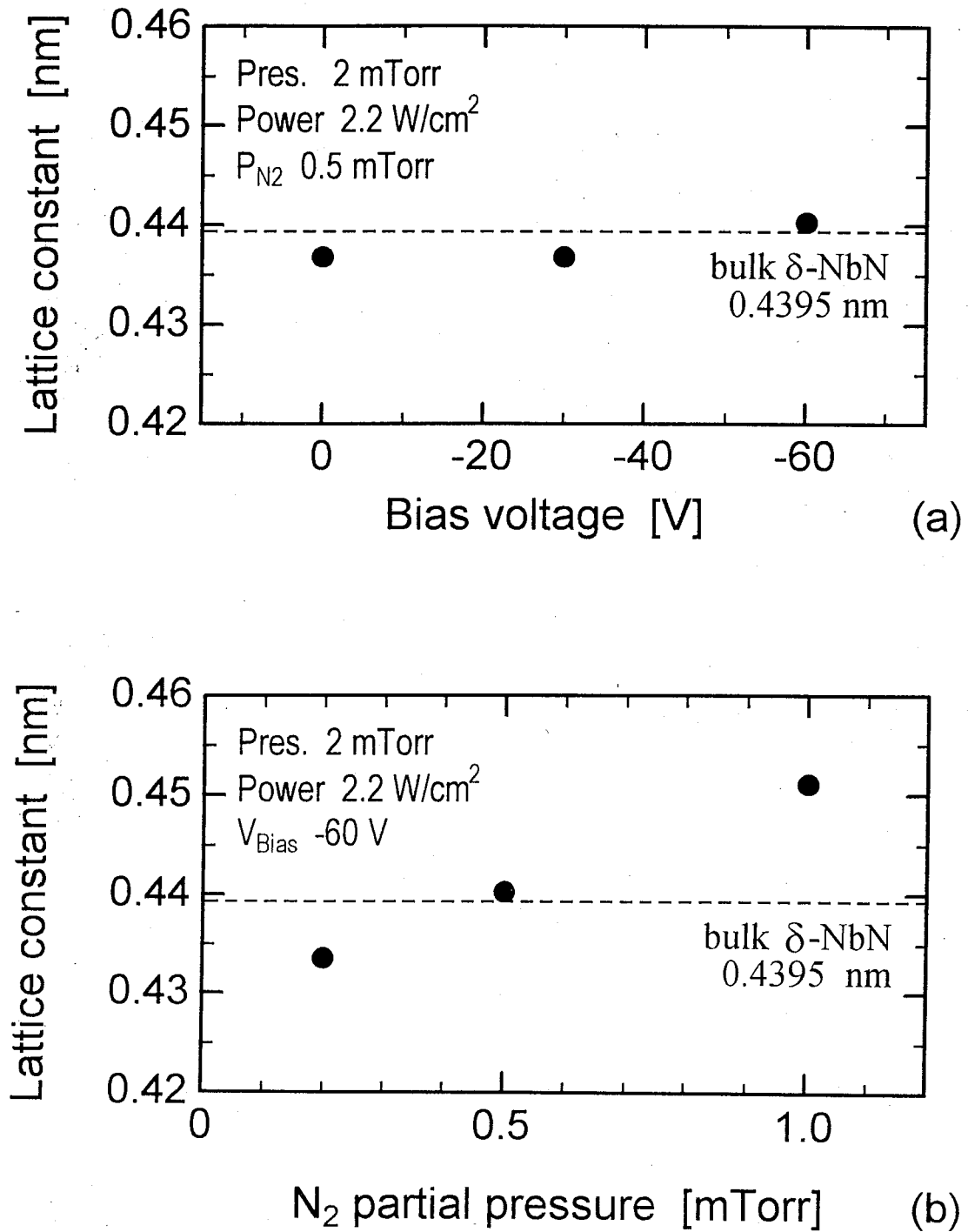


Fig. 5.2.9 Dependence of the lattice constant of NbN on (a) bias voltage and (b) partial pressure of N₂ deduced from the δ -NbN(111) X-ray diffraction peak.

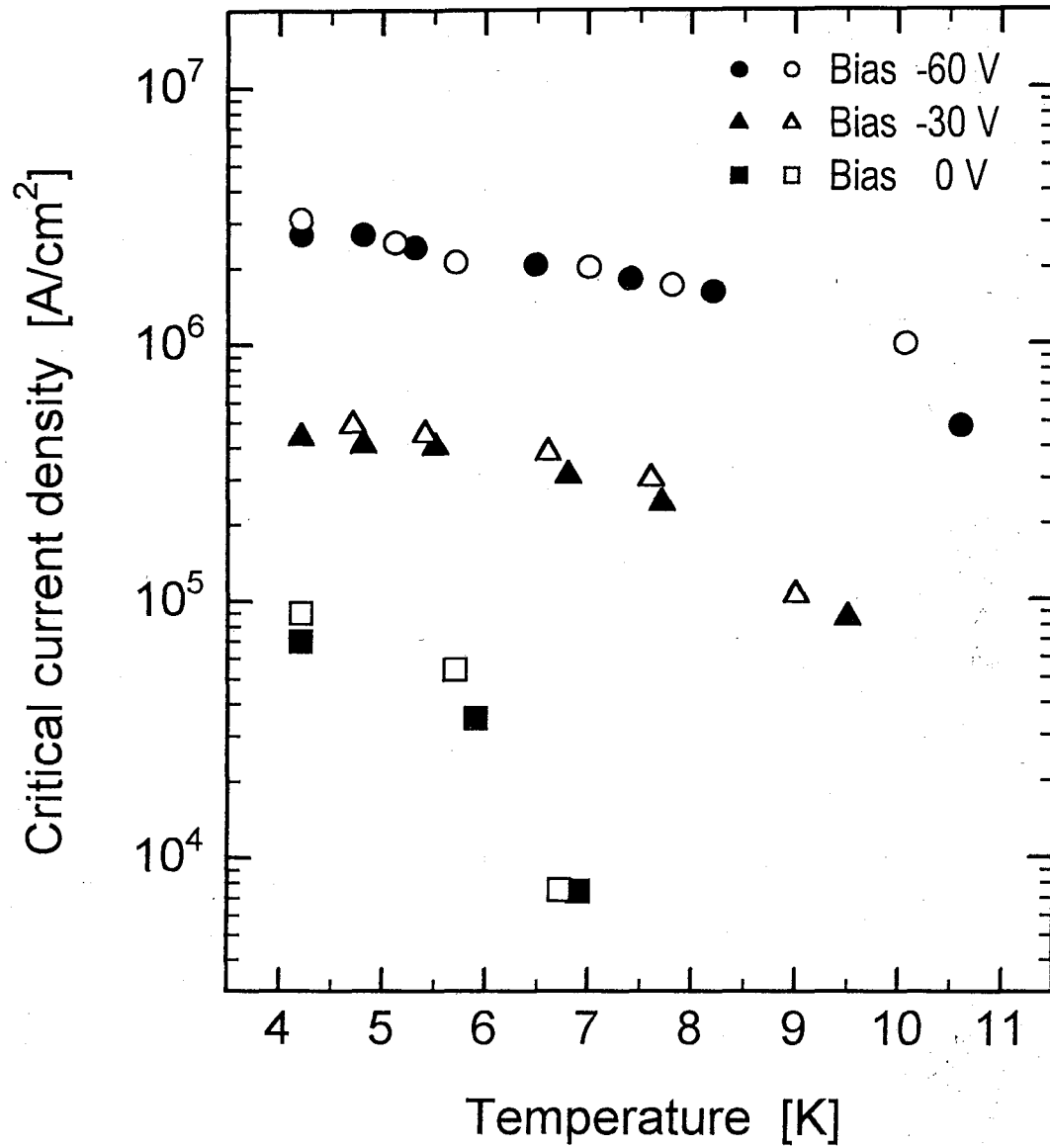


Fig. 5.2.10 Dependence of the superconducting critical current density on temperature.

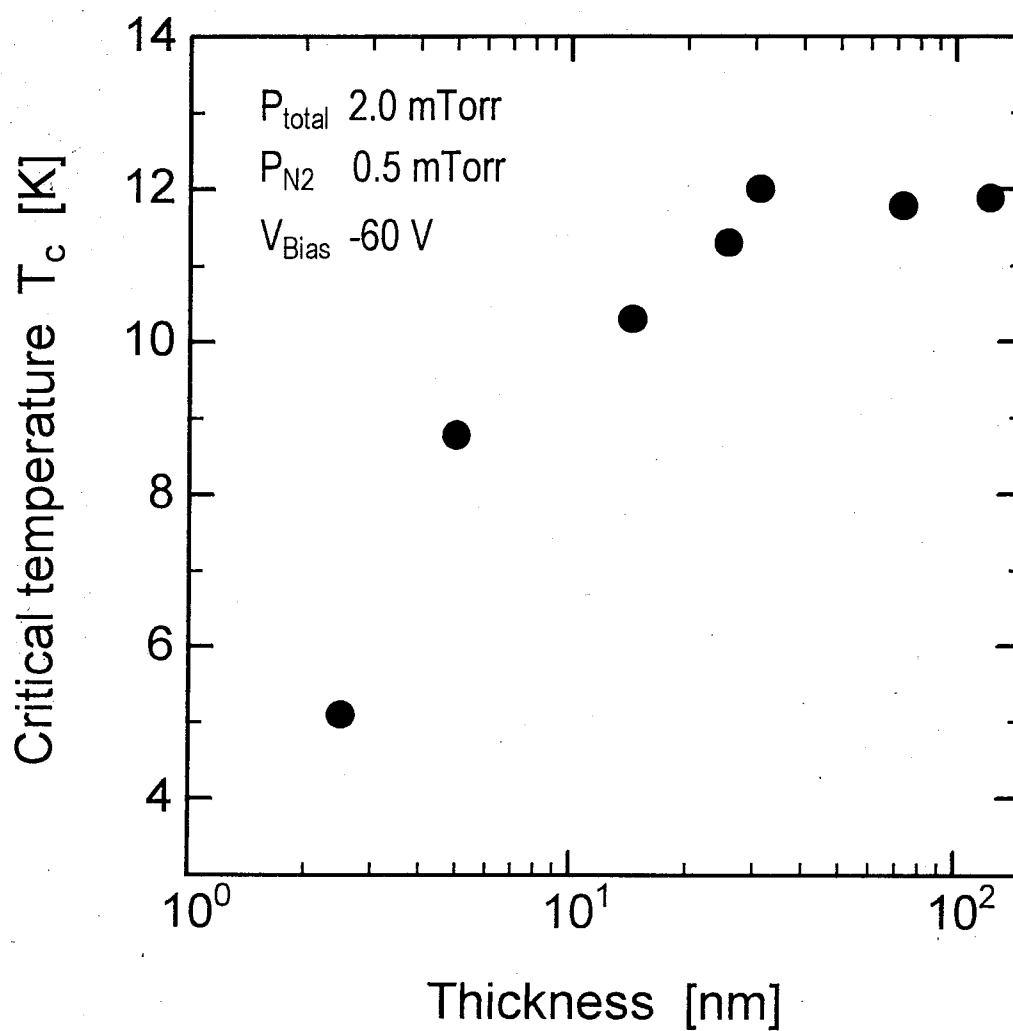


Fig. 5.2.11 Critical temperature dependence on NbN thickness.

thickness to exhibit superconducting property similar to the case of Nb discussed in previous section. Since NbN is more stable and less influential from the ambient oxygen than Nb, the 3 nm thick NbN still showed superconductivity below 5 K. This is an encouraging result for considering any superconducting devices using an extremely thin superconducting film, such as the previously-mentioned SETs modified by AFM nano-oxidation process.

5.3 Weak Link Device of NbN / ZnO / NbN Stacked Structure

5.3.1 Utilization of ZnO thin film as a normal layer

For the application of the heavily-doped semiconductors to the cryoelectronic devices, superconducting weak link device was considered. It is inevitable to control the channel length of the normal layer of the order of 0.1 μm or less for the superconducting operation. For starters, heavily boron-doped zinc oxide (B-doped ZnO) was newly employed for the normal layer to realize a stacked junction, which is one of the easy structure to control the channel length.

The ZnO thin film was deposited by metalorganic chemical vapor deposition (MOCVD) technique under the condition summarized in Table 5.3.1 using the apparatus illustrated in Fig. 5.3.1. Dimethylzinc (DEZn) and D_2O were used for the sources of zinc and oxygen, respectively, and they were introduced to the reacting chamber by Ar carrier gas. The B_2H_6 diluted with hydrogen was also introduced from another gas inlet for the boron doping to obtain n^+ -ZnO thin film. The gases are decomposed thermally and the deposition occurs. Figure 5.3.2 shows the dependence of the resistivity of the obtained ZnO film on the B_2H_6 flow rate. By changing the flow rate, we can control the electrical characteristics of ZnO films and obtained a film whose electron concentration was $1.5 \times 10^{20} \text{ cm}^{-3}$ grown at optimized conditions with a thickness of 50 nm. Its superconducting coherent length in this ZnO film was estimated to be about 10 nm at 4.2 K, which is a hopeful value for the Josephson coupling through the film.

Table 5.3.1 Deposition condition of B-doped ZnO.

Pressure	6 Torr
Flow Rate	
D_2O	124.5 $\mu\text{mol} / \text{min}$
DEZn	81.3 $\mu\text{mol} / \text{min}$
2 % B_2H_6/H_2	0.25 ~ 5.0 sccm
Substrate Temperature	158 ~ 208 $^{\circ}\text{C}$
Deposition Time	1 ~ 30 min

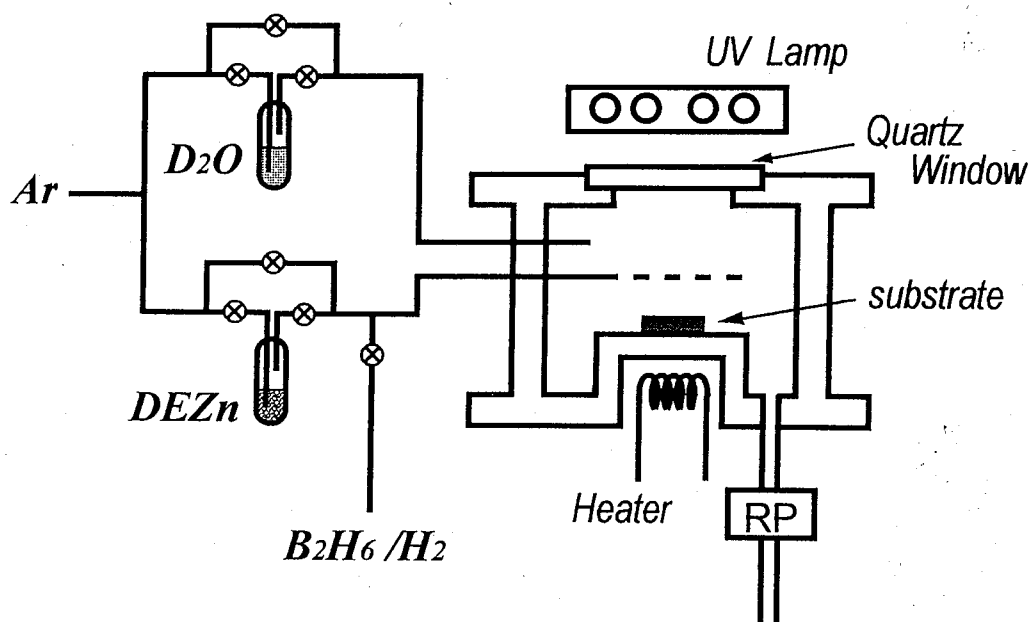


Fig. 5.3.1 Schematic of the MOCVD system for depositing ZnO film.

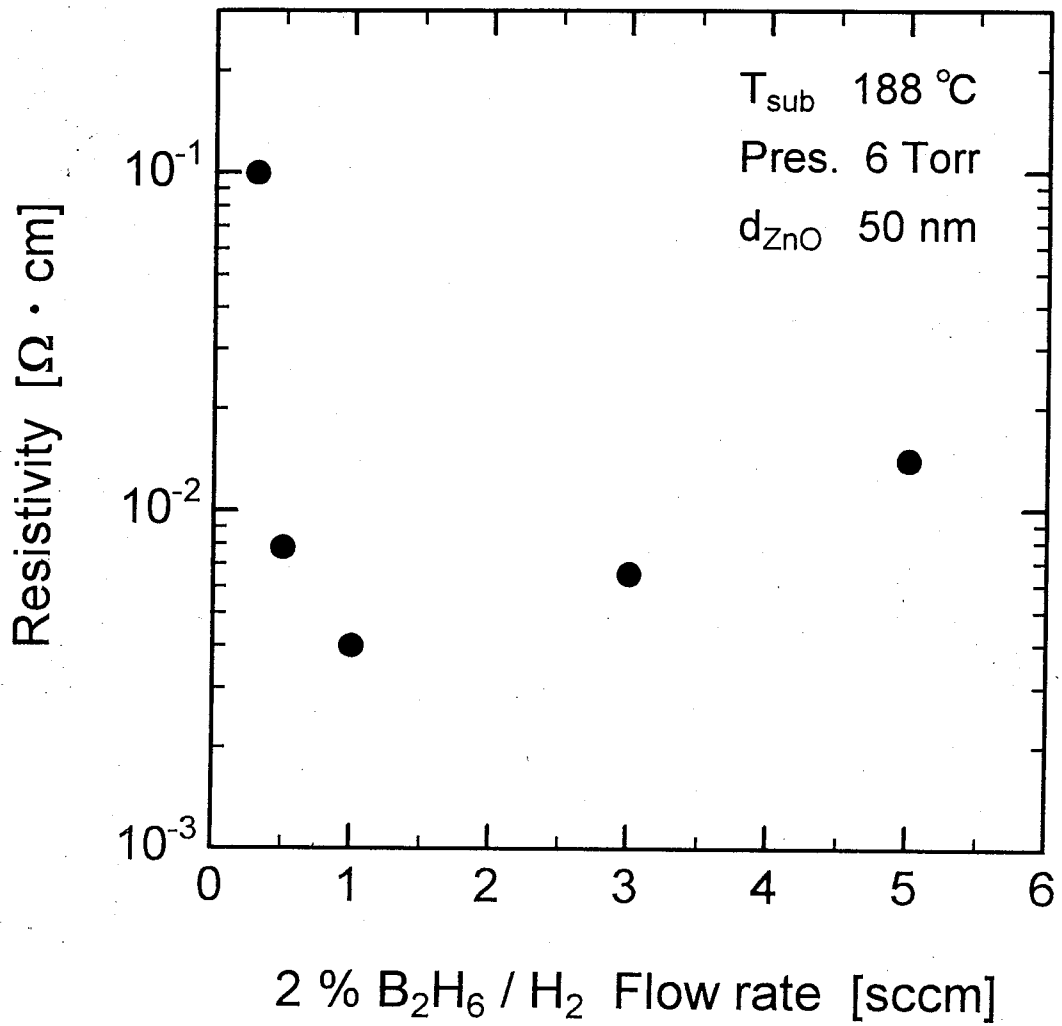


Fig. 5.3.2 Dependence of the resistivity of ZnO thin film on B_2H_6 flow rate.

5.3.2 *Fabrication process*

Since the ZnO film is polycrystalline, the superconducting weak link device was fabricated in a stacked structure. By stacking the ZnO by superconducting electrodes, we can easily control the channel length of the normal layer which corresponds to the thickness of the intermediate ZnO film although it requires considerable number of lithography. In order to realize a superconducting device operation in this system, superconducting electrodes must be stable against thermal process and oxidation. Therefore, the NbN was selected for them. The process flow of the device and its schematic are illustrated in Figs. 5.3.3 and 5.3.4(b), respectively. First of all, an i-Si substrate was cleaned by organic solvents and diluted HF. As for the substrate, insulating material was preferable such as a glass or SiO₂/Si to prevent leakage current in the device operation. However, NbN of better quality was only obtained by utilizing bias sputtering technique in our deposition system as mentioned in the previous section and good NbN film could not be deposited on any insulating substrate as the electrical bias could not be applied on. Therefore, a silicon wafer of a high resistivity ($\sim 1 \text{ k}\Omega\cdot\text{cm}$) was used as a substrate because the carriers freeze out at device operating temperature (around 4.2 K) and the substrate exhibits semi-insulating properties at that temperature range, which would less affect the electrical leakage. After the substrate preparation, NbN was deposited on it by DC magnetron sputtering and patterned by photolithography and lift-off to form a lower superconducting electrode. The intermediate B-doped ZnO was then deposited in about 50 nm by MOCVD method. Its thickness can be controlled by the deposition time. After etching the ZnO except for that in junction region by diluted HCl, top NbN electrode was formed in similar manner to the lower one. Thus, the NbN/ZnO/NbN stacked junction was fabricated. Cross sectional SEM image of the junction area was shown in Fig. 5.3.4(a). Since the ZnO layer was deposited by CVD technique, its coverage seems to be smooth enough to prevent the electrical shortage between the top and lower electrodes. Junction size of the device was 10 μm square or 20 μm square.

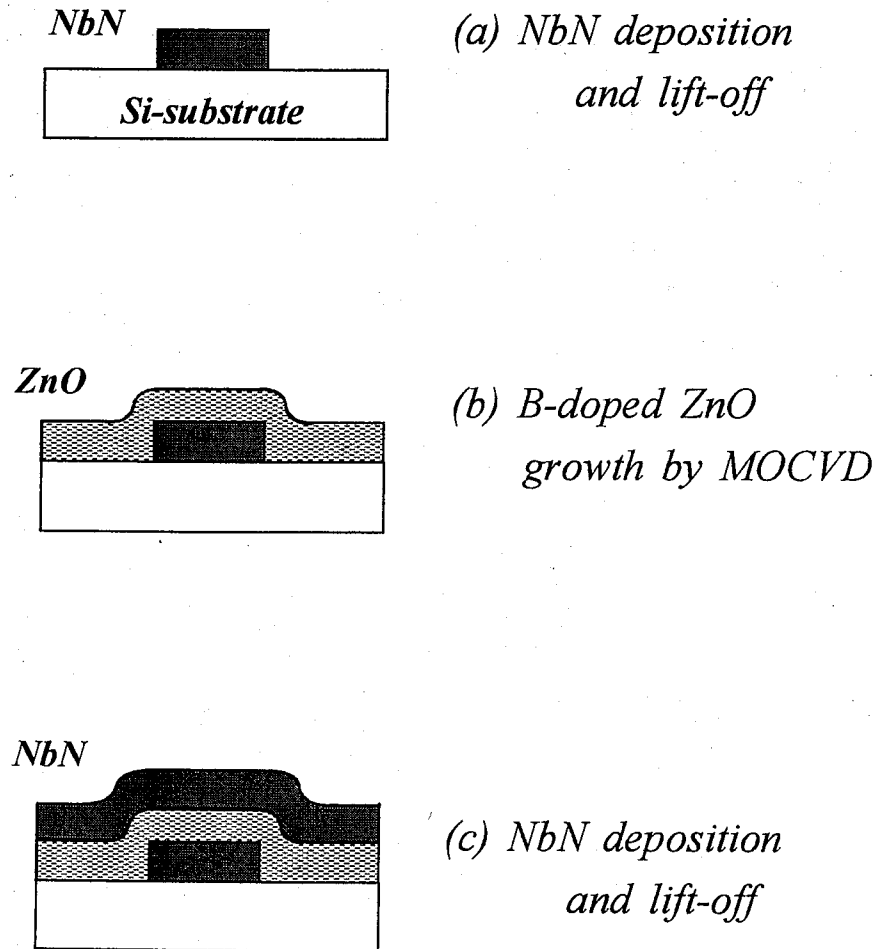


Fig. 5.3.3 Fabrication process for NbN / ZnO / NbN weak link device.

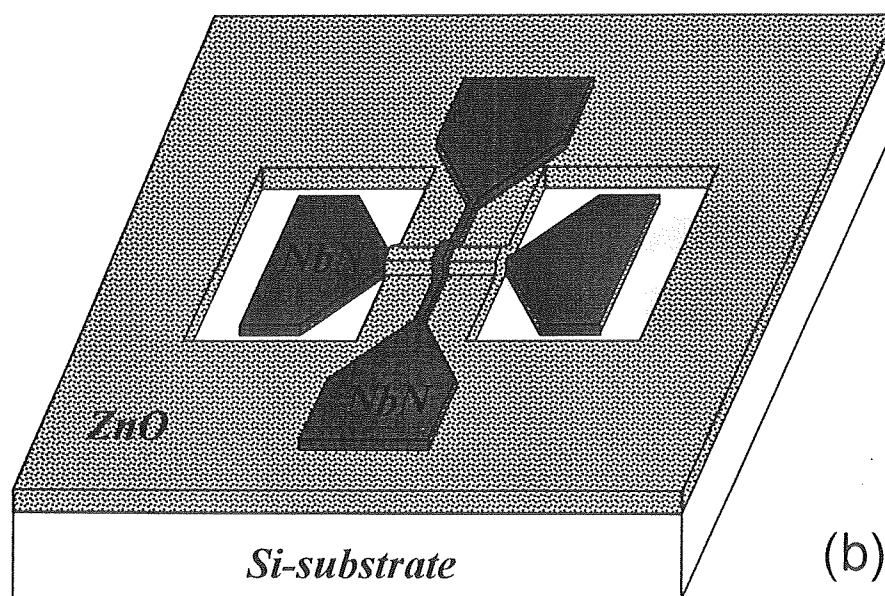
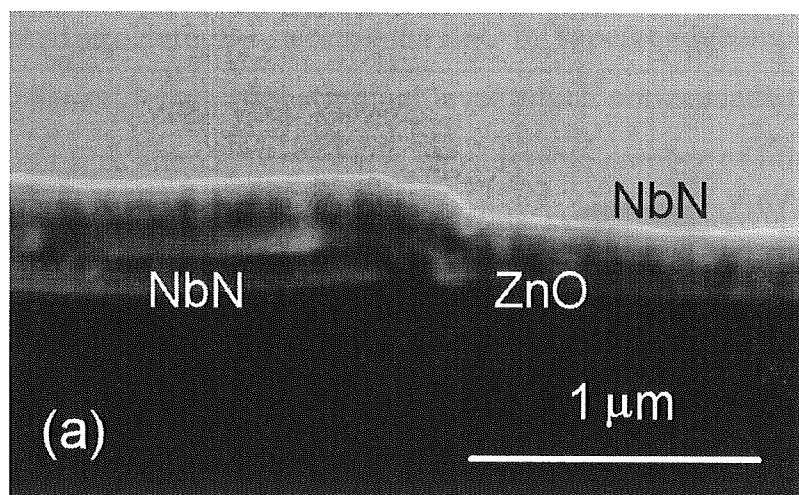


Fig. 5.3.4 Cross sectional SEM image (a) and schematic (b) of the NbN / ZnO / NbN trilayer superconducting weak link device.

5.3.3 Electrical characteristics

Electrical characterization of the weak link device of NbN/ZnO system was next performed. The device was set in a helium cryostat and the measurement was done by four point probe method. Figure 5.3.5 shows the current-voltage characteristic of the device measured at 4.2 K whose normal layer thickness was about 40 nm. As can be seen, superconducting current flowed through the n⁺-ZnO layer, which would be based on the proximity effect. This preliminary result suggests that the heavily B-doped ZnO can be applicable to the Josephson junctions. The $I_c R_n$ product of the device was estimated to be about 1.5 mV, which is a consistent value compared to the superconducting energy gap. Figure 5.3.6 shows the temperature dependence of the critical current of another device. We can see that the critical current decreases with increasing the temperature, which is roughly due to the temperature dependence of the coherent length and the thermal fluctuation. Theoretically, critical current (I_c) dependence on temperature was reported to follow the following equation [30],

$$I_c = \frac{C_1}{4} (1-t) \sqrt{t} \left(\cosh^2 \left(\frac{C_2 \sqrt{t}}{2} \right) \right)^{-1}, \quad (5-1)$$

where t represents T/T_c , C_2 represents $L/\xi_n(T_c)$ and C_1 is the fitting parameter. The ξ_n means the coherence length of the ZnO and T_c of this device was about 10 K. By changing the C_2 in order to best fit the data, value of 3.5 explains the experimental data as shown in Fig. 5.3.6. However, we obtained the value of ξ_n from the fitting to be about 17 nm, which is a little large compared to the value of 6 nm from the theoretical calculation using eq. 4-3. This discrepancy will be discussed later.

Since a number of junctions was fabricated, relation of the critical current density (J_c) on thickness of the ZnO was examined comparing the devices whose coherence lengths were calculated to be almost same. The result is shown in Fig. 5.3.7. Although there were two plots, less superconducting current flowed through the thicker ZnO layer. By using following equation, coherent length was further investigated,

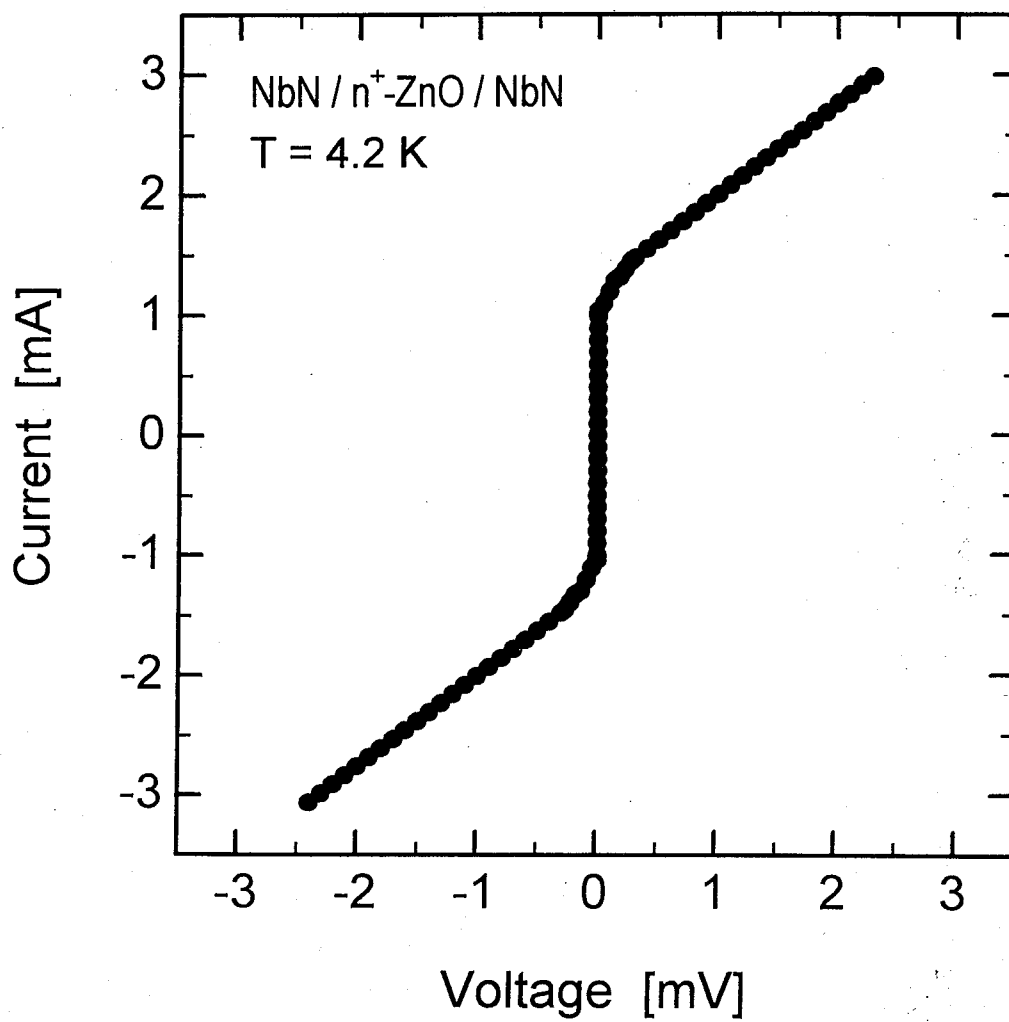


Fig. 5.3.5 Current-voltage characteristic of NbN / ZnO / NbN weak link device.

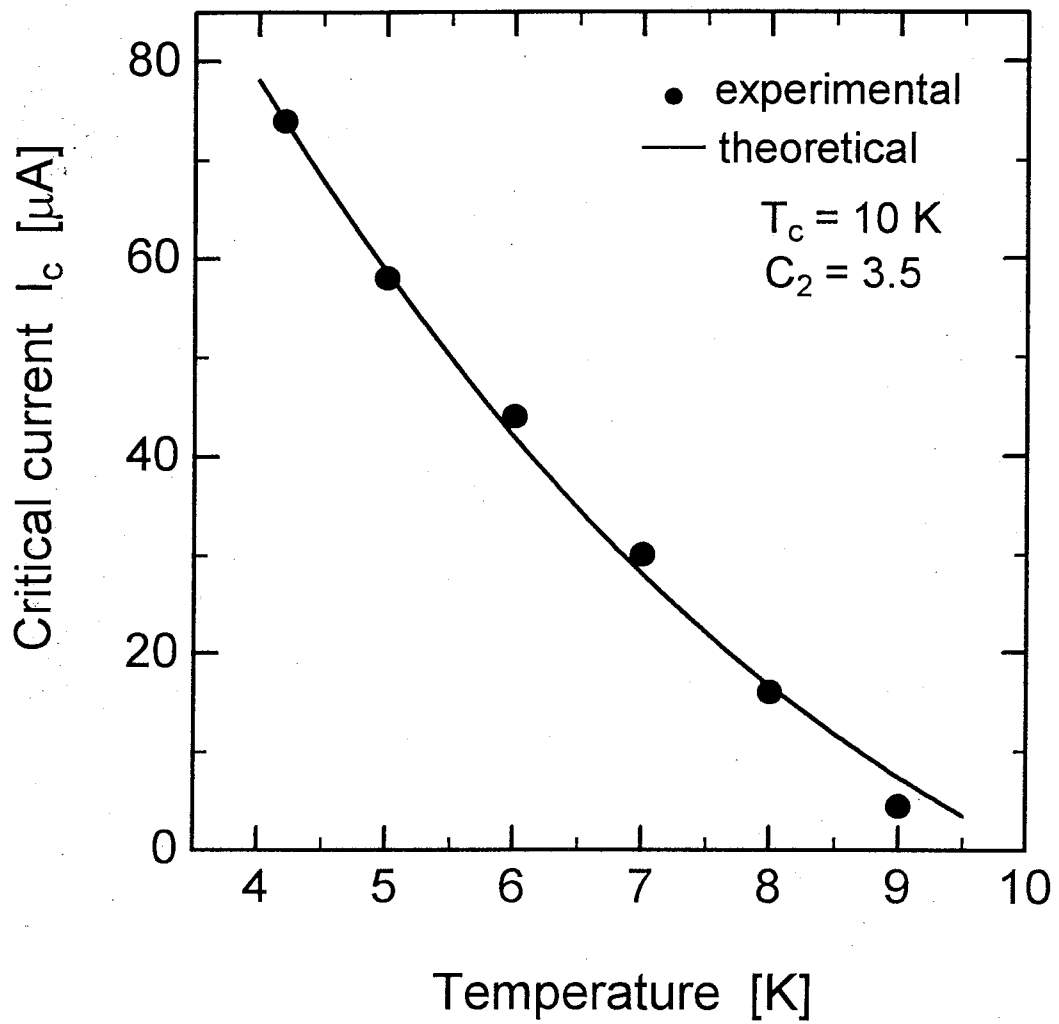


Fig. 5.3.6 Temperature dependence of the critical current of the weak link.

$$I_c \propto \frac{1}{\xi_n} \exp\left(-\frac{L}{\xi_n}\right) \quad , \quad (5-2)$$

where L means the channel length of the normal layer or thickness of ZnO layer. From the experimental fitting, the ξ_n was calculated to be 37 nm, which is also large compared to the theoretical one. These discrepancies would be attributed to the film nonuniformity. Since the ZnO is polycrystalline, there should have existed a relatively thin area which might have governed the electrical characteristics or the influence of the grain boundary where the electrons could more easily flow through them than through the grains with tunneling the potential barrier in the grain boundary.

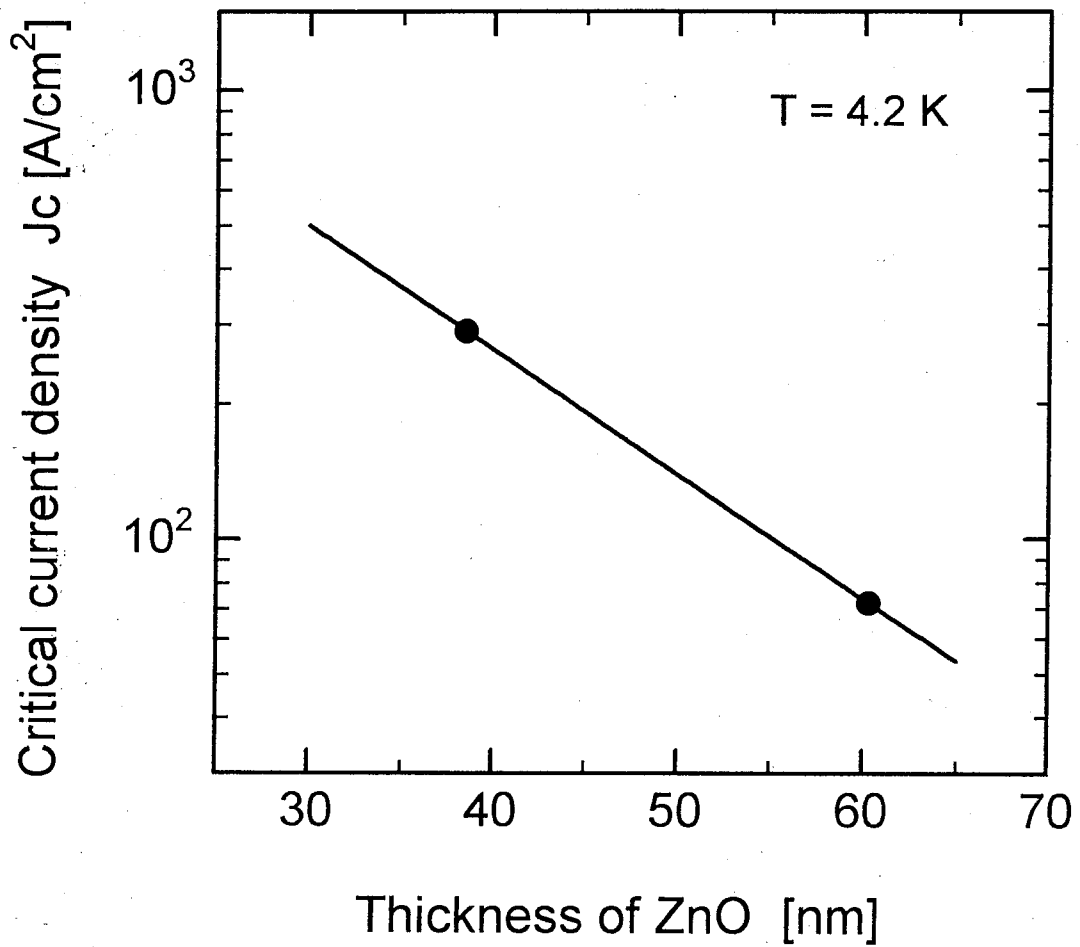


Fig. 5.3.7 Dependence of critical current density on intermediate ZnO thickness.

5.4 Weak Link Device of Nb / n^{++} -Si / Nb Coplanar Structure

5.4.1 Utilization of n^{++} -Si as a normal layer

Heavily-doped semiconductors are applicable to the superconducting weak link device as a normal layer. In the previous section, B-doped ZnO was employed. However, it is not always suitable to use polycrystalline material in stacked junction as discussed because the controllability of the device electrical parameters is relatively inferior due to the influence of the grain boundary or the film uniformity and because the poor extensionality to the three-terminal operation in that structure. Therefore, application of single crystalline material was next considered. As mentioned in Chapter 4, we have a technology to grow epitaxial heavily-doped semiconductor thin films such as n^{++} -Si or p^{++} -GaAs. Their applicability was also confirmed from the theoretical calculation of their coherence lengths. Considering the device structure, stacked junction is no longer applicable but a coplanar structure is one of the choices. For Josephson coupling between the superconducting electrodes through the heavily-doped semiconductor, however, it requires a channel length of the order of the coherence length and it is estimated to be about 0.1 μm or less. This situation means that the conventional photolithography managed to or could not meet the demands; therefore, other techniques such as the electron-beam lithography should be used for realizing the device in coplanar structure. Although the fabrication becomes complex, following advantages are expected in this structure, such as low capacitance (which raise the cut-off frequency together with R_n being small), rich extensionality to the three-terminal device, and junction characterization.

As discussed extensively in Chapter 3, one of these studies is the nanofabrication using carbonaceous microstructures deposited by SEM. In particular, we can easily obtain carbon wire which is thinner than 0.1 μm and it can be positively used as an etching mask for fabricating nanowires. Therefore in this chapter, utilization of this carbonaceous wire for defining the channel length of the weak link device in coplanar structure was first developed. Namely, the wire was used as a lift-off mask or suspended mask. This means that the width of the carbon wire determines the channel length since the width can be ranged from as small as 30 nm. New fabrication process was proposed in this section and the carbon wire was

successfully employed to define the channel length of the Nb/n⁺⁺-Si/Nb coplanar weak link device.

5.4.2 Fabrication of sub-micron gap structure using a-C wire

As a-C itself is stable against acid, its removal from the fabricating device after the definition of the gap is the key issue which is similar problem to the dry etching mask discussed before. Therefore, a bilayer resist system was newly employed. The details of the process flow are illustrated in Fig. 5.4.1. First, a ZnO buffer layer is deposited on a Si substrate by MOCVD method (a). The application of this layer is one of the key features of this process and it is due for both forming a suspended mask and removing the a-C wire. Since polycrystalline ZnO can be easily etched by any acid and has a relatively high conductivity as well as a flat surface morphology [31], its usage for electron-beam induced process is advantageous compared to the usage of insulating SiO₂. Conventional photolithography follows for defining a channel electrode. Then, the a-C wire is deposited by SEM to bridge the photoresist across the channel, which divides the channel into two regions and defines a channel length (b). After the writing, ZnO is etched using diluted HF which makes a stencil structure and leaves the wire hanging over the Si substrate forming a suspended mask (c). A niobium electrode is then deposited (d). Finally, the structure is patterned and the a-C wire is removed by the lift-off (e). Through this process, a patterned structure with a gap whose length is almost equivalent to the width of the a-C wire can be realized. As it was previously pointed out, the width of the wire can be controlled (from a few 100 nm to as small as 30 nm) by changing the electron-beam condition. Moreover as shown in Fig. 5.4.2, the channel length could be controlled by writing the wires in parallel, which makes a fat wire and contributes to realize a long channel length. The thickness of the photoresist and height of the a-C wire were about 1 μm and 200 nm, respectively. Although the a-C wire was not thicker than the photoresist, the patterned photoresist was confirmed to have a tapered structure from the SEM image in Fig. 5.4.2(d) and this situation is considered to prevent the a-C wire from being cut during the following processes. The SEM image also

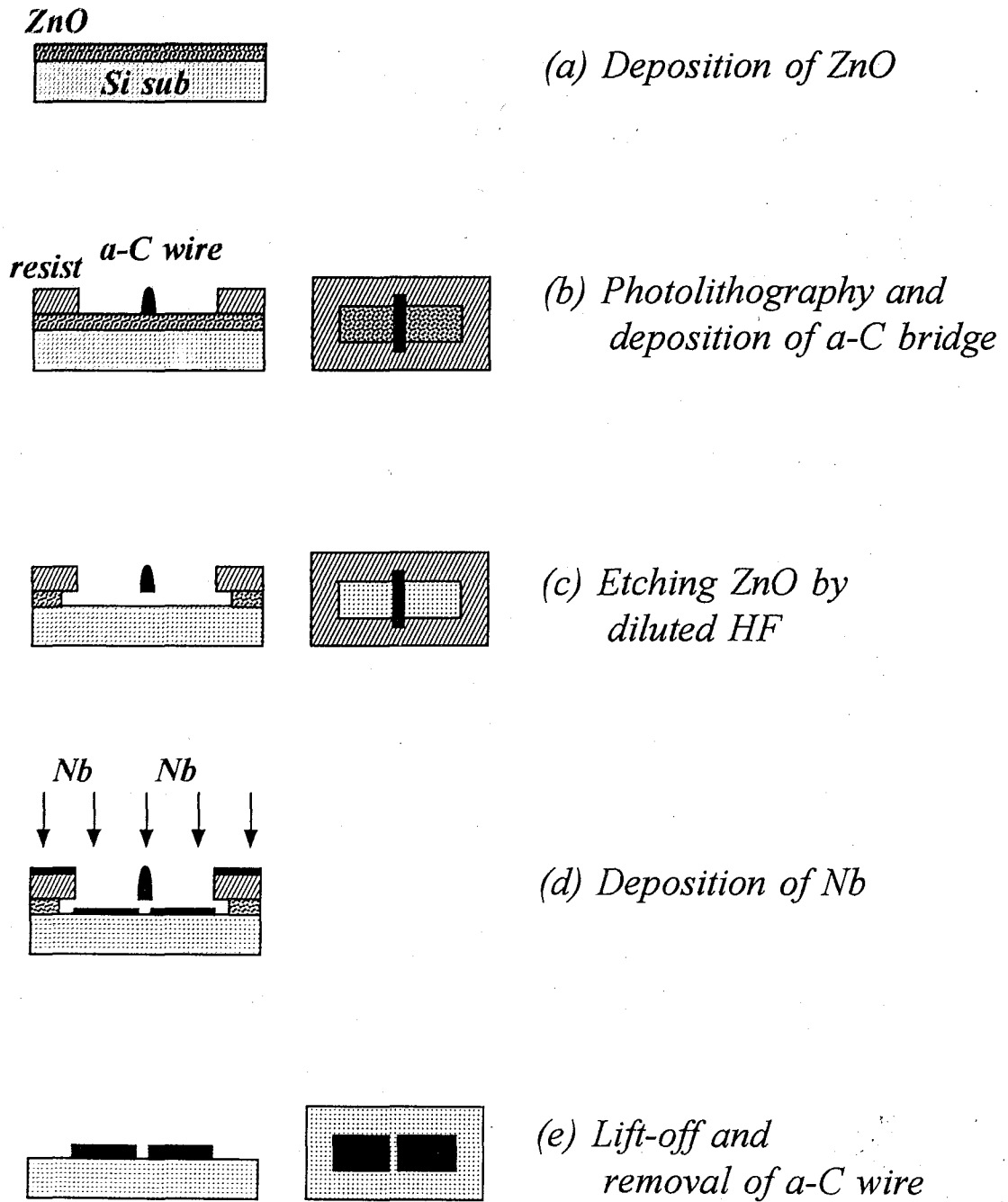


Fig. 5.4.1 Fabrication process for coplanar structure with sub-micron gap.

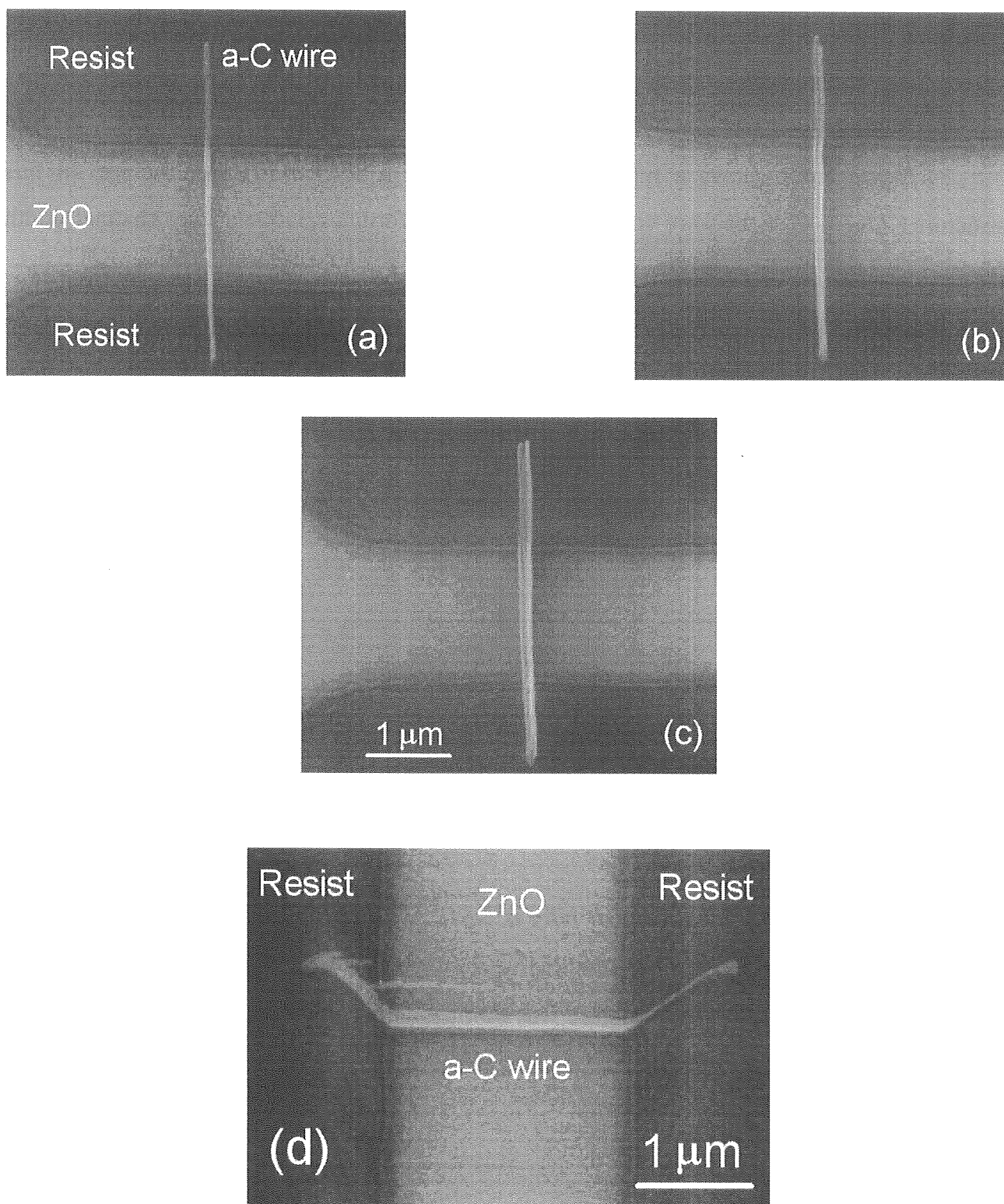


Fig. 5.4.2 SEM images of the a-C bridges over the ZnO / Si substrate. One a-C wire (a), two a-C wires (b), and three a-C wires (c) were deposited in parallel. The structure was also monitored from tilt angle (d).

reveals the clear deposition of carbon wire on the insulating resist as it was thin enough to be processed by the electron-beam and as the conducting ZnO existed underneath. Therefore we could make coplanar-type metal electrodes with a sub-micron gap structure through this process.

Figure 5.4.3 shows a typical SEM image of a fabricated gap structure. In this structure, three a-C wires were connected in series to form a relatively long channel width ($\sim 20 \mu\text{m}$) simply because of the limit of the scanning area of our SEM system. Furthermore, each a-C wires was overwritten three times to make wires with high aspect ratio in order to strengthen the a-C bridge. Eventually, an electron dose is calculated to be about $0.6 \text{ nC}/\mu\text{m}$. By optimizing the a-C wire in this manner, a sub-micron gap structure was successfully fabricated whose width and length were about $20 \mu\text{m}$ and 60 nm , respectively. Since the wires were overwritten, the length of the gap became large compared to the minimum obtainable width of the a-C wire ($\sim 30 \text{ nm}$). This is due to the fact that a longer beam irradiation leads to the lateral growth of the wire as well as to its vertical growth. In Fig. 5.4.3, no residue of the a-C in the gap can be seen, which ensures its complete removal during the lift-off process as the wire hangs over the Si surface and does not come into contact with the deposited metal.

5.4.3 *Electrical characteristics of Nb / n⁺⁺-Si / Nb junction*

Regarding the application of this process to device fabrication, a superconducting weak link device in a coplanar structure was fabricated using a heavily phosphorous-doped Si epitaxial film as a channel material. It was grown on a Si (100) substrate by the plasma enhanced chemical vapor deposition (PECVD) technique and it has an electron concentration of $1 \times 10^{21} \text{ cm}^{-3}$. Since the n⁺⁺-Si is highly degenerated and has a high electron concentration, the coherence length of the superconducting wave function penetrating into the semiconductor region, which is the proximity effect [32], is long enough to facilitate the observation of the superconducting current flow between the source and drain electrodes in our available scale of the structure.

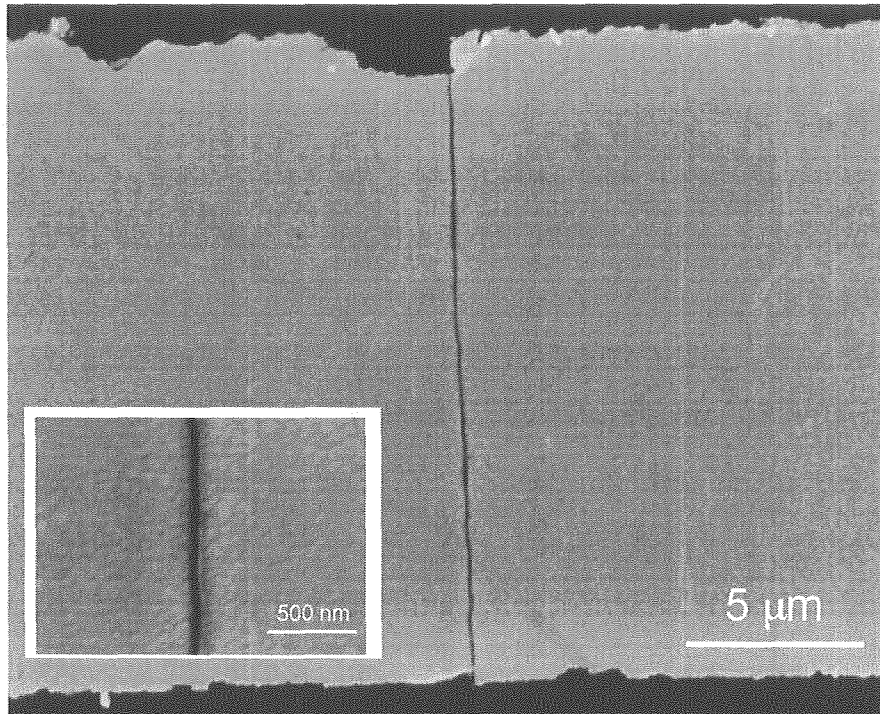


Fig. 5.4.3 SEM image of the Nb / Si / Nb coplanar structure with a gap length of about 60 nm fabricated with a-C suspended mask. Inset shows the gap in high magnification.

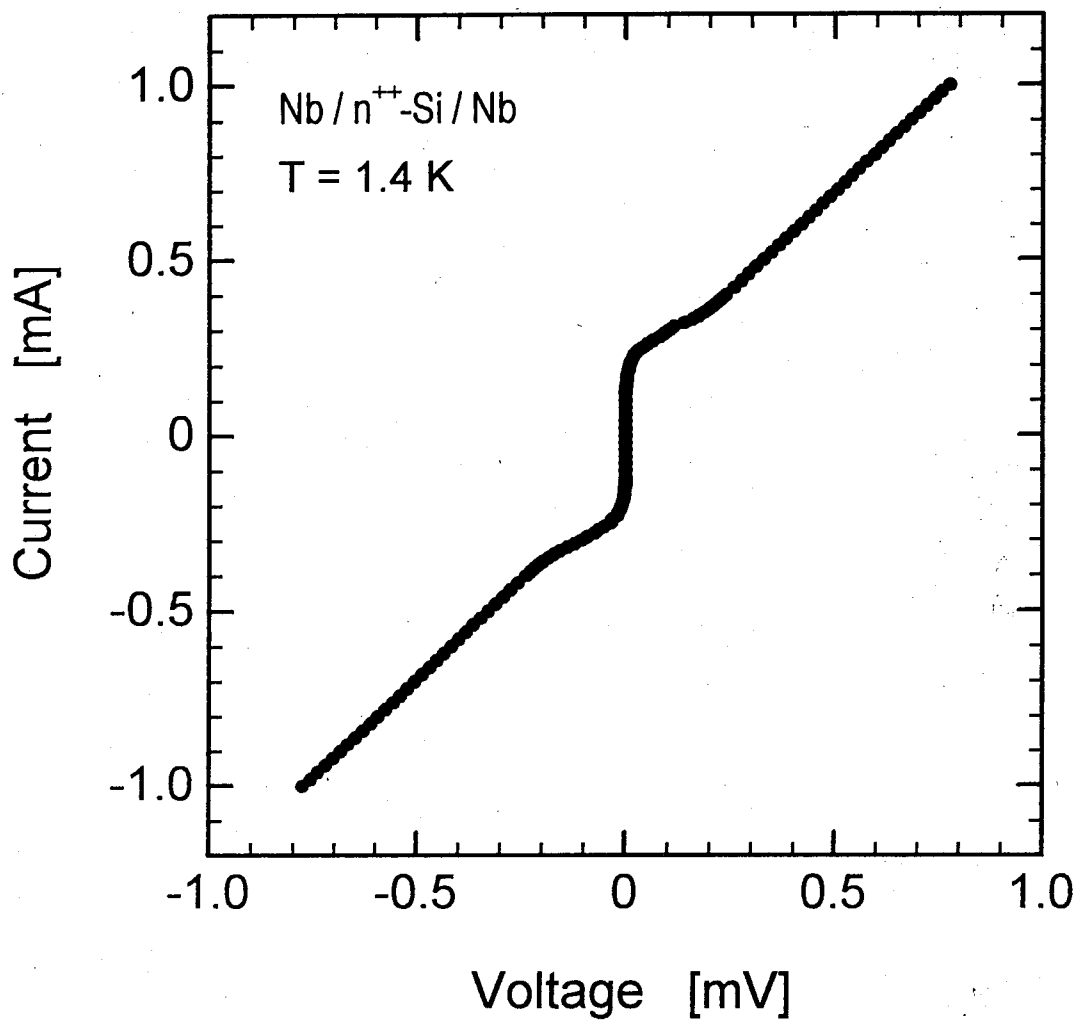


Fig. 5.4.4 Current-voltage characteristic of Nb / n⁺⁺-Si / Nb weak link device.

Source and drain electrodes consisted of superconducting Nb, and n^{++} -Si channel length was about 0.1 μm in this device. Figure 5.4.4 shows an I - V curve of the device measured at 1.4 K. We can see that the I - V curve shows a resistively-shunted junction (RSJ) model like characteristic and the superconducting current flows through the n^{++} -Si layer. This result suggests the applicability of this process to the device fabrication process, and also demonstrates the realization of Nb/ n^{++} -Si/Nb weak link device in a coplanar structure using a heavily-doped semiconductor whose carrier concentration is of the order of 10^{21} cm^{-3} for the first time. The $I_c R_n$ product of this device was estimated to be 0.2 mV. This value is consistent with the reported value in the Si weak link devices, however, the normal resistance was a little large in this device compared with the value estimated from the device structure and from the electrical measurement performed previously on the film. This would be due to the contamination at the interface between the Nb and n^{++} -Si, which is known as a critical issue in the weak link devices since the cooper pairs must tunnel through this layer as well as the Schottky barrier. In this case, the n^{++} -Si substrate was chemically cleaned in a wet process but not in the dry process in the chamber. The Ar^+ ion cleaning and its effectiveness have ever been reported [33, 34]. Introduction of this treatment might contribute to the better electrical performance in the device.

5.5 Summary

In this chapter, results of the fabrication of superconducting weak link devices using heavily-doped semiconductors as a normal layer were described in detail. Based on the theoretical estimation performed in Chapter 4, structural design was also investigated. First of all, the Nb and NbN were selected as superconducting materials and both deposited by DC magnetron sputtering technique. Through the optimization of the Ar or N₂ gas pressure, bias voltage and sputtering conditions, fairly high superconducting transition temperatures were obtained in both materials (8.1 K for Nb and 14.2 K for NbN). Very flat surface of the obtained Nb thin film enabled to be modified by the AFM nano-oxidation process and led to the successful fabrication of single-electron transistors operating at room temperature. Moreover, the materials were employed to the superconducting electrodes of the weak link devices. Polycrystalline B-doped ZnO was first applied in a stacked junction using NbN as the electrodes. Superconducting properties were successfully obtained and theoretical fittings from the point of the coherence length were also performed. Furthermore, heavily P-doped Si epitaxial film whose electron concentration was $1 \times 10^{21} \text{ cm}^{-3}$ was also considered for its application. In order its realization in a coplanar structure, new process was developed to fabricate a sub-micron gap structure which was indispensably required in this device. By employing the carbonaceous wire and a ZnO buffer layer, metal electrodes having a gap length of about 60 nm was skillfully fabricated which corresponds to the width of the carbon suspended mask. This process was successfully applied to fabricate Nb/n⁺⁺-Si/Nb weak link device, and its electrical characteristics showed superconducting behavior at 1.4 K. This is the first demonstration of the device using degenerated semiconductors whose carrier concentration is of the order of 10^{21} cm^{-3} .

References

- [1] M. Gurvutch, M. A. Washington and H. A. Huggins: *Appl. Phys. Lett.* **42** (1983) 472.
- [2] A. Shoji, M. Aoyagi, S. Kosaka, F. Shinoki and H. Hayakawa: *Appl. Phys. Lett.* **46** (1985) 1098.
- [3] S. Kotani, T. Imamura and S. Hasuo: *Tech. Digest Int. Electron Devices Meeting (1988)* pp. 884.
- [4] H. Nakagawa, G. Pepe, H. Akob, L. Frunzio, R. Cristiano, E. Esposito, S. Pagano, G. Peluso, A. Barone and S. Takada: *Jpn. J. Appl. Phys.* **32** (1993) 4535.
- [5] M. Kusunoki, H. Yamamori, A. Fujimaki, Y. Takai and H. Hayakawa: *Jpn. J. Appl. Phys.* **32** (1993) L1609.
- [6] R. Monacco and A. Oliva: *Appl. Phys. Lett.* **64** (1994) 3042.
- [7] L. A. Abelson, K. Dely, N. Martinez and A. D. Smith: *IEEE Trans. Appl. Supercond.* **5** (1995) 2727.
- [8] M. Maezawa and A. Shoji: *Appl. Phys. Lett.* **70** (1997) 3603.
- [9] T. Nishino, M. Miyake, Y. Harada and U. Kawabe: *IEEE Electron Devices Lett.* **EDL-6** (1985) 297.
- [10] T. Nishino, M. Hatano, H. Hasegawa, F. Murai, T. Kure, A. Hiraiwa, K. Yagi and U. Kawabe: *IEEE Electron Devices Lett.* **10** (1989) 61.
- [11] K. Inoue and T. Kawakami: *J. Appl. Phys.* **65** (1989) 1631.
- [12] A. W. Kleinsasser, T. N. Jackson, D. McIntuff, F. Rammo, G. D. Petit and J. M. Woodall: *Appl. Phys. Lett.* **55** (1989) 1909.
- [13] T. Hato, H. Akaike, T. Takai and H. Hayakawa: *Jpn. J. Appl. Phys.* **31** (1992) 1039.
- [14] W. M. van Huffelen, T. M. Klapwijk, D. R. Heslinga, M. J. de Boer and N. van der Post: *Phys. Rev. B* **47** (1993) 5170.
- [15] H. Takayanagi, T. Akazaki, J. Nitta and T. Enoki: *Ext. Abstr. Int. Conf. Solid State Devices and Materials (1994)* pp. 580.
- [16] H. Ihara: *Surf. Sci.* **7** (1986) 255 [in Japanese].
- [17] M. Hatano, T. Nishino and U. Kawabe: *J. Vac. Sci. Technol. A* **6** (1988) 2381.

- [18] T. Shiota, T. Imamura and S. Hasuo: *J. Appl. Phys.* **70** (1991) 6958.
- [19] J. Shirakashi, M. Ishii, K. Matsumoto, N. Miura and M. Konagai: *Jpn. J. Appl. Phys.* **35** (1996) L1524.
- [20] J. A. Dagata, J. Schneir, H. H. Harary, C. J. Evans, M. T. Postek and J. Bennett: *Appl. Phys. Lett.* **56** (1990) 2001.
- [21] H. Sugimura, T. Uchida, N. Kitamura and H. Masuhara: *J. Vac. Sci. Technol. B* **12** (1994) 2884.
- [22] J. A. Dagata: *Science* **270** (1995) 1625.
- [23] E. S. Snow, D. Park and P. M. Campbell: *Appl. Phys. Lett.* **69** (1996) 269.
- [24] J. Shirakashi, K. Matsumoto, N. Miura and M. Konagai: *Ext. Abstr. Int. Conf. Solid State Devices and Materials (1997)* pp. 490.
- [25] K. S. Kesker, T. Yamashita and Y. Onodera: *Jpn. J. Appl. Phys.* **10** (1971) 370.
- [26] R. W. Guard, J. W. Savage and D. G. Swarthout: *Trans. AIME* **239** (1967) 643.
- [27] G. Oya and Y. Onodera: *J. Appl. Phys.* **45** (1974) 1389.
- [28] J. R. Gavaler, J. Gregg, R. Wilmer and J. W. Ekin: *IEEE Trans. Magn* **19** (1983) 418.
- [29] M. Dohyama and R. Yamamoto: *"Superconducting Materials"* [in Japanese] (Tokyo Univ. Press, Tokyo, 1987) pp. 241.
- [30] J. Seto and T. V. Duzer: *Low Temp. Phys.* **LT-13** (Plenum press, New York, 1974) pp. 328.
- [31] B. Sang and M. Konagai: *Jpn. J. Appl. Phys.* **35** (1996) L602
- [32] J. Seto and T. V. Duzer: *Appl. Phys. Lett.* **19** (1971) 488.
- [33] A. Serfaty, J. Aponte and M. Octavio: *J. Low Temp. Phys.* **63** (1986) 23.
- [34] D. R. Heslinga, W. M. van Huffelen, T. M. Klapwijk, S. J. M. Bakker and E. W. J. M. van der Drift: *Cryogenics* **30** (1990) 1009.

Chapter 6

Evaluation of Carbonaceous Material for Microscopic Devices

6.1 Introduction

To produce microscopic devices, such as single electron transistors (SETs), utilization of electron-beam lithography for patterning each device is the most commonly applied technique so far [1-3]. However, it is not always the simplest technique for use in the device fabricating process, and an establishment of simple and unique processes to make minute structures is required. Among the newly developed techniques, a beam-induced process, such as an etching [4, 5] and a deposition of materials [6-8], has potential for use in manufacturing due to its easy and resistless microprocessing. The direct writing and deposition is one of its notable techniques for producing the stacked structures. As mentioned before, its key features are that various materials and structures can be deposited in arbitrary positions by changing a precursor or the scanning of an electron-beam, its lateral size can be ranged from 10 nm to a few 10 μm , and it is applicable to obtain a material with a fairly wide range of resistivity from metallic to semi-insulating by just changing a precursor molecule. These features are quite attractive especially for the direct fabrication of the microscopic junctions of metal/insulator systems.

In chapter 3, the deposition of carbonaceous wires originating from the residual gases in the chamber using scanning electron microscope (SEM) was performed and its applications to the tip of AFM cantilever and the device process, especially the etching mask, were examined. However, properties of the carbonaceous material itself have not yet been considered. From a point of its application to the fabrication of microscopic devices consisting of this material, its electrical characterization is inevitable. Therefore in this chapter, evaluation of this material is provided and the results of its application to a metal/insulator/metal (MIM) diode in a stacked structure are reported using Au and carbonaceous microfilm as metal electrodes and an intermediate insulator, respectively.

Furthermore, in order to shrink the junction size to sub 1 μm , the metal electrodes in another device were directly fabricated using an ion-beam-induced reaction technique in which a tungsten carbide (WC_x) was grown using $\text{W}(\text{CO})_6$. Namely, MIM diodes of WC_x/C system were fabricated and investigated. In addition to the electrical characterization, Raman scattering spectroscopy was also carried out and the optical investigation of the carbon microfilm was supplemented in advance.

6.2 Characterization of Carbon Microfilm

6.2.1 Deposition of carbon microfilm

Carbonaceous films such as diamond-like amorphous carbon (DLC) films have been deposited by many researchers using chemical vapor deposition [9-11], sputtering [12-14] or ion-beam deposition [15-17] mainly for its applications to the coating material for magnetic media or for reactive surfaces. That is because the DLC film has low friction characteristics, high wear resistance, optical transparency, chemical inertness and high electrical resistivity [18, 19]. By using these general techniques, carbon film is deposited on an entire substrate. Therefore, additional processes are required in case of fabricating and defining a small device. While by using the EBID technique, a square-shaped carbonaceous film can be grown at an arbitrary position by two dimensional electron-beam scanning. This is a great advantage for fabricating nanometer-size devices. Although this technique is not suitable for large area deposition, it is quite effective if applied to the small discrete devices where the film is necessary in small area, as it does not require the lithography or lift-off techniques to define each device. Therefore the fabrication of microfilm by this method is necessary for establishing the direct fabrication of discrete devices.

The carbon deposition was carried out in a surface analysis mode of SEM which is a two-dimensional electron-beam scanning mode. Detail deposition conditions are almost the same with the case of the fabrication of carbon nanowire which is described in Chapter 3. The growth rate mainly depends on the lateral size of scanning area and it is about 0.5 nm/min in a size of 5 μm square and the electron dose was about 5 $\text{nC}/\mu\text{m}^2$ at that time, which made a 30 nm thick carbonaceous film.

Figures 6.2.1(a) and (b) show the SEM and AFM images of the surface of the carbonaceous film deposited on a Si substrate. In the SEM image in Fig. 6.2.1(a), each corner of the film has round shaped structure. They are originally the markers grown in conic shapes in advance of the film growth. We can see from the figures that the surface is smooth with the roughness being less than about 2 nm. Although the surface morphology shows some stripes due to the scanning beam deposition, no pinholes were observed. Therefore, it could be applicable to the device having stacked structure. Since this film was deposited in

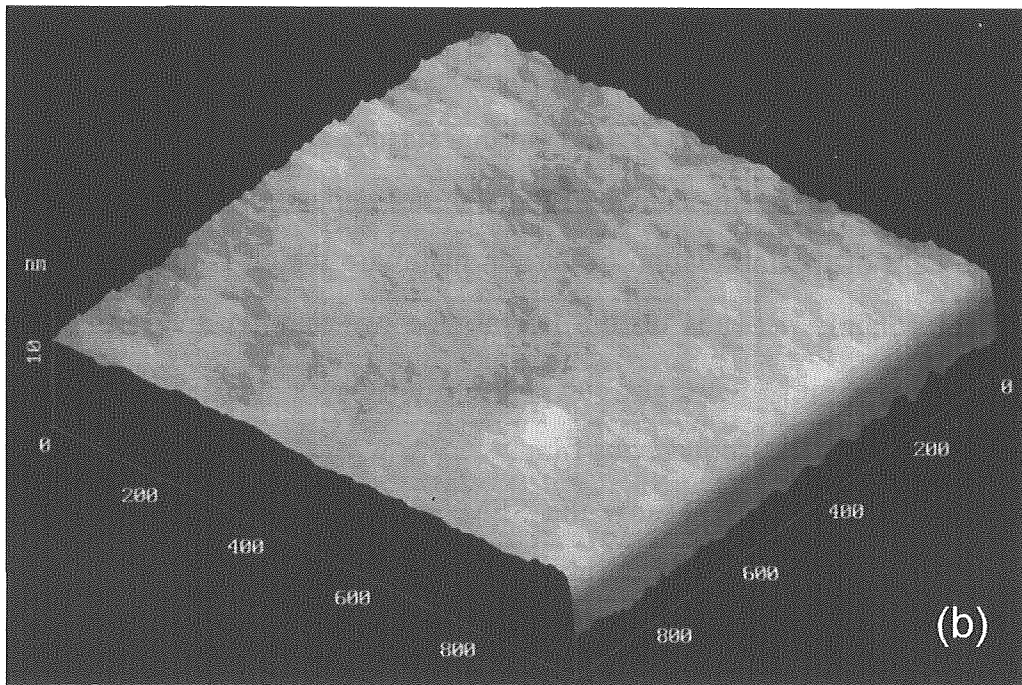
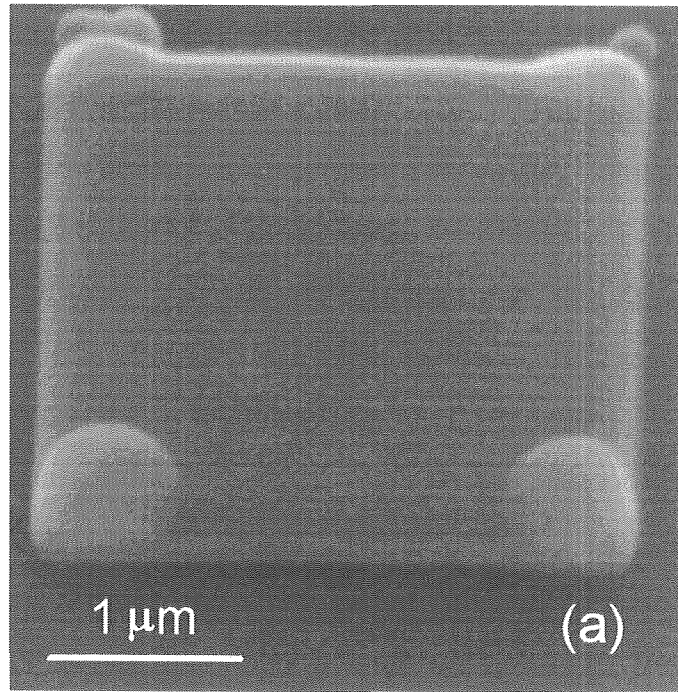


Fig. 6.2.1 SEM (a) and AFM (b) images of the surface of the carbonaceous microfilm.

the electron-beam conditions optimized for obtaining narrow carbon wires, the radius of the beam was thought to be small, which is more likely to make a stripe on a film surface especially in a large area deposition. To obtain a film with less stripe structure on the surface, deposition with a fat electron-beam might be considered.

6.2.2 Raman spectroscopy

To characterize the structure of this carbon film, a Raman scattering spectroscopy measurement was performed. The spectrum was obtained in a backscattering configuration with the Ar⁺ 514.5 nm line at room temperature and recorded with a Jobin Yvon Ramanor U-1000 double grating monochromator equipped with a photonmultiplier and photon-counting electronics. Since the carbon film could not be deposited in a large area and the growth rate is not high, the film was prepared in a 3 μm square with about 200 nm in thickness, and the spectrum was taken with the Ar⁺ laser whose diameter was 3 μm. To measure the Raman spectrum, we first used a beam diameter of about 1 μm spotted onto a much smaller film, however, the irradiated area was completely etched possibly because of the evaporation or oxidation by air with the aid of the local heating effect. Therefore, the laser power density and the film size were optimized to obtain the Raman spectrum. The result is shown in Fig. 6.2.2. Two broad peaks centered around 1350 cm⁻¹ and 1550 cm⁻¹ are seen. The data were fit by two peaks with Gaussian line shapes and it was divided into the peaks around 1320 cm⁻¹ and 1570 cm⁻¹. The 1350 cm⁻¹ band is called the disorder band (D-band) and is assigned to the A_{1g}-type mode at the K point of the Brillouin zone activated by the disorder [20]. Another 1580 cm⁻¹ band is called the graphite band (G-band) and corresponds to one of the E_{2g} modes, which has been assigned to the vibrational mode corresponding to the movement in opposite directions of two neighboring carbon atoms in a graphite sheet [21, 22]. Judging from the obtained Raman spectrum and the Gaussian fittings, the carbonaceous film grown by EBID from residual hydrocarbon molecules is considered to consist of a mixture of tetrahedrally (sp³) and trigonally (sp²) bonded carbon as these features are distinctive profiles of a hydrogenated amorphous carbon (a-C:H) or a DLC [11,

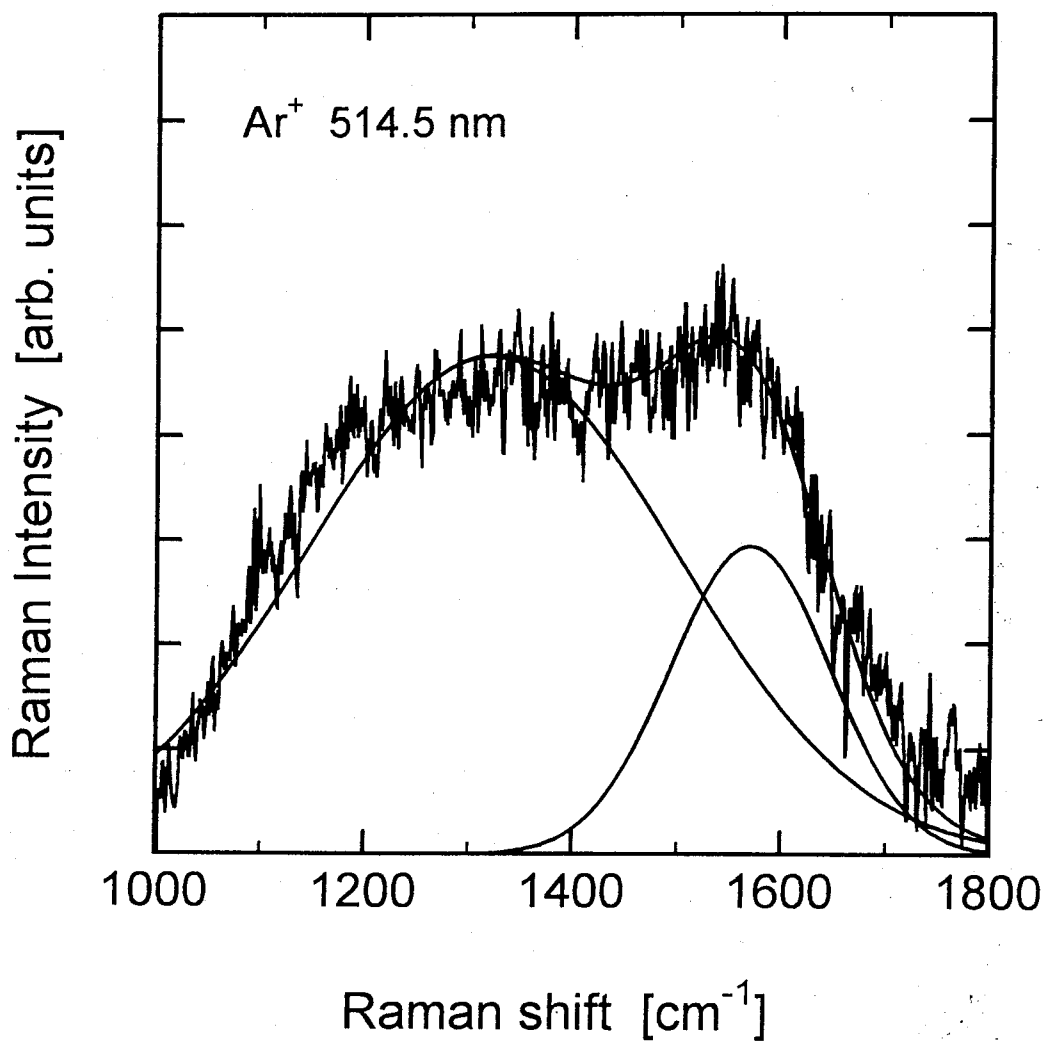


Fig. 6.2.2 Raman spectrum from the carbon microfilm.

12, 23]. Accordingly, this carbon film is determined to have an amorphous structure mainly consisting of carbon.

6.2.3 AFM nano-oxidation of carbonaceous film

As the film deposited by the EBID using SEM had been regarded as being carbonaceous material and it was confirmed to have an amorphous structure consisting of carbon, another characterization of this film was performed by AFM nano-oxidation method. As this process was described in Chapter 5, it is one of the successful nanostructure fabrication techniques ever established for realization of single-electron transistors [24]. So far, a metal or a semiconductor thin film was modified to produce nanoscopic oxidized wires and this process was considered anodization [25, 26]. In this study, our carbonaceous film was processed by this method.

The AFM image in Fig. 6.2.3 shows the surface of the film after the AFM nano-oxidation was processed. As was expected, the film exhibits a ditch with a depth of about 20 nm along the line scanned by the AFM cantilever. This structure suggests that the oxidation occurred but not leaving an oxidized wire, as the main consisting element of carbon was resulted to react with ambient water or oxygen-containing species adsorbed on the film and made a carbon oxide (CO_x) gases. Namely, this complementary result with the case of metal oxide reveals the incorporation of carbon, hydrogen, sulfur or nitrogen atoms, whose oxides are in gas phase at room temperature, in the film deposited from the precursors of the residual molecules in the SEM chamber. Figure 6.2.3 gives another important information that the ditch is not uniform. Considering both the metal oxide wire has uniform structure [25, 26] and this process is driven by electrochemical reaction between the substrate and a negatively biased AFM tip, this ununiformity suggests that the electrical resistivity of this carbonaceous film is high resulting that the anodization current could not flow smoothly and reaction occurs explosively at the pass where the resistivity is relatively low such as grain boundary. One point could be supplemented that the anodization voltage was about 10 times larger than the case of modification of metal thin film. This also suggests the carbonaceous film having high resistivity.

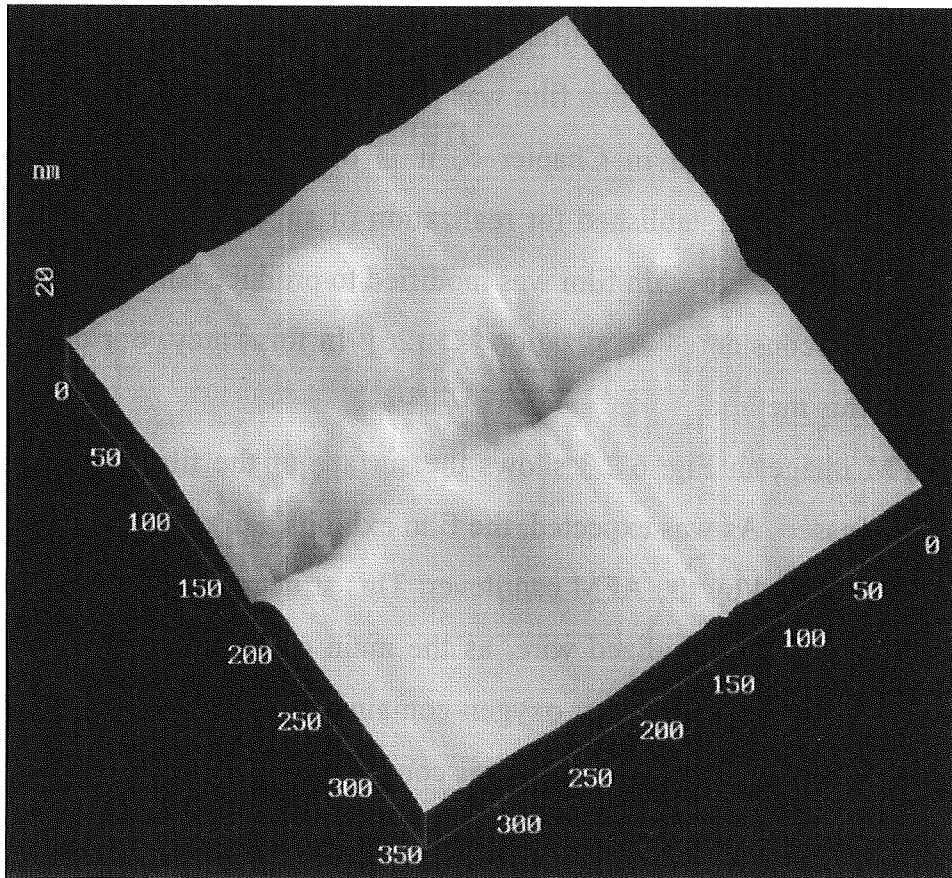


Fig. 6.2.3 AFM image of the surface of the carbonaceous microfilm after the AFM nano-oxidation was performed.

6.3 Metal / Insulator / Metal Diode of Au / a-C System

6.3.1 Metal / insulator / metal junction

Electrical properties of this amorphous carbon film was extensively evaluated next. From the previous study, it was quite difficult to measure the electrical resistance from an amorphous carbon wire by the four-point-probe method as the carbon was almost an insulator. Therefore, its evaluation was performed with the carbon microfilm sandwiched between metals, which formed a metal/insulator/metal (MIM) diode structure, to lower the measuring resistance.

Electrical characterization in the form of the MIM diode is one of the skillful ways if considering its application to the microscopic tunneling devices. As will be discussed later, it gives information on various electrical properties of each consisting system. In this study, the carbonaceous film was stacked between metals and it was expected to work as an insulator since it had exhibited insulating properties from the preliminary measurements and since fabrication of metal/insulator/semiconductor (MIS) diode using carbon film grown by other methods has ever been reported by other group [27]. Through this investigation, the a-C applicability to the device consisting material would be recognized. Because this film was preferable to be deposited in very small area, it could be expected to be employed to the insulating thin film in the minute MIS transistors or the potential barrier in the tunneling devices much more in the single-electron transistors (SETs).

6.3.2 Fabrication process

Fabrication of the MIM diode was carried out as follows and its process flow is illustrated in Fig. 6.3.1. Thermally oxidized Si was used as a substrate. Although the SiO₂ is an insulator, it was thin enough to be processed by SEM. Therefore, the deposition was not affected by electron charge up. First, a Au base electrode was fabricated using the evaporation and the lift-off techniques. To prevent the electrical shortage at unintentional edge of the electrode residue, double resist system using spin-on glass (SOG) was employed to form a stencil structure. Then the carbonaceous film was deposited over the base electrode

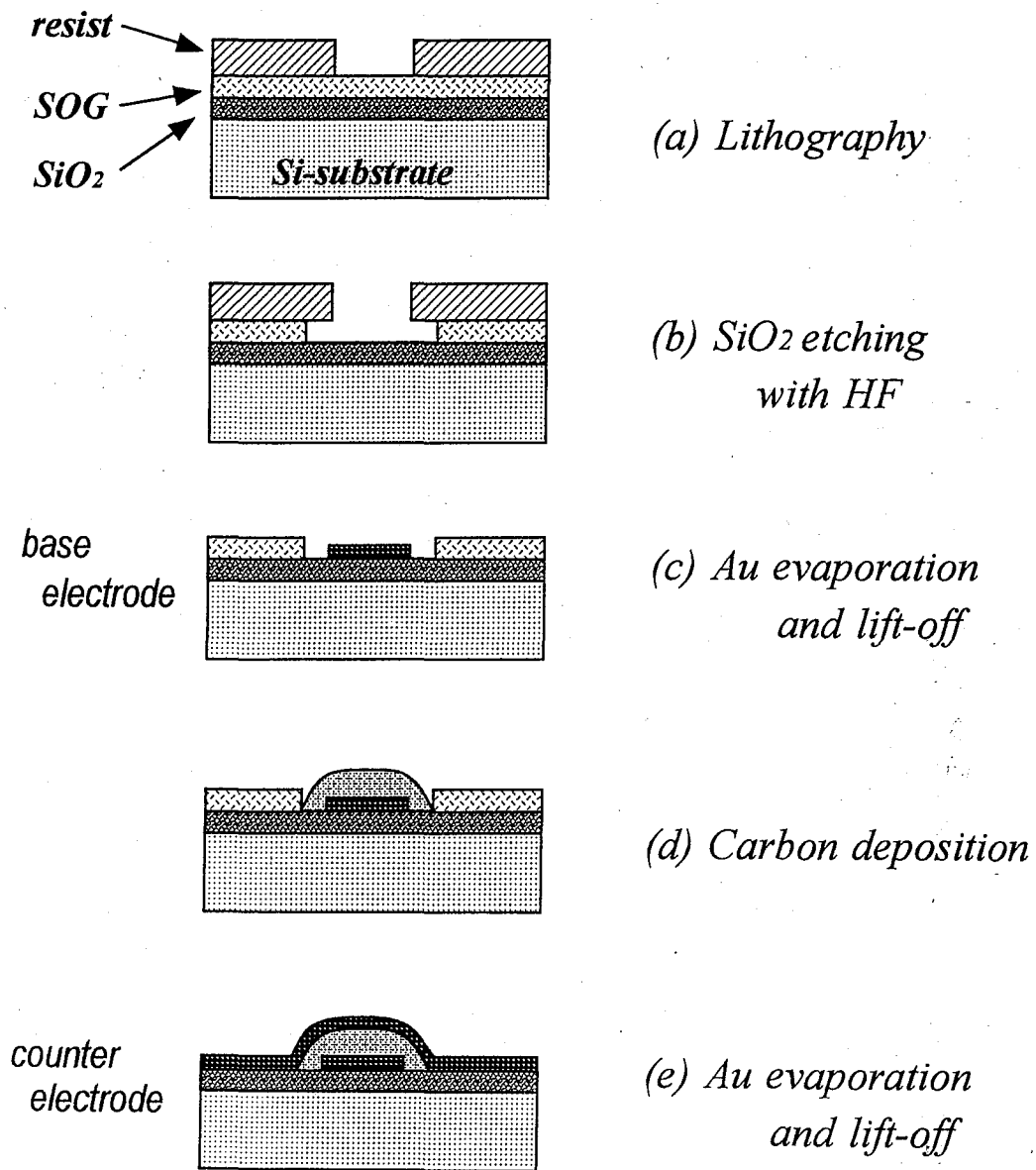


Fig. 6.3.1 Fabrication process for MIM diode of Au / a-C system.

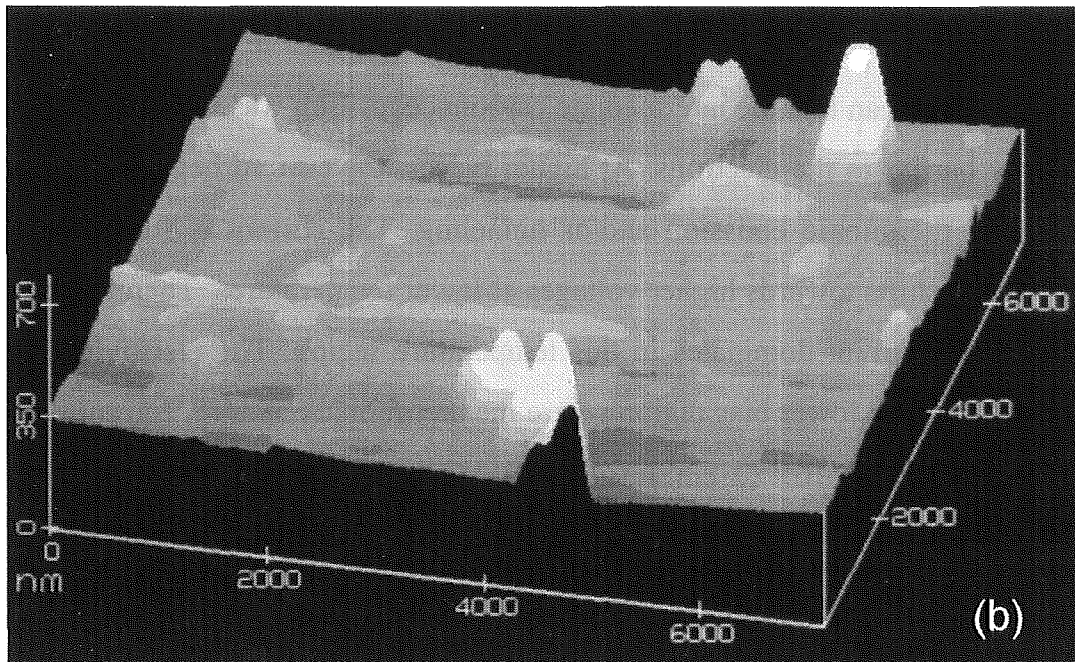
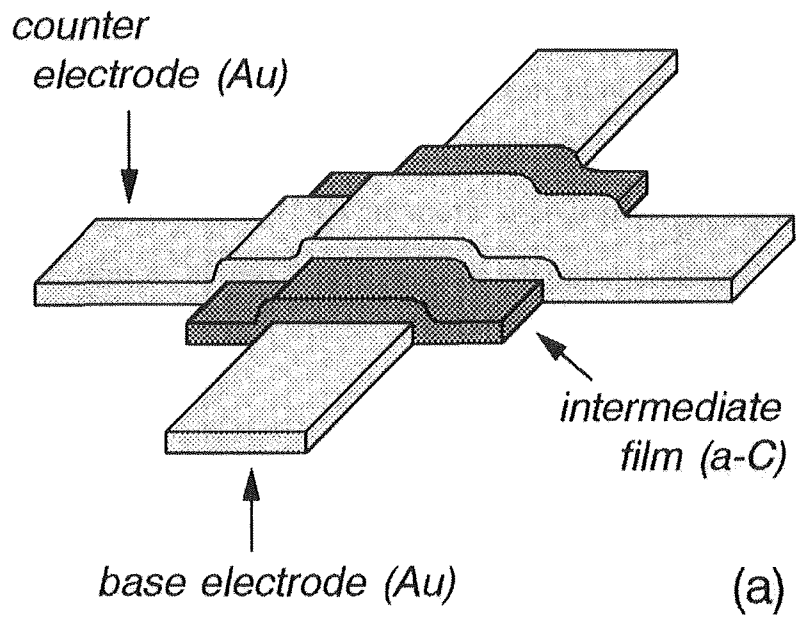


Fig. 6.3.2 Schematic (a) and AFM image (b) of the MIM diode of Au / a-C system. Junction size is about 3 μm square.

in the junction region by SEM. Finally, a counter (top) electrode was evaporated and patterned similar to the base electrode after the removal of SOG layer. A schematic and an AFM image of the device are shown in Figs. 6.3.2(a) and (b), respectively. The smooth edge profile of the base electrode indicates that no electrical short path exists between the base and counter electrodes, whereas the edge of the counter electrode is a little rough since the edge treatment was not performed on it. From the AFM image, thickness of the carbonaceous film was measured to be 30 nm and the junction size $3 \mu\text{m} \times 3 \mu\text{m}$.

6.3.3 Electrical characteristics

MIM diodes of Au/a-C system were fabricated with various thickness of the intermediate a-C film. The current-voltage characteristics were measured at 300 K and 175 K and Figs. 6.3.3(a) and (b) show their results of the a-C thickness of 30 nm and 60 nm, respectively. The I - V curves show non-linear characteristics and the current is suppressed in the low bias region. Comparing two cases, the current is smaller in the diode of thicker a-C film. These results mean that the intermediate carbonaceous film was working as an insulator and an energy barrier to the electrons. At higher biases, the current begins to flow through the film due to thermionic emission and/or tunneling. The current is suppressed and the threshold voltage shifts towards higher voltages at lower temperatures. Therefore, it is found that the tunneling current dominates in this temperature region. The resistivity of the film was estimated from the lower bias region where the thermionic emission current is negligible and it was on the order of $10^{11} \Omega \cdot \text{cm}$. It is consistent with the reported values on the a-C film [28-30].

In order to further investigate the electrical results, theoretical fitting to the data of the temperature dependence of the I - V curve was next considered to estimate a relative dielectric constant of this a-C film. The current flowing through this MIM diode was considered to be the sum of the thermionic emission current (J_{TH}) and the Fowler Nordheim tunneling current (J_{FN}). They are expressed in following equations,

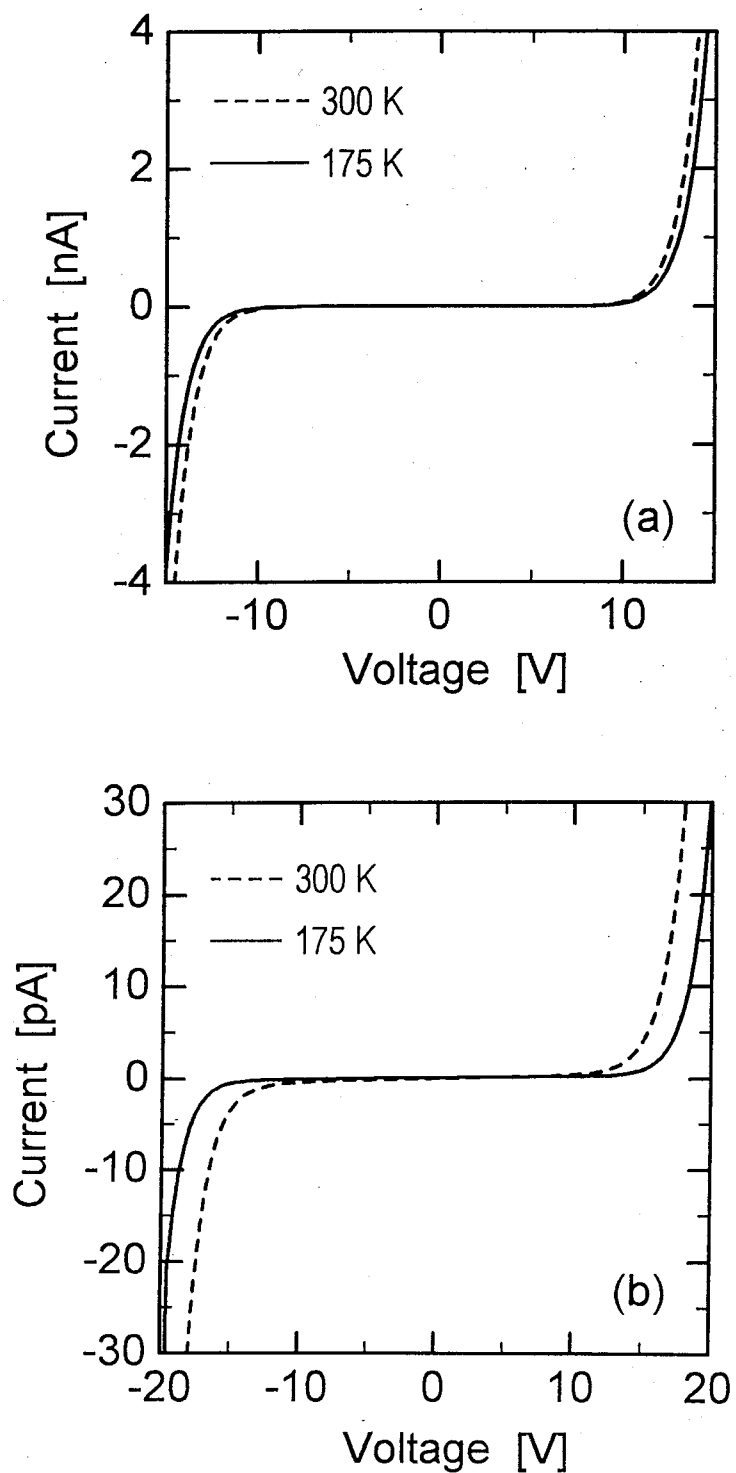


Fig. 6.3.3 $I-V$ curves of the MIM diode of Au / a-C system. Thickness of the intermediate carbon films are (a) 30 nm and (b) 60 nm.

$$J_{TH} = -AT^2 \exp\left(-\frac{q\Phi_B}{kT}\right) \quad (6-1)$$

$$J_{FN} = AE^2 \exp\left(-\frac{8\pi\sqrt{2m^*m_0}(q\Phi_B)^3}{3qhE}\right) \quad (6-2)$$

where k is the Boltzman constant, m^* is an effective mass of an electron, E is an applied electric field and T is the temperature. In these equations, Φ_B indicates an effective potential barrier height subtracting an effect of the image force from an intrinsic barrier height (Φ_{B0}) expressed as,

$$\Phi_B = \Phi_{B0} - \sqrt{\frac{qE}{4\pi\epsilon_r\epsilon_0}} \quad (6-3)$$

where ϵ_r represents a relative dielectric constant.

From these equations, we can see that only the J_{TH} depends on the temperature. Therefore, the increment of the current on temperature could be assumed to be due to the thermally induced electrons, and they were fitted to the experimental data from the I - V curves at 300 K and 175 K. In this calculation, only the relative dielectric constant becomes variable and the result is shown in Fig. 6.3.4. The calculation performed on the 30 nm thick a-C film diode revealed that ϵ_r of 4.8 led to the closest fit to the data. It is generally recognized that the dielectric constant of a diamond is around 5.5, and that of diamond-like carbon is quite dependent on the hydrogen concentration in the film. Consequently, our result is considered to be in accordance with the accepted value.

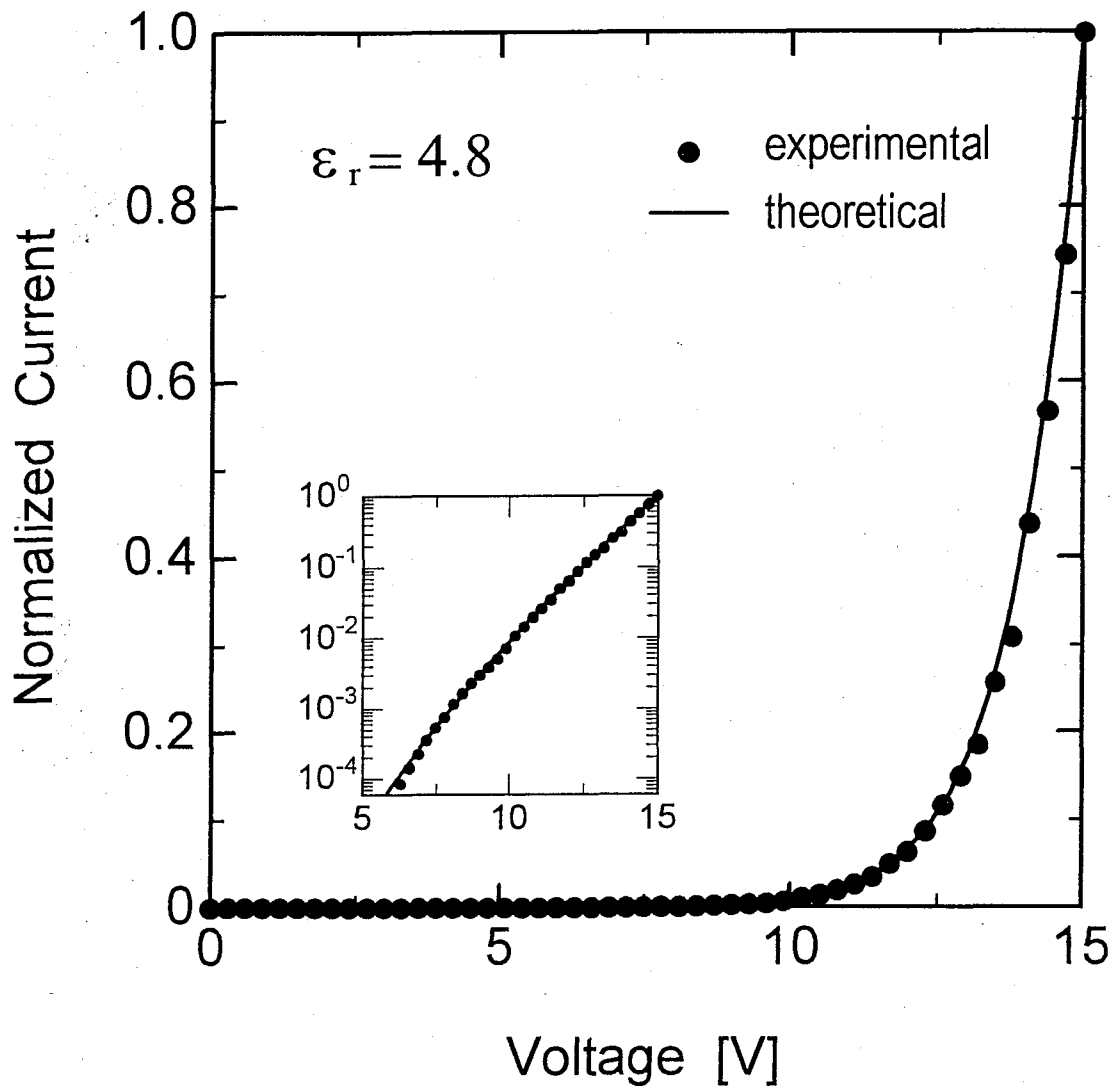


Fig. 6.3.4 Contribution of thermoionic emission current on the MIM diode of Au / a-C system. The inset shows the same curve with a logarithmic vertical axis. The current is normalized with the value at 15 V.

6.4 MIM Diode of WC_x / a-C System

6.4.1 Fabrication process

This technique of depositing carbon film by SEM is effective when used in a situation where microscopic dimensions are required, because the growth mechanism is based on the electron-beam-induced reaction. Therefore, it is more advantageous if employed to a smaller MIM diode. However, there is a certain limit in the conventional photolithography for patterning the metal electrodes from a point of the accuracy in the alignment and drastic shrinkage of the device. Accordingly, a technique to obtain WC_x as a metal electrode was employed, which is grown by a similar beam-induced reaction process. In this study, to avoid a modification of the SEM by introducing some metalorganic gases the metal was prepared by using a focused-ion-beam (FIB) system, in which the ion source is elemental gallium, with an ion-beam-induced deposition technique. Namely, the insulating amorphous carbon was grown by the electron-beam and the metallic WC_x by the ion-beam so as to fabricate a stacked MIM junction. Since both depositions are performed by focused beam scanning, it is considered to be extremely effective for the direct fabrication of microscopic devices in the size ranging from 10 nm to a few 100 nm.

The WC_x was deposited from W(CO)₆ as being a precursor. The deposition conditions are summarized in Table 6.4.1. For the comparison, those of the electron-beam were also added in the table. This technique has been widely studied for application to device process or to mask repair [31-36]. In this study, it was employed to fabricate the upper and lower electrodes of the MIM diode. The process flow is described as follows and illustrated in Fig. 6.4.1. First, Au contact pads and electrodes were patterned on a thermally oxidized silicon substrate by the evaporation of gold and the lift-off techniques, which is similar to the previous case of Au/a-C/Au diodes. They had a gap between the electrodes and the length was about 5 μm. The WC_x wire was deposited from one side of the edge of Au electrode (source electrode) to the junction area by FIB. The length, width and height of the wire were about 3 μm, 230 nm and 100 nm, respectively. To obtain good electrical contact between the WC_x wire and the Au electrode, the WC_x was squarely deposited in the contact region in a 1 μm square. The amorphous carbon film grown by SEM then covered the other

end of the wire. Finally, the upper WCx wire was deposited, bridging to the other edge of the Au electrode (drain electrode). Its AFM image is shown in Fig. 6.4.2. In this device, the upper and lower electrodes did not completely overlap to prevent the electrical shortage or the leakage of current between the two WCx electrodes, which might be caused by the dose of elemental Ga absorbed into the amorphous carbon film during the deposition of the upper electrode using FIB. The junction size was about 150 nm square.

Table 6.4.1. Deposition conditions of a-carbon and WCx using SEM and FIB, respectively.

Material	Carbon	WCx
Equipment	SEM (Hitachi S-800)	FIB (Micrion JFIB-2100)
Beam Source	electron	Ga ⁺
Beam Spot Size	2 nm	11 nm
Precursor	pump oil	W(CO) ₆
Pressure	1~3 × 10 ⁻⁶ Pa	2 × 10 ⁻³ Pa
Acceleration Voltage	30 kV	30 kV
Beam Current	35 pA	4.2 pA
Electron (Ion) Dose	5 nC/μm ²	2 nC/μm ²
Working Distance	15 mm	25 mm

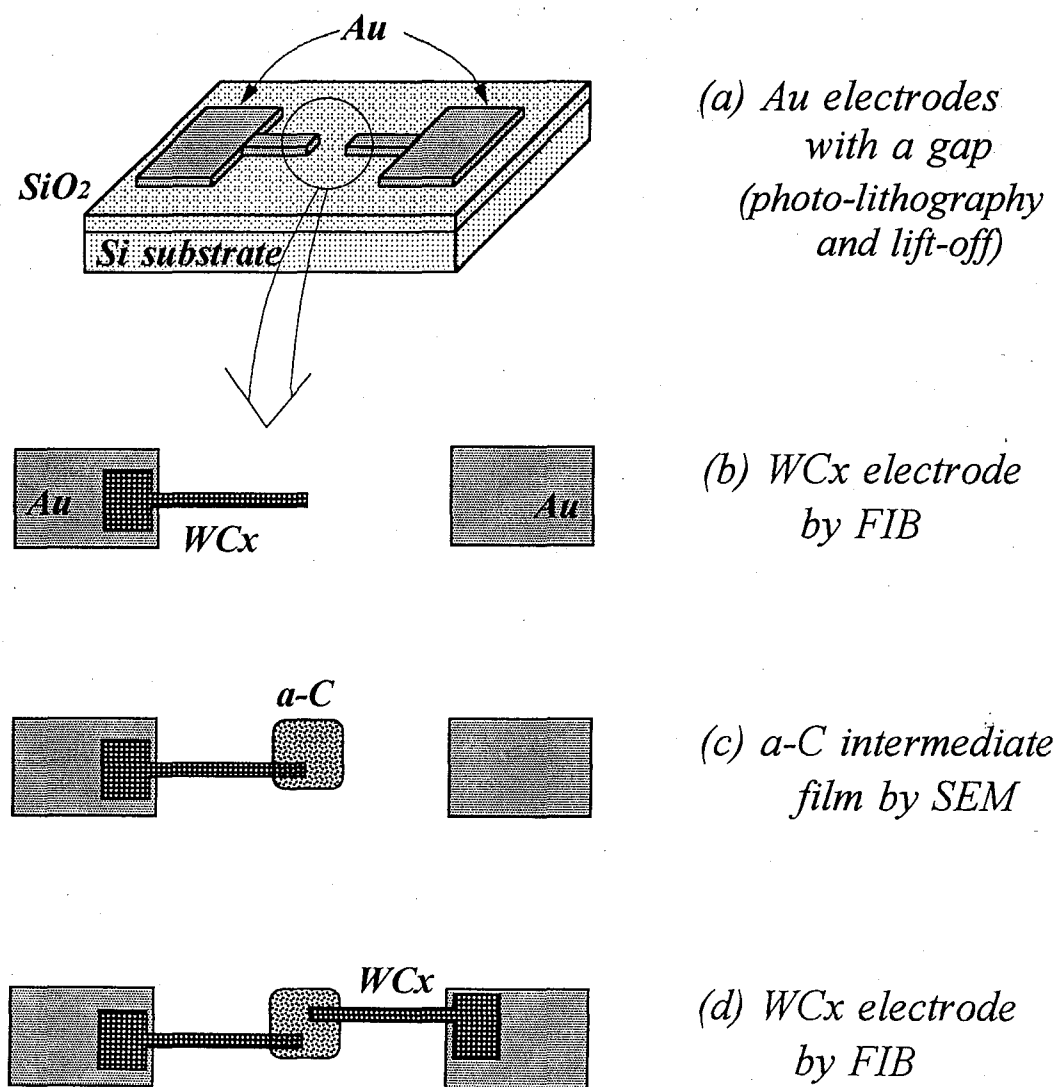


Fig. 6.4.1 Fabrication process for WCx / a-C stacked junction.

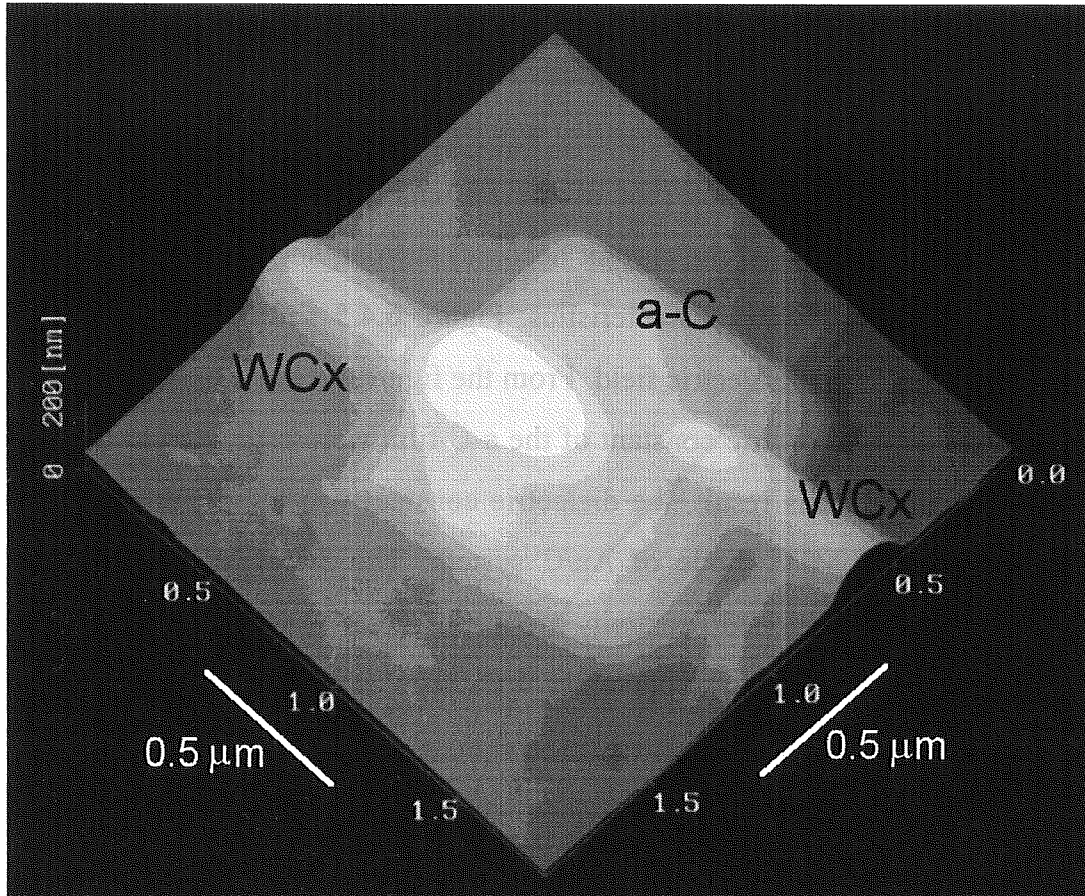


Fig. 6.4.2 AFM image of the MIM diode of WCx / a-C system. Junction size is about 150 nm square.

6.4.2 Electrical characteristics

The I - V characteristics of the MIM diode of WCx/a-C system at 74 K and 290 K are shown in Fig. 6.4.3. Similar to the Au/C system, clear nonlinearity was observed, indicating that the amorphous carbon film was working as an insulator and a potential barrier to the electron. The resistivity of this film was estimated from the low bias region at about $10^7 \Omega \cdot \text{cm}$ at 74 K. This value is three to four orders of magnitude smaller than the one obtained from the Au/a-C/Au diodes. This discrepancy will be discussed later.

In Fig. 6.4.4, an arrhenius plot of the I - V characteristic is shown. In the higher temperature region, the slope of the current becomes steeper, suggesting that the thermionic emission current dominates the characteristics. Figure 6.4.5 shows the dependence of the effective barrier height on the electric field. From the figure, an intrinsic barrier height in this system and the relative dielectric constant of the a-C film were estimated to be 0.19 eV and 12, respectively. Due to this result, the dielectric constant was almost double compared to that obtained from the MIM diode of Au/C system. The discrepancies of the dielectric constant and formerly-mentioned resistivity are attributed to the Ga^+ bombardment into the carbon film during the deposition of the upper WCx wire. Since the acceleration voltage was as high as 30 kV, it could be considered that the dose of the elemental Ga into the carbon film around the junction area led to the increment of ϵ_r , and its existence inside the film increased the leakage current, causing the estimated resistivity to be smaller. This influence of Ga^+ is inevitable in the ion-beam reaction process but not in the electron-beam. However, the high resistivity of the insulating amorphous carbon and enough height of Φ_{B0} remained in the MIM diode. By an optimization of the device structure and a further reduction of its size, realization of the microscopic tunneling device of the WCx/a-C system fabricated with a beam-induced process could be expected.

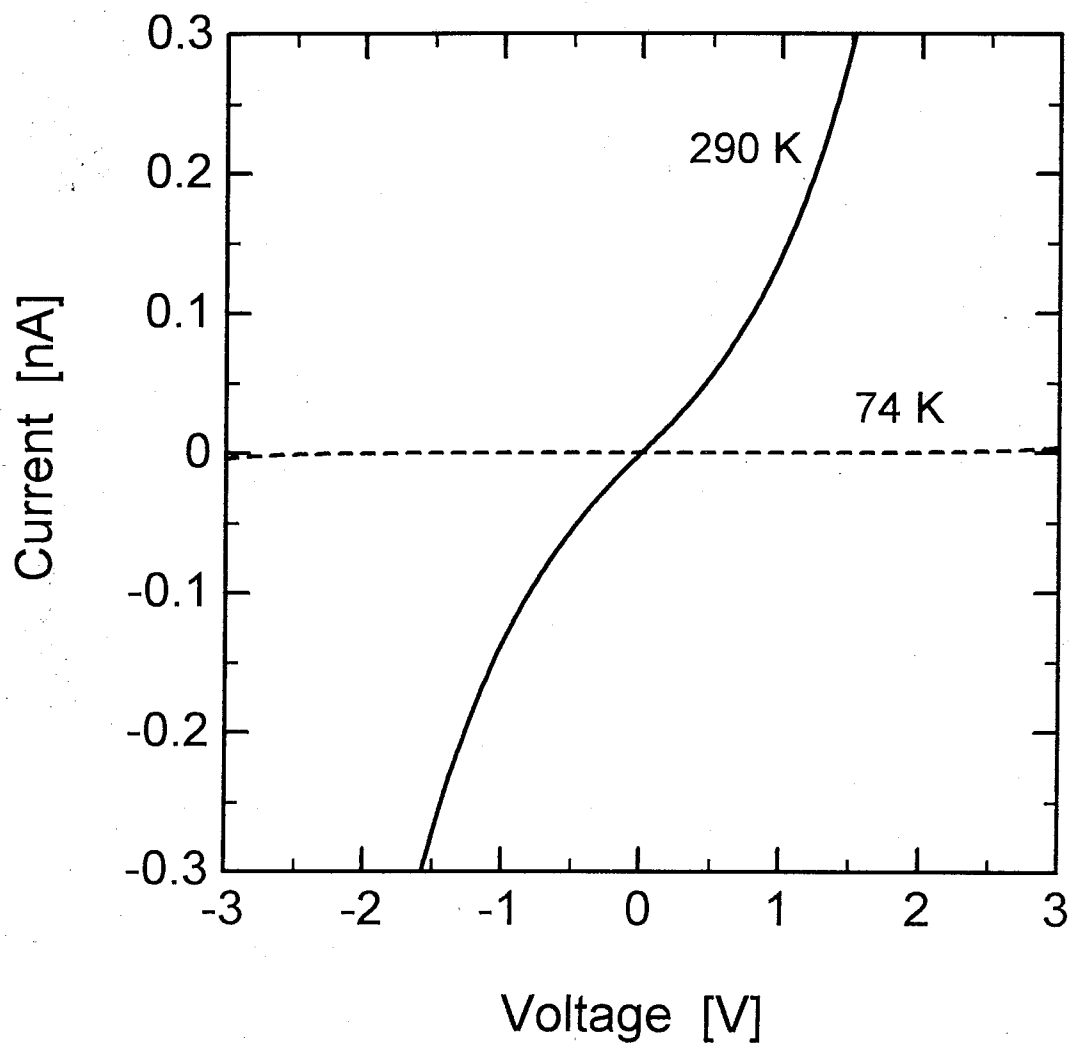


Fig. 6.4.3 *I-V* curve of the MIM diode of WC_x / a-C system.

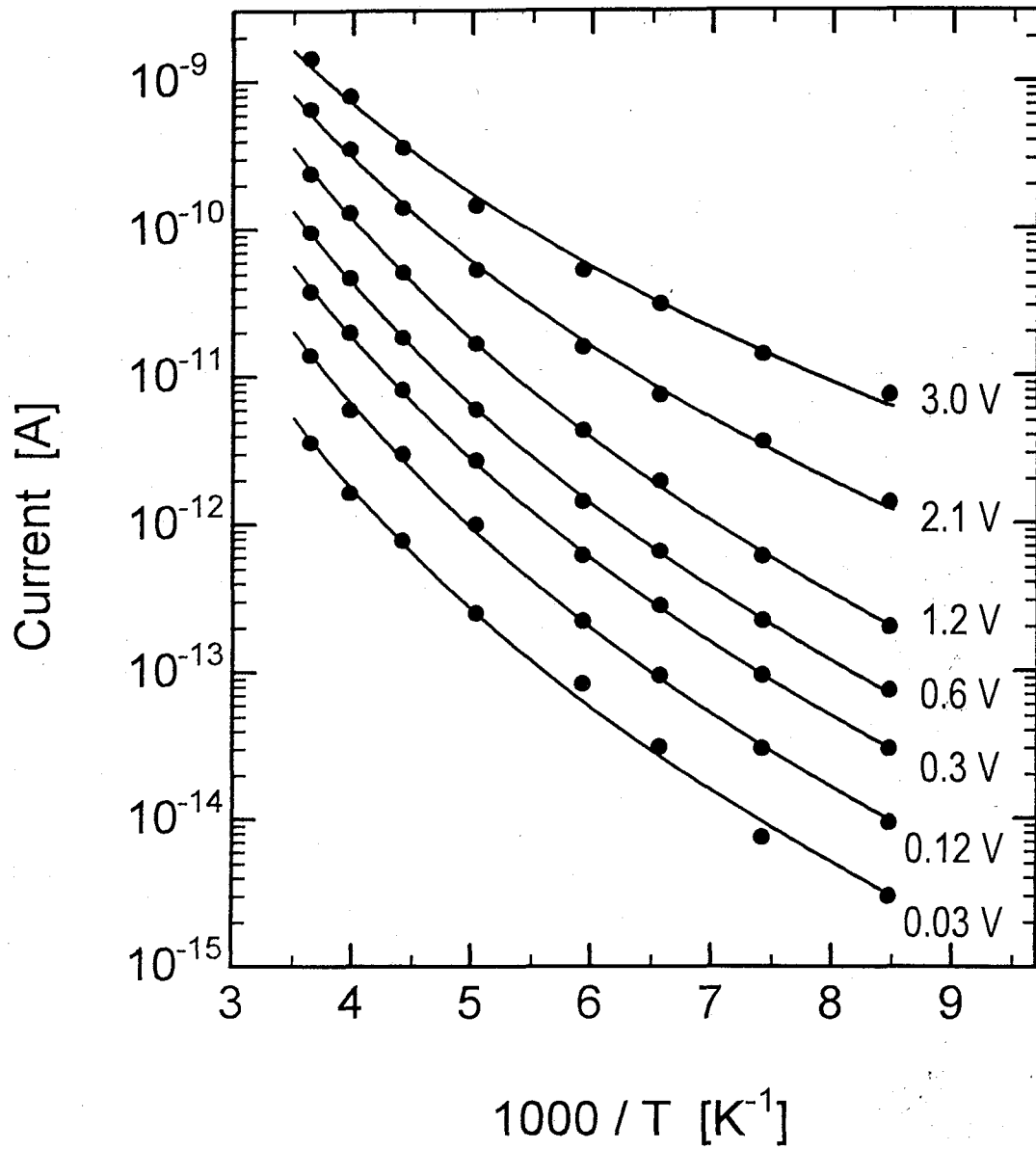


Fig. 6.4.4 Temperature dependence of the I - V curve of the $WC_x/a-C$ diode. Monitored bias voltage is from 0.03 V to 3.0 V.

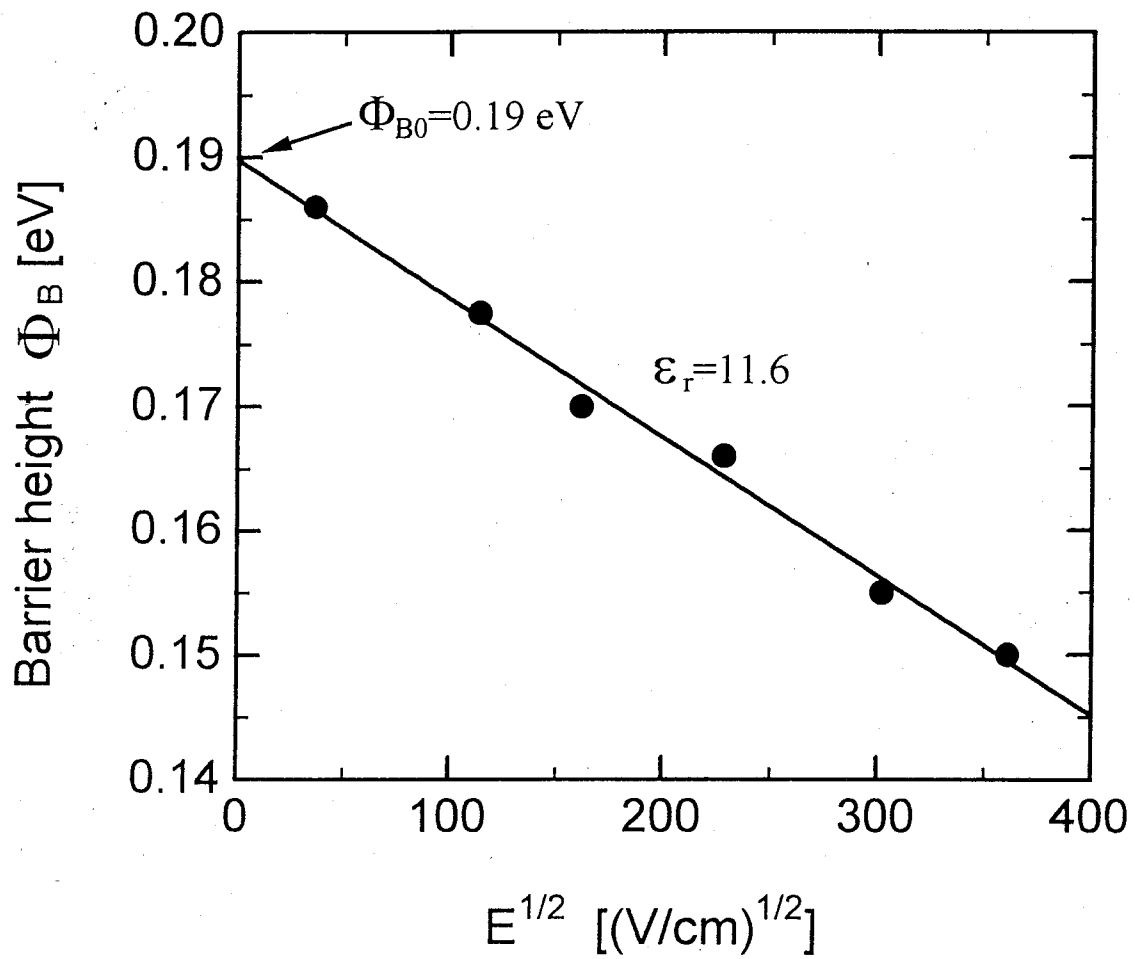


Fig. 6.4.5 Dependence of the barrier height on the applied electric field.

6.5 Summary

In this chapter, evaluation and characterization of the carbon microfilm deposited by the EBID technique using SEM were extensively performed. In particular, its optical as well as the electrical properties were characterized and it was applied to the intermediate layer of the MIM diodes. From Raman scattering spectroscopy, distinctive peaks of diamond-like carbon were observed, indicating an amorphous structure in the film. The result from the AFM nano-oxidation process also supports the fact that the film consists of carbon. Moreover, the fabrication of the MIM diodes was carried out using Au and WC_x as metal electrodes and a-C as an intermediate layer. Nonlinear I - V characteristics were obtained from both devices indicating the a-C layer working as a potential barrier to the electron. Temperature dependence of the I - V curve from the Au/a-C/Au diode was theoretically studied and the dielectric constant of the a-C was estimated at approximately 5 and this value is consistent with the reported one. Furthermore, the tungsten carbide was used in the metal electrode in the MIM diode fabricated by the ion-beam-induced deposition technique for the application to the nanostructure devices. The intrinsic barrier height in the WC_x / a-C system was estimated at 0.19 eV.

References

- [1] Y. Nakamura, C. D. Chen and J. S. Thai: *Jpn. J. Appl. Phys.* **35** (1996) L1465.
- [2] Y. Takahashi, H. Namatsu, K. Kurihara, K. Iwadate, M. Nagase and K. Murase: *IEEE Trans. Electron Device* **43** (1996) 1213.
- [3] T. Wada, M. Hirayama, S. Haraichi, K. Ishii, H. Hiroshima and M. Komuro: *Jpn. J. Appl. Phys.* **34** (1995) 6961.
- [4] J. Taniguchi, I. Miyamoto, N. Ohno and S. Honda: *Jpn. J. Appl. Phys.* **35** (1996) 6574.
- [5] S. Matsui and K. Mori: *Appl. Phys. Lett.* **51** (1987) 1498.
- [6] K. L. Lee and M. Hatzakis: *J. Vac. Sci. Technol. B* **7** (1989) 1941.
- [7] K. T. K. Platen, L. M. Buchmann, H. C. Petzold and W. H. Brunger: *J. Vac. Sci. Technol. B* **10** (1992) 2690.
- [8] Y. Ochiai, H. Watanabe, J. Fujita, M. Baba, S. Manako and S. Matsui: *Jpn. J. Appl. Phys.* **32** (1993) 6147.
- [9] F. K. King: *IEEE Trans. Magn.* **MAG-17** (1981) 1376.
- [10] M. Ramsteiner, J. Wagner, C. Wildand and P. Koidl: *J. Appl. Phys.* **62** (1987) 729.
- [11] D. S. Knight and W. B. White: *J. Mater. Res.* **4** (1989) 385.
- [12] M. Yoshikawa, G. Katagiri, H. Ishida, A. Ishitani and T. Akamatsu: *J. Appl. Phys.* **64** (1988) 6464.
- [13] M. A. Tamor and W. C. Vassell: *J. Appl. Phys.* **76** (1994) 3823.
- [14] T. J. Knno and R. Sinclair: *Acta Metall. Mater.* **43** (1995) 471.
- [15] E. G. Spencer, P. H. Schmit, D. H. Joy and F. J. Sansalone: *Appl. Phys. Lett.* **29** (1976) 118.
- [16] J. J. Moravec and T. W. Orent: *J. Vac. Sci. Technol.* **18** (1981) 226.
- [17] M. Yoshikawa, N. Nagai, M. Matsui, H. Fukuda, G. Katagiri, H. Ishida, A. Ishitani and I. Nagai: *Phys. Rev. B* **46** (1992) 7169.
- [18] S. Agarwal and E. Li: *IEEE Trans. Magn.* **29** (1993) 264.
- [19] H. Tsai and D. B. Bogy: *J. Vac. Sci. Technol. A* **5** (1987) 3287.

- [20] F. Tuinstra and J. L. Koenig: *J. Chem. Phys.* **53** (1970) 1126.
- [21] A. F. Hebard, J. M. Rosseinsky, R. C. Haddon, D. W. Murphy, S. H. Glarum, T. T. M. Plastre, A. P. Ramirez and A. R. Kortan: *Nature* **360** (1991) 600.
- [22] Z. Zhang, C. C. Chen, S. P. Kelty, H. Dai and C. M. Lieber: *Nature* **353** (1991) 333.
- [23] N. H. Cho, K. M. Krishnan, D. K. Veirs, M. D. Rubin, C. B. Hopper, B. Bhushan and I. B. Bogy: *J. Mater. Res.* **5** (1990) 2543.
- [24] J. Shirakashi, K. Matsumoto, N. Miura and M. Konagai: *Ext. Abstr. Int. Conf. Solid State Devices and Materials (1997)*, pp. 490.
- [25] K. Matsumoto, S. Takahashi, M. Ishii, M. Hoshi, A. Kurokawa, S. Ochimura and A. Ando: *Jpn. J. Appl. Phys.* **34** (1995) 1387.
- [26] J. Shirakashi, M. Ishii, K. Matsumoto, N. Miura and M. Konagai: *Jpn. J. Appl. Phys.* **3** (1996) L1524.
- [27] P. V. Koeppe, V. J. Kapoor, M. J. Mirtich, B. A. Banks and D. A. Gulino: *J. Vac. Sci. Technol. A* **3** (1985) 2327.
- [28] A. Bubenzer, B. Dischler, G. Brandt and P. Koidl: *J. Appl. Phys.* **54** (1983) 4590.
- [29] T. Mori and Y. Namba: *J. Vac. Sci. Technol. A* **1** (1983) 23.
- [30] C. Weissmantel, K. Bewilogua, K. Breuer, D. Dietrich, U. Ebersbach, H. J. Erier, B. Rau and G. Reisse: *Thin Solid Films* **96** (1982) 31.
- [31] P. G. Blauner, J. S. Ro, Y. Butt and J. Melngailis: *J. Vac. Sci. Technol. B* **7** (1989) 609.
- [32] Z. Xu, T. Kosugi, K. Gamo and S. Namba: *J. Vac. Sci. Technol. B* **7** (1989) 1959.
- [33] J. S. Hub, M. I. Shepard and J. Melngailis: *J. Vac. Sci. Technol. B* **9** (1991) 173.
- [34] M. J. Vasile, D. Grigg, J. E. Griffith, E. Fitzgerald and P. E. Russell: *J. Vac. Sci. Technol. B* **9** (1991) 3569.
- [35] J. Puzetz and L. W. Swanson: *J. Vac. Sci. Technol. B* **10** (1992) 2695.
- [36] Y. Gotoh, T. Ohtake, N. Fujita, K. Inoue, H. Tsuji and J. Ishikawa: *J. Vac. Sci. Technol. B* **13** (1995) 465.

Chapter 7

Single-Electron Transistors with Amorphous Carbon Nanostructures

7.1 Introduction

Progress in the field of the nanofabrication technology includes the active development of microdevices. In particular, great interest and expectations have been raised on single-electron transistors (SETs) as future electronic devices. An electrometer or a transistor of extremely low power dissipation are specific devices to be expected in SETs since they have an electrical sensitivity of less than one electron, and the controllability of a single charge, respectively. Fabrication processes for realizing single-electron tunneling devices include not only the conventional electron-beam lithography technique [1-6] but also the newly developed scanning probe microscope (SPM) [7-9] and beam-induced reaction processes [10, 11] as were presented in detail in Chapter 2. Moreover, various aspects of SETs are rapidly being investigated.

Among the studies concerning SET devices, this study has focused attention on the direct writing technique using the electron-beam-induced deposition (EBID) method. Direct processing without lithography is one of its notable advantages. In particular, by using a scanning electron microscope (SEM) system, amorphous carbon could be deposited at arbitrary place and in arbitrary structures with size on the order of 10 nm without any modification of the SEM as was discussed in detail through this dissertation.

In this chapter, this technique is applied to fabricate microscopic devices which mainly consist of amorphous carbon dots forming a one-dimensional array or a double junction with side-gated structure. They are arranged in series between fine tungsten carbide electrodes which are deposited by focused ion beam (FIB). Therefore, microscopic tunnel junctions are prepared by the beam-induced reaction processes, which are simple and unique techniques for the microfabrication. Use of carbon in a dot shape is concentrated in order to

realize a device with multiple or double capacitive junctions using air barrier. Its electrical properties are intensively characterized. Namely, the carbon dots are employed as conducting electrodes through which the tunnel current flows. As a result, single-electron charging effects were clearly observed at room temperature.

7.2 One-Dimensional a-Carbon Dot Arrays

7.2.1 *Multiple tunnel junction using amorphous carbon dots*

One of the skillful structures to observe single-electron charging effects is the multiple tunnel junction system whose effective tunnel junctions are well isolated from the harmful electromagnetic environment which strongly influences the charging properties of single tunnel junctions [12]. In this case, since each junction is disconnected by high resistive resistors, it is protected from the environment and the individual junctions can be quasi-current biased in a one-dimensional array, even though the array itself is voltage biased. Therefore, for the first step of the fabrication of the single-electron devices, some of the amorphous carbon dots are deposited and arranged in series which are due to the individual islands between the metal electrode. They are fabricated by SEM from the residual hydrocarbon molecules as a precursor, and this means that the ratio of sp^3 / sp^2 -bonded carbon incorporated in the film is not specially controlled. For the tunnel barrier, the air is used, which is considered appropriate to the device in terms of the simple process (any modification is required for barrier formation) and potential barrier height (the highest to any material). Since the air barrier is used, the environment during the measurement would affect the electrical characterization. Therefore the measurement is performed in vacuum.

7.2.2 *Fabrication process*

The tunneling devices were fabricated on a thermally oxidized silicon substrate (SiO_2/Si) through the process flow illustrated in Fig. 7.2.1. They consisted of Nb electrodes deposited by DC magnetron sputtering and patterned by the lift-off technique with an approximately 2 μm gap between source and drain electrodes. In order to prepare finer metallic leads for the electrodes, tungsten carbide (WC_x) wires were fabricated between the Nb electrodes by FIB using $W(CO)_6$ as a precursor. Its deposition conditions are the same as those described in previous chapter. These WC_x wires of 150 nm width were bridged to the junction area, leaving a 300~500 nm gap into which the a-C dots were filled. During the a-carbon deposition, the pressure in the SEM chamber was about $1\sim 4 \times 10^{-6}$ Pa and the

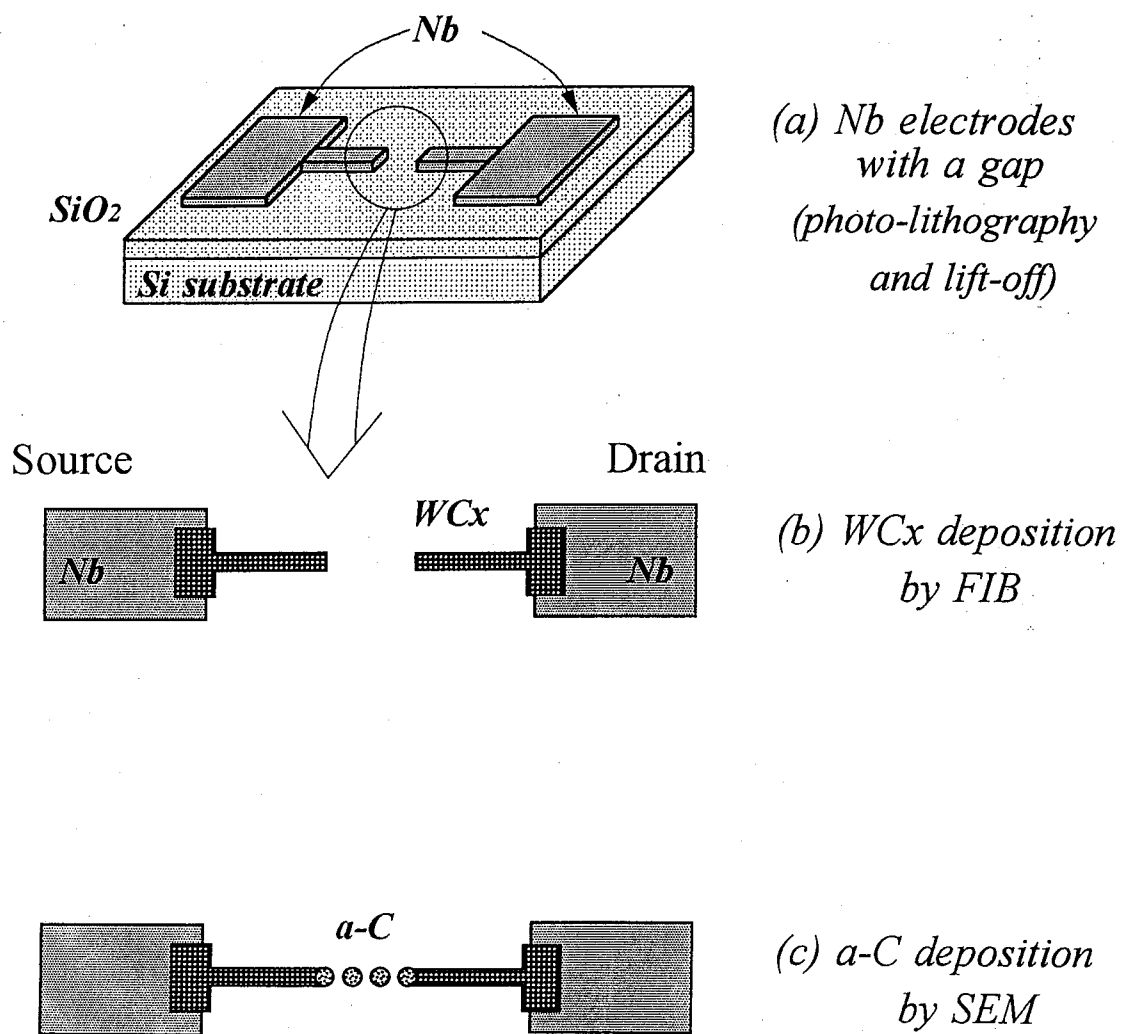


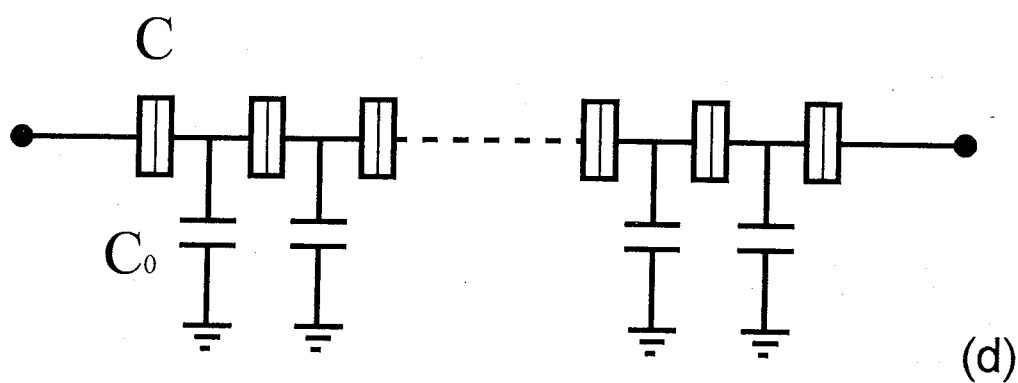
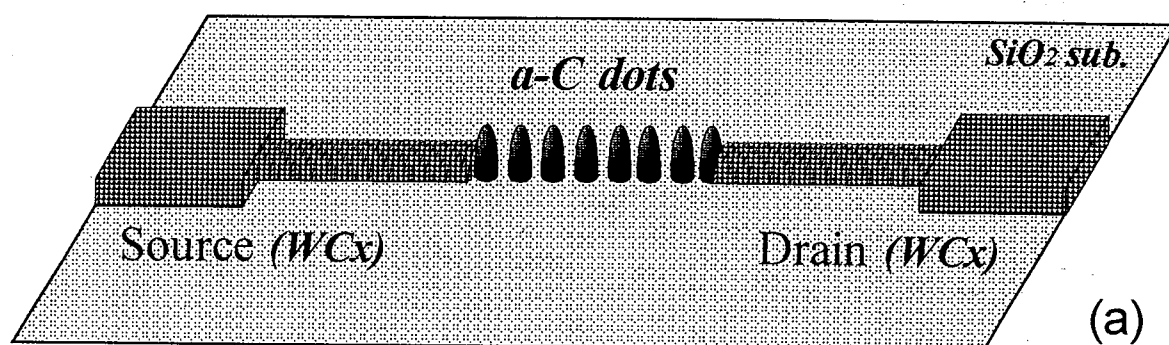
Fig. 7.2.1 Fabrication process for SET with one-dimensional a-C dot array.

acceleration voltage was set at 30 kV. Long beam irradiation leads to lateral as well as vertical growth, therefore the irradiated time was optimized for forming minute dots which leads to a low self-capacitance. The electron dose was set at about 0.5 nC, which resulted in a-C dot diameters of 30~40 nm. Schematic and SEM images of the fabricated multiple junction are shown in Figs. 7.2.2(a), (b) and (c), respectively. From the SEM images, we can see the WCx lead wires and the a-C dots between the wires. Dot sizes were estimated to be about 40 nm in diameter with gaps of less than 10 nm.

7.2.3 *Electrical characteristics*

Electrical measurements were performed in a shield room using an HP4156A precision semiconductor parameter analyzer under an asymmetric bias condition. The probe chamber was evacuated by the turbo molecular pump during the measurement and maintained at about 1×10^{-3} Torr. Since this device uses the air as the potential barrier, measurement in the evacuated environment is preferable for excluding the influence of the minute dust or atmospheric moisture. Current-voltage characteristics of the device with 4 carbon dots in series were measured at 9.4 K whose SEM image corresponds to the Fig. 7.2.2(b). The result is shown in Fig. 7.2.3. The thick line represents the drain current-drain voltage curve and the thin line represents the conductance. In the range near the zero voltage bias region, the current was suppressed within about ± 60 mV, which indicated that the Coulomb blockade was in effect. This suggests that the tunneling current flowing through the a-C dots between the WCx electrodes dominated the characteristics. Since the a-carbon had a high resistivity estimated previously at Chapter 6, tunneling was considered to occur through the almost insulating dots.

Using the Coulomb gap voltage in Fig. 7.2.3, the sum of the junction capacitance (C_{Σ}) was estimated to be about 1.3 aF. For this multiple tunneling system, there is an argument that the electrical properties are explained by the behavior of not a single charge but a so-called charge soliton [12].



C : junction capacitance
C₀ : self-capacitance

Fig. 7.2.2 Schematic (a) and corresponding equivalent circuit configuration (d) of multiple tunnel junction by a-C dot array.

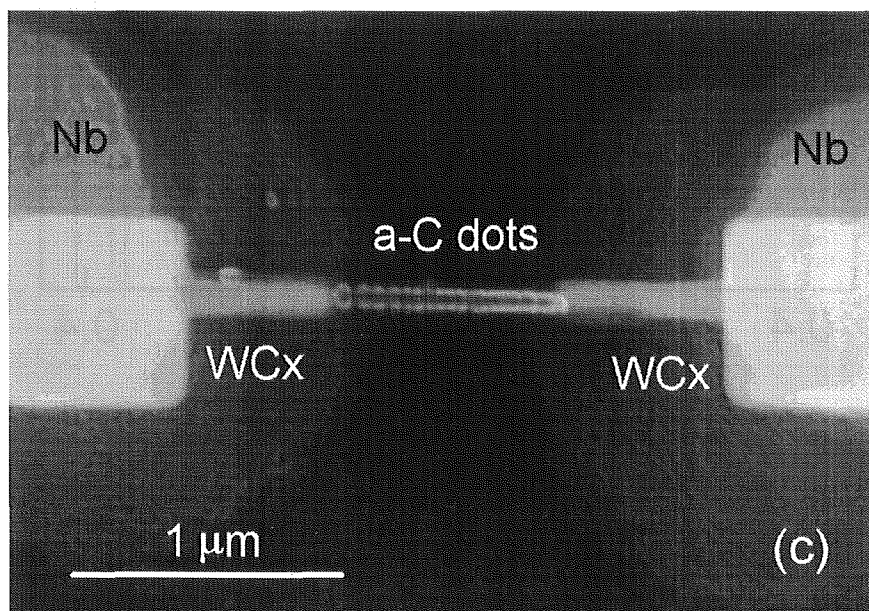
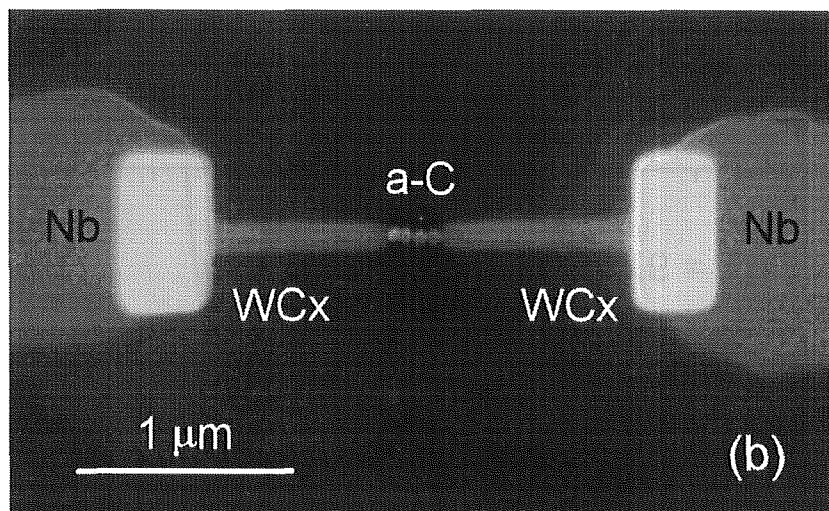


Fig. 7.2.2 SEM images of multiple tunnel junctions formed by one-dimensional amorphous carbon dot array. Four and about 20 a-C dots in series are shown in (b) and (c), respectively.

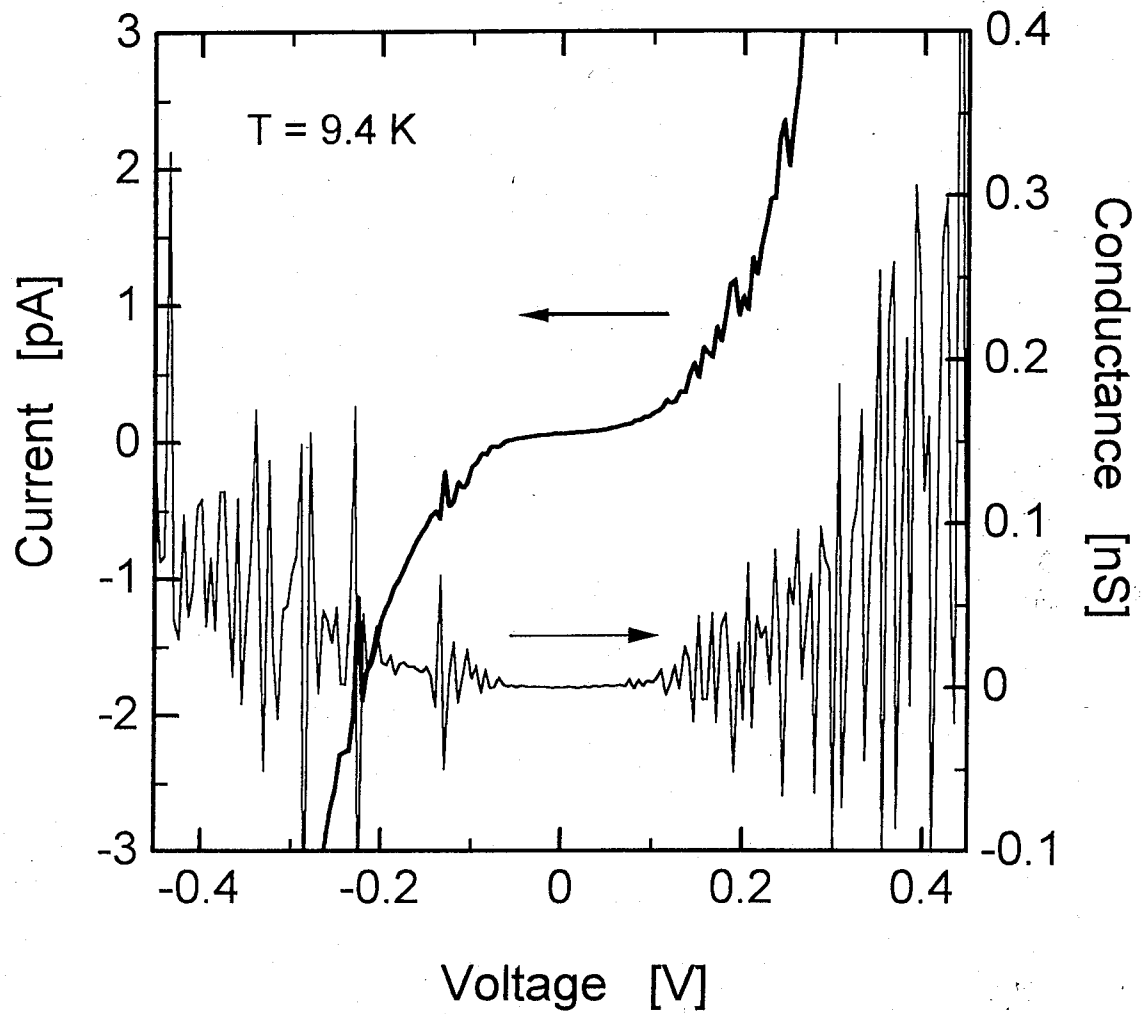


Fig. 7.2.3 Electrical characteristics at 9.4 K of the device with four a-C dots. The thick line represents the $I-V$ curve and the thin line represents the conductance.

To describe a one-dimensional array of N number of junctions, the junction capacitance (C) and self-capacitance (C_0) are specified as shown in Fig. 7.2.2(d). The array is assumed to be homogeneous for simplicity. If a single-electron is placed on the k^{th} electrode of an infinitely long array, a potential φ_k will be generated and an effective capacitance (C_{eff}) can be defined, such that $\varphi_k = -e/C_{\text{eff}}$, where C_{eff} can be deduced as

$$C_{\text{eff}} = \sqrt{C_0^2 + 4CC_0} \quad (7-1)$$

The potential of an arbitrary electrode i as a function of the distance from the charged k^{th} electrode can be calculated, and expressed as following equation,

$$\varphi_i = -\frac{e}{C_{\text{eff}}} \left(\frac{C}{C + C_0 + C_h} \right)^{|i-k|} = -\frac{e}{C_{\text{eff}}} \exp\left(-\frac{|i-k|}{M}\right), \quad (7-2)$$

where C_h is the capacitance of a half infinite array. In other words, the potential falls off exponentially with a characteristic fall off length M which can be introduced from the eq. 7-2 as

$$M^{-1} = \ln\left(\frac{C_{\text{eff}} + C_0}{C_{\text{eff}} - C_0}\right) \quad (7-3)$$

For the case of a single electron on the k^{th} electrode, there is a potential distribution with a maximum value of $\varphi_k = -e/C_{\text{eff}}$. The potential falls off exponentially on both sides. If an electron tunnels from electrode k to electrode $k+1$, this potential distribution will move one step to the right. Since this potential distribution does not change its form as it moves, it may be called a *soliton*. The soliton extends over approximately $2M$ junctions. Typically, the value M has been reported of the order of 3-5.

Being back to the device shown in Fig. 7.2.2(b), there are four fabricated dots,

therefore it would be inaccurate to consider them to be an infinite array of capacitances in the discussion of charge solitons. However, estimation of the C_{eff} from the structural parameters was attempted in order to enable numerical discussions. Assuming that the carbon dots were spherical having a diameter of 40 nm, the C_{eff} was deduced to be about 13 aF, and the parameter M was calculated to be 0.43. The capacitive discrepancy and the small M value were due to the deduction of the self-capacitance being relatively large compared to the junction capacitance. This numerical result suggests that the characteristics in Fig. 7.2.3 cannot be explained by the behavior of the charge solitons or by considering the device to belong to a multiple tunneling system. It should be noted that the difficulty in estimating the junction capacitance and the self-capacitance remains essential since each carbon dot is not exactly spherical but has a conical structure. It could be pointed out here that the four dots were not individuals but some were coupled, resulting in a device with one or two homogeneous junctions. It is difficult to monitor by SEM or SPM whether some of the dots were structurally coupled or not, however, the SEM image in Fig. 7.2.2(b) might suggest that this device had only one junction (air gap) at the center of the dot array. In this case, C_S of the device was in good agreement with that determined from the Coulomb gap voltage. Namely, although the device appeared to have four dots, only one junction practically functioned as a capacitor and the others functioned as a part of the resistive lead wires.

In Fig. 7.2.4, electrical characteristics measured at 9.4 K for a similar tunneling device with about 20 carbon dots arranged in series are shown. Its SEM image is also shown in Fig. 7.2.2(c). The thick line indicates the drain current-drain voltage characteristic and the thin line represents the conductance. The Coulomb staircase with a period of about 1 V is clearly observed for this device. This relatively large period is due to the multiple junction of dots and results in the low capacitance of the device. The conductance was smaller than that of the previous device with four dots. This is related to the high resistivity of the carbon dots and longer carbon electrodes. Similar discussions as for the previous device could be developed here, however, the estimation of the capacitances from the structural parameters is far more difficult. Furthermore in this device, some of the dots were in fact structurally coupled, which was revealed by the SEM image in Fig. 7.2.2(c), and resulted in the

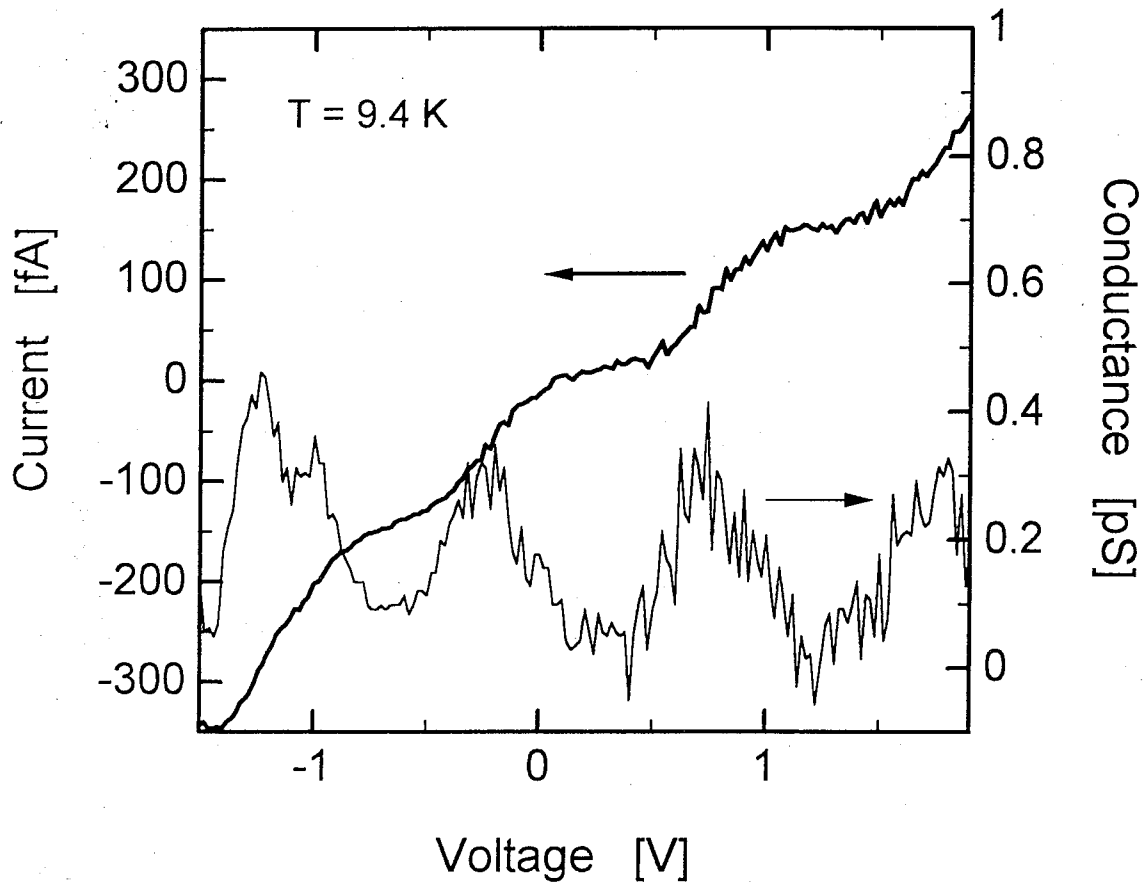


Fig. 7.2.4 Electrical characteristics at 9.4 K of the device with about 20 a-C dots. The thick line represents the $I-V$ curve and the thin line represents the conductance.

formation of long carbon dots (or wires), so that the number of the junctions was reduced from 4 to 2. In other words, this device was composed of not 20 homogeneous dots but some bunched dots with a few capacitive junctions. Accordingly, the electrical properties of this device shown in Fig. 7.2.4 were not considered to be due to soliton-like conductance. Therefore, the fact that the Coulomb staircase was observed in this device can be attributed to the inhomogeneity of dots and the capacitive asymmetry.

Based on these preliminary results that the single-electron charging effects were observed in a system consisting of carbon dots, the following could be pointed out. Although a conducting metal was employed for neither the island region nor the capacitive material, a material of relatively poor conductivity, such as our a-C, could be employed for realizing SETs, providing that a sufficient electron barrier height existed in the junction. Moreover, the high resistivity leads to the suppression of the leakage current through the device. Therefore, the utilization of amorphous carbon dots is considered to be effective. In addition, this EBID technique was demonstrated to be one of the practicable tools for the direct fabrication of SETs.

7.3 Double Junction with Side-Gated Structure

7.3.1 *Double junction using amorphous carbon dot and wire*

In this section, application of the a-C microstructures to the SETs is further investigated. Double tunnel junctions consisting of a-C wires and a dot with a gate electrode are fabricated for the consideration of the simple device structure, the simple numerical characterization, and the three terminal device operation. Amorphous carbon microstructures are modified to the source, drain electrodes and the capacitive island deposited by using SEM. As the amorphous carbon wire is found to function as a highly resistive wire in the previous section, the environmental effect is considered to be able to be minimized although some negative influence should be taken noticed, such as the lower source-drain current by introducing longer a-C wire. The air barrier is similarly employed in this device. The gate electrode consisting of tungsten carbide deposited by FIB is also supplemented. It is led from the Nb pad and locates in coplanar structure which forms a side gate.

7.3.2 *Fabrication process*

Fabrication process for the double junction device is almost the same with the previously discussed multiple tunneling system and illustrated in Fig. 7.3.1. Schematic and typical SEM image of the device are shown in Fig. 7.3.2(a) and (b), respectively. In the gap between the Nb source and the drain electrodes, fine electrodes consisting of WCx were similarly fabricated using FIB system with a precursor of $W(CO)_6$. These WCx wires are due for the leads from the dull edge of Nb electrodes to the microscopic a-C electrodes. In addition, the WCx gate was supplemented and formed a side-gated structure with about 1 μm gap between the gate and the tunnel junction. Finally, between the WCx source and the drain electrodes, a-C wires and a dot were deposited using SEM. Since this study focuses on a simple process for making minute structures, residual hydrocarbon molecules in the SEM chamber were taken as precursors and resulted to build amorphous carbon microstructures. Width and diameter of the a-C wires and the dot were about 40 nm. From the SEM image in Fig. 7.3.2(b), we can see that the a-C dot and the electrodes were separated in about 50~80

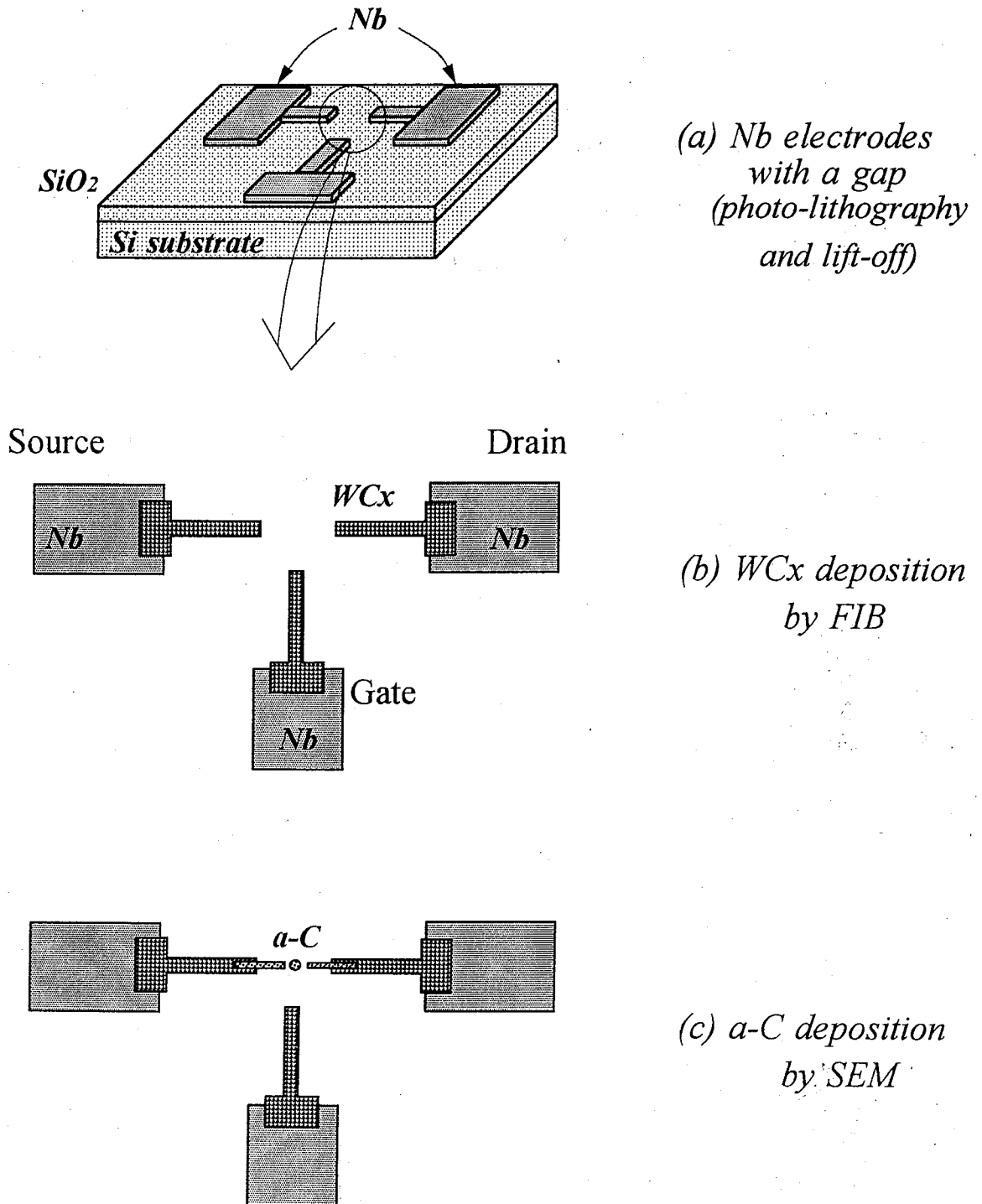


Fig. 7.3.1 Fabrication process for SET of double junction with side gate.

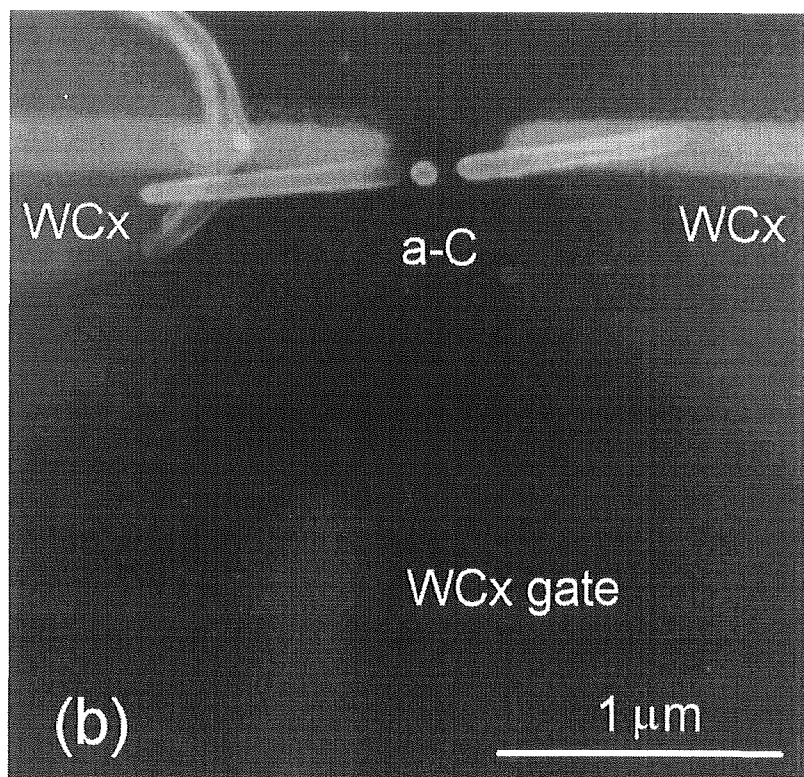
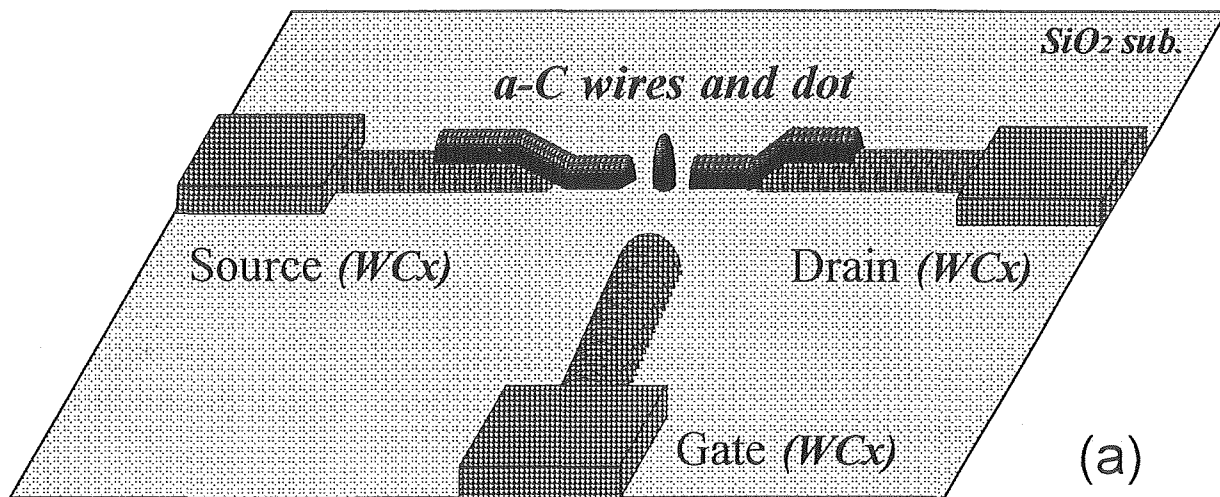


Fig. 7.3.2 Schematic (a) and SEM image (b) of the double junction with side gate.

nm, which means that the air gap would be the potential barrier for each electron. It should be noted here that our FIB system was not so suitable for the fabrication of the minute dot (island) because of relatively large ion-beam spot size (11 nm) compared to that of the electron beam of our SEM (~2 nm). Although conical WCx dot could be deposited, it has a large diameter and long tail, which causes an electrical shortage between the source and the drain electrodes. With this respect, the WCx microstructures fabricated by ion-beam-induced deposition was only employed to the preparation of fine electrodes with a gap of 0.2~0.5 μm .

7.3.3 *Electrical characteristics*

Electrical measurements were performed in the electromagnetically shielded room using same apparatus in the same condition described in previous section. Figure 7.3.3 shows a drain current-drain voltage characteristic of a device having two tunnel junctions measured at 9.3 K. The length of the air gap between the source, drain and the island were about 20~80 nm, and the diameter of the dot was about 80 nm. In the I - V curve shown in Fig. 7.3.3, we can see Coulomb staircase with a period of about 0.7 V. Since this study recorded the staircase from the one-dimensional a-C dot arrays, this characteristics ensures that the a-C microstructures are also applicable to the simple double junction device. The sum of the junction capacitance (C_{Σ}) of the device was estimated to be about 0.3 aF from the Coulomb gap voltage. As the estimated C_{Σ} was small enough, operation at higher temperature could be expected. Besides, this device did not have a gate electrode, we next fabricated a similar two junction device with a gate electrode for the observation of the gate modulation in the I - V curve.

SEM image of the fabricated three-terminal device is shown in Fig. 7.3.4(a). We can see the double junction consisted of a-carbon dot and wires and the gate electrode consisted of WCx which was led from the Nb pad. Figures 7.3.4(b) and (c) show a drain current-drain voltage (I_D - V_{DS}) characteristic and a drain current-gate voltage (I_D - V_g) characteristic, respectively, and both of them were recorded at as high as 294 K. Coulomb staircase and periodic Coulomb blockade oscillation are clearly seen in these figures at surprisingly high

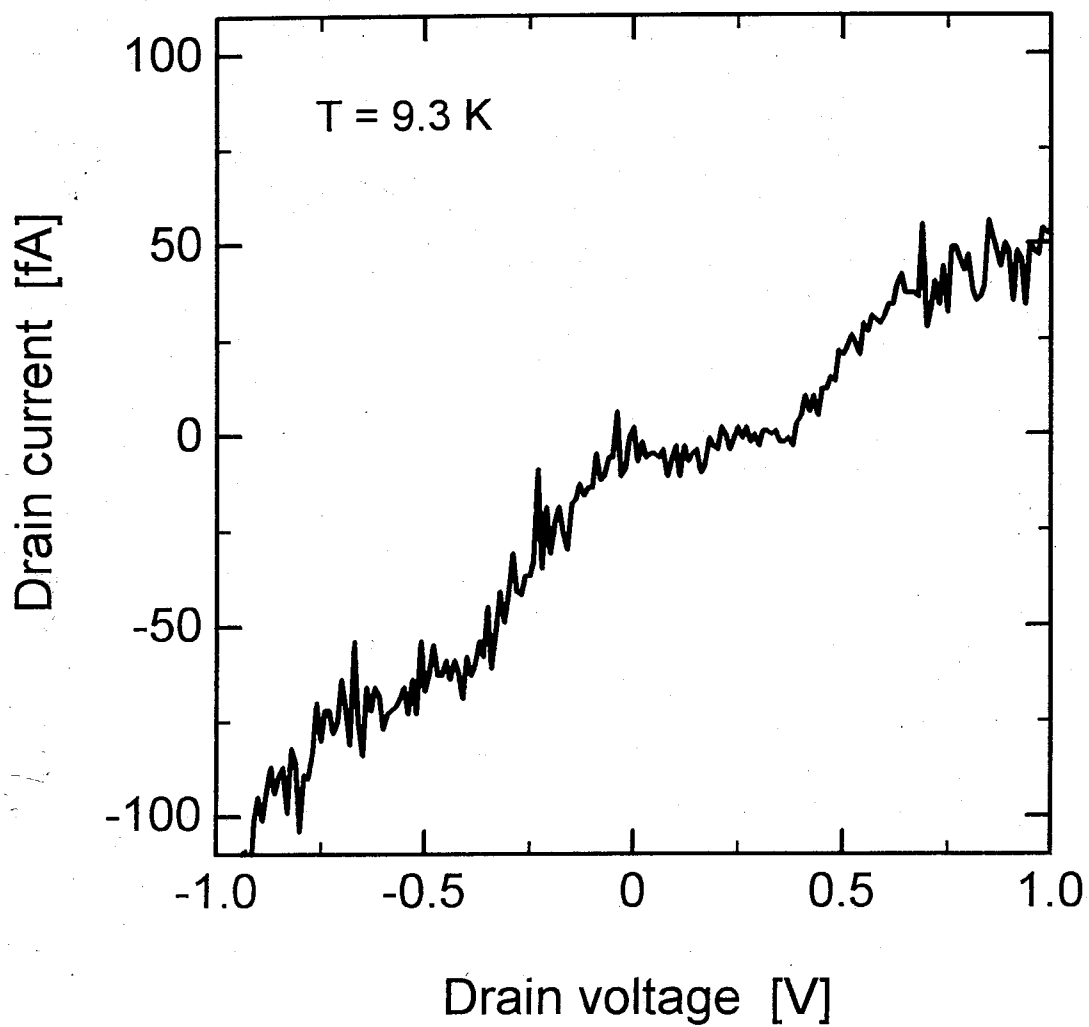


Fig. 7.3.3 Drain current-drain voltage characteristic of SET of double junction.

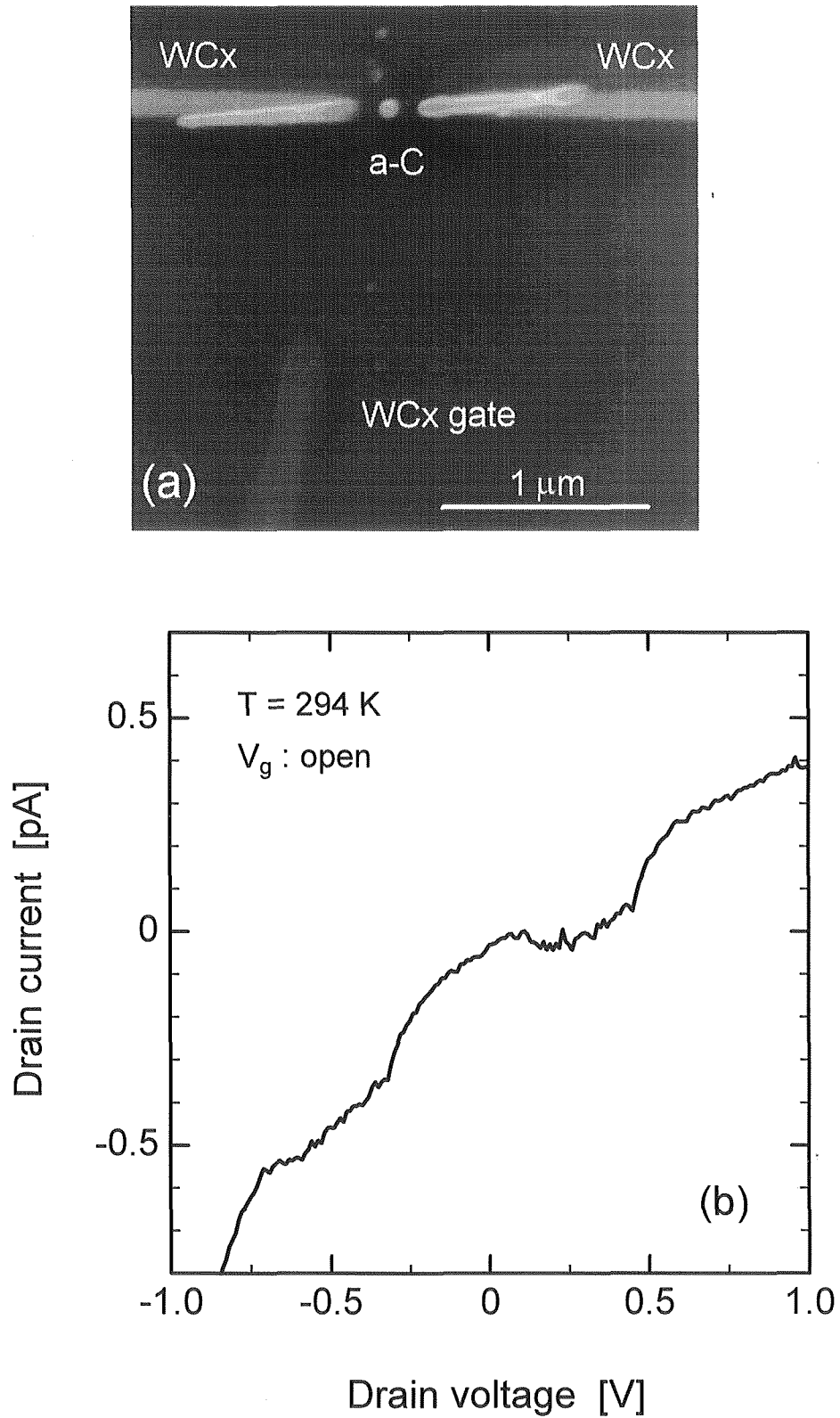


Fig. 7.3.4 SEM image (a) and drain current-drain voltage characteristic (b) of SET of double junction.

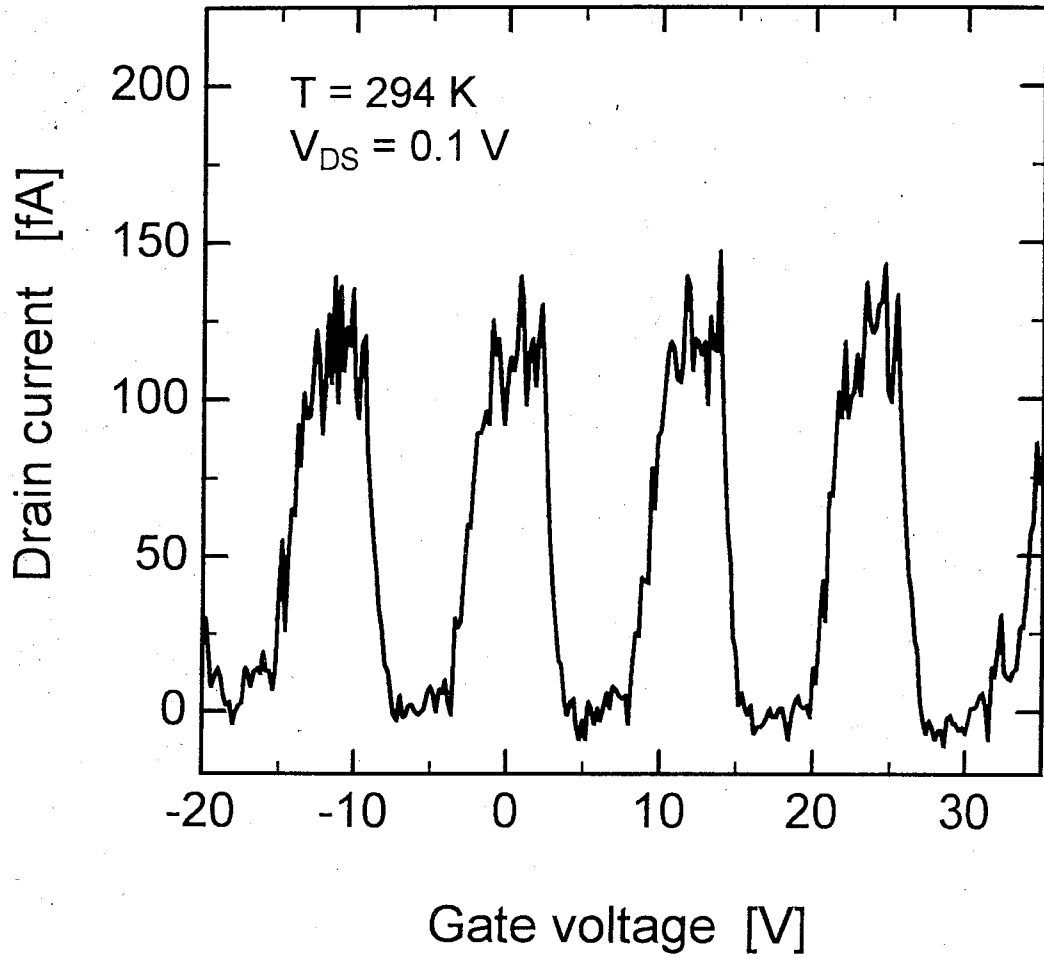


Fig. 7.3.4(c) Drain current-gate voltage characteristic of the SET.

temperature. This clear periodic oscillation at room temperature is so far the first demonstration in the device fabricated by beam-induced reaction process. In this device, the air gap length seems to be a little longer (about 80 nm) and tunneling phenomena would not occur judging from this value. However, single-electron charging effects were clearly observed at room temperature. These results suggest that some of the new electron transport from the source to drain through the air must be considered in this system, which will be discussed later. In Fig. 7.3.4(b), plateau of the stairs are not sufficiently flat but the steps were observable, and this would be due to the thermal fluctuations. The gate modulation shown in Fig. 7.3.4(c) is notable. We can see that each electron tunneling was clearly controlled by applying gate voltage and the leakage current induced by the gate bias did not affect the characteristics and remained negligible although it was applied as much as 20~30 V. These would be attributed to the use of the air gap for the potential barrier and the use of amorphous carbon as this material has relatively poor electrical conductivity. From the oscillation and the staircase periods, the junction capacitance was deduced. The gate capacitance (C_g) was estimated to be about 0.013 aF and that of the junction (C_1+C_2) was about 0.19 aF. The calculated values from the structural parameters roughly agreed well to them; C_g and (C_1+C_2) are about 0.018 aF and 0.22 aF, respectively.

In order to clarify the reproducibility of the SETs which operate at room temperature, various SETs were fabricated through the above method. One of the electrical result is shown in Fig. 7.3.5(b) whose SEM image is also shown in Fig. 7.3.5(a). Clear Coulomb blockade in about 0.55 V and Coulomb staircase were observed in the drain current-drain voltage characteristic at 294 K. Coulomb blockade modulation by the gate voltage was also confirmed in this device, which ensured its room temperature operation.

Considering from the device structure, the length of the air gap is long for the electron tunneling, and the island with conical structure is not so small compared to the reported SETs of other material systems [3, 8, 10, 13]. However, the gate modulation in Fig. 7.3.4(c) clearly reveals the single-electron charging effect in our systems. Some of the consideration can be developed here. One of the hopeful possibilities is that our a-C might have low work function and could easily emit electrons to the air causing a relatively long

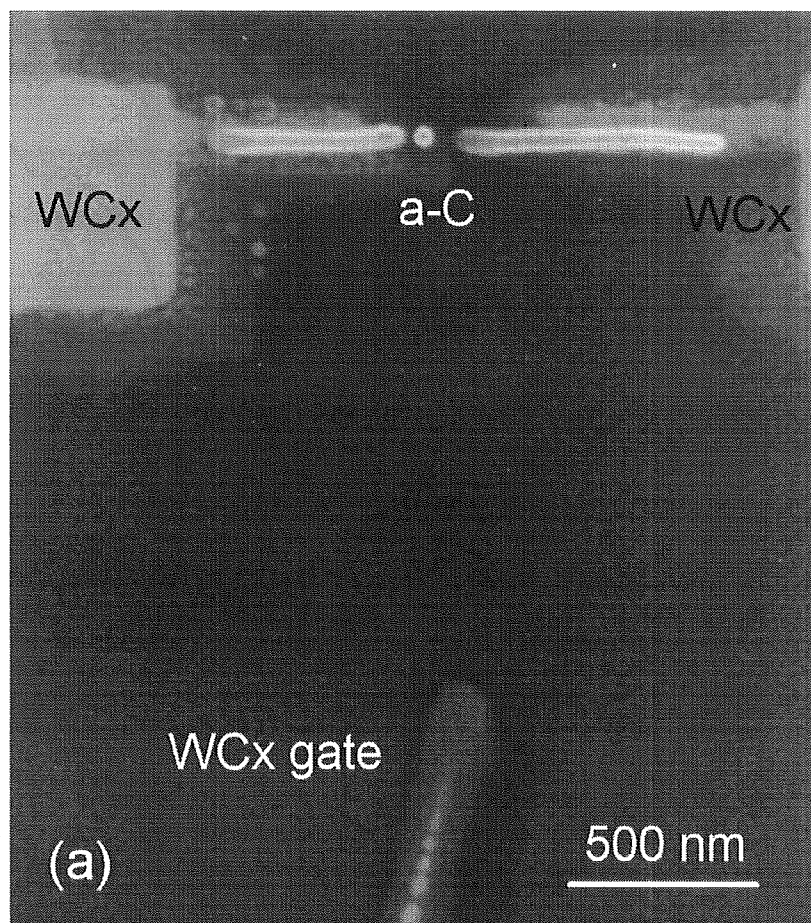


Fig. 7.3.5(a) SEM image of the SET of double junction system consisted of amorphous carbon dot and wires. Tungsten carbide (WCx) gate was supplemented.

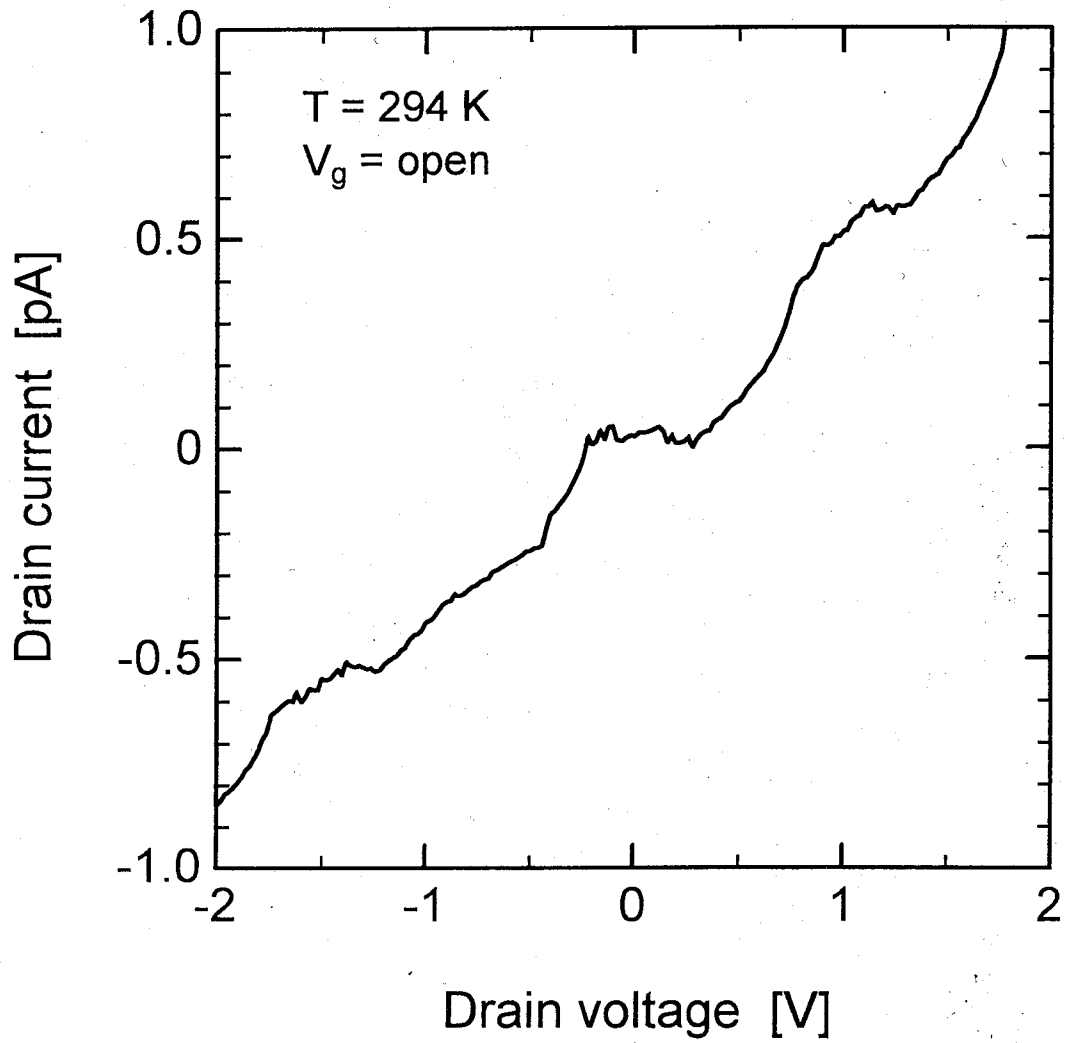


Fig. 7.3.5(b) Drain current-drain voltage characteristic of the SET of double junction.

way tunneling (or emission). As the a-C or diamond like carbon (DLC) is known to have low work function and its research for the application to the vacuum emitting device is in active [14-16]. Furthermore, the following possibility could be considered next which is related to the favorable material property of a-carbon. The amorphous carbon might have formed a depletion layer near the surface due to the defects in the film. This makes the effective size of the dot to be estimated smaller. In other words, the a-C dot was surrounded by the Schottky barrier causing its effective self-capacitance small enough for the Coulomb island which is preferable for the high temperature operation of SETs although the tunnel region becomes long. Therefore, our successful result might owe to the usage of amorphous carbon for the capacitance element, and this kind of material might be suitable for the fabrication of SETs if one wants to realize them in not nanoscopic but microscopic structures.

Other consideration is based on the facts that the a-C dot has conical structures (approximately Gaussian curve) and its tail could have coupled to the edge of the a-C source and drain wires. In addition, the junction area is inevitably monitored by SEM for the alignment, which causes deposition of ultra-thin a-C film in the observed area. Therefore, during the processing by SEM, some of the tungsten related molecules adsorbed on the substrate surface or gallium atoms implanted during the FIB process were decomposed or irradiated by the electron-beam to form a metallic clusters inside the a-C dot, wire and maybe the ultra-thin film which cover the source and drain electrodes. Namely, that kind of metallic nanoparticles inside the a-C might have dominated the electrical characteristics. This possibility rises from the usage of FIB before the a-C deposition. However, any single-electron charging effect has not been observed at room temperature from the devices which had not the a-C dot in the center of the source-drain gap. In addition, clear Coulomb staircase or Coulomb blockade oscillation could not be observed from such multiple metal clusters unless its junction and self-capacitance are all homogenous, which would not be possible in the real devices. In order to clarify the influence of FIB process or the use of metal carbonyl molecules, electrical estimation of the a-C wire (no island) and the fabrication of the SETs without using FIB system are now under investigations. Moreover, the possible electron emissivity from the a-C should also be studied in detail, especially the properties of the

barrier height or the work function. This research will reveal possibility to employ new material system for the SETs. As a result, mechanism of the electron transport in this system should be discussed further, however, the realization of room temperature SETs with such an unique process, that is the beam-induced reaction process, should be noticed as one of the potentials for the future electronic device fabrication.

7.4 Summary

In order to utilize the microscopic deposition technique by SEM for the direct fabrication of the discrete devices, the single-electron transistor was targeted as it is one of the potential candidates for the future electronic devices. For its realization, beam-induced reaction techniques such as the electron- and ion-beam-induced depositions were used since they enable simple microfabrications. Amorphous carbon dots were deposited by using conventional SEM system from the residual hydrocarbon molecules in the chamber as usual, and fine metallic leads consisted of tungsten carbide were made by FIB system.. The dots were employed to the island region of the tunneling devices, and its electrical characterization was extensively investigated in this chapter. Various SETs were fabricated with introducing the air gap for the tunnel barrier to the electron. At 9.4 K, Coulomb blockade and Coulomb staircase were successfully observed in the devices with one-dimensional a-carbon dot arrays. Moreover, in the devices of double tunnel junctions consisting of a-carbon dot and wires, Coulomb staircase and periodic Coulomb blockade oscillation were clearly observed at not only 9.3 K but also as high as 294 K. These indicated that the amorphous carbon dots were applicable and practicable to the SETs, and the beam-induced reaction process was found to be an effective technique for realizing these microscopic tunneling devices. Although there still remains unknown factors such as the electron transport through the device, this first demonstration of the room temperature operation in the amorphous carbon-based SETs will open a new possibility for their simple and fast fabrication.

References

- [1] K. Nakazato, R. J. Blaikei, J. R. A. Cleaver and H. Ahmed: *Electron Lett.* **26** (1993) 384.
- [2] Y. Takahashi, A. Fujiwara, M. Nagase, H. Namatsu, K. Kurihara, K. Iwadate and K. Murase: *Ext. Abstr. 14th Symp. Future Electron Devices (1995)* pp. 73.
- [3] Y. Nakamura, C. -D. Chen and J. -S. Tsai: *Jpn. J. Appl. Phys.* **35** (1996) L1465.
- [4] K. Jinushi, H. Okada, T. Hashizume and H. Hasegawa: *Jpn. J. Appl. Phys.* **35** (1996) 1132.
- [5] H. Ishikuro and T. Hiramoto: *Appl. Phys. Lett.* **71** (1997) 3691.
- [6] A. Toriumi, J. Koga, K. Uchida and A. Ohata: *Ext. Abstr. 3rd Int. Workshop on Quantum Functional Devices (1997)* pp. 23.
- [7] K. Matsumoto, M. Ishii, K. Segawa, Y. Oka, B. J. Vertanian and J. S. Harris: *Appl. Phys. Lett.* **68** (1996) 34.
- [8] J. Shirakashi, K. Matsumoto, N. Miura and M. Konagai: *Jpn. J. Appl. Phys.* **36** (1997) L1257.
- [9] J. Shirakashi, K. Matsumoto, N. Miura and M. Konagai: to be published in *Appl. Phys. Lett.* (1998).
- [10] T. Wada, M. Hirayama, S. Haraichi, K. Ishii, H. Hiroshima and M. Komuro: *Jpn. J. Appl. Phys.* **34** (1995) 6961.
- [11] K. Komuro and H. Hiroshima: *Microelectronic Engineering* **35** (1997) 273.
- [12] P. Delsing: “*Single Charge Tunneling*”, ed. H. Grabert and M. H. Devoret (Plenum Press, New York, 1992) pp. 249.
- [13] K. Tsukagoshi, K. Nakazato and T. Sato: *Ext. Abstr. 16th Symp. Future Electron Devices (1997)* pp. 67.
- [14] M. W. Geis, J. C. Twichell, J. Macaulay and K. Okano: *Appl. Phys. Lett.* **67** (1995) 1328.
- [15] K. C. Walter, H. H. Kung and C. J. Maggiore: *Appl. Phys. Lett.* **71** (1997) 1320.
- [16] N. A. Fox, W. N. Wang, T. J. Davis, J. W. Steeds and P. W. May: *Appl. Phys. Lett.* **71** (1997) 2337.

Chapter 8

General Conclusions

In this dissertation, the establishment of microstructure fabrication was mainly concentrated together with its application to the fabrication of mesoscopic and microscopic devices. The scanning electron microscope (SEM) was chosen as a processing tool and the electron-beam-induced deposition technique was extensively studied. As a result, not only the fabrication of the nanoscopic structures but also its successful applications to the fabrication of superconducting weak link devices or single-electron transistors were demonstrated. Moreover, some of the heavily-doped semiconductors were electrically investigated and anomalous characteristics were first observed in one of them. In this chapter, those conclusions are stated in detail to clarify the successfully achieved results throughout this dissertation.

For the fabrication of microscopic structures, utilization of electron-beam-induced deposition technique was demonstrated using SEM in Chapter 3. Without its modification, the carbonaceous material could be deposited only at the place where the electron-beam was spotted by employing residual hydrocarbon molecules adsorbed on the substrate surface. Higher acceleration voltage and lower electron-beam current were found optimal for obtaining narrow wires, and this is due to the sharper electron-beam and less enhanced lateral growth. By optimizing the electron-beam conditions, the narrow carbonaceous wires whose width was about 30 nm were successfully fabricated. The wires were observed by atomic force microscope (AFM) with the carbonaceous needle deposited on top of the cantilever. This processing enabled to obtain clear AFM image from the structures with high aspect ratio. For their application to the device process, the carbonaceous wires were employed to the dry etching masks to obtain Si nanowires. By employing spin-on glass layer to remove the masks, Si wires whose width was about 60 nm were fabricated and moreover, the n^{++} -Si nanowire was also electrically investigated. These results indicated its applicability to the device fabrication processes.

To realize one of the future electronic devices, superconducting weak link device was taken noticed using heavily-doped semiconductors as a normal layer material in Chapter 4. For the starters, various degenerated semiconductor thin films such as P-doped Si, C-doped GaAs, InN grown on GaAs substrate, and B-doped ZnO were investigated. Since they had the carrier concentration of the order of $10^{20} \sim 10^{21} \text{ cm}^{-3}$, temperature dependence of the electrical resistivity showed metallic conducting characteristics, which were also confirmed from the theoretical fittings. However, the epitaxial n^{++} -InN thin films grown on a sapphire substrate exhibited anomalous electrical characteristics below 4.2 K. Transition similar to the normal to the superconductor was observed, and its peculiar characteristics was found to be dependent on the electron concentration and external magnetic field. Its origin was extensively investigated from many aspects, however it has not been revealed yet. Any influence from the superconducting elemental indium could be considered although it has not been characterized from either the X-ray spectroscopy or surface observation by SEM and AFM.

After the theoretical consideration of the practicability of these degenerated semiconductors including anomalous InN to the superconducting weak link devices in the late part of Chapter 4, the n^+ -ZnO and n^{++} -Si were practically employed to them in Chapter 5. As the superconducting electrodes, niobium (Nb) and niobium nitride (NbN) were deposited by DC magnetron sputtering technique, and bias-sputtering was found effective to obtain a film of better superconducting properties. By using polycrystalline ZnO film as a normal layer of the device which was sandwiched by NbN electrodes, superconducting current flowed through the layer and its superconducting characteristic was examined from various aspects with theoretical fittings. Furthermore, in the fabrication of Nb/ n^{++} -Si/Nb coplanar junction, new process using carbonaceous wire was proposed to determine the gap length between the Nb electrodes. The wire was successfully applied to the stencil mask to make a suspended structure with the aid of the ZnO buffer layer, and the gap length of about 60 nm was obtained. This new process was also demonstrated to realize the weak link device. The superconducting characteristic was also observed at 1.4 K. In addition to the proposal of this fabrication process using carbonaceous wire, realization of weak link device using n^{++} -Si

whose electron concentration is of the order of 10^{21} cm^{-3} is the first demonstration.

For the active application of these carbonaceous microstructures to the electronic devices, its optical as well as electrical characterization was carried out in Chapter 6. From the Raman scattering spectroscopy performed on the carbon micro-film, the peaks originating from the amorphous carbon were clearly recorded and the material deposited from our SEM was determined to be an amorphous carbon. The a-carbon was employed to the intermediate layer of metal/insulator/metal (MIM) junctions. Temperature dependence of the I - V curve showed non-linear characteristics, and the resistivity and dielectric constant were estimated to be about $10^{11} \Omega \cdot \text{cm}$ and about 5, respectively, which were consistent values for the a-carbon. The MIM diode using WCx as the metal electrodes were also fabricated to concern the device in minute size. Similar result with the above case was obtained and the introduction of WCx deposited by ion-beam-induced deposition technique using focused ion beam (FIB) was performed.

For the ultimate application of the minute a-carbon microstructures, its dot shape was employed to the island region in single-electron transistors described in Chapter 7. First, they were arranged in series to form a one-dimensional array in order to function as a multiple tunneling system using air gap as a potential barrier. Single-electron charging effects, such as Coulomb blockade and Coulomb staircase were observed in the multiple a-C dot system at 9.4 K. Furthermore, a simple double tunnel junction system consisting of a-C dot and wires were similarly fabricated using SEM and FIB for the a-C structures and conducting lead electrodes, respectively. In this device, Coulomb staircase and Coulomb blockade oscillation were clearly observed at not only low temperature but also room temperature. Since the self-capacitance of the dot and tunneling air region were estimated to be large in order the single-electron operation at 294 K, possible electron transport was considered. Although it has not been clarified yet, it could be due to the easy electron emissiveness from the diamond-like amorphous carbon which enabled the long way tunneling and the existence of the depletion layer near the surface which made an effective size of the dot being relatively small, or the existence of the gallium nanoparticles inside the SiO_2 substrate which might govern the electrical characteristics.

Through this dissertation, the above results were successfully obtained. The beam-induced deposition technique was confirmed to be one of the practicable processes for the future microscopic device fabrications. In particular, it is the key features that it could be applicable to both lithographic mask for fine structure patterning and direct production of discrete devices. Although this study did not introduce any precursor gases from outside of the chamber to control the depositing material from the point of the easy processing without modifying SEM system, positive introduction of metalorganic or hydrocarbon gases would be necessary for widening its applicability and its advantages for the simple microstructure fabrication.

For the concluding remarks, the author wishes that this study would contribute to open or play any part of creating a new field of the future microscopic devices which helps to promote quality of our future daily activities.

Acknowledgments

The author is greatly indebted to Professor Makoto KONAGAI and Associate Professor Akira YAMADA for their continual guidance and encouragement throughout his study at under- and post-graduate courses.

The author expresses his sincere gratitude to Professors Masakiyo MATSUMURA, Shunri ODA and Mitsumasa IWAMOTO for their participation in the examination of this dissertation and for providing him useful suggestions.

The author gratefully acknowledges Professors Toyosaka MORIIZUMI, Masahiko NAOE, Masanori ABE, Kazuhito FURUYA, Associate Professors Osamu SUGIURA, Masahiro ASADA, Yasuyuki MIYAMOTO, Takamichi NAKAMOTO, Shigeki NAKAGAWA, and Professor emeritus Kiyoshi TAKAHASHI (Teikyo University of Science & Technology) for their critical comments and encouraging remarks.

The author expresses his acknowledgments to Associate Professor Matsuo SEKINE for providing us the sputtering system, Professor Nobuhiko NISHIDA and Associate Professor Yuichi OKUDA for their assistance in low temperature measurements, Professors Akio YAMAMOTO (Fukui University) and Akira YOSHIDA (Toyohashi University of Technology) for supplying us the InN samples, and Dr. H. T. Grahn (Paul-Drude-Institut) for the fruitful discussions.

This dissertation really owes to the thoughtful discussions with Doctors Jun-ichi SHIRAKASHI and Kazuhiko MATSUMOTO (Electrotechnical Laboratory), and the author also acknowledges them for the cooperation in SET measurement and AFM observation.

The author's successful experimental results owe to Dr. Nobuaki KOJIMA (Toyota Technological Institute) and Mr. Hideaki ISHII (NTT) for their preliminary technical assistance in developing the nanostructure fabrication processes using SEM, Doctors Jia YING and Takayuki OSHIMA (Hitachi Co., Ltd) for their guidance in epitaxial Si growth, and Dr. Wilson Walery Wenas (Institute of Technology Bandung) for his technical assistance in ZnO preparation.

The author thanks all the members of Matsumura, Sugiura, Oda, Furuya, Arai,

Asada, Miyamoto and Watanabe Labs for providing experimental equipments and technical guidance.

Finally the author appreciates all the members of Konagai and Yamada Labs, especially Messrs. Katsuya ABE, Kyosuke MIYAGI (Toyota Co., Ltd.), Norihisa NIHANDA (Honda R&D Co., Ltd.) and Tetsuyuki NUMAGUCHI for their technical assistance throughout his experimental studies. Thanks are also extended to the following secretaries, Mss. Yuko YOSHIDA, Kimiko FURUKAWA, Kiyoko TAKEMURA and Masayo YAMASHITA, for their helpful assistance and support during the author's research activities.

List of Publications

< Papers & Letters >

- [1] N. Miura, H. Ishii, A. Yamada and M. Konagai
"Application of Carbonaceous Material for Fabrication of Nano-Wires with a Scanning Electron Microscopy"
Jpn. J. Appl. Phys. **35**(8B) (1996) L1089-L1091.
- [2] J. Shirakashi, M. Ishii, K. Matsumoto, N. Miura and M. Konagai
"Surface Modification of Niobium (Nb) by Atomic Force Microscope (AFM) Nano-Oxidation Process"
Jpn. J. Appl. Phys. **35**(11B) (1996) L1524-L1527.
- [3] J. Shirakashi, M. Ishii, K. Matsumoto, N. Miura and M. Konagai
"Nanometer-scale surface modification of Nb thin film by atomic force microscope (AFM) nano-oxidation process and its application to single electron transistors (SETs)"
Transactions of the Materials Research Society of Japan, Vol.20 (1996) 255-258.
- [4] N. Miura, H. Ishii, A. Yamada, M. Konagai, Y. Yamauchi and A. Yamamoto
"Anomalous Electrical Characteristics of Epitaxial InN Films Having a High Electron Concentration at Very Low Temperature"
Jpn. J. Appl. Phys. **36**(3A) (1997) L256-L259.
- [5] N. Miura, H. Ishii, J. Shirakashi, A. Yamada and M. Konagai
"Electron-beam-induced deposition of carbonaceous microstructures using scanning electron microscopy"

Appl. Surf. Sci. 113/114 (1997) 269-273.

- [6] J. Shirakashi, K. Matsumoto, N. Miura and M. Konagai
"Nb/Nb Oxide-Based Planar-Type Metal/Insulator/Metal (MIM) Diodes Fabricated by Atomic Force Microscope (AFM) Nano-Oxidation Process"
Jpn. J. Appl. Phys. 36(8B) (1997) L1120-L1122.
- [7] J. Shirakashi, K. Matsumoto, N. Miura and M. Konagai
"Single-Electron Transistors (SETs) with Nb/Nb Oxide System Fabricated by Atomic Force Microscope (AFM) Nano-Oxidation Process"
Jpn. J. Appl. Phys. 36(9AB) (1997) L1257-L1260.
- [8] N. Miura, A. Yamada and M. Konagai
"Fabrication of Sub-Micron Tungsten Carbide (WC_x) / Amorphous Carbon (a-C) Stacked Junction by Beam-Induced Reaction Processes"
Jpn. J. Appl. Phys. 36(9AB) (1997) L1275-L1278.
- [9] N. Miura, T. Numaguchi, A. Yamada, M. Konagai and J. Shirakashi
"Single-Electron Tunneling through Amorphous Carbon Dots Array"
Jpn. J. Appl. Phys. 36(12A) (1997) L1619-L1621.
- [10] N. Miura, A. Yamada and M. Konagai
"Fabrication of Sub-Micron Gap Structures using Directly-Deposited Amorphous Carbon Wire"
to be published in Jpn. J. Appl. Phys. 37(4) (1998).
- [11] J. Shirakashi, K. Matsumoto, N. Miura and M. Konagai
"298 K operation of Nb/Nb oxide-based single-electron transistors with reduced size of tunnel junctions by thermal oxidation"

to be published in Appl. Phys. Lett. (1998).

- [12] N. Miura, T. Numaguchi, A. Yamada, M. Konagai and J. Shirakashi
"Room Temperature Operation of Amorphous Carbon-Based Single-Electron Transistors Fabricated by Beam-Induced Deposition Techniques"
to be published in Jpn. J. Appl. Phys. (1998).
- [13] J. Shirakashi, K. Matsumoto, N. Miura and M. Konagai
"Room Temperature Nb-Based Single-Electron Transistors"
to be published in Jpn. J. Appl. Phys. **37**(3B) (1998).
- [14] J. Shirakashi, K. Matsumoto, N. Miura and M. Konagai
"Single-Electron Charging Effects in Nb/Nb Oxide-Based Single-Electron Transistors at Room Temperature"
to be published in Appl. Phys. Lett. (1998).

< International Conferences >

- [1] J. Shirakashi, M. Ishii, K. Matsumoto, N. Miura and M. Konagai
"Nanometer-Scale Surface Modification of Nb Thin Film by Atomic Force Microscope (AFM) Nano-Oxidation Process and Its Application to Single Electron Transistors (SETs)"
1996 The Materials Research Society of Japan Symposium (1996 MRS-J), May 22-24, 1996, Chiba, Japan. Conf. Proceedings, pp. 96.
- [2] J. Shirakashi, M. Ishii, K. Matsumoto, N. Miura and M. Konagai
"Single Electron Transistors (SETs) with Nb/Nb Oxides System Fabricated by Atomic Force Microscope (AFM) Nano-Oxidation Process"

1996 IEEE 54th Device Research Conference (DRC '96), June 24-26, 1996, CA, USA. Conf. Digest, pp. 182-183.

- [3] J. Shirakashi, M. Ishii, K. Matsumoto, N. Miura and M. Konagai
"Surface Modification of Niobium (Nb) by Atomic Force Microscope (AFM) Nano-Oxidation Process"
1996 38th Electronic Materials Conference (EMC '96), June 26-28, 1996, CA, USA. Technical Program with Abstracts, pp. 53.
- [4] N. Miura, H. Ishii, J. Shirakashi, A. Yamada and M. Konagai
"Electron-Beam-Induced Deposition of Carbonaceous Microstructures Using Scanning Electron Microscopy"
8th International Conference on Solid Films and Surfaces (ICSFS-8), July 1-5, 1996, Osaka, Japan. The book of Abstracts, pp. 5.
- [5] J. Shirakashi, M. Ishii, K. Matsumoto, N. Miura and M. Konagai
"Fabrication and Characterization of Nb/Nb Oxides-Based Single Electron Transistors (SETs)"
1996 International Conference on Solid State Devices and Materials (SSDM '96), August 26-29, 1996, Yokohama, Japan. Extended Abstracts, pp. 440-442.
- [6] A. Yamada, N. Miura, H. Ishii and M. Konagai
"Application of Carbonaceous Materials for Nanostructure Fabrication with a Scanning Electron Microscopy"
Regional Symposium on Materials Science, December 10-12, 1996, Quezon City, Philippines. Proceedings, pp. 10-14.
- [7] N. Miura, T. Numaguchi, A. Yamada and M. Konagai
"Sub-Micron Tungsten Carbide/Amorphous Carbon Stacked Diode Fabricated by

Ion- and Electron-Beam-Induced Deposition Technique"

1997 International Conference on Solid State Devices and Materials (SSDM '97),
September 16-19, 1997, Hamamatsu, Japan. Extended Abstracts, pp. 258-259.

[8] J. Shirakashi, K. Matsumoto, N. Miura and M. Konagai

"Room Temperature Nb-Based Single-Electron Transistors"

1997 International Conference on Solid State Devices and Materials (SSDM '97),
September 16-19, 1997, Hamamatsu, Japan. Extended Abstracts, pp. 490-491.

[9] N. Miura, T. Numaguchi, A. Yamada, M. Konagai and J. Shirakashi

"Single Electron Charging Effects from the One Dimensional Carbon Dots Array"

The 3rd International Workshop on Quantum Functional Devices (QFD '97),
November 5-7, 1997, Maryland, USA. Extended Abstracts, pp. 209-210.

[10] J. Shirakashi, K. Matsumoto, N. Miura and M. Konagai

"Room temperature Nb / Nb oxide-based single-electron transistors"

1997 IEEE International Electron Devices Meeting (IEDM '97), December 7-10,
1997, Washington, DC, USA. Technical Digest, pp. 175-178.

< Domestic Conferences >

[1] 賈瑛、大島隆文、三浦成久、山田明、小長井誠、高橋清、魏龍、谷川庄一郎

"低温形成高濃度リンドーブSiエピタキシャル薄膜の欠陥評価"

第53回応用物理学会学術講演会、16p-ZG-11、1992年秋季、大阪

[2] 山田明、三浦成久、小島信晃、小長井誠

"走査型電子顕微鏡を用いた極微細構造の作製"

第42回応用物理学関係連合講演会、30p-P-9、1995年春季、神奈川

- [3] 三浦成久、石井英明、山田明、小長井誠
"走査型電子顕微鏡を用いた極微細構造の作製(Ⅱ)"
第56回応用物理学学会学術講演会、26a-B-6、1995年秋季、石川
- [4] 白樫淳一、石井正巳、松本和彦、三浦成久、小長井誠
"AFM超微細酸化法によるMetal(Nb)/Insulator(Nb-Oxide)/Metal(Nb)接合"
第56回応用物理学学会学術講演会、28p-ZW-10、1995年秋季、石川
- [5] 三浦成久、石井英明、岡本保、山田明、小長井誠、山内康之、山本高勇
"高電子濃度エピタキシャルInNの異常極低温電気的特性"
第43回応用物理学関係連合講演会、26p-ZB-7、1996年春季、埼玉
- [6] 石井英明、三浦成久、山田明、小長井誠
"走査型電子顕微鏡を用いたSi細線の作製"
第43回応用物理学関係連合講演会、28p-ZS-10、1996年春季、埼玉
- [7] 白樫淳一、松本和彦、三浦成久、小長井誠
"AFM超微細酸化法により作製したNb/Nb-Oxide系極微小トンネル接合"
第43回応用物理学関係連合講演会、26p-ZA-5、1996年春季、埼玉
- [8] N. Miura, H. Ishii, T. Okamoto, A. Yamada, M. Konagai, Y. Yamauchi and A. Yamamoto
"Anomalous Electric Behavior of Epitaxial InN Films Below 4.2K"
15th Electronic Materials Symposium (EMS '96), July 10-12, 1996, Izu-Nagaoka, Japan. Symposium Record, pp. 41-44.

- [9] 白樫淳一、石井正巳、松本和彦、三浦成久、小長井誠
"AFM超微細酸化法により作製したNb/Nb oxide系単一電子トランジスタ"
第57回応用物理学会学術講演会、9a-B-11、1996年秋季、福岡
- [10] 三浦成久、石井英明、山田明、小長井誠
"走査型電子顕微鏡により堆積したカーボン性薄膜の評価"
第44回応用物理学関係連合講演会、30a-Y-4、1997年春季、千葉
- [11] 白樫淳一、石井正巳、松本和彦、三浦成久、小長井誠
"AFM超微細酸化法により作製したNb/Nb oxide系単一電子トランジスタ(2)"
第44回応用物理学関係連合講演会、30a-SZQ-27、1997年春季、千葉
- [12] 三浦成久、沼口鉄幸、山田明、小長井誠
"カーボンコンタミネーションドットを用いた多重トンネル接合"
第58回応用物理学会学術講演会、4a-ZK-11、1997年秋季、秋田
- [13] 白樫淳一、松本和彦、三浦成久、小長井誠
"室温Nb/Nb oxide系単一電子トランジスタ"
第58回応用物理学会学術講演会、4p-C-7、1997年秋季、秋田
- [14] 沼口鉄幸、三浦成久、山田明、小長井誠、白樫淳一
"電子ビーム励起堆積法を用いた単電子トランジスタの室温動作"
第45回応用物理学関係連合講演会、30a-YE-1、1998年春季、東京 (発表予定)

< Others >

- [1] N. Miura, H. Ishii, A. Yamada and M. Konagai
"Electron-Beam-Induced Deposition of Carbonaceous Material and Its Applications to Microstructure Fabrication"
3rd International Symposium on Quantum Effect Electronics, November 7, 1996, Tokyo, Japan. Program and Abstracts, pp. 44-47.
- [2] A. Yamada, N. Miura, T. Numaguchi and M. Konagai
"Fabrication of Single-Electron Transistors by Beam-Induced Reaction Processes"
4th International Symposium on Quantum Effect Electronics, October 16, 1997, Tokyo, Japan. Program and Abstracts, pp. 35-39.

< Award >

第3回 応用物理学会 講演奨励賞

白樫淳一、松本和彦、三浦成久、小長井誠

"室温Nb/Nb oxide系単一電子トランジスタ"

第58回応用物理学会学術講演会、4p-C-7、1997年秋季、秋田

< 新聞、雑誌発表 >

- [1] 日刊工業新聞 1997年11月6日 (木) 「科学技術」欄
- [2] 電子情報通信学会誌 1/1998 pp.108 「NEWS」欄

電子ビーム励起たい積法による
室温動作単電子トランジスタの開発

東京工業大学工学部電気電子工学科小長井誠教授、山田明助教授の研究グループは、電子線を用いた直接加工技術を用いることにより、室温で動作する単電子トランジスタ (SET) の開発に初めて成功した。

SET は、電子一つ一つを制御することにより論理素子を構成するものであり、究極のデバイスとして期待されている。通常この SET は、図 1 に示すように金属細線および金属の微小ドットにより構成され、電子はこのドットを介して流れていく。このドットが極めて微小なとき、一つの電子がドットに入ると次の電子が入れなくなり電流が制限されるというクーロンブロッケード現象がある。SET は、この流れをゲート電極により制御したものである。しかしながら、この SET を作製するためには最先端の微細加工技術が必要であったり、極低温でしか特性が観測されないという欠点があった。

そこで本研究では電子ビーム励起たい積法に着目し、走査型電子顕微鏡 (SEM) を用いて 40 nm 程度の微小アモルファス状カーボンを作製することにより SET を作製した。加速電圧

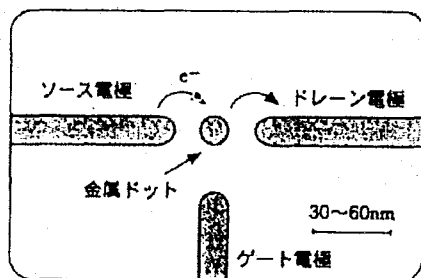


図1 単電子トランジスタ (SET) の模式図

は 30 kV、ビーム電流は 35 pA である。排気系には、油拡散ポンプを用いており、このポンプの残留オイルが電子ビーム照射により分解し、アモルファス状カーボンの形成種となる。本研究では、この市販 SEM を改造することなしに用いている。SET の作製時間は、この作製条件で約 20 分程度である。

本研究で作製した素子の電気的特性を図 2 に示す。ソース・ドレイン間電圧を 0.1 V、ゲート電圧を -20 V から 30 V まで変化させて測定した。測定は室温で行った。ゲート電圧を変化させることにより、ドレイン電流が流れる状態と流れない状態が実現されており、典型的な SET の特性を示している。これは、ゲート電圧の印加によりドット部分の静電ポテンシャルが変化し、クーロンブロッケードの起きる条件と起きない条件が交互に現れるためである。

今後は、本手法の単電子メモリへの応用が期待される。[関連記事] 日刊工業新聞 1997.11.6 (担当委員 山路哲男)

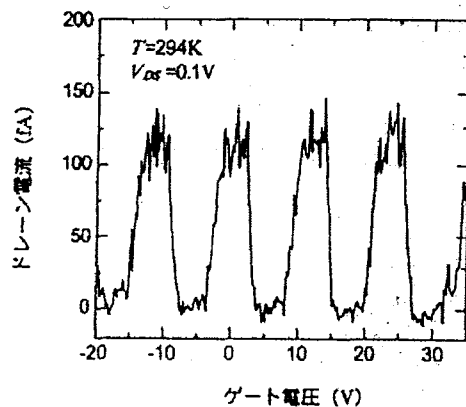


図2 得られた素子の室温におけるドレイン電流とゲート電圧特性 (ゲート振動)